RHEINISCHE FRIEDRICH–WILHELMS–UNIVERSITÄT
BONN

Submillimeter Studies of Low-Mass Star Forming Regions

Dissertation

zur

Erlangung des Doktorgrades (*Dr. rer. nat.*)

der

Mathematisch-Naturwissenschaftlichen Fakultät

der

Rheinischen Friedrich–Wilhelms–Universität, Bonn

vorgelegt von

Anastasia Eleni TSITALI

aus

Thessaloniki, Greece

Bonn 2013

Angefertigt mit Genehmigung der Mathematisch-Naturwissenschaftlichen Fakultät der Rheinischen Friedrich–Wilhelms–Universität Bonn

1. Gutachter: Prof. Dr. Karl Menten
2. Gutachter: Prof. Dr. Pavel Kroupa
Tag der Promotion: 08.04.2014
Erscheinungsjahr: 2014

Diese Dissertation ist auf dem Hochschulschriftenserver der ULB Bonn unter
http://hss.ulb.uni-bonn.de/diss_online elektronisch publiziert

RHEINISCHE FRIEDRICH–WILHELMS–UNIVERSITÄT BONN

Abstract

by Anastasia Eleni Tsitali

for the degree of

Doctor rerum naturalium

The nearby molecular clouds Chamaeleon I and III (Cha I, Cha III) constitute excellent targets for low-mass star formation studies. Their large starless core population presents the opportunity to explore the earliest phases of star formation, prior to the formation of the protostellar object. The prestellar phase can offer valuable constraints for the initial conditions necessary for star formation to occur. The apparent similarity between the stellar initial mass function and the core mass distribution suggests that the prestellar core fragmentation plays a determining role in the subsequent evolution of the self-gravitating dense cores to stars. A deep understanding of the physical processes taking place during the prestellar phase and the dynamical evolution of these objects is therefore essential in order to constrain the multiple core collapse models and obtain a complete picture of star formation.

The first part of the thesis focusses on an object in the Cha I molecular cloud, Cha-MMS1. Cha-MMS1 is very likely to be in the theoretically predicted intermediate evolutionary phase between the prestellar and protostellar phases, the first hydrostatic core. The dynamical state of this object is examined through molecular line observations obtained with the APEX and Mopra telescopes. The molecular emission is modelled using a radiative transfer code in order to derive constraints on the kinematics of the envelope, which are then compared to MHD simulations for the first core phase. Both the derived internal luminosity of Cha-MMS1 and the constrained infall velocity structure of the envelope are consistent with predictions of MHD simulations for the first core phase. Excess emission in high-density tracers additionally suggests the possible presence of a compact, slow outflow driven by Cha-MMS1, which is the main predicted observational signature of first cores. Overall, Cha-MMS1 does not belong to the prestellar phase. The kinematics of its envelope are consistent with a first hydrostatic core candidate, but it cannot be ruled out that this object might also be a Class 0 protostar. A future detection of a slow, compact outflow with ALMA would serve as definite proof that Cha-MMS1 is indeed a first hydrostatic core.

The second part of the thesis presents a molecular line survey that was conducted with the APEX and Mopra telescopes toward the starless core populations of the Cha I and III molecular clouds. Cha I is an actively star-forming cloud, whereas Cha III shows no sign of ongoing star formation. The main goal of this work is to determine the driving factors that have led to the strikingly different star formation activities in Cha I and III and to deduce the future dynamical evolution of the clouds. The

kinematics of the starless cores are examined through a virial analysis and a search for infall motions. The chemical differences between Cha I and III are investigated through the observed fractional molecular abundances of the cores and by a comparison to predictions of chemical models. It is observationally derived that 15–30 % of the Cha I cores and 10–25 % of the Cha III cores will likely become prestellar and therefore form stars in the future. Interactions between the starless cores will not be dynamically significant in either cloud, thus eliminating competitive accretion as a likely process in these clouds. The analysis of the kinematics in the cores shows that turbulence has likely not affected the different star formation activities in Cha I and III. Nevertheless, a difference in chemistry between Cha I and III is seen in the fractional abundances of $C^{18}O$ and CH_3OH. The HC_3N to N_2H^+ abundance ratio is then examined as an evolutionary indicator in the prestellar phase through comparison to predictions of collapse and static chemical models. In the framework of these models, this abundance ratio is proven to be a good evolutionary tracer. An evolutionary "gradient" was thus seen within Cha I, with the cores in its southern part being younger than the cores in the central region of Cha I. The suggested interpretation is that the southern Cha I cores will undertake the same evolutionary path as the central Cha I cores, given that they belong to the same cloud. Interestingly, the Cha III cores have similar HC_3N to N_2H^+ abundance ratios as the southern Cha I cores. Therefore, both the measured HC_3N to N_2H^+ abundance ratio and the detected infall signatures indicate that Cha III is younger than Cha I, and therefore on the verge of forming stars. This conclusion points to the existence of an evolutionary sequence in the Chamaeleon complex, with the youngest Cha III cloud to the eldest Cha I cloud, and with Cha II likely at an intermediate evolutionary state. The dynamical state of Cha II is therefore worth investigating in the future through both an unbiased, continuum survey as well as molecular line observations.

To Annie, Anastasia & Zisis

Words are flowing out like endless rain into a paper cup
They slither wildly as they slip away across the universe.
Thoughts meander like a restless wind inside a letter box
They tumble blindly as they make their way
across the universe.

John Lennon, 'Across the Universe'

Contents

Chapter 1

From molecular clouds to star forming cores

There is no matter as such – mind is the matrix of all matter.

Max Planck

Contents

1.1 Molecular clouds and dense cores

Stars are born within the overdense, gaseous, and dusty regions in molecular clouds, mostly in clusters (Lada & Lada, 2003). Molecular clouds are found in the dense environment of the galactic disc (e.g., Solomon et al., 1985), orbiting around the galactic centre. Their main characteristic is that their gaseous content is mostly in molecular form as opposed to other regions in the galaxy consisting of atomic, neutral gas or photoionised HII gas. The transition from atomic to molecular phase occurs by compression of matter within the spiral arms (e.g., Solomon & Rivolo, 1989; Heyer & Terebey, 1998). HII regions are found close to massive OB stars or supernova remnants, which heat up and ionise the gas in their vicinity through strong stellar winds (e.g., Diaz-Miller et al., 1998).

The factor that plays the critical role in determining the state of galactic gas (ionised, atomic, molecular) is the density of the material itself. The gas density can be altered by many processes, for example by shock waves produced by supernova explosions, propagating in the

neighbouring regions and compressing the matter on their way through the Interstellar Medium (ISM) (e.g., Mac Low & Klessen, 2004a; Mac Low, 2003). As the ISM is predominantly composed of hydrogen with most of the remaining matter being in the form of helium (mass fractions $X_H \sim 0.72$ and $Y_{He} \sim 0.27$; Przybilla et al., 2008), it follows that clouds within the ISM also have hydrogen as their main constituent. The densities of atomic regions range from ~ 0.6 cm^{-3} (warm HI gas, ~ 5000 K) to ~ 30 cm^{-3} (cool HI gas, ~ 100 K), whereas molecular gas can have densities of ~ 100 cm^{-3} (diffuse H_2, ~ 50 K) to $\sim 10^3 - 10^6$ cm^{-3} (dense H_2, $\sim 10 - 50$ K)[1]. In general, the more diffuse and the less dense the matter is, the easier it can be penetrated by UV radiation and cosmic rays, which heat up the gas to higher temperatures. The high density of molecular clouds acts as a shield mechanism, which prevents UV radiation from penetrating and ionising the gas within the deeper regions of the cloud (e.g., Krumholz, 2012). A molecular region is usually surrounded by less dense atomic gas (HI) envelopes, both on small and large scales (e.g., Bohlin et al., 1978; Elmegreen & Elmegreen, 1987; Nguyen Luong et al., 2011). There is, therefore, a progression from atomic to molecular gas that is driven by the external pressure and density gradient (e.g., Elmegreen, 1993).

Molecular clouds (e.g., Fig. 1.1) vary in size and matter content, but the largest ones are known as Giant Molecular Clouds (GMCs). GMCs, such as the Orion or Taurus molecular clouds within the Gould Belt (Herschel, 1847; Gould, 1879) [2] in our galaxy have typical masses and diameters of $\sim 10^5$–10^6 $M_\odot$ and ~ 50 pc, respectively (e.g., Blitz, 1993; Williams et al., 2000). Regions of overdensity with respect to their surroundings in the molecular clouds are usually referred to as dense cores (see e.g., Williams et al., 2000; Ward-Thompson et al., 2007). Dense cores contain the necessary material for star formation to occur and are therefore the precursors of stars, while molecular clouds are thought of as stellar nurseries. A dense core may form a single star or a binary, while regions containing multiple dense cores (which might therefore form multiple stars) are called cluster-forming cores (see Ward-Thompson et al., 2007) or star-forming clumps (Williams et al., 2000). There are two main theories regarding how dense cores are formed: the first is in favour of a slow, quasi-static formation with an evolution governed by ambipolar diffusion (e.g., Mouschovias, 1991; Mouschovias et al., 2006) or the local dissipation of turbulence (e.g., Myers & Lazarian, 1998). The second theory comprises of a fast, dynamic core evolution whereby density enhancements are caused by supersonic turbulence (Hartmann et al., 2001; Ballesteros-Paredes et al., 2003). Recent studies performed with the *Herchel* Space Telescope indicate that the formation of filaments precedes core formation, and the cores form once filaments become gravitationally unstable and fragment into cores (see e.g., André et al., 2010; Fiege & Pudritz, 2000).

1.1.1 The role of dust grains in clouds

Even though molecular clouds are primarily made of gas, one of their important, albeit less abundant, constituents that defines many of their properties is dust. Dust grains have sizes of ~ 0.1 μm and within the dense environment of the cores, they are usually found in the form of silicates and carbon compounds. Their property of absorbing optical starlight and

[1] Values for densities and temperatures were obtained from Draine (2011).

[2] A "ring" (as seen in projection) in our galaxy, at an inclination of $\sim 20^\circ$ to the galactic plane containing several molecular clouds within a distance of 500 pc.

Figure 1.1: The Chamaeleon I molecular cloud. *Credit:* G. Rhemann & Luhman (2008).

therefore obscuring embedded young stellar objects and background stars, is the reason why molecular clouds are often referred to as 'dark clouds' (see Fig. 1.2). This light attenuation, or "extinction", provides a useful measure of the dust content in clouds, and corrections for the extinction are significant to unveil "hidden" star populations. Dust acts as a "coolant" of the dense gas by re-emitting the absorbed starlight in the infrared within the dense regions, but it can also operate as a heating mechanism in more diffuse gas when UV radiation is present and photoelectrons are ejected from the grains' surface.

Dust grains greatly influence the chemical composition of clouds, as their surfaces serve as catalysts for chemical reactions (e.g., Watson & Salpeter, 1972). As gas molecules and

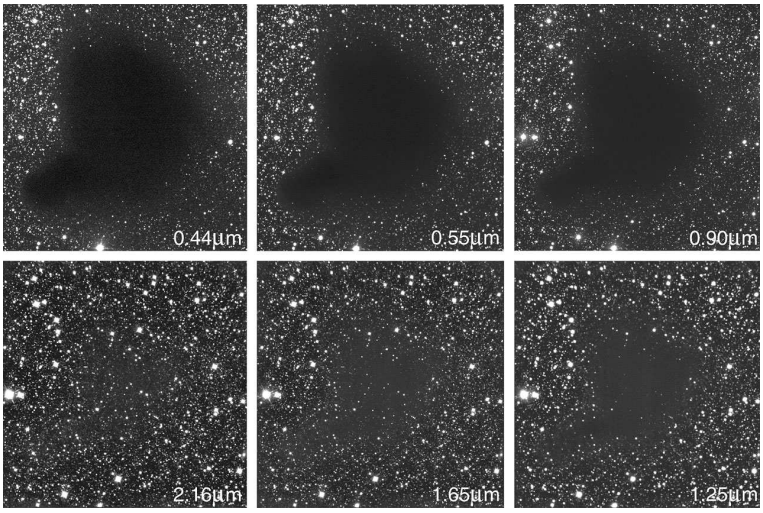

Figure 1.2: The 'dark cloud' Barnard 68 (d ~ 160 pc) in Ophiuchus. The cloud suffers from extinction at short wavelengths making it opaque to starlight, while it gradually becomes more transparent towards longer wavelentgths in the near-infrared. *Credit: ESO*.

atoms "stick" to the grains' surface in the cold inner parts of the dense cores ("freezing-out" process, "depletion" of molecules), they are able to react with each other by moving across their surface, thus forming new molecules. For instance, the formation of H_2 from H is thought to be primarily catalysed by dust grains (e.g., Gould & Salpeter, 1963). These new molecules are then desorbed into the gas phase once the temperature within the dense core has sufficiently increased from shock waves or once a protostellar object starts producing energy (see Sect. 1.2) so that it allows evaporation from the grain surface. Finally, their feature of polarising light by attenuating starlight along the grain's long axis, as well as the property to align their short axis to the magnetic field lines, allows us to use them as a diagnostic tool to determine the orientation of the magnetic field in molecular clouds (Hiltner, 1949; Hall, 1949; Lazarian, 2007).

1.2 The stability of clouds

The formation of stars is, in principle, a battle between the inward force of self-gravity and the outward force exerted by the internal pressure within one condensation, in which battle self-gravity must be the winning force for a star to eventually form. In the case of a stronger outward pressure, the matter within a condensation slowly disperses, with self-gravity not being able to hinder the destructive forces of pressure. In the scenario of a dense core with its self-gravity dominating over the thermal pressure, the gas becomes *gravitationally unstable* and starts collapsing towards its centre of mass. It thus leads to a core of gradually increasing density from which one or more stars may form. An easy way to quantify this process is using the so-called Jeans mass and Jeans radius.

1.2.1 Jeans theorem

The Jeans theorem is a simple way to examine the stability of clouds and is valid under the assumptions of an isothermal, spherical and initially static cloud with a uniform density. As clouds can, in reality, have a very irregular morphology and inner turbulence (condition of an initially static cloud is unrealistic), this analysis cannot provide an accurate description of instabilities within the clouds. Nevertheless, it can serve as a first and simple step towards assessing a cloud's dynamical state.

We assume that a spherical cloud of radius r, described by an initial density ρ_0, is perturbed by a random fluctuation that creates a density enhancement. If the motion of the gas is approximated as a fluid, then the force, F, acting on its surface is (following equations from Ward-Thompson & Whitworth, 2011):

$$-\oint_A P \, \mathrm{d}A = -\int_V \nabla P \, \mathrm{d}V \,, \tag{1.1}$$

where A is the surface area of the fluid, V its volume, and P the pressure. Since the force per unit volume is $-\nabla P$, the acceleration, $\alpha = \frac{\mathrm{d}\mathbf{v}}{dt}$, due to pressure becomes

$$\mathbf{F} = m\,\boldsymbol{\alpha} \Leftrightarrow \frac{\mathbf{F}}{V} = \frac{m}{V}\,\boldsymbol{\alpha} \Leftrightarrow -\nabla P = \rho\,\boldsymbol{\alpha} \Leftrightarrow \frac{d\mathbf{v}}{dt} = \frac{-\nabla P}{\rho}. \tag{1.2}$$

The vector quantities are shown in bold. The pressure of the spherical cloud can then be analytically described as

$$\left.\begin{aligned} P &= c_s^2\,\rho_0 \\ P &\sim \nabla P\, R \end{aligned}\right\} \Rightarrow \frac{\nabla P}{\rho_0} = \frac{c_s^2}{R} \Rightarrow \frac{\mathrm{d}v}{\mathrm{d}t} = \frac{c_s^2}{R}, \tag{1.3}$$

where $c_s = \sqrt{\frac{k_b T}{m_{mol}}}$ is the isothermal speed of sound and m_{mol} is the mean molecular mass of the gas. On the other hand, the *magnitude* of the inward gravitational acceleration, g, can be described as

$$\left.\begin{aligned} g &= -\frac{G\,M}{R^2} \\ M &\sim \rho_0\, R^3 \end{aligned}\right\} \Rightarrow g \sim -\,G\,\rho_0\,R. \tag{1.4}$$

The magnitude of the net acceleration of the medium in the radial direction therefore is

$$\frac{dv}{dt} = \frac{c_s^2}{R} - G\,\rho_0\,R. \tag{1.5}$$

A positive net acceleration indicates that the internal pressure exceeds self-gravity, therefore hindering the matter to collapse inwards. If, however, the net acceleration is negative, that signifies that self-gravity overpowers the internal pressure and the cloud becomes *gravitationally unstable*. It therefore collapses under its own gravity. Hence, the requirement for gravitational collapse is

$$\frac{c_s^2}{R} < G\,\rho_0\,R \Rightarrow R > \frac{c_s}{\sqrt{G\,\rho_0}}. \tag{1.6}$$

The radius of the cloud must therefore be larger than the critical Jeans radius, R_J, in order for gravitational collapse to occur. The equivalent (Jeans) mass, M_J, is the minimum mass required for a cloud to become gravitationally unstable

$$M_J \sim \frac{4\pi R_J^3 \rho_0}{3} \sim \frac{4\pi c_s^3}{3\sqrt{G^3\,\rho_0}}. \tag{1.7}$$

If a core were to collapse in the absence of an opposing internal pressure, then the time it would need to freely collapse under its own gravity is called the free-fall time (Spitzer, 1978) and is given by

$$t_{ff} = \sqrt{\frac{3\pi}{32G\rho}}. \tag{1.8}$$

There are many physical processes that can support a core against self-gravity and either merely delay or halt core collapse. Some of those are thermal pressure generated by particle collisions, turbulent motions (which can both help and hinder infall), and magnetic fields.

1.2.2 Virial theorem

The virial theorem gives the condition for dynamical equilibrium of spherical systems. Its general form includes the kinetic, gravitational, rotational, external pressure, internal pressure, and magnetic energy terms. It can be derived by the equation of motion, which is expressed as (McKee, 1999):

$$\rho\frac{\mathrm{d}\mathbf{v}}{\mathrm{d}t} = -\nabla P + \frac{1}{4\pi}(\nabla\times\mathbf{B})\times\mathbf{B} + \rho\mathbf{g}. \tag{1.9}$$

A full derivation of the virial theorem can be found in Ward-Thompson & Whitworth (2011) and Draine (2011). The virial theorem finally reads (McKee, 1999)

$$\frac{1}{2}\ddot{I} = 2E_{\mathrm{k,th,tot}} + E_{\mathrm{mag}} + E_{\mathrm{g}}, \tag{1.10}$$

where I is the cloud moment inertia,

$$I = \int r^2 \mathrm{d}m, \tag{1.11}$$

and $E_{\mathrm{k,th,tot}}$ is the sum of the internal and external kinetic energies (the subsctript *th* is used to emphasize that pressure effects are also taken into account):

$$E_{\mathrm{k,th,tot}} = E_{\mathrm{k,th,int}} - E_{\mathrm{k,th,ext}}. \tag{1.12}$$

If the ambient external pressure on the cloud, P_{ext}, is constant, then

$$E_{\mathrm{k,th,ext}} = \frac{3}{2}P_{\mathrm{ext}}V. \tag{1.13}$$

The sum of the internal thermal and kinetic energies is given by (see McKee, 1999):

$$E_{\mathrm{k,th,int}} = \int_V \left(\frac{3}{2}P_{\mathrm{th}} + \frac{1}{2}\rho v^2\right)\mathrm{d}V \Bigg\} \Rightarrow E_{\mathrm{k,th,int}} = \int_V \left(\frac{3}{2}\rho(c_s^2 + \frac{1}{3}v^2)\right)\mathrm{d}V, \tag{1.14}$$
$$P_{th} = \rho c_s^2. \Big\}$$

where $\frac{1}{M}\int(c_s^2 + \frac{1}{3}v^2)\mathrm{d}M$ is the *velocity dispersion* squared of the cloud (McKee, 1999):

$$\sigma^2 = \frac{1}{M}\int(c_s^2 + \frac{1}{3}v^2)\mathrm{d}M \Rightarrow \sigma^2 = \frac{P_{\mathrm{int,mean}}}{\rho}. \tag{1.15}$$

We can re-write equation 1.14 as

$$E_{\mathrm{k,th,int}} = \frac{3}{2}P_{\mathrm{int,mean}}V \tag{1.16}$$

We therefore obtain,

$$E_{\mathrm{k,th,int}} - E_{\mathrm{k,th,ext}} = \frac{3}{2}(P_{\mathrm{int,mean}} - P_{\mathrm{ext}})V. \tag{1.17}$$

The potential energy from self-gravity alone, E_g, can be estimated as

$$E_g = -\frac{3}{5}a\left(\frac{GM^2}{R}\right) \tag{1.18}$$

for a spherical cloud, where the value of a depends on the cloud's density distribution. Substituting these terms into equation 1.10 we get

$$\frac{1}{2}\ddot{I} = 3(P_{\mathrm{int,mean}} - P_{\mathrm{ext}})V - \frac{3}{5}a\left(\frac{GM^2}{R}\right) + E_{\mathrm{mag}} \tag{1.19}$$

The term due to the magnetic field is analysed in Sect 1.2.2.3. For a state of equilibrium (steady-state), it is required that $\ddot{I} = 0$. Therefore, the equation for virial *equilibrium* is

$$3(P_{\mathrm{int,mean}} - P_{\mathrm{ext}})V - \frac{3}{5}a\left(\frac{GM^2}{R}\right) + E_{\mathrm{mag}} = 0. \tag{1.20}$$

1.2.2.1 Virial mass

We first consider the case of a nonrotating, unmagnetised ($E_{\mathrm{mag}} = 0$) spherical cloud with no external pressure ($P_{\mathrm{ext}} = 0$). The virial theorem states that for such a system to be in equilibrium the following condition must apply:

$$E_g + 2E_{\mathrm{k,th,int}} = 0, \tag{1.21}$$

where the gravitational energy for a spherical cloud is

$$E_g = -\frac{3aGM^2}{5R}, \tag{1.22}$$

where a depends on the density distribution of the cloud. For a uniform sphere, $a = 1$. The internal kinetic energy can be expressed in terms of the gas velocity (Ward-Thompson & Whitworth, 2011):

$$E_{\mathrm{k,th,int}} = \frac{3}{2}P_{\mathrm{int,mean}}V \Rightarrow E_{\mathrm{k,th,int}} = \frac{3}{2}M\sigma^2 \sim \frac{1}{2}Mv^2 \tag{1.23}$$

The variables v and σ are the rms velocity (square root of average velocities-squared) and the observed velocity dispersion, respectively. Combining these equations we obtain the critical mass for equilibrium, called the virial mass:

$$M_{\mathrm{vir}} = \frac{5R\sigma^2}{aG} \sim \frac{5Rv^2}{3aG} \tag{1.24}$$

A core with a mass greater than its virial mass will collapse under its own gravity.

1.2.2.2 Bonnor-Ebert mass

For a spherical, unmagnetised ($E_{\rm mag} = 0$), isothermal core in hydrostatic equilibrium ($v = 0$), bounded by a constant external pressure, $P_{\rm ext}$, and having an internal pressure, $P_{\rm th}$, the condition for virial equilibrium becomes

$$E_g + 3(P_{int,mean} - P_{\rm ext})V = 0 \tag{1.25}$$

Since $v = 0$, the mean internal pressure is only a function of the density and the isothermal sound speed. If the sound speed (c_s) is constant then

$$P_{int,mean} = \rho c_s^2 \text{ (from equation 1.14).} \tag{1.26}$$

If the gravitational energy can be expressed as $-\frac{3aGM^2}{5R}$, with a being a constant that depends on the density distribution of the cloud, then the virial equilibrium equation is (Draine, 2011):

$$-\frac{3aGM^2}{5R} + 3Mc_s^2 - 4\pi R^3 P_{\rm ext} = 0 \tag{1.27}$$

Solving for the external pressure we obtain (Draine, 2011):

$$P_{\rm ext} = \frac{1}{4\pi R^3}\left(3Mc_s^2 - \frac{3aGM^2}{5R}\right). \tag{1.28}$$

The gas can remain in equilibrium as long as the external pressure does not exceed a certain value. This maximum pressure can be found by maximising equation 1.28. For any external pressure not exceeding the critical value, there is a critical mass above which the gas is no longer in equilibrium. This is the Bonnor-Ebert (BE) mass (Bonnor, 1956; Ebert, 1957) and it is given by

$$M_{\rm BE} = 1.18\frac{c_s^4}{G^{3/2}P_{\rm ext}^{1/2}}. \tag{1.29}$$

1.2.2.3 Collapse of a magnetised core

Magnetic fields are present throughout the ISM and play an important role in supporting molecular clouds against self-gravity. In the simple case where the magnetic energy dominates over the kinetic energy, ie., $E_{\rm mag} \gg E_{\rm k,th,tot}$, the kinetic energy term can then be omitted. In this case, the condition for virial equilibrium becomes (Ward-Thompson & Whitworth, 2011):

$$E_{\rm mag} = -E_g \Rightarrow E_{\rm mag} = \frac{3GM^2}{5R}. \tag{1.30}$$

with the gravitational energy being that of a uniform density sphere. The magnetic energy is given by (Ward-Thompson & Whitworth, 2011):

$$E_{\rm mag} \sim \frac{B_{\rm mean}^2 V}{8\pi} \tag{1.31}$$

where $B_{\rm mean}$ is the combination of the magnetic field threading the cloud and that acting on its surface. The magnetic flux within the cloud, Φ, can be computed as

$$\Phi = \int_0^R 2\pi r B {\rm d}r \tag{1.32}$$

Therefore, the magnetic energy term becomes,

$$E_{\rm mag} = \frac{1}{8\pi} B^2_{\rm mean} \frac{4}{3}\pi R^3 \Rightarrow E_{mag} = \frac{\Phi^2}{6\pi^2 R} \tag{1.33}$$

The magnetic flux Φ within the cloud remains constant, as it is a conserved quantity. During a small contraction or expansion of the cloud, the ratio of E_g to E_{mag} then remains constant, as both terms are proportional to R^{-1}. There is a critical mass above which the gravitational energy overcomes the magnetic energy and collapse begins.

We follow a slight contraction of the cloud to derive this critical value (equations from Ward-Thompson & Whitworth, 2011). A contraction leads to a compression of the magnetic field lines, and hence, a higher magnetic field strength. Since the magnetic flux is conserved

$$\Phi_0 = \Phi_1 \Rightarrow R_0^2 B_0 = R_1^2 B_1 \Rightarrow B_1 = \left(\frac{R_0}{R_1}\right)^2 B_0 \tag{1.34}$$

where B_1 is the value of the magnetic field after the compression, at time t_1. This corresponds to a magnetic field energy of

$$E_{mag,1} = \frac{1}{8\pi} B_1^2 V = \frac{R_0^4 B_0^2}{6R_1} \tag{1.35}$$

There is an extra and equal term for the magnetic field energy, which finally gives

$$E_{\rm mag,1} = \frac{R_0^4 B_0^2}{3R_1} \tag{1.36}$$

For virial equilibrium to hold at time t_1 it is required that

$$E_{\rm mag,1} = -E_{g,1} \Rightarrow \frac{R_0^4 B_0^2}{3R_1} = \frac{3GM^2}{5R_1} \Rightarrow M_{\rm cr} = R_0^2 B_0 \sqrt{\frac{5}{9G}} \tag{1.37}$$

where $M_{\rm cr}$ is the critical mass above which the cloud becomes unstable. Therefore, there exists a critical mass-to-flux ratio (e.g., Mouschovias, 1976; Crutcher, 1999) such that above this value the gravitational energy overcomes the magnetic stresses and the cloud succumbs to its collapse and eventually forms a star. If the mass-to-flux ratio is below the critical value, then the magnetic field support is too strong for gravitational collapse to occur. The critical ratio reads (Ward-Thompson & Whitworth, 2011):

$$\left(\frac{M}{\Phi}\right)_{\rm cr} \sim \frac{M_{cr}}{R_0^2 B_0} \sim \frac{M_{cr}}{R_1^2 B_1} \sim \sqrt{\frac{5}{9G}}. \tag{1.38}$$

A cloud with a mass-to-flux ratio larger than the critical value is called magnetically *supercritical*, while in the opposite case it is referred to as magnetically *subcritical*:

$$\left(\frac{M}{\Phi}\right)_{\rm cl} > \left(\frac{M}{\Phi}\right)_{\rm cr} \Rightarrow \text{supercritical} \Rightarrow \textit{unstable} \text{ against collapse}$$
$$\left(\frac{M}{\Phi}\right)_{\rm cl} < \left(\frac{M}{\Phi}\right)_{\rm cr} \Rightarrow \text{subcritical} \Rightarrow \textit{stable} \text{ against collapse}$$

1.3 From dense cores cores to protostars

1.3.1 Ambipolar diffusion

So far, estimates of the mass-to-flux ratio in molecular clouds and dense cores indicate values of approximately a factor ~ 2 higher than the critical ratio for collapse (e.g., Crutcher, 1999; Crutcher et al., 2004; Kirk et al., 2006; Troland & Crutcher, 2008), or roughly critical to four times supercritical (Falgarone et al., 2008). These studies confirm the importance of the magnetic fields during the star formation process, especially at core densities $\sim 10^3$–10^4 cm^{-3} (Troland & Crutcher, 2008), and indicate that ambipolar diffusion should be accounted for in star formation models. Finally, the observations are indicative of equipartition of the kinetic and magnetic energies, suggesting that turbulence also provides support against core collapse (e.g., Zweibel & McKee, 1995; Crutcher, 1999; Falgarone et al., 2008).

The ionisation degree within the dense cores plays a major role in determining the core's subsequent evolution (e.g., Ciolek & Mouschovias, 1995). It is difficult to accurately determine observationally, as it is largely dependent on the cosmic ray ionization rate (e.g., Herbst & Klemperer, 1973). Studies have indicated values around e.g., 10^{-8}–10^{-6} (Caselli et al., 1998) and $10^{-7.5}$–$10^{-6.5}$ (Williams et al., 1998) in dense cores, and an even lower value for a core near dynamic collapse, i.e. $\sim 10^{-9}$ (Caselli et al., 2002d). The ions, free electrons, and charged dust grains gyrate around the magnetic field lines, and additionally couple the neutral gas to the magnetic field through frequent collisions. It is therefore expected that during the contraction of a core, both gas and field lines move as one and the mass-to-flux ratio remains constant (flux freezing; e.g., Mouschovias, 1976). This has two direct implications. First, as the gas can mostly only move parallel to the magnetic field thus providing support along the opposite direction (e.g. Li & Shu, 1996), the core acquires a flattened shape with the elongated direction perpendicular to the magnetic field lines. Secondly, any collapse motions perpendicular to the field lines proceed in a very slow manner and tend to compress the magnetic field lines at the centre of the core. The magnetic field, therefore, acquires an "hour-glass" shape. This is usually referred to as "hour-glass pinching", an example of which can be seen in the observed magnetic field vectors of the embedded protostellar system NGC1333 - IRAS4A (Figure 1.3) (Girart et al., 2006). Hints of magnetic pinching are also found in source-averaged maps of Class O protostars (e.g., Chapman et al., 2013), in other dense cores (e.g., Lai et al., 2002; Sugitani et al., 2010), hot molecular cores (e.g., Girart et al., 2009), or other young star-forming regions (e.g., Rao et al., 2009).

Flux-freezing is expected to be very efficient in regions with a high fractional ionisation. This is especially the case in diffuse gas, where cosmic ray and UV ionisation is a frequent process. The cosmic ray ionisation rate is found to be around $\sim 10^{-16}$–10^{-18} s^{-1} in dense cores (e.g., Caselli et al., 1998), while it reaches $\sim 10^{-15}$ in diffuse clouds (e.g., McCall et al., 2003). Within these regions the ion-gas collision rate is high, thus ensuring that the magnetic field is coupled to the neutral gas through the ions. Nevertheless, since dense cores ($n \sim 10^4$ – 10^6 cm^{-3}) are mostly shielded from UV and cosmic ray ionisation, their fractional ionisation is very low. In such dense environments the flux-freezing approximation may fail. This allows the neutral gas to drift through the ions and collapse inwards parallel to the magnetic field lines. This drifting mechanism is called *ambipolar diffusion* (e.g., Mouschovias, 1977).

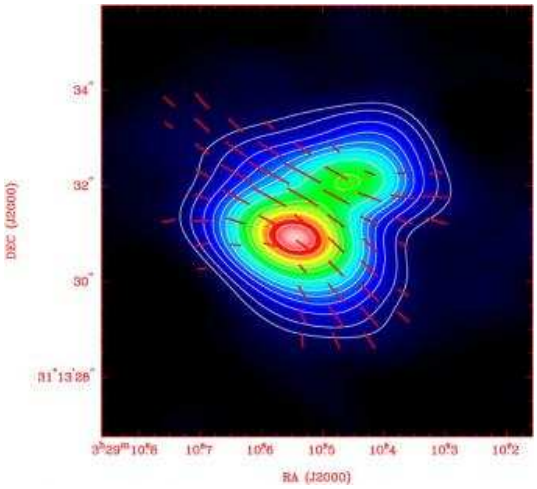

Figure 1.3: Magnetic field line vectors plotted in red, derived from dust polarisation measurements in the embedded protobinary NGC1333 - IRAS4A (Girart et al., 2006). The 877 μm dust continuum map (angular resolution $1.56'' \times 0.99''$) obtained with the Submillimeter Array (SMA) is shown in the background. The x-axis of the box corresponds to a size of $\sim$ 1700 AU.

In general, an increase of the degree of ionisation seems to decrease the ambipolar diffusion rate and as a result, increase the magnetic support of the cloud (Fiedler & Mouschovias, 1993). Through ambipolar diffusion, the decoupled neutral gas contracts towards the centre and the mass-to-flux ratio gradually increases until it finally exceeds the critical value and the core becomes magnetically supercritical, while still being engulfed by the subcritical, magnetically supported cloud (e.g., Mouschovias, 1977; Fiedler & Mouschovias, 1993; Ciolek & Mouschovias, 1994a). Through ambipolar diffusion cores that are initially magnetically subcritical can therefore become magnetically supercritical (Ciolek & Mouschovias, 1994a). The time required for ambipolar diffusion to take place and alter the state of a core from sub- to supercritical, is called the *ampibolar diffusion time-scale* (e.g., Spitzer, 1968; Mouschovias, 1979):

$$\tau_{AD} \propto \frac{\langle \sigma u \rangle}{\pi G m_H} \chi, \tag{1.39}$$

where $\chi = n_i/n_H$ is the fractional ionisation and $\langle \sigma u \rangle$ the average of the thermal velocity and collision cross-section. In conclusion, the ambipolar diffusion time-scale can be dynamically important for cores of high density and low fractional ionisation (e.g., Zweibel, 2002), which are initially magnetically subcritical. The predicted timescales for such clouds can last up to $\sim$ 10 times the local free-fall time in the absence of turbulence (e.g., Mouschovias, 1987). Observationally, lifetimes of 2-5 times the free-fall time have been estimated for dense cores (Ward-Thompson et al., 2007). In the case of a low density, subcritical core, with a high fractional ionisation, flux-freezing might never let ambipolar diffusion take place, thus hindering star formation.

1.3.2 Angular momentum problem

In the last sections the support of a cloud core by its internal pressure and magnetic field was examined but the role of its rotational kinetic energy has not yet been discussed. All objects in the galaxy are "born" with inherent rotational motions arising from their orbit around the galactic centre as well as from turbulent motions within the objects themselves. As angular momentum is conserved, is expected that the rotational energy within a collapsing core keeps increasing as its radius decreases:

$$E_{\rm rot} = \frac{1}{2} I\omega^2 = \frac{1}{5} MR^2\omega^2, \tag{1.40}$$

where spherical symmetry is assumed and ω is the angular velocity of the core. Since angular momentum is conserved, the initial rotational energy of the core, $E_{\rm rot,0}$, and its rotational energy at a later time, $E_{\rm rot,1}$, should be equal:

$$\omega_0 R_0^2 = \omega_1 R_1^2. \tag{1.41}$$

At this later time, the ratio of the rotational to gravitational energies should be equal in order for equilibrium to ensue. Assuming a gravitational potential energy of $|E_g| \propto \frac{GM^2}{R}$ and a rotational energy of $E_{\rm rot} \propto M\omega^2 R^2$ (see Ward-Thompson & Whitworth, 2011),

$$\frac{E_{\rm rot,1}}{|E_{\rm g,1}|} \propto \frac{M\omega_1^2 R_1^2}{GM^2/R_1} \sim 1 \Rightarrow \frac{M\omega_0^2 R_0^4/R_1^2}{GM^2/R_1} \sim 1 \Rightarrow \frac{E_{\rm rot,0}}{|E_{\rm g,0}|}\,\frac{R_0}{R_1} \sim 1. \tag{1.42}$$

The rotational and gravitational potential energies become equal at the critical radius:

$$R_{\rm rot,cr} \sim \frac{E_{\rm rot,0}}{|E_{\rm g,0}|} R_0. \tag{1.43}$$

Goodman et al. (1993) use the following analytical expression for the ratio of the rotational to gravitational energy for a sphere with a uniform density, which makes use of the observed velocity gradient, Gr, of a source:

$$\beta = \frac{1}{4\pi G\rho}\frac{Gr}{\sin^2 \mathrm{i}}, \tag{1.44}$$

with i being the inclination of the rotation axis to the line-of-sight. The critical radius is the smallest radius the core can contract to before the core's rotation halts the collapse, and it is dependent on the initial ratio of $E_{\rm rot}$ to $E_{\rm g}$ only. Observations of dense cores show that the rotational-to-gravitational energy ratio (β) has a value much less than 1 ($\sim$ 0.01–0.1; e.g., Goodman et al., 1993; Barranco & Goodman, 1998; Caselli et al., 2002a; Pirogov et al., 2003). Similar results are also found in theoretical studies (e.g., Jappsen & Klessen, 2004). These ratios imply radii far greater than the observed radii of stars, thus posing the problem that cores seem to have an excess of angular momentum that must be removed before being able to contract to the observed stellar radii ($\sim 10^8$ m). For instance, a value of $\beta \sim 0.006 - 0.02$ was found for the Chamaeleon I dense core Cha-MMS1 (Tsitali et al., 2013). Cha-MMS1 has a radius of $\sim$ 7130 AU, or $\sim 10^{15}$ m (Belloche et al., 2011a). The maximum value of $\beta \sim 0.02$ for Cha-MMS1 therefore gives a critical radius of 2×10^{13} m, which is still

$\sim 10^5$ times greater than a typical stellar radius. Therefore, there must be a mechanism in place that is responsible for removing angular momentum from the system so that a star can be formed (angular momentum problem; e.g., Spitzer, 1978; Bodenheimer, 1995; Belloche, 2013; Hennebelle, 2013).

One solution to this issue is provided by the magnetic fields threading the cores. As a core contracts and rotates simultaneously, the magnetic field lines experience both a strengthening effect due to compression and a twisting effect due to rotation. Due to the coupling of gas and the magnetic field, the inner core is in effect connected to material outside the "boundaries" of the core itself through the magnetic field lines that extend to the ISM. The twisting of the lines into helical shapes creates magnetic torques, which result in magnetorotational instabilities within the core. These instabilities can travel from the inner core to the region outside the core along the field lines, thus transfering angular momentum outwards. The propagating instabilities are known as torsional *Alfvén waves*, and this process of removing excess angular momentum is called *magnetic braking* (e.g., Mestel, 1985; Mouschovias, 1987). When a fraction of the core's mass is also expelled outwards along with the Alfvén waves, it acquires the form of a *bipolar outflow* with matter ejected from either magnetic pole of the core, which releases more angular momentum from the system. After sufficient angular momentum has been removed, the rotational support forces the core to a flattened morphology, which eventually leads to the formation of an *accretion disc* (e.g., Yorke et al., 1993, 1995; Yorke & Bodenheimer, 1999) around the central source (or protostar). Interactions of the stellar object with the accretion disk also lead to subsequent loss of angular momentum (see review; Belloche, 2013).

1.3.3 Starless and prestellar cores

The prestellar cores are a subcategory of the starless cores. Starless cores are dense cores without evidence for an embedded object (e.g., Beichman et al., 1986; di Francesco et al., 2007). A prestellar core is a starless core that is gravitationally bound and thus likely to form stars (Ward-Thompson et al., 1994; André et al., 2000; di Francesco et al., 2007; Ward-Thompson et al., 2007). Prestellar cores are characterised by flat inner density profiles that become proportional to r^{-2} after a few thousand AU (e.g., Ward-Thompson et al., 1994; Andre et al., 1996; Ward-Thompson et al., 1999). Steeper density profiles have been observed towards the "edges" of dense cores ($\propto r^{-3}, r^{-4}$; Bacmann et al., 2000; Alves et al., 2001). The density profiles of starless and prestellar cores are often consistent with a pressure bounded Bonnor-Ebert sphere (e.g., Alves et al., 2001; Kirk et al., 2005; Ballesteros-Paredes et al., 2007). The flat inner profiles are also consistent with predictions of ambipolar diffusion driven collapse models (Mouschovias, 1991; Ward-Thompson et al., 1994; Ciolek & Mouschovias, 1994b). As prestellar cores are very cold ($T \sim 10$ K), they mostly emit in the far-infrared and submillimeter wavelengths. Ground radio telescopes and space infrared observatories are, therefore, the most convenient tools for observing this initial phase of star formation.

As cores are usually optically thin in submillimeter dust emission, their mass can be derived from dust continuum observations. Assuming isothermality, their mass can be estimated

as (André et al., 2000):

$$M(R) = \pi R^2 < \Sigma >_R = \frac{S_\nu(\theta) d^2}{\kappa_\nu B_\nu(T_{\rm dust})}, \tag{1.45}$$

where $< \Sigma >_R$ is the average mass column density, $S_\nu(\theta)$ the dust continuum flux density, d the distance to the source, κ_ν the dust opacity, $B_\nu(T_{\rm dust})$ the Planck function, and θ the projected angular radius, R/d.

One way to judge if a core is prestellar is by comparing the core's dust mass to its *virial* mass, which takes both thermal and non-thermal motions into account through the observed velocity dispersion. A core is gravitationally bound if its dust mass exceeds half its virial mass. In this case, the core will not disperse under the effects of its inner turbulence and gravitational forces will likely lead to the subsequent collapse of the core and the formation of a star. When the core's mass is equal to its virial mass it is referred to as virialised, while if it exceeds this value it is said to be collapsing:

$$\left.\begin{array}{ll} \dfrac{M_{\rm core}}{M_{\rm vir}} > 0.5 & \Rightarrow \text{gravitationally bound} \\ \dfrac{M_{\rm core}}{M_{\rm vir}} = 1 & \Rightarrow \text{virialised} \\ \dfrac{M_{\rm core}}{M_{\rm vir}} > 1 & \Rightarrow \text{collapsing} \end{array}\right\} \Rightarrow \text{prestellar} \tag{1.46}$$

When the velocity information of a source is not available, then a Bonnor-Ebert or Jeans analysis can be performed to assess the dynamical state of the cores, assuming that the non-thermal kinetic energy is negligible.

1.3.4 First hydrostatic cores: the missing link

The theoretical predictions of Larson (1969) introduced for the first time an evolutionary stage intermediate that of the prestellar core phase and the protostellar phase. It was found that in the course of the gravitational collapse of a dense core, and before the formation of a protostar, a hydrostatic object forms called a first hydrostatic core (FHSC). The first core formation occurs after the isothermal phase of the collapse, when radiative cooling is no longer an efficient process within the core. An adiabatic core then forms at its centre in which thermal pressure and gravitational forces are at a balance. It has an initial central temperature of $\sim$ 170 K and a density of $\sim 2 \times 10^{-10}$ g cm^{-3}.

The FHSC is a short-lived phase, with typical lifetimes of a few 100 to a few 1000 yr, depending on the magnetisation level of the core. These objects are characterised by luminosities of less than ~ 0.25 L$_\odot$, and by slow, compact outflows with typical velocities of ~ 3 km s^{-1} and with an extent of $\sim 200 - 800$ AU (Commerçon et al., 2012). Detecting these slow, compact outflows is currently one of the main FHSC diagnostic signatures.

Due to their faint, and short-lived nature, detecting FHSCs is an observational challenge and only a handful of candidates have been detected so far. As they represent the first stage towards forming a protostar, gaining a deeper knowledge of their formation, evolution, and properties can offer significant constraints on the initial conditions of star formation.

1.3.5 Young stellar objects[3]

After the formation of the first core, the central temperature continues to rise. Once it exceeds $\sim$ 2000 K, the dissociation of H_2 begins. This process is very energy demanding and as a result the thermal pressure becomes unable to balance the gravitational forces and collapse once again ensues. This so-called "second collapse" leads to the formation of a central protostar, or "second core" (Larson, 1969). The evolution of a newly formed protostar towards a main-sequence star is usually split in four distinct phases. The objects in each of these four evolutionary phases are called Young Stellar Objects (YSOs), the first two of which describe the protostellar system and the last two the pre-main sequence object that has formed.

A common way to identify YSOs is through their spectral energy distributions (SEDs). Due to the significant amount of gas and dust surrounding a YSO, most of the star's radiation is absorbed and reprocessed to longer wavelengths. This excess infrared emission which stems from the star's disk and envelope results in SEDs that differ from a simple stellar photosphere spectrum. The shape of the SED can be used to categorize YSOs into groups of different evolutionary stages. The most commonly used classification system was introduced by Lada (1987), which divides YSOs into three classes depending on the spectral slope of their SED, α, computed for the range from 2 μm to 24 μm, and is given by

$$\alpha = \frac{dlog[\lambda F(\lambda)]}{dlog\lambda)}. \tag{1.47}$$

According to this system, Class I objects have $0 < \alpha \lesssim 3$, Class II YSOs have $-2 \lesssim \alpha \leq 0$, and finally Class III objects correspond to $-3 < \alpha \lesssim -2$. André et al. (1993) suggested the use of Class 0 objects for YSOs more deeply embedded and younger than Class I objects, whose envelope mass is greater than the stellar mass. Class 0 objects cannot be distinguished from Class I objects through their α values, but they can be distinguished empirically with submillimeter data. As they are deeply embedded, their detections in the infrared are often due to scattered light from their envelope while in several cases they are not detected at the shorter infrared wavelengths ($\lambda \lesssim 2$ μm). Greene et al. (1994) updated this classification, adding the "Flat Spectrum Sources" in the original system that can be thought of as an intermediate stage between the Class I and Class II phases. This final addition by Greene et al. (1994) led to the modification of the α value boundaries to $\alpha \geq 0.3$ (Class I), $-0.3 \leq \alpha < 0.3$ (Flat Sources), $-1.6 \leq \alpha < -0.3$ (Class II), and $\alpha < -1.6$ (Class III).

This system is regularly thought of as an evolutionary sequence, from the youngest deeply embedded Class 0 protostars, to the oldest Class III YSOs that are only left with the remains of an accretion disk. The spectral slope α therefore decreases as a YSO evolves, directly reflecting the decrease of the excess infrared emission due to the continuous envelope dissipation (Greene & Lada, 1996). The shape of the SED and the resulting spectral slope, however, are greatly affected by the inclination of the source, as they are purely observational properties, and one particular YSO could move from one Class to another depending on the viewing angle (Whitney et al., 2003; Dunham et al., 2006; Crapsi et al., 2008). For instance, a Class I source would exhibit a much flatter SED if it were viewed pole-on since its radiation would

[3] As summarised in Tsitali et al. (2010).

travel through a less opaque medium, whereas edge-on inclinations would result in considerable dust and envelope emission in the far-infrared and submillimeter wavelengths. Therefore a classification system of physical "Stages" was introduced by Robitaille et al. (2006) that directly corresponds to an evolutionary sequence based on the object's physical properties obtained by modeling the SEDs. A Stage 0 object has more than half of its total mass in the envelope and the transition from Stage 0 to I is marked when the system is no longer "envelope dominated". The distinctions between stages can be determined using the system's envelope accretion rate, disk mass, and stellar mass.

CHAPTER 2

The Chamaeleon I and III molecular clouds

Of all the things visible, the highest is the heaven of the fixed stars.

Nicolaus Copernicus

Contents

2.1 Recent advances in low-mass star formation

Star formation within our Galaxy has been extensively studied with numerous submillimeter studies of nearby molecular clouds. The Gould Belt (Herschel, 1847; Gould, 1879) consists of a ring of molecular clouds as seen in projection at roughly $\sim 20^{\circ}$ to the galactic plane that lie within a distance of ~ 500 pc from our solar system, which are great targets for low-mass star formation studies. Numerous infrared to millimeter wavelength surveys were conducted to map portions of the Gould Belt clouds. Studies with SCUBA (450 – 850 μm) at the JCMT (e.g., Johnstone et al., 2000), MAMBO (1.2 mm) at the IRAM-30m telescope (e.g., Motte et al., 1998), Bolocam (1.1 mm, 2.1 mm) at the CSO (e.g., Enoch et al., 2006), as well as the *Herschel* (55 – 672 μm; Pilbratt et al., 2010; André et al., 2010) and *Spitzer Space Telescopes* (Spitzer IRAC; 3.6 – 8 μm, MIPS; 20 – 160 μm; eg., Evans et al., 2009) gave a census of star formation from mid-IR to millimeter wavelengths. Various aspects of star formation could thus be probed, from the protostellar phase and the formation of protoplanetary disks that are seen more prominently in the IR to the deeply embedded starless and prestellar cores traced out by their (sub)millimeter emission. A great number of young stellar objects were detected and studied via Spitzer imaging of Gould Belt clouds through the Legacy project "From molecular clouds to star-forming disks" (c2d – Evans et al., 2003, 2009).

The *Herchel* Gould Belt (André et al., 2010) surveys probed the very early phase of star formation (prior the protostellar phase) and provided valuable information regarding the origin of the stellar IMF, the structure of the ISM, and the formation of dense cores. Some of the nearby clouds mapped by *Herschel* in search for prestellar and the deeply embedded Class

0 protostars are for instance Taurus, Perseus, Serpens, Aquila, Lupus, Chamaeleon, Ophiuchus, and Orion. Herschel revealed a pronounced filamentary structure of the cold ISM in all molecular clouds observed, regardless of their star formation activity (e.g, André et al., 2010; Molinari et al., 2010; Bontemps et al., 2010; Men'shchikov et al., 2010; Ward-Thompson et al., 2010; Arzoumanian et al., 2011; Palmeirim et al., 2013; Kirk et al., 2013) and a characteristic width of $\sim$ 0.1 pc for the filaments (André et al., 2010; Arzoumanian et al., 2011; Hennebelle, 2013). This characteristic width is likely associated with MHD turbulence dissipation at these lengths (e.g., Padoan et al., 2001), and more specifically, it has been suggested that is related to dissipation of accretion-driven turbulence by ion-neutral friction (Hennebelle, 2013; Hennebelle & André, 2013). Most dense cores are found to be formed in filaments (e.g., André et al., 2010; Men'shchikov et al., 2010) and an extinction threshold of Av $\sim$ 5–7 for *prestellar* cores is seen (e.g., Onishi et al., 1998; Johnstone et al., 2004; Enoch et al., 2006; Kirk et al., 2006; André et al., 2010; Belloche et al., 2011a). No such extinction threshold is seen for starless (non-prestellar) cores (e.g., Belloche et al., 2011b). The non-star forming Polaris cloud does indeed have visual extinctions less than 8, supporting the evidence for a ubiquitous extinction threshold for prestellar cores. Based on these recent studies, the efficiency of core mass to stellar mass conversion is $\sim$ 30 % (e.g., André, 2013).

It has been suggested that dense cores arise from the fragmentation of supercritical filaments satisfying the observed extinction threshold (e.g., Larson, 1985; Fiege & Pudritz, 2000; Padoan & Nordlund, 2002; Myers, 2009; Inutsuka & Miyama, 1997). The presence of filaments even in non-star forming clouds, as in Polaris (Miville-Deschênes et al., 2010; Ward-Thompson et al., 2010), is an indication that filaments precede prestellar core formation (André et al., 2010; André, 2013). The emmerging formation mechanism is that first, filaments form as an effect of the dissipation of large-scale of MHD turbulence (e.g., Padoan et al., 2001; Hennebelle, 2013). Those filaments whose mass per unit length exceeds the critical value for nearly isothermal filaments ($M_{\rm line,crit} = 2c_s^2/G$; supercritical, or $2\sigma_{\rm tot}^2/G$; virialised, $\sigma_{\rm tot}$; total velocity dispersion, c_s; isothermal sound speed), become locally gravitationally unstable and fragment into several prestellar cores (Fiege & Pudritz, 2000; Inutsuka & Miyama, 1992, 1997; Pon et al., 2011). The critical mass per unit length for a magnetised, nearly isothermal filament only deviates from the unmagnetised value by a factor of less than $\sim$ 2 (see Fiege & Pudritz, 2000; André, 2013). Such fragmentation has been resolved observationally with *Herschel* in the Vela C molecular cloud, which does not belong to the Gould Belt, but harbours both low-mass and high-mass star forming regions (e.g., Hill et al., 2012).

Prestellar cores thus originate from the fragmentation of supercritical filaments (André et al., 2010; André, 2013). This early stage fragmentation might be the process defining the shape of the prestellar CMF, and ultimately, that of the stellar IMF (André et al., 2010). Indeed, links between the two are seen in various clouds in both earlier submillimeter studies and the recent *Herschel* studies (e.g., Motte et al., 1998; Testi & Sargent, 1998; Johnstone et al., 2000; Motte et al., 2001; Enoch et al., 2006; Alves et al., 2007; Nutter & Ward-Thompson, 2007; Enoch et al., 2008; André et al., 2010; Könyves et al., 2010a; Sadavoy et al., 2010; Belloche et al., 2011a).

2.2 The Chamaeleon cloud complex

The proximity of the Gould Belt clouds (d < 500 pc) makes them an excellent laboratory not only for star formation in general, but in particular for low-mass star formation studies. The Chamaeleon cloud complex is one of the nearest clouds within the Gould Belt, located at a distance of just ∼ 150 pc (Knude & Høg, 1998; Whittet et al., 1997) and consisting of three clouds, Chamaeleon I, II, and III. At such distances deep integrations can reveal very faint starless cores, thus extending imaging studies to very low mass limits.

A deep, unbiased dust continuum survey at 870 μm performed with LABOCA at APEX, revealed a large number of starless cores in Cha I and III (60 and 29 cores, respectively; Belloche et al., 2011a,b). Starless cores were found at extinctions larger than 5 mag in Cha I (Belloche et al., 2011a), thus supporting the existence of a star formation threshold for *prestellar* cores. This threshold does not hold in Cha III for the starless, mostly *gravitationally unbound* cores (∼ 93 %) that are located at regions with extinctions as low as ∼ 1.9 mag (Belloche et al., 2011b). As *Herschel* revealed for most Gould Belt clouds, a filamentary structure is also seen in Cha I and III in the dust continuum (e.g., Belloche et al., 2011a,b; Winston et al., 2012) as well as in $C^{18}O$ 1–0 for Cha I (Haikala et al., 2005) and Cha III (Gahm et al., 2002).

Cha I is the most active star forming cloud within the three, having produced more than 200 protostars, while Cha III contains no known protostars (Luhman, 2008). Mizuno et al. (1999) derived a star formation efficiency of 13 % and 0 % for Cha I and III, respectively. The highest dense gas fraction is found in Cha I (∼ 24 %), with the lowest one being ∼ 4 % in Cha III, as traced by the $C^{18}O$ 1–0 emission (Mizuno et al., 1999, 2001). There are no observed outflows or Herbig-Haro objects in Cha III (Schwartz, 1977), whereas there have been several such detections in Cha I (e.g., Mattila et al., 1989; Gómez et al., 2004; Belloche et al., 2006). Boulanger et al. (1998) obtained a mass of ∼ 1400 $M_\odot$ for Cha III and ∼ 1000 $M_\odot$ for Cha I from CO observations.

Despite the differences between Cha I and III, the LABOCA continuum survey showed that the properties of the starless core population are similar in both clouds (Belloche et al., 2011a,b). This remarkable difference in star formation activity in two clouds, despite them belonging to the same complex, as well as their large population of low-mass starless cores makes them excellent targets for studies of low-mass star formation and in particular, prestellar core formation. (Belloche et al., 2011a,b) suggested that Cha I is reaching the end of its star formation activity, while two scenarios were unfolding for Cha III: if it is younger than Cha I, then star formation might not have commenced yet, while an older Cha III would signify its inability to form stars, with its starless cores likely to disperse under the efffect of their inner turbulence.

2.3 Goals of PhD project

The Chamaeleon clouds are seen from the southern hemisphere only (declination ∼ −80°), and thus the single-dish telescopes APEX (Chile) and Mopra (Australia) are excellent tools to study these regions. The unbiased, dust continuum survey at 870 μm was conducted with the same sensitivity in both Cha I and III (Belloche et al., 2011a,b) thus making comparisons

between the starless core population in the two clouds more robust. However, the difference in star formation activity in Cha I and III remained unclear given the starless cores' similar properties and the fact that they belong to the same cloud complex. A molecular line survey of the starless core population of Cha I and III with APEX and Mopra was therefore launched to complement the dust continuum study. The central goal of this survey was to search for distinct differences in Cha I and III that could account for the differing star formation activities. Through the line survey the kinematics of the cores in Cha I and III could be probed and analyzed in order to obtain an overall picture of the dynamical evolution the starless cores will likely follow. The question about whether Cha III is younger than Cha I and will therefore form stars in the future, or if its cores will disperse without ever forming stars is explored in Chapter 5.

While studying the core population of Cha I, the very intriguing object in Cha I, Cha-MMS1, could not be overlooked. Cha-MMS1 was suggested to be either at the very early stage of a Class 0 protostar or at the phase of the first hydrostatic core (e.g., Belloche et al., 2006; Reipurth et al., 1996). With the first hydrostatic cores being the missing link between the prestellar and protostellar phases, studying first core candidates in detail can reveal valuable information about the very first stage of protostar formation. This is not a straightforward process, given the short-lived and deeply embedded nature of these objects. Cha-MMS1 was found to have a very low internal luminosity of $\sim$ 0.015 $L_{\odot}$ (Belloche et al., 2011a), no extended outflow in CO 3–2 (Belloche et al., 2006), and no mid-IR ($\leq$ 8μm) Spitzer detection (Belloche et al., 2006), therefore satisfying the criteria for first core objects. The unclear and promising nature of Cha-MMS1 prompted molecular line observations with APEX and Mopra in various transitions for an in-depth analysis of its kinematics and likely nature. Chapter 4 presents the analysis and results of this study: the kinematics of Cha-MMS1 are explored and its envelope's velocity structure is constrained through radiative transfer modelling. The infall velocity profile of Cha-MMS1 is then compared to predictions of MHD collapse models as a final step in assessing Cha-MMS1's dynamical state.

These two projects present a detailed picture of the star formation in Cha I and III by focussing on their starless and prestellar core population. In addition, they provide greater insight into the the phase preceding the protostar formation by performing an in-depth study of the first core candidate Cha-MMS1. Before the results of these two projects are outlined in Chapters 4 and 5, the tools used to analyse and interpret the single-dish molecular line data are first presented in Chapter 3.

CHAPTER 3

Probing star-forming regions with molecular transitions

You see, wire telegraph is a kind of a very, very long cat. You pull his tail in New York and his head is meowing in Los Angeles. Do you understand this? And radio operates exactly the same way: you send signals here, they receive them there. The only difference is that there is no cat.

Albert Einstein

Contents

3.1 Chemistry in dense cores

With the detection of the first interstellar molecules in the late thirties and early fourties (Merrill, 1934; Swings, 1937; Swings & Rosenfeld, 1937; Adams, 1941), the field of observational astrochemistry began. The first line detections came in the form of absorption dips in the optical spectra of stars, arising from light absorption by diffuse clouds. Despite the early observational proof that interstellar molecules can indeed form in space despite the UV fields of stars, molecular studies were not given much focus (e.g., Bates & Spitzer, 1951; Townes & Schawlow, 1955) until the detection of OH by Weinreb et al. (1963) and OH maser emission by Weaver et al. (1965). Ammonia (NH_3) and H_2O were eventually observed in the galaxy

(Cheung et al., 1968; Knowles et al., 1969). Since then more than 170 molecules have been discovered in physically diverse regions such as interstellar clouds, planetary and stellar atmospheres, gaseous envelopes of giant stars, comets, and star-forming regions (Müller et al., 2005). Molecules are invaluable tracers of the interstellar gas and its physical properties, offer a cooling mechanism for energy to be radiated away during the core collapse, and play a role in the core's ionisation fraction through dissociative and radiative recombination. Interpreting the observed molecular emission, however, requires a deep understanding of the way radiation is transferred through the ISM as well as the chemical processes taking place within the cores (see e.g., Turner & Ziurys, 1988).

During the initial phase of star formation, the chemistry within dense cores is dominated by low-energy gas-phase reactions and grain surface reactions in the cold core interiors. The high density and dust content of dense cores act as an effective shield to the destructive UV radiation from nearby stars (e.g., Bergin et al., 2004). While molecules in the outer core regions can be photodissociated into their constituent atoms, UV radiation cannot penetrate the inner regions of the cores. Simple and complex molecules are thus able to form and survive for a longer period of time, offering clues about the conditions within the cores and with their abundances acting as 'evolutionary clocks'.

H_2 and CO are highly abundant molecules in dense cores, with CO having a typical abundance of $\sim 10^{-4}$ relative to H_2 (e.g., Aikawa et al., 2005; Garrod et al., 2008; Furuya et al., 2012). Their self-shielding property means that the H_2 and CO molecules at the outer layers absorb all incident UV photons and thus protect the inner molecules from photodissociation (e.g., Solomon & Wickramasinghe, 1969; Hollenbach et al., 1971). In the denser regions of the cloud, this role is taken over by dust grains. CO is formed through gas-phase collisions alone, while the formation of H_2 is catalysed on dust grain surfaces, which absorb the released energy of the reaction (e.g., Gould & Salpeter, 1963). Despite H_2 being the primary constituent of molecular clouds, the lack of a permanent dipole moment and the wide spacing of its energy levels makes the symmetric H_2 molecule nearly impossible to detect in rotational emission lines at such temperatures. One of the popular alternative probes of molecular clouds is the abundant CO molecule. CO is usually collisionally excited, with its first rotational energy level being elevated from the ground state by only 5.5 K. CO's first two energy levels are easily populated, but as this molecule is highly abundant within the cores, the 2–1 and 1–0 rotational transitions quickly become optically thick once the density reaches its critical value for excitation ($\sim 10^3$ cm^{-3}). Rarer isotopes of molecules having a lower abundance can be used as optically thin probes when their most abundant isotope's emission is saturated.

Organic molecules are formed during the first stages of dense core evolution through both gas-phase and gas-grain collisions when atomic carbon is still abundant in the core (e.g., Garrod et al., 2008; Hasegawa et al., 1992; Herbst & Leung, 1989). The available carbon becomes "trapped" in molecules as CO, HCN, or CS, depending on the initial sulphur, oxygen, and nitrogen abundances, as well as other more complex organic molecules such as HC_3N or CH_3OH (methanol) (e.g., Aikawa et al., 2005; Garrod et al., 2008). The complex inorganic molecules NH_3 (ammonia) and N_2H^+ trace high-density regions of $\sim 10^4 - 10^5$ cm^{-3} and are good probes of the inner parts of molecular cores (e.g., Benson et al., 1998; Tafalla et al., 2002, 2004). At the high inner densities and low temperatures characteristic of the inner core, CO is depleted onto the icy mantles of dust grains (e.g., Caselli et al., 2002c; Bacmann et al.,

2002; Bergin et al., 2002; Pagani et al., 2005). Even though CO freezes-out at high densities ($n \sim 10^4$ cm^{-3}), an anticorrelation is both predicted and observed with NH_3 and N_2H^+, which increase in abundance at these densities (e.g., Aikawa et al., 2001; Tafalla et al., 2004). That is likely due to a combination of them being excited at high densities, a slower formation than CO through neutral-neutral reactions (resulting in N atoms still being abundant when CO absorption is occuring), and the fact that CO is not present to react with N_2H^+ and produce N_2 (di Francesco et al., 2007). High abundances of NH_3 and N_2H^+ is therefore often used as an indication of a more evolved, "late" core chemical phase, even though they still deplete at higher densities (e.g., Crapsi et al., 2004; Belloche & André, 2004).

Cosmic rays also play a major role in the chemistry of dark clouds by creating a sufficient amount of ions that can trigger ion-molecule reactions. The cosmic ray ionisation of H_2 is an important step towards forming the H_3^+ ion (e.g., Solomon & Werner, 1971), which is at the origin of many of the most important ion-molecule reactions (Herbst & Klemperer, 1973). H_3^+ and its deuterated forms are believed to be good probes of the innermost parts of dense cores where most heavier molecules, including ammonia and N_2H^+ have likely depleted onto the dust grains (e.g., Walmsley et al., 2004; Sipilä et al., 2010). Reactions of H_3^+ with oxygen are more frequent than with H_2 due to the lower energy barrier. These reactions lead to the formation of H_2O^+ and OH^+, which are both very important molecules for the cloud's chemistry (e.g., Herbst & Klemperer, 1973; Gerin et al., 2010). Hydrogen also reacts with carbon to form hydrocarbons such as CH and CH_2 (e.g., Herbst & Klemperer, 1973). Heavier, more complex molecules are formed though successive ion-molecule reactions that eventually form neutral species through dissociative recombination.

The surfaces of dust grains are the catalysts for the formation of new molecules. Apart from catalysing the formation of H_2, carbon, oxygen, and hydrogen atoms "stick" to the grain's surface and diffuse to different positions around the grain until reactions between them occur. Water ice and CO, therefore, form on the grains, as well as species such as CH_4, CO_2, CH_3OH, H_2CO, and other long carbon chains (e.g., Gillett & Forrest, 1973; Gibb et al., 2004; Bergin et al., 2005; Öberg et al., 2011). The molecules can be desorbed into the gas phase when the released energy of the reactions heats the grain's surface enough to "free" the newly formed species. Incident UV photons, electrons, and cosmic rays onto the dust grain surfaces also supply the energy required to surpass the energy barrier of a reaction and therefore make surface reactions a more efficient process (e.g., Hartquist & Williams, 1990; Bergin et al., 1995; Öberg et al., 2009).

During the formation of a protostar within the dense core, the higher central temperatures result in the evaporation from the grain surfaces of the in situ formed organic molecules (e.g., Bacmann et al., 2003; Whittet et al., 2011; Bacmann et al., 2012). The gas-phase abundance of the carbonated species thus increases and the chemistry of the gaseous envelope is largely dependent on the evolution of the young stellar object in its centre. The high temperatures close to the newly formed star, or within the shock regions generated from the "collision" of protostellar outflows with the envelope gas are then able to excite the higher energy vibrational molecular transitions.

3.2 Radiative processes

3.2.1 Radiative transfer

The term radiative transfer is used to describe the physical processes that govern the propagation of radiation through a certain medium. The properties of dense cores through spectral emission are examined in the subsequent chapters, so it is important to understand not only how this emission is generated, but also how it is affected and altered by its immediate surroundings during its propagation.

As radiation travels through a medium it can undergo absorption or scattering, which result in a decrease of the incident light's intensity, or a process called stimulated emission, which can enhance its intensity. In order to describe these processes in a mathematical manner, we define the following parameters: We assume that the (frequency dependent) specific intensity of the radiation field of a given source, I_ν, passes through a medium of length ds, normal to an area dA. The medium is described by density ρ and opacity κ_ν. The latter quantity varies depending on the intrinsic dust grain properties and the frequency of the incident radiation. Depending on the frequency of the propagating radiation, part of it will be absorbed as it travels through the distance ds by the grains in a manner that is linearly proportional to the length and the opacity of the medium:

$$d(absorption) = -\kappa_\nu I_\nu ds. \tag{3.1}$$

Scattering can act both ways in attenuating or increasing the incident radiation, by either re-emitting it in different directions or by "adding" scattered photons (from other incoming light) to the direction of propagation. When it acts in an attenuating manner, its effect is also proportional to I_ν, and it is included in the absorption term shown above. Spontaneous emission acts as a positive contribution to the propagating radiation as

$$d(emission) = j_\nu ds, \tag{3.2}$$

where j_ν denotes the emissivity of the medium, a property independent of I_ν. The total change in intensity is the cumulative effect of the two processes described, hence giving (Stahler & Palla, 2005):

$$dI_\nu = d(absorption) + d(emission), \tag{3.3}$$

$$dI_\nu = -\kappa_\nu I_\nu ds + j_\nu ds, \tag{3.4}$$

$$\frac{dI_\nu}{ds} = -\kappa_\nu I_\nu + j_\nu. \tag{3.5}$$

If the photon mean free path is larger than the length of the medium that it is passing through, then it can in principle travel through it without part of the radiation being absorbed. In this case, we say that the medium is *optically thin* in the respective frequency, with its optical depth

$$d\tau_\nu = \kappa_\nu ds, \tag{3.6}$$

being $\tau_\nu \ll 1$. In the opposite scenario, where $\tau_\nu \gg 1$, the medium is *optically thick* and the radiation we observe comes from a limited region in the foreground of the medium. We can

shift the dependence of the intensity from the frequency to the optical depth, τ_ν, by dividing equation 3.7 with the opacity, κ_ν. The emissivity over the opacity is the source function, $S_\nu = \frac{j_\nu}{\kappa_\nu}$. We therefore obtain:

$$\frac{dI_\nu}{d\tau_\nu} = -I_\nu + S_\nu. \tag{3.7}$$

Under the assumption of a uniform medium, the emissivity j_ν and the source function S_ν are uniform. After integrating the above equation the following solution is derived (Ward-Thompson & Whitworth, 2011):

$$I_\nu = I_\nu(B)e^{-\tau_\nu} + S_\nu(B)(1 - e^{-\tau_\nu}), \tag{3.8}$$

where $I_\nu(B)$ and $S_\nu(B)$ are the background intensity and source function, respectively. In the case of negligible background intensity, the radiation propagating through a medium of optical depth τ_ν changes as

$$I_\nu = S_\nu(B)(1 - e^{-\tau_\nu}). \tag{3.9}$$

As mentioned earlier, the medium can be either optically thin or thick in a specific frequency, thereby giving $I_\nu = S_\nu(B)\tau_\nu$ for τ_ν much smaller than unity, and $I_\nu = S_\nu(B)$ for τ_ν much larger than unity. When the medium is in thermodynamic equilibrium, its source function is given by the temperature dependent Planck function, B_ν:

$$B_\nu(T) = \frac{2h\nu^3}{c^2}\frac{1}{e^{\frac{h\nu}{k_BT}} - 1}, \tag{3.10}$$

where B_ν describes the intensity emitted by the surface of a blackbody, T is the dust temperature of the medium, c is the speed of light, k_B is the Boltzmann constant, and h the Planck constant. For continuum emission studies, when the background intensity is negligible and if the dust temperature is uniform, we can substiture S_ν(B) by the Planck function to obtain the grey body equation (Ward-Thompson & Whitworth, 2011)

$$I_\nu(T) = \frac{2h\nu^3}{c^2}\frac{(1 - e^{-\tau_\nu})}{e^{\frac{h\nu}{k_BT_{\rm dust}}} - 1}. \tag{3.11}$$

This equation is useful in estimating the dust temperature and opacity for a given frequency. Another useful approximation for radio frequencies is the Rayleigh-Jeans approximation. It states that for very low frequencies or long wavelengths, ie., for $h\nu \ll k_BT$

$$B_\nu(T) \approx \frac{2\nu^2 k_BT}{c^2}, \tag{3.12}$$

as the fraction of the exponential approaches zero and Taylor expansion can be applied.

3.2.2 Critical density

The total energy of a molecule is the sum of its rotational, vibrational, and electronic energies. Emission from molecular transitions arises from de-excitation from a certain state to a lower rotational, vibrational, or electronic energy state. The excitation of a specific energy

state mostly arises from collisions of the respective molecule with H_2. Electronic transitions produce emission or absorption in the optical or UV regime. Emission from vibrational transitions can be seen in the infrared, and spectral emission from rotational transitions is in the submillimeter to millimeter range. Due to the low temperatures within dense cores ($\sim$ 10 K), only the rotational energy levels within the ground vibrational state can usually be excited. The (quantised) rotational energy of a particular rotational level J (quantum number) for a linear molecule is given by

$$E_{\mathrm{rot}} = \frac{\hbar^2}{2I} J(J+1) = BhJ(J+1) \tag{3.13}$$

where B is the "rotational constant", I the molecule's moment of inertia, $\hbar$ the Dirac constant (or reduced Planck constant), and h the Planck constant. The rotational constant B decreases the higher the inertia of the molecule is, and as a result the spacing between the energy levels decreases for heavier molecules.

There exists a critical density for every molecular transition at which the collisional deexcitation of a particular state equals its deexcitation through spontaneous decay. The critical density is expressed as

$$n_{crit} = \frac{A_{\mathrm{ul}}}{\gamma_{\mathrm{ul}}}, \tag{3.14}$$

where $\gamma_{\mathrm{ul}} = \sigma v$ is the molecular collision rate and A_{ul} the Einstein coefficient for spontaneous emission from a level u down to a level l. When the gas density is much higher the critical density of a particular transition, the system is in local thermodynamic equilibrium (LTE) with its surroundings and gas kinetic temperature becomes equal to the molecule's excitation temperature. For such a system, the population of the energy levels can be approximated by Boltzmann's distribution:

$$\frac{n_u}{n_l} = \frac{g_u}{g_l} \exp\left(\frac{-\Delta E}{k_B T_{\mathrm{exc}}}\right), \tag{3.15}$$

where n_u and n_l are the densities of molecules in the upper and lower level, and g_u and g_l are the upper and lower level degeneracies (given by 2J+1 for a linear molecule), where J is the rotational quantum number of the transition. ΔE is the energy difference between the two states and T_{exc} the excitation temperature. The Boltzmann distribution can also be written in terms of the partition function Z as

$$\frac{n_u}{n} = \frac{g_u \exp\left(\frac{-E_u}{k_B T_{\mathrm{rot}}}\right)}{Z(T_{\mathrm{rot}})}, \tag{3.16}$$

where n is the total density of the species and T_{rot} is the rotation temperature; in LTE, $T_{\mathrm{rot}} = T_{\mathrm{exc}}$ and both are equal to the kinetic temperature, T_{k}. The molecular partition function is a statistical measure of the energy contributions (rotational, vibrational, electronic) from all available energy levels of the molecule. In LTE it is given by

$$Z(T_{\mathrm{exc}}) = \Sigma_i \left\{ g_i \exp\left(\frac{-E_i}{k_B T_{\mathrm{exc}}}\right)\right\}, \tag{3.17}$$

where the sum of the bracket is calculated for all levels.

The molecule emits most strongly when the density is greater than the critical value and on the other hand, emission is negligible for densities much lower than the critical value. Given that every molecular transition has a unique critical density, each will therefore trace different physical conditions and regions within a core.

3.2.3 Spectra from radio observations

It is common in radio astronomy for a spectrum to be plotted as a function of the antenna temperature, T_A^*, and the line-of-sight velocity instead of its intensity I_ν and frequency ν. The brightness temperature T_b, is the temperature that a black body in thermal equilibrium would have to have in order to reproduce the observed intensity at a frequency ν:

$$I_\nu = B_\nu(T_b). \tag{3.18}$$

The effective radiation temperature, $J_\nu(T_b)$, is defined as

$$J_\nu(T_b) = \frac{B_\nu(T_b)c^2}{2\nu^2 k_B} \tag{3.19}$$

In the Rayleigh-Jeans approximation $J_\nu(T_b) = T_b$. For sources smaller than the beam size, the source brightness temperature is given by (Wilson et al., 2009)

$$T_b = T_{\rm MB}\frac{\theta_0^2}{\theta_s^2}, \tag{3.20}$$

where $T_{\rm MB}$ is the main-beam temperature, θ_0 and θ_s are the observed and actual sizes of the source, with $\theta_0^2 = \theta_s^2 + \theta_b^2$ (θ_b; beam size). The brightness temperature is therefore larger than the main-beam temperature. The *corrected* antenna temperature is given by $T_A^* = T_A/F_{\rm eff}$, where $T_{\rm A}$ is the antenna temperature. T_A^* and $T_{\rm MB}$ are related as

$$T_{\rm MB} = \frac{F_{\rm eff}}{B_{\rm eff}}T_A^* \tag{3.21}$$

for sources smaller than the beam, where $F_{\rm eff}$ and $B_{\rm eff}$ are the telescope forward and beam efficiencies, and the ratio $\frac{B_{\rm eff}}{F_{\rm eff}}$ is the main-beam efficiency $\eta_{\rm MB}$.

Another important aspect of the observed transitions is that owing to the Doppler shift effect (i.e., $\Delta\nu/\nu_{\rm rest} = \Delta v/c$), they are shifted to either lower or higher frequencies with respect to their rest frequency

$$\nu_{\rm obs} \sim \nu_{\rm rest}\left(1 + \frac{v}{c}\right) \tag{3.22}$$

where v is the radial velocity of the source (velocity along the line-of-sight) and ν_{obs} and ν_{rest} are the observed and the emitting frequencies, respectively. The observed spectrum is also usually broadened by bulk motions Δv due to the relative velocity of the molecules that absorb and re-emit the radiation. The broadening $\Delta\nu$ is given by

$$\Delta\nu = \frac{\Delta v}{c}\nu_{\rm rest}. \tag{3.23}$$

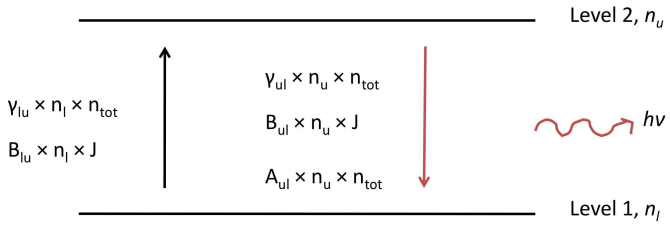

Figure 3.1: Schematic of the energy levels and the population for the two level atom.

3.2.4 Energy level populations and the two-level system

This section presents the simple case of an atom with only two energy levels. The population of each level depends on collisional, radiative, and spontaneous processes that are described by the Einstein coefficients. Excitation to the upper level, u, can occur either through collisions with other molecules or radiatively with the absorption of an incident photon. The collisional excitation rate coefficient and the Einstein absorption coefficient are denoted as $\gamma_{\rm lu}$ and $B_{\rm lu}$, respectively. In the case of deexcitation from the upper to the lower state, $\gamma_{\rm ul}$ and $B_{\rm ul}$ represent the collisional deexcitation rate and the Einstein stimulated emission coefficients. Stimulated emission occurs when an incident photon from the ambient radiation field of intensity I (averaged over all frequencies) causes deexcitation and the simultaneous emission of a photon of the same energy. An additional process contributing to the deexcitation rate is the Einstein spontaneous emission. Spontaneous emission results in the decay of an electron to a lower energy state without any influence by external factors.

Assuming a total density $n_{\rm tot}$ of the main collision partner ($\approx n_{\rm H_2}$) and upper and lower level populations n_u and n_l, the populations of both levels in equilibrium are described by (equations from Stahler & Palla, 2005):

$$\gamma_{\rm lu} n_{\rm tot} n_l + B_{\rm lu} n_l I = \gamma_{\rm ul} n_{\rm tot} n_u + B_{\rm ul} n_u I + A_{\rm ul} n_u. \tag{3.24}$$

At the limit of high-density, as is the case in the dense core interiors, the collisional transitions greatly exceed radiative transitions. With collisional excitation and deexcitation being the main driving source of the observed transitions, the previous equation can be rewritten as

$$\gamma_{\rm lu} n_l = \gamma_{\rm ul} n_u \Rightarrow \frac{\gamma_{\rm lu}}{\gamma_{\rm ul}} = \frac{n_u}{n_l}. \tag{3.25}$$

In these high densities where LTE holds, the ratio of the upper to the lower level populations can be expressed through the Boltzmann distribution (equation 3.15)

$$\frac{\gamma_{\rm lu}}{\gamma_{\rm ul}} = \frac{g_u}{g_l} \exp\left(\frac{-\Delta E}{k_B T_{\rm k}}\right). \tag{3.26}$$

On the other hand, in the limit of low densities, the opposite occurs. Collisional processes are negligible and only radiative transitions are significant. The system is now in thermal

equilibrium with the radiation field, which has a temperature $T_{\rm rad}$. Equation 3.24 then becomes

$$I = \frac{A_{\rm ul} n_u}{B_{\rm lu} n_l - B_{\rm ul} n_u} \Rightarrow I = \frac{\frac{A_{\rm ul}}{B_{\rm ul}}}{\frac{B_{\rm lu} n_l}{B_{\rm ul} n_u} - 1} \Rightarrow I = \frac{\frac{A_{\rm ul}}{B_{\rm ul}}}{\frac{B_{\rm lu} g_l}{B_{\rm ul} g_u} \exp\left(\frac{\Delta E}{k_B T_{\rm rad}}\right) - 1} \tag{3.27}$$

The radiation intensity is given by the Planck function in thermal equilibrium:

$$I_\nu = \frac{2h\nu^3}{c^2} \frac{1}{\exp\left(\frac{h\nu}{k_B T_{\rm rad}}\right) - 1}. \tag{3.28}$$

A direct comparison of the two previous equations gives useful relations for the Einstein coefficients:

$$\begin{aligned} A_{\rm ul} &= \frac{2h\nu_{\rm ul}^3}{c^2} B_{\rm ul} \\ B_{\rm lu}\, g_l &= B_{ul}\, g_u. \end{aligned} \tag{3.29}$$

To derive a relation between the total density $n_{\rm tot}$, the populations n_u and n_l, and the temperatures T_k and $T_{\rm exc}$, equation 3.24 is divided by $\gamma_{\rm ul}$, and the Boltzmann distribution and equations 3.29 are taken into account to obtain:

$$\frac{g_u}{g_l}\left(\exp\frac{-\Delta E}{k_B T_k} + \frac{n_{\rm crit} c^2 I}{n_{\rm tot} 2h\nu^3}\right) = \frac{n_u}{n_l}\left(1 + \frac{n_{\rm crit} c^2 I}{n_{\rm tot} 2h\nu^3} + \frac{n_{\rm crit}}{n_{\rm tot}}\right), \tag{3.30}$$

where $n_{\rm crit}$ is defined in equation 3.14. The ratio of the upper to lower state populations are described by the Boltzmann distribution for an excitation temperature $T_{\rm exc}$.

The integrated intensities of molecular spectra are commonly used to derive the column densities of the respective molecules along the line-of-sight. However, an important aspect to consider when deriving column densities is the opacity of the observed molecular transition. An optically thick transition is not a good tracer of the total molecular column density as part of the core acts as a black-body in this frequency. On the other hand, in the case of an optically thin spectrum the observed emission is produced collectively by all molecules along the line-of-sight and its column density is therefore directly proportional to the observed integrated intensity. The column density at the lower energy state is (Belloche, 2002)

$$N_l = \frac{8\pi}{c^3} \frac{g_l}{g_u} \frac{\nu_{\rm ul}^3}{A_{\rm ul}} \frac{1}{1 - \exp\frac{-h\nu_{\rm ul}}{kT_{\rm exc}}} \int \tau_\nu {\rm d}v, \tag{3.31}$$

where τ_ν is the optical depth at the respective frequency. In the presence of a background radiation field, the observed intensity $I_{\nu,\rm obs}$ with respect to the continnum becomes

$$I_{\nu,\rm obs} = (B_\nu(T_{\rm exc}) - B_\nu(T_{bg}))(1 - e^{-\tau_\nu}), \tag{3.32}$$

with $B_\nu(T_{\rm exc})$ and $B_\nu(T_{\rm bg})$ being the Planck law at the excitation and background temperatures, respectively. We have assumed that the background intensity can be described well by $B_\nu(T_{bg})$ (e.g., when describing the CMB). The Planck function is related to the effective radiation temperature through

$$J_\nu(T) = \frac{c^2}{2k\nu^2} B_\nu(T), \tag{3.33}$$

1 in the Rayleigh-Jeans approximation. Therefore, the column density at the lower energy level as a function of the integated effective radiation temperature over all velocities (ie., integrated intensity) and for optically thin transitions becomes (Belloche, 2002),

$$N_l = \frac{8\pi}{c^3}\frac{g_l}{g_u}\frac{\nu_{\rm ul}^3}{A_{\rm ul}}\ \frac{1}{1-\exp\frac{-h\nu_{\rm ul}}{kT_{\rm exc}}}\ \frac{1}{J_\nu(T_{\rm exc})-J_\nu(T_{\rm bg})}\ \int J_\nu(T)\,{\rm d}v. \tag{3.34}$$

To obtain the *total* column density of the molecule we have to use the partition function in the following manner:

$$N_{\rm tot} = \frac{N_l}{g_l}\,Z(T)\exp\left(\frac{\Delta E}{k_B T_k}\right), \tag{3.35}$$

B_e is the rotational constant of the molecule in units of frequency. From equation 3.17, the partition function under LTE for our system and for a linear molecule is

$$Z(T_{\rm k}) = \Sigma_l\ \left\{(2l+1)\exp\left(\frac{-\Delta E}{k_B T_{\rm k}}\right)\right\}, \tag{3.36}$$

Expanding equation 3.35 the total molecular column density becomes (Belloche, 2002)

$$N_{\rm tot} = \frac{8\pi\nu_{\rm ul}^3}{c^3 g_u A_{ul}}\exp\frac{\Delta E}{k_{\rm b}T_{\rm k}}\ \frac{Z(T_{\rm k})}{1-e^{\frac{-h\nu_{\rm ul}}{k_{\rm b}T_{\rm k}}}}\ \frac{1}{J_\nu(T_{\rm k})-J_\nu(T_{\rm bg})}\int J_\nu(T_{\rm b})\,{\rm d}v \tag{3.37}$$

3.3 Kinematics of dense cores

3.3.1 Systemic velocity

The systemic (centroid) velocity of the source is the average velocity along the line-of-sight of all emitting molecules. The method that was used to derive systemic velocities in the following chapters is through a least-square fitting procedure using a three-parameter function for spectra that have a Gaussian shape. The three-parameter function is (see Belloche, 2013)

$$T_{\rm peak}\exp\left((-4ln(2))\frac{(v-v_{\rm sys})^2}{FWHM^2}\right), \tag{3.38}$$

where T_{peak} is the peak temperature of the spectrum, $FWHM$ is the full width at half maximum, and $v_{\rm sys}$ is the source systemic velocity.

3.3.2 Turbulence

Turbulent motions are present on both small and large scales within molecular clouds and they observationally manifest themselves as a broadening effect in the spectral emission. The non-thermal and thermal motions along with the magnetic field support the cloud against gravitational collapse (e.g., Arons & Max, 1975; Gammie & Ostriker, 1996; Nakamura & Li, 2005). Turbulence is found to be subsonic or transonic on small scales within dense, prestellar cores (e.g., Larson, 1981; Myers, 1983; Goodman et al., 1998; Belloche et al., 2001; Di Francesco et al., 2004; André et al., 2007; Ward-Thompson et al., 2007; Miettinen et al., 2010; Pineda

et al., 2010). The non-thermal velocity dispersion, $\sigma_{\rm nth}$, is found to be uniform and no larger than the thermal dispersion at scales below $\sim$ 0.1 pc ("coherence" scale: Goodman et al., 1998; Barranco & Goodman, 1998; Caselli et al., 2002a; Tafalla et al., 2004; Pineda et al., 2010), while it starts increasing at larger radii in a manner that follows the Larson scaling law (Larson, 1981). The dispersion-size relation of Larson (1981) ($\Delta v \sim R^a$, $a \sim 0.38$) was found to be similar to the Kolmogorov-Obhukov law, $\sigma \propto L^{1/3}$, where L is the size over which the dispersion is measured. The latter describes the cascade of initially highly energetic turbulent eddies down to smaller scales where they dissipate within molecular clouds. Turbulence dissipation is higher in the core interiors, with the outer "unshielded" layers being more exposed to ambient non-thermal motions. For a sample of cloud cores of differing masses, it appears that non-thermal motions increase as a function of the enclosed mass.

The total observed velocity dispersion is given by the quadratic sum of its thermal and non-thermal constituents:

$$\sigma^2_{\rm obs} = \sigma^2_{\rm th} + \sigma^2_{\rm nth}, \tag{3.39}$$

and the thermal dispersion (gas rms velocity) by

$$\sigma_{\rm th} = \sqrt{\frac{k_B T_k}{m}}, \tag{3.40}$$

where $m = \mu m_H$, with μ being the molecular weight of the tracer used, and m_H the hydrogen mass. To compute the mean thermal dispersion, the molecular weight of the mean particle is used ($\mu \sim 2.37$). The observed $FWHM$ is related to the total observed dispersion through

$$FWHM = \sigma_{\rm obs} \sqrt{8\, ln2}. \tag{3.41}$$

3.3.3 Infall

Proving unambiguously that a part of an interstellar cloud is in the process of infall has not been straightforward. Within the context of free-fall collapse of isothermal spheres, the mass enclosed within a certain radius of the free-falling envelope scales as $M \propto r^{3/2}$ ($\rho \propto r^{-3/2}$), and the infall velocity as $v \propto r^{-0.5}$ (see e.g., Shu, 1977). The infall velocity, therefore, increases as smaller radii are approached. Combining the two relations, we obtain a proportionality of $M \propto v^{-3}$, which states that in the simple scenario of spherical collapse there is less and less mass enclosed within progressively smaller radii where the material is infalling at higher velocities (Hartmann, 2001).

The combination of an asymmetric, blueshifted, optically thick line and emission from an optically thin line peaking in-between the blue and red peaks, is widely used as a signature of infall under the assumption that the excitation temperature increases towards the centre of the core (Leung & Brown, 1977; Walker et al., 1986; Zhou, 1992; Myers et al., 1995, 1996). Optically thin lines cannot be used alone to detect infall, as their emission is symmetric and centrally peaked, and it does not distinguish between infalling, outflowing, or turbulent motions. The emission from the optically thin transition is expected to peak at a velocity characterized by the maximum excitation temperature, which is the centre of the core in the spherically symmetric case. As it probes the central velocity of the core, it is expected to peak somewhere in-between the red and blue peaks of the optically thick spectrum, thus indicating

that the asymmetry of the optically thick line is indeed produced by the object itself and not by meterial lying along the line-of-sight due to projection effects.

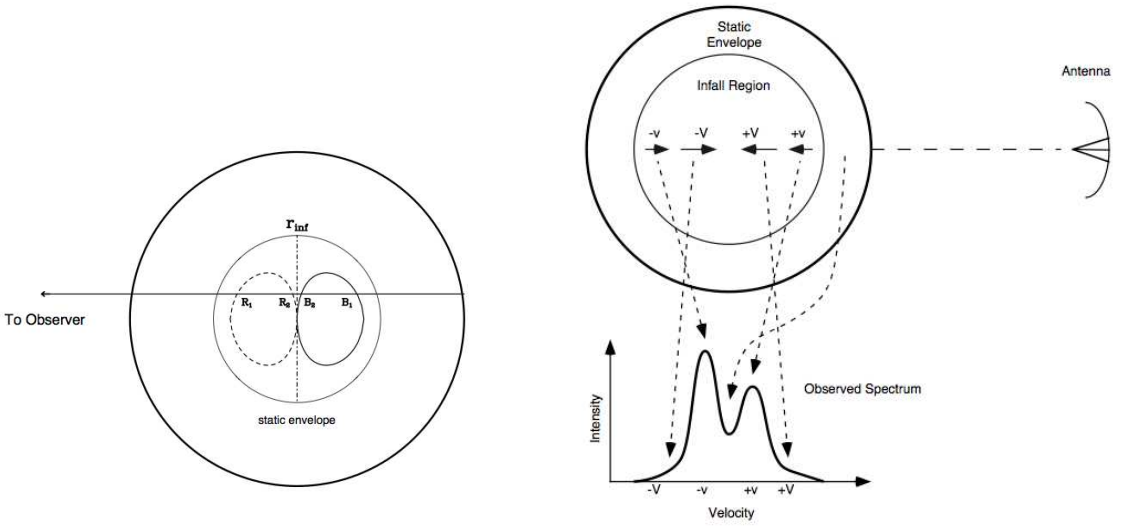

Figure 3.2: Infall signature schematic. *Left*: the spherically symmetric collapsing core of radius $r_{\rm inf}$ is surrounded by a static envelope. The ovals signify loci of constant line-of-sight velocity for free-fall (i.e., $v \propto r^{-0.5}$), with the blueshifted and redshifted halves of the core containing the solid and dashed ovals, respectively. The positions B_1, B_2, R_1, and R_2 are the intersection positions along the line-of-sight. *Right*: a direct correspondence between the features of an optically thick, double-peaked spectrum with the regions of the infalling core and static envelope that produce them. The line wings arise due to faster collapse close to the centre. From Evans (2003).

The schematics in Fig. 3.2, taken from Evans (2003), illustate the physical mechanism giving rise to this signature. The left panel shows an infalling envelope with radius $r_{\rm inf}$ that is enclosed by a static envelope. When we observe the core with an optically thick transition, we cross oval-shaped loci of constant line-of-sight velocities. Fig. 3.2 shows two such loci, one in the redshifted and one in the blueshifted part of the core. If the excitation temperature increases towards the centre, then point R_2 has a higher excitation temperature than R_1, and similarly, the excitation temperature at B_2 is higher than B_1. However, due to the optical depth of the transition, R_2 and B_1 are obscured from the observer and only emission from points R_1 and B_2 are observed. As R_1 has a lower excitation temperature than B_2, the resulting emission from the redshifted part of the core will be weaker than the blueshifted emission, thus creating an asymmetric spectrum that cannot be described by a single temperature Gaussian profile. Absorption from the outer envelope layers might also give rise to a self-absorption dip. An absoprtion dip would result in the spectrum having two clearly defined peaks (blue and red), thus emphasising the observed asymmetry in intensity. Fig. 3.2 shows which parts of the infalling and static envelope correspond to each of the spectral features.

A simple way to quantify the observed asymmetry is by comparing the blue to the red peak brightness (or antenna) temperature, $T_{\rm blue}/T_{\rm red}$ (Myers et al., 1995). However, this ratio does not account for the velocity shift of the optically thin line with respect to the blue peak of the optically thick spectrum. The velocity shift can be quantified by the nondimensional parameter, δV, that Mardones et al. (1997) introduced to "measure" the observed asymmetry. This parameter is estimated as

$$\delta V = \frac{V_{thick} - V_{thin}}{\Delta V_{thin}}, \tag{3.42}$$

where $V_{\rm thick}$ and $V_{\rm thin}$ are the velocities of the brightest optically thick peak and the optically thin peak, and ΔV_{thin} is the linewidth of the optically thin transition.

A different approach to quantifying the infall asymmetry is the so-called skewness (Gregersen et al., 1997). The skewness is a convenient method for spectra without well defined peaks, for which a peak brightness ratio is not relevant.

$$Skewness = \frac{\Sigma[T_A^*(v - v_{LSR})^3 \delta v]}{\Sigma(T_A^* \delta v)} \Bigg/ \left(\frac{\Sigma[T_A^*(v - v_{LSR})^2 \delta v]}{\Sigma(T_A^* \delta v)} \right)^{3/2}. \tag{3.43}$$

This parameter is the ratio of the third moment to the $\frac{3}{2}$ power of the second moment distribution, with $v_{\rm LSR}$ and δv being the centroid velocity of the source and the channel width, respectively. Both equations 3.42 and 3.43 give negative values for the infall profiles (blue peak stronger than red) and values for the opposite profile (red peak stronger than blue). The latter, "inverse signature" is often interpreted as indication for expanding motions (Evans, 2003), but it is generally not as well understood as the infall signature.

3.3.4 Rotation

Determining the rotational velocity structure of prestellar cores and protostellar envelopes is not a straightforward undertaking. One needs to be able to disentangle rotation from other motions likely to be present, such as turbulence and infall, while at the same time using a tracer that is not affected by depletion or optical depth effects.

Observations in an optically thin molecular tracer can be used to derive the core's average velocities along the line-of-sight. The first step to investigate rotation within a core is to search for a velocity gradient perpendicular to the rotation axis. A planar least squares fit of the centroid velocity measurements can reveal whether one is present within the core. A linear velocity gradient corresponds to solid-body rotation within the envelope and it has a magnitude of $\Omega sini$, where i is the inclination of the rotation axis to the line-of-sight. The function used for the planar fitting is of the form $v_{cen} = v_0 + \alpha da + \beta db$ (Goodman et al., 1993), where da and db are expressed in radians and correspond to the right ascension and declination offsets, v_0 is the cloud systemic velocity, and α and β are the projections of the velocity gradient (per radian) on the right ascension and declination axes (Goodman et al., 1993).

Position velocity (hereafter, P-V) diagrams are a useful and simple tool in visualising the velocity gradients within a core. A uniform, linear gradient is expected for a core rotating as a solid-body, with the angular velocity being independent of the distance along the line-of-sight (Goodman et al., 1993; Belloche, 2013). On the other hand, a non-uniform, "S-shaped" P-V diagram is thought to arise from differential motions, whereby the gradient becomes steeper

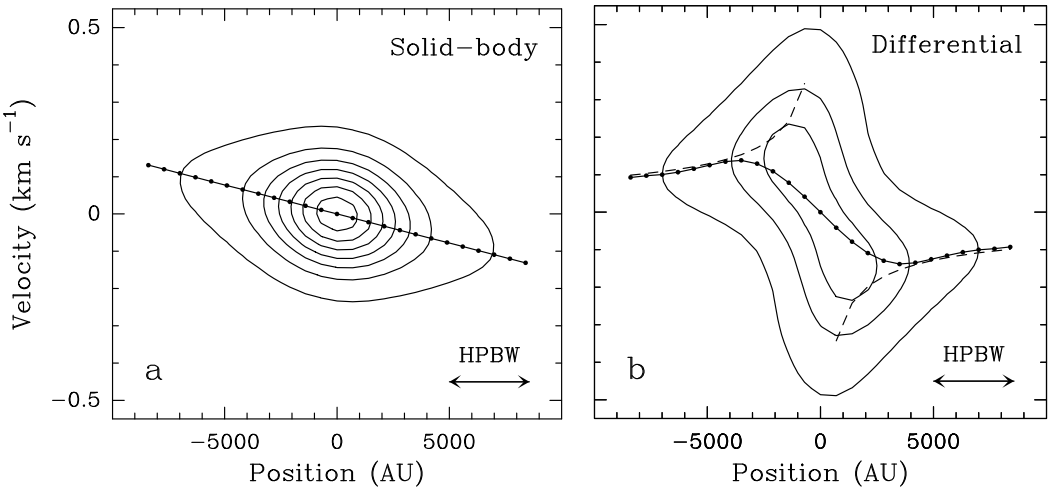

Figure 3.3: Position-velocity diagrams (parametric model) for a protostellar envelope undergoing (a) solid-body (Ω = 4.2 km s^{-1}) and (b) differential ($\Omega = 12(R/3500AU)^{-1.5}$ km s^{-1} pc^{-1}) rotation. The solid curve and the dots show the centroid velocity at each position, while the contours correspond to $C^{34}S$ emission ($HPBW$ = 3600 AU). The dashed curve shows how the velocity gradient would appear in the limit of infinite resolution. Plots from (Belloche et al., 2002; Belloche, 2013).

at smaller scales (see e.g., Belloche et al., 2002). This implies the spinning up of the core towards the centre and the overall dependence of the angular velocity with the radius.

An example of solid-body and differential rotation as manifested on a P-V diagram is shown in Fig. 3.3. The central part of the characteristic "S shape" of differential rotation is due to the finite resolution of the observations. If we could resolve the velocity structure of the inner core we would then observe velocity curves that increase in magnitude in opposite directions on either side of the central position. However, the finite angular resolution makes the transition of the observed velocities seem smoother.

3.4 MAPYSO Radiative Transfer Code

MAPYSO is a 2D Monte-Carlo radiative transfer code (Blinder, 1997; Belloche et al., 2002) that is used in the work presented about the first core candidate Cha-MMS1 in the following chapter. It operates in two successive steps. Initially, it computes the one dimensional population of the different energy levels at non-LTE through a Monte-Carlo code (adapted from Bernes, 1979). The MAPYSO code then computes the radiative transfer along the line-of-sight in either one or two-dimensional geometries, convolving with the antenna beam. Details about the model input parameters and output spectra are given in Chapter 4 and Section 4.3.

Chapter 4

The dynamical state of the first hydrostatic core candidate Cha-MMS1

Absence of evidence is not evidence of absence.

Carl Sagan

Contents

Abstract

Context: First hydrostatic cores represent a theoretically predicted intermediate evolutionary link between the prestellar and protostellar phases. Studying the observational characteristics of first core candidates is therefore vital for probing and understanding the earliest phases of star formation.

Aims: We aim to determine the dynamical state of the first hydrostatic core candidate Cha-MMS1.

Methods: We observed Cha-MMS1 in various molecular transitions with the APEX and Mopra telescopes. Continuum data retrieved from the *Spitzer Heritage Archive* were used to estimate the internal luminosity of the source. The molecular emission was modelled with a radiative transfer code to derive constraints on the kinematics of the envelope, which were then compared to predictions of magneto-hydrodynamic simulations.

Results: We derive an internal luminosity of 0.08 $L_\odot$ – 0.18 $L_\odot$ for Cha-MMS1. An average velocity gradient of 3.1 ± 0.1 km s^{-1} pc^{-1} over ∼ 0.08 pc is found perpendicular to the filament in which Cha-MMS1 is embedded. The gradient is flatter in the outer parts and, surprisingly, also at the innermost ∼ 2000 AU to 4000 AU. The former features are consistent with solid-body rotation beyond 4000 AU and slower, differential rotation beyond 8000 AU, but the origin of the flatter gradient in the innermost parts is unclear. The classical infall signature is detected in HCO^+ 3–2 and CS 2–1. The radiative transfer modelling indicates a uniform infall velocity in the outer parts of the envelope. In the inner parts (at most 9000 AU), an infall velocity field scaling with $r^{-0.5}$ is consistent with the data, but the shape of the profile is less well constrained and the velocity could also decrease toward the centre. The infall velocities are subsonic to transonic, 0.1 km s^{-1} – 0.2 km s^{-1} at $r \geq 3300$ AU, and subsonic to supersonic, 0.04 km s^{-1} – 0.6 km s^{-1} at $r \leq 3300$ AU. Both the internal luminosity of Cha-MMS1 and the infall velocity field in its envelope are consistent with predictions of MHD simulations for the first core phase. There is no evidence of a fast, large-scale outflow stemming from Cha-MMS1, but excess emission from the high-density tracers CS 5–4, CO 6–5, and CO 7–6 suggests the presence of higher velocity material at the inner core.

Conclusions: Its internal luminosity excludes Cha-MMS1 being a prestellar core. The kinematical properties of its envelope are consistent with Cha-MMS1 being a first hydrostatic core candidate or a very young Class 0 protostar.

The content of this Chapter has been published in the journal Astronomy & Astrophysics. A. E. Tsitali, A. Belloche, B. Commerçon, and K. M. Menten, A&A, 557, A98.

4.1 Introduction

Many advances have recently been made in the field of early low-mass star formation, spanning from the prestellar phase to the formation and evolution of Young Stellar Objects (YSOs), e.g., with the *Spitzer* c2d Legacy Project ("From Molecular Cores to Planet-Forming Disks", Evans et al., 2003) and the *Herschel* Gould Belt Survey (André et al., 2010). In particular, *Herschel* (Pilbratt et al., 2010) has provided valuable insight into the early star formation processes. Most dense starless cores in molecular clouds appear to be located along a complex network of long, thin filaments, suggesting that filament formation precedes the core formation process (Arzoumanian et al., 2011; Hill et al., 2011; André et al., 2010; Men'shchikov et al., 2010; Molinari et al., 2010). The study of these early stages is necessary in order to address open questions such as the origin of the stellar Initial Mass Function (IMF), its relationship with the prestellar phase and the Core Mass Function (CMF; e.g., André et al., 2009), and the initial conditions needed for star formation to occur. Recent results from the *Herschel* survey confirm the resemblance of the prestellar CMF to the stellar IMF in the Aquila and Polaris clouds (Könyves et al., 2010b; André et al., 2010). Such a resemblance has already been seen in various molecular clouds with ground-based single-dish telescopes, such as in the Ophiuchus molecular cloud (Motte et al., 1998) or in the Pipe nebula (Rathborne et al., 2009).

It has recently become common to split the population of starless cores in molecular clouds into two categories, the gravitationally bound and unbound cores. Prestellar cores represent the subset of starless cores that are self-gravitating and will thus very likely form stars (e.g., di Francesco et al., 2007; André et al., 2009), while the gravitationally unbound starless cores may be transient objects ("failed" cores) or objects on the verge of becoming prestellar (e.g. Belloche et al., 2011b). The gravitational collapse of a prestellar core leads to the formation of a stellar embryo, the protostar. This marks the beginning of the Class 0 phase, during which the central object accretes mass from its protostellar envelope (André et al., 2000). Theoretically, the early work of Larson (1969) already showed that the formation of the central protostar must be preceded by the formation of a larger, less dense, first hydrostatic core (hereafter FHSC). The FHSC thus represents an intermediate evolutionary stage between the prestellar and protostellar phases. The detection of FHSCs is observationally very challenging because of their very short expected lifetime.

4.1.1 FHSC: a theoretical background

The formation of the first hydrostatic core emerged from theory for the first time with Larson (1969), but only a handful of objects have recently been observed and suggested as likely candidates. Larson (1969) describes the process of forming a protostar from a parent molecular core using a spherical collapse model that ignores magnetic fields and rotation. The initial phase is characterised by an isothermal contraction of the molecular core. When the central density exceeds 10^{-13} g cm^{-3} the radiative cooling ceases to be efficient and an opaque, adiabatic core forms at the centre. The rise in temperature results in an increase in the thermal pressure, and finally, when the pressure balances the gravitational force the collapse ceases and the first hydrostatic core is formed. The initial central temperature of the FHSC is estimated to be around 170 K with an initial central density of $2{\times}10^{-10}$ g cm^{-3}. The so-called second,

more compact (protostellar) core is formed after the dissociation of H_2 and subsequent collapse, when the central temperature reaches 2×10^4 K and the density reaches 2×10^{-2} g cm^{-3} (Larson, 1969).

Various theoretical studies predict observational characteristics of the first core phase. Internal luminosities of up to $\sim$ 0.1 $L_\odot$ (Masunaga et al., 1998; Saigo & Tomisaka, 2011) or $\sim$ 0.25 $L_\odot$ (Commerçon et al., 2012) have been predicted. First cores are characterised by radii and masses in the ranges of $\sim$ 5 AU – 10 AU and 0.05 $M_\odot$ – 0.1 $M_\odot$, respectively (Masunaga et al., 1998; Saigo et al., 2008). Their lifetimes range from a few 100 yr to a few 1000 yr, increasing with the rate of rotation. Commerçon et al. (2012) derive lifetimes ranging from $\sim$ 1000 yr to $>$ 4000 yr for rotating, magnetised 1 $M_\odot$ cores with 3D radiation-MHD simulations. The FHSC lifetime is shorter for higher levels of magnetisation owing to the stronger magnetic braking that increases the mass accretion rate. These short lifetimes imply that first cores are rare and thus difficult to observe, although we note that Tomida et al. (2010) predict much longer lifetimes ($> 10^4$ yr) for first cores formed in very low-mass cloud cores (0.1 $M_\odot$).

Outflows at the first core phase are thought to be a significant observational signature characterising this evolutionary stage. Machida et al. (2008) used 3D resistive MHD simulations to study the driving mechanisms of outflows in the star formation process. Their predictions distinguish between an extended, slow molecular outflow driven by the first core and a highly collimated, fast jet later driven by the protostellar core that exhibit typical velocities of $\sim$ 3 km s^{-1} and 30 km s^{-1}, respectively. The outflow driven by the first core is predicted to be extremely compact, spanning $\sim$ 200 AU – 800 AU in extent just before the start of the second collapse (Commerçon et al., 2012, 2010; Machida et al., 2008). The first core outflows are thought to result from the twisting of the magnetic field lines due to the rotation of the collapsing core, whose amplified toroidal component leads to the subsequent transfer of angular momentum to the gas outside of the core (Tomisaka & Tomida, 2011).

4.1.2 Cha-MMS1 and its evolutionary stage

Chamaeleon-MMS1 (hereafter Cha-MMS1 for short) is a dense core embedded in a filament ($\sim$ 0.5 pc in length) within the Chamaeleon I molecular cloud (Belloche et al., 2011a) at a distance of 150 pc (Whittet et al., 1997; Knude & Høg, 1998). Several previous studies of Cha-MMS1 suggest that it is an object at a very early evolutionary stage.

Reipurth et al. (1996) discovered Cha-MMS1 in dust continuum emission at 1.3 mm. They suggested that Cha-MMS1 is the driving source of the nearby HH 49/50 objects and identified it as a Class 0 protostar based on that association. During the Class 0 protostellar phase, the central object is deeply embedded within its collapsing envelope, which comprises more than half of the system's mass (André et al., 1993). Lehtinen et al. (2001) confirms this classification based on a *tentative* far-infrared detection, but Lehtinen et al. (2003) argues that Cha-MMS1 possibly represents an evolutionary stage earlier than Class 0 based on its lack of thermal free-free emission at cm wavelengths. Cha-MMS1 is embedded in a gravitationally-bound $C^{18}O$ core (Haikala et al., 2005). High deuterium fractionations of HCO^+ and N_2H^+ were derived, consistent with Cha-MMS1 being an evolved prestellar core or a young protostellar envelope (Belloche et al., 2006).

A faint *Spitzer* 24 μm and 70 μm detection indicates the presence of a central object in Cha-MMS1, either a FHSC or a protostar (Belloche et al., 2006). Belloche et al. (2011a) derived a very low internal luminosity of ~ 0.015 $L_\odot$ for this object based on the correlation between the 70 μm flux density and internal luminosity established by Dunham et al. (2008) for protostellar objects. As most Class 0 protostars feature an outflow (André et al., 2000), a search for a large-scale outflow driven by Cha-MMS1 was performed in CO 3–2 with APEX but none was found (Belloche et al., 2006). The non-detection of an outflow around Cha-MMS1 on scales of $\sim 10^4$ AU suggests that the central object may be less evolved than a Class 0 object. It could possess an outflow that is too compact to have been detected with the resolution of the previous studies, which would agree with the predictions of the FHSC observational signatures. Furthermore, Cha-MMS1, the Class 0 protostar IRAM 04191+1522 (hereafter, IRAM 04191) and the Very Low Luminosity Object (VeLLO) L1521F (Crapsi et al., 2004; Bourke et al., 2006) are located at approximately the same distance, and a direct comparison of their *Spitzer* fluxes supports the idea that Cha-MMS1 is less evolved (Belloche et al., 2006). Bearing all this in mind, Cha-MMS1 could be at the stage of the FHSC between the prestellar and Class 0 phases. However, its classification as such is very difficult to observationally confirm until a compact (200 AU – 800 AU; Commerçon et al., 2010, 2012), slow outflow with velocities in the range of 2 km s^{-1} – 4 km s^{-1} (Tomisaka, 2002; Machida et al., 2008; Commerçon et al., 2010; Hennebelle & Fromang, 2008) is detected. We therefore merely consider it as a FHSC candidate.

4.1.3 FHSC candidates

The detection of seven candidate first cores has been claimed so far: Cha-MMS1 (Belloche et al., 2006, 2011a), L1448-IRS2E (Chen et al., 2010), Per-Bolo 58 (Enoch et al., 2010; Dunham et al., 2011), L1451-mm (Pineda et al., 2011), CB17-MMS (Chen et al., 2012), B1-bS, and B1-bN (Pezzuto et al., 2012). All but one (B1-bS) are VeLLOs (internal luminosity $L_{\rm int} < 0.1\ L_\odot$), in agreement with the range of luminosities predicted for FHSCs. With $L_{\rm bol} \sim 0.49\ L_\odot$, B1-bS might be too luminous for a FHSC. L1448-IRS2E, Per-Bolo 58, and L1451-mm drive outflows that have been interferometrically detected. L1448-IRS2E drives an outflow with velocities of $\sim$ 25 km s^{-1}, one order of magnitude higher than predicted for a first core by MHD simulations (Machida et al., 2008). This suggests that it is at the more evolved second core stage so is likely ruled out as a first core candidate. Per-Bolo 58, L1451-mm, and CB17-MMS all have outflow velocities in agreement with theoretical predictions (see Sect. 4.1.1). However, the outflows of Per-Bolo 58 and CB17-MMS extend over 6000 AU – 8000 AU, with dynamical times $\sim 10^4$ yr, about one order of magnitude longer than the expected first core lifetime in a *magnetised* collapsing dense core. Lifetimes in the range $\sim$ 4000 yr – 10000 yr are produced by non- or very-weakly magnetised simulations, but no outflow is produced at the FHSC stage in these cases (e.g, Commerçon et al., 2012). L1451-mm is therefore the only candidate driving an outflow with properties (maximum velocity 2.3 km s^{-1}, dynamical time 1.6×10^3 yr) consistent with current theoretical predictions at the first-core stage. There has been no outflow detection for the B1-bS and B1-bN condensations in Perseus, but the SED fitting of their *Herschel* and *Spitzer* (where applicable) fluxes seems to be consistent with the presence of a central object surrounded by a dusty envelope

Table 4.1: Parameters of 2010 APEX CHAMP$^+$ observations.

Transition	f[a] (MHz)	σ_ν[b] (kHz)	$HPBW$[c] ($''$)	δf[d] (kHz)	δV[e] (km s^{-1})	$N_{\rm pos}$[f]	$F_{\rm eff}$[g] (%)	$B_{\rm eff}$[g] (%)	$T_{\rm sys}$[h] (K)	rms[i] (mK)
^{13}CO 6–5	661067.2766	0.5	9.2	183	0.083	7	95	36	1000-1200	76-85
CO 6–5	691473.0763	0.5	8.8	183	0.079	14	95	36	900-1900	108-185
CO 7–6	806651.8060	5.0	7.5	183	0.068	14	95	36	2200-6900	217-608

Notes. [(a)] Rest frequency taken from the Cologne Database for Molecular Spectroscopy (CDMS, http://www.astro.uni-koeln.de/cdms). [(b)] Frequency uncertainty taken from the CDMS catalogue. [(c)] Angular resolution. [(d)] Channel spacing in frequency. [(e)] Channel spacing in velocity. [(f)] Number of observed positions. [(g)] Forward and main-beam efficiencies from CHAMP$^+$ webpage. [(h)] System temperature. [(i)] rms sensitivity in $T_a^\star$ scale.

that is younger than the Class 0 phase (Pezzuto et al., 2012).

The goal of this study is to set constraints on the kinematics of the envelope of Cha-MMS1 to test if it is consistent with Cha-MMS1 being in the FHSC stage. The structure of this Chapter is as follows. In Sect. 5.2 we summarise the observational details, we then present our results in Sect. 4.3 and in Sect. 4.4 we perform radiative transfer modelling of the spectra towards Cha-MMS1. The discussion and conclusions follow in Sects. 5.5 and 5.6, respectively.

4.2 Observations

We performed observations towards the dense core Cha-MMS1 at α_{2000}=11^{h}06^{m}33^s.13, δ_{2000}=-77°23′35.1′′[1] with the APEX and Mopra telescopes on the central core position as well as on offset positions close to the core along directions parallel and perpendicular to the filament in which it is embedded (see Fig. 4.1). The data were reduced with the CLASS software[2].

4.2.1 2010 APEX observations

Observations with APEX[3] using the CHAMP$^+$[4] heterodyne SSB receiver were carried out in 2010 July, in the following molecular transitions: ^{13}CO 6–5, CO 6–5, and CO 7–6. CHAMP$^+$ is a 2×7 pixel array receiver connected to a Fast-Fourier-Transform spectrometer backend array (FFTS). It operates in two frequency bands simultaneously, around 690 GHz and 810 GHz. The channel spacing is 183 kHz. The corresponding velocity resolution for each transition is given in Table 4.1. All three transitions were observed with the central CHAMP$^+$ pixel pointed on the central core position at α_{J2000}=11^{h}06^{m}33^s.13, δ_{J2000}=-77°23′35.1′′. In addition to the central position, CO 6–5 and CO 7–6 were also observed with the central CHAMP$^+$ pixel be-

[1]Position from *Spitzer* observations (Belloche et al., 2011a).

[2]see http://www.iram.fr/IRAMFR/GILDAS.

[3]The Atacama Pathfinder Experiment telescope (APEX) is a collaboration between the Max-Planck Institut für Radioastronomie, the European Southern Observatory, and the Onsala Space Observatory.

[4]see http://www3.mpifr-bonn.mpg.de/div/submmtech/heterodyne/ champplus/champmain.html.

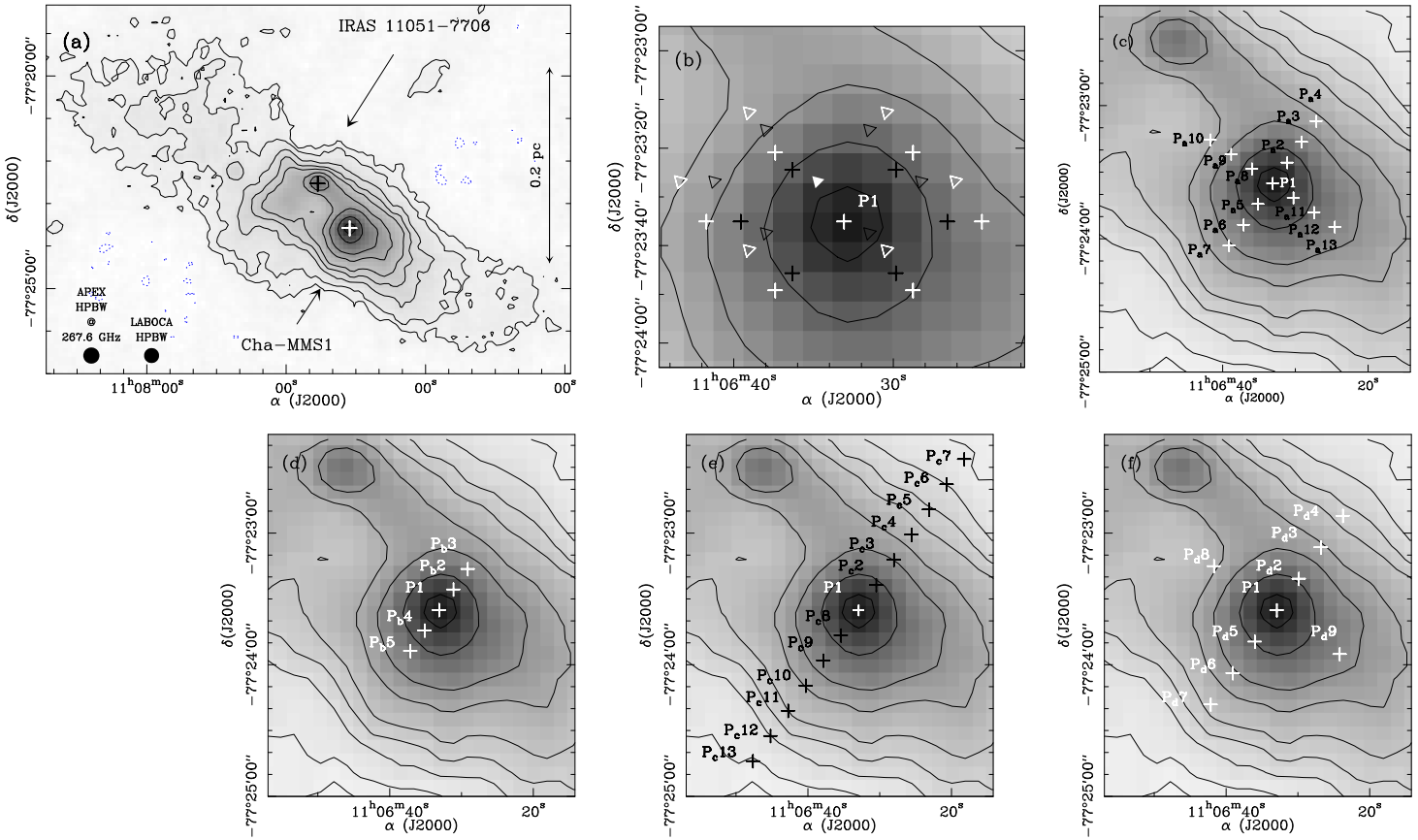

Figure 4.1: (a) 870 μm map of the filament in which Cha-MMS1 is embedded, obtained with LABOCA as part of an unbiased survey of Chamaeleon I (Belloche et al., 2011a). The contour levels correspond to $-a$, a, $2a$, $4a$, $6a$, $8a$, $12a$, $16a$, $24a$, $32a$, with a = 36 mJy/21″-beam (3σ). The white cross at α_{J2000}=$11^h06^m33^s.13$, δ_{J2000}=-77°23′35.1″ is the *Spitzer* position of Cha-MMS1. The position of the nearby Class I object IRAS 11051-7706 is also shown with a black cross. (b)-(f) Zoom-in of the positions (P, white/black crosses/triangles) observed with APEX and Mopra. P_1 is the central position. Panel (b) refers to CO 6–5 (white crosses), ^{13}CO 6–5 (white crosses), and CO 7–6 (black crosses), (c) to HCO^+ 3–2 and $H^{13}CO^+$ 3–2, (d) to CS 5–4, $H^{13}CO^+$ 4–3, and CO 4–3, (e) to $C^{17}O$ 2–1 and $C^{18}O$ 2–1 (all with APEX), and (f) to the Mopra observations (see Table 4.3). The spacing between adjacent positions is 11.4″ in panels (c) and (d), and 14″ in panel (e). In panel (f), it is 17.5″ for the positions perpendicular to the filament and 35″ for the positions along the filament. For panel (b) the pixel spacing of the CHAMP$^+$ array is 20″ for the white and 15″ for the black crosses relative to P1. The black (CO 7–6) and white (CO 6–5) open triangles mark the positions observed with CHAMP$^+$ centred on the offset position at (5.3″, 8.3″) relative to Cha-MMS1 (filled triangle).

Table 4.2: Parameters of 2011 APEX observations.

Transition	f[a] (MHz)	σ_ν[b] (kHz)	$HPBW$[c] ($''$)	Receiver	Backend	δf[d] (kHz)	δV[e] (km s^{-1})	$N_{\rm pos}$[f]	$F_{\rm eff}$[g] (%)	$B_{\rm eff}$[g] (%)	$T_{\rm sys}$[h] (K)	rms[i] (mK)
$C^{18}O$ 2–1	219560.3541	1.5	27.7	APEX-1 SSB	XFFTS2	76	0.104	13	95	75	232-240	136-195
$C^{17}O$ 2–1	224714.1870	80	27.1	APEX-1 SSB	XFFTS2	76	0.101	13	95	75	200-217	87-99
CS 5–4	244935.5565	2.8	24.9	APEX-1 SSB	XFFTS2	76	0.093	5	95	75	215-420	23-25
$H^{13}CO^+$ 3–2	260255.3390	9.7	23.4	APEX-1 SSB	XFFTS2	76	0.088	13	95	74	250-262	63-75
HCO^+ 3–2	267557.6259	1.1	22.8	APEX-2 SSB	FFTS1	122	0.137	13	95	74	200-306	120-152
$H^{13}CO^+$ 4–3	346998.3440	11.9	17.5	FLASH345 2SB	XFFTS	76	0.066	5	95	73	280-305	48-53
CO 4–3	461040.7682	0.5	13.2	FLASH460 DSB	AFFTS	183	0.119	5	95	60	1083-1288	234-360

Notes. [a] Rest frequency taken from the CDMS catalogue. The frequencies given here for the $H^{13}CO^+$ 3–2 and 4–3 transitions do not account for their hyperfine structure. See the CDMS catalogue for the specific frequencies corresponding to each hyperfine structure component of the transitions. [b] Frequency uncertainty taken from the CDMS catalogue. [c] Angular resolution. [d] Channel spacing in frequency. [e] Channel spacing in velocity. [f] Number of observed positions. [g] Forward and main-beam efficiencies. [h] System temperature. [i] rms sensitivity in $T_a^\star$ scale.

Table 4.3: Parameters of Mopra observations

Transition	f[a]	σ_ν[b]	$HPBW$[c]	δf[d]	δV[e]	$N_{\rm pos}$[f]	$B_{\rm eff}$[g]	$T_{\rm sys}$[h]	rms[i]
	(MHz)	(kHz)	($''$)	(kHz)	(km s^{-1})		(%)	(K)	(mK)
c-C_3H_2 $3_{2,2}$-$3_{1,3}$	84727.6909	3.4	40.6	34	0.12	1	34	185	18
$HC^{18}O^+$ 1–0	85162.2231	4.8	40.4	34	0.12	1	34	185	18
$H^{13}CO^+$ $1_{2,2}$–$0_{1,1}$ [j]	86754.3004	3.9	39.7	34	0.12	1	34	165	17
$HN^{13}C$ $1_{2,3,3}$–$0_{1,2,2}$ [j]	87090.8297	3.8	39.5	34	0.12	1	34	165	14
HNCO $4_{0,4,5}$-$3_{0,3,4}$ [j]	87925.2178	0.3	39.2	34	0.11	1	34	164	16
HCO^+ 1–0	89188.5247	4.1	38.6	34	0.11	1	34	147	17
HC_3N 10_{11}–9_{10} [j]	90979.0024	1.0	37.9	34	0.11	9	34	208-230	17-32
^{13}CS 2–1	92494.3080	50.0	37.2	34	0.11	9	34	208-230	17-29
N_2H^+ $1_{2,3}$–$0_{1,2}$ [j]	93173.7642	2.4	37.0	34	0.11	9	34	213-233	19-31
$C^{34}S$ 2–1	96412.9495	2.2	35.7	34	0.10	9	34	216-235	19-35
CH_3OH–*E* $2_{1,2}$-$1_{1,1}$	96739.362	5.0	35.6	34	0.10	9	34	229-251	20-33
CH_3OH–*A* $2_{0,2}$-$1_{0,1}$	96741.375	5.0	35.6	34	0.10	9	34	229-251	20-33
CH_3OH–*E* $2_{0,2}$-$1_{0,1}$	96744.550	5.0	35.6	34	0.10	9	34	229-251	20-33
$C^{33}S$ 2–1	97172.0639	0.2	35.4	34	0.10	9	34	229-251	20-34
CS 2–1	97980.9533	2.3	35.2	34	0.10	9	34	229-251	20-32

Notes. [a] Rest frequency taken from the CDMS catalogue. [b] Frequency uncertainty. [c] Angular resolution. [d] Channel spacing in frequency. [e] Channel spacing in velocity. [f] Number of observed positions. [g] Main beam efficiency. [h] Range of system temperature. [i] rms sensitivity in $T_a^\star$ scale. [j] Transition with hyperfine structure.

ing centred on an offset position ($\Delta\alpha$, $\Delta\delta$) = (5.3$''$, 8.3$''$) relative to the centre of Cha-MMS1 (see Fig. 4.1b). The observations were done in position-switching mode with the reference position at ($\Delta\alpha$, $\Delta\delta$) = (-600$''$, 4$''$). The reference position was checked to be free of emission with an rms sensitivity of 0.06 K and 0.24 K for the central pixel in CO 6–5 and CO 7–6, respectively, and for the spectral resolution given in Table 4.1.

The observations were carried out on four different days, in the last two of which ^{13}CO 6–5 was observed in parallel to CO 7–6. A comparison to the CO 7–6 spectra of the first two days of observation suggests that there is a pointing offset in the south-west direction parallel to the filament of up to $\sim$ 5$''$ between the CO 6–5/CO 7–6 and ^{13}CO 6–5/CO 7–6 datasets. The forward and beam efficiencies used to convert antenna temperatures $T_a\star$ into main-beam temperatures can be found in Table 4.1 along with further information on line frequencies, system temperatures, and noise levels. The focus was optimised on Saturn and Mars and the pointing in CO 6–5 emission on the star IRAS 07454-7112.

4.2.2 2011 APEX Observations

We carried out observations with the APEX telescope in 2011 April, June, and December in the following molecular transitions: CS 5–4, $H^{13}CO^+$ 3–2, HCO^+ 3–2, $H^{13}CO^+$ 4–3, CO 4–3, $C^{18}O$ 2–1, and $C^{17}O$ 2–1. The observations were done in position-switching mode with the reference position at α_{J2000}=$11^h05^m23^s.7$, δ_{J2000}=-77°11′02.2$''$. The reference position

is free of emission with an rms of 0.12 K in HCO^+ 3–2 and 0.33 K in CO 4–3 for the spectral resolution given in Table 4.2. The corresponding beamwidth, forward, and main beam efficiencies are listed in Table 4.2. The positions observed for each transition are shown in Figs. 4.1c to e, overlaid on the 870 μm map of the filament seen in Fig. 4.1a. All positions lie either perpendicular (position angle −35° east from north) or parallel to the filament. The transitions CS 5–4, $H^{13}CO^+$ 4–3, CO 4–3, $C^{18}O$ 2–1, and $C^{17}O$ 2–1 were only observed perpendicular to the filament, while $H^{13}CO^+$ 3–2 and HCO^+ 3–2 were also observed parallel to it. Table 4.2 gives information about the frontend and backend used for each transition, their respective spectral resolutions, the resulting system temperatures, and rms noise levels. The telescope pointing was checked every 1 h to 1.5 h and was performed on IRAS 07454-7112. The pointing accuracy is ∼2″ (rms). The focus was optimised on either Saturn, Jupiter, or Mars, and repeated approximately every 3 h.

4.2.3 Mopra observations

We observed with the Mopra telescope towards the central position of Cha-MMS1 along with eight other offset positions perpendicular and parallel to the filament (see Fig. 4.1f) in 2011 May in several molecular transitions using the zoom mode of the high-resolution spectrometer MOPS. The receiver was tuned at two different frequencies, 94554 MHz and 87190 MHz. Only the central position was observed for the latter. Position-switching observations were done with the reference position at α_{J2000}=$11^h05^m23^s.7$, δ_{J2000}=-77°11′02.2″. It was checked that is was free of emission with an rms sensitivity ranging from 46 mK – 52 mK in all transitions for the spectral resolution given in Table 4.3. The transitions that are used for the analysis in this Chapter are listed here: CS 2–1, $C^{34}S$ 2–1, ^{13}CS 2–1, $C^{33}S$ 2–1, HC_3N 10–9, $HN^{13}C$ 1–0, N_2H^+ 1–0, HCO^+ 1–0, $H^{13}CO^+$ 1–0, $HC^{18}O^+$ 1–0, HNCO 4–3, c-C_3H_2 $3_{2,2}$-$3_{1,3}$, CH_3OH–*A* $2_{0,2}$–$1_{0,1}$, and CH_3OH–*E* $2_{1,2}$–$1_{1,1}$. The final reduced dataset was obtained after averaging both polarisations. We did, however, notice some differences in integrated intensity for the two polarisations of up to ∼ 10% (see Appendix A for more details about this discrepancy). The channel spacing was 34 kHz. The range of system temperatures $T_{\rm sys}$ for each transition is given in Table 4.3. The beam efficiency used to convert antenna temperatures $T_a^\star$ into main-beam temperatures is 0.34. This value was derived from a detailed calibration analysis (see Appendix A). The telescope pointing was checked approximately every hour on U Men for Cha-MMS1, and AH Sc and IK Tau for the calibration sources Oph A SM1N and IRAM 04191, respectively. The transitions, their rest frequencies, and the number of observed positions are listed in Table 4.3.

4.2.4 Spitzer archive data

We used MIPS1 24 μm and MIPS2 70 μm continuum data taken from the *Spitzer Heritage Archive*[5] (AORkeys: 19978496, 3962112, 19979264).

[5]see http://irsa.ipac.caltech.edu/data/SPITZER/docs/ spitzerdataarchives/.

4.2.5 CO 3–2 data

Cha-MMS1 was observed in CO 3–2 in 2005 with the APEX telescope, and the data were presented in Belloche et al. (2006). We used the CO 3–2 data along the direction perpendicular to the filament in conjuction with the other CO transitions and isotopologues when modelling the spectra in Sect. 4.4.

4.3 Results

4.3.1 Internal luminosity derivation

We performed aperture photometry on MIPS1 24 μm and MIPS2 70 μm *Spitzer* data, and derived flux densities for the dense core Cha-MMS1. We used the IDL procedure aper.pro[6] with the following aperture and background inner and outer radii: 16″ (18″ - 39″) and 13″ (20″ - 32″) for the 70 μm and 24 μm data, respectively. Fine-scale aperture corrections of 2.16 for MIPS1 and 1.17 for MIPS2 were taken from the *MIPS Instrument Handbook*[7]. The flux densities derived before and after correction are given in Table 4.4. In the following, we use the average value of the two independent, aperture-corrected 70 μm flux density measurements to estimate the internal luminosity of Cha-MMS1. We determine the internal luminosity of Cha-MMS1 with two methods.

4.3.1.1 Method 1

Dunham et al. (2008) calculated the internal luminosity of low-luminosity protostars based on a parametric model consisting of a protostellar envelope, a disk, and an outflow cone, coupled to a 2D radiative transfer code. They derived the following empirical relation between the internal luminosity of a protostar and its observed 70 μm flux:

$$L_{int} = 3.3 \times 10^8 F_{70}^{0.94} L_{\odot}, \tag{4.1}$$

where F_{70} is normalised to 140 pc and is in cgs units (cm^{-2} s^{-1}). With this equation, we derive an internal luminosity of 0.025 ± 0.003 $L_{\odot}$ after correction for the distance of Cha-MMS1.

4.3.1.2 Method 2

Commerçon et al. (2012) have recently presented the evolution of the 24 μm and 70 μm flux densities in the course of the first core lifetime, as well as the time evolution of the FHSC internal luminosity via 3D radiation-magnetohydrodynamic (hereafter, RMHD) simulations of a 1 $M_{\odot}$ dense core collapse. A 3D RMHD simulation for the case of a 5 $M_{\odot}$ dense core collapse was also computed (see Sect. 4.5.4.2). Both models have a strong initial magnetisation level (MU2 model; Commerçon et al., 2012).

We looked for a correspondence between Cha-MMS1's 24 μm and 70 μm flux densities and the model flux density predictions of FHSC obtained for the 1 $M_{\odot}$ and 5 $M_{\odot}$ dense cores.

[6] From the IDL Astronomy User's Library (http://idlastro.gsfc.nasa.gov/contents.html).

[7] see http://irsa.ipac.caltech.edu/data/SPITZER/docs/mips/ mipsinstrumenthandbook/1/.

Table 4.4: Flux densities of Cha-MMS1 from aperture photometry.

Instrument	λ^{a} (μm)	AORkey[b]	$F_{\lambda}{}^{c}$ (mJy)	F_{λ}^{corrd} (mJy)
MIPS2	70	19978496	139 ± 32	300 ± 70
		3962112	184 ± 25	397 ± 54
		average		349 ± 44
MIPS1	24	19978496	2.82 ± 0.64	3.3 ± 0.7
		3962112	2.32 ± 0.60	2.7 ± 0.8
		19979264	2.50 ± 0.63	2.9 ± 0.7
		average		3.0 ± 0.4

Notes. [(a)] Wavelength. [(b)] AORkey of *Spitzer* observations. [(c)] Flux density from aperture photometry. [(d)] Flux density after fine-scale correction.

In the case of the 1 $M_{\odot}$ model, we find consistent flux densities within a factor of $\sim$ 2 for inclinations to the line-of-sight $45° < i < 60°$, and a first core age of 850 yr. In this case, the internal luminosity prediction is $\sim$ 0.08 $L_{\odot}$ – 0.13 $L_{\odot}$, at least three times higher than the internal luminosity derived using the relation by Dunham et al. (2008).

In the 5 $M_{\odot}$ case at inclinations $30° < i < 45°$ and for a first core age of $\sim$ 2680 yr, the observed and predicted 24 μm flux densities are consistent within a factor of $\sim$ 2.5, and we thus obtain an internal luminosity estimate of $\sim$ 0.13 $L_{\odot}$ – 0.18 $L_{\odot}$.

In the framework of this MHD model, the overall range is $\sim$ 0.08 $L_{\odot}$ – 0.18 $L_{\odot}$ for inclinations of $30° \leq i < 60°$. The internal luminosity derived from the empirical relation of Dunham et al. (2008) is therefore lower by a factor of $\sim$ 3 – 7 compared to the predictions of 3D RMHD simulations.

We adopt an internal luminosity of $\sim$ 0.1 $L_{\odot}$ as an approximation, which is within the luminosity range we derived based on the RMHD simulations. We use this value for the radiative transfer modelling that follows in Sect. 4.4. Even if we were to adopt the upper limit of 0.18 $L_{\odot}$, the temperature profile of the inner envelope would not significantly change (Equation 4.7, Sect. 4.4.1).

4.3.2 Spectra towards Cha-MMS1

Figures 4.2 and 4.3 show the spectra of the transitions observed with APEX and Mopra towards the central position of Cha-MMS1. Apart from ^{13}CS 2–1 and C^{33}S 2–1 for which we can only draw upper limits, most transitions are detected. Tables 4.5 to 4.9 give the centroid velocities derived for these transitions after performing Gaussian or hyperfine-structure fits in CLASS to the observed spectra ("GAUSS" and "HFS" methods). Only the spectra that have either a Gaussian shape or a well-defined hyperfine structure and no self-absorption features can be fitted in this way. Tables 4.5 to 4.9 list the systemic velocities of groups of transitions observed at the same offset positions (see Fig 4.1). The centroid velocities of transitions that were only observed at the central position of the core are given in Table 4.6.

4.3.2.1 Issues with the systemic velocity

It is apparent from Fig. 4.3 that all the APEX spectra are redshifted by 0.1 km s^{-1} compared to the systemic velocity derived from a hyperfine-structure fit to the N_2H^+ 1–0 multiplet observed with Mopra. There is therefore a problem with one of the two datasets. As the shift is seen for both the high and low-density APEX tracers (e.g., $H^{13}CO^+$ 4–3 and $C^{18}O$ 2–1), it is not likely to be an intrinsic characteristic of the source, but rather an instrumental effect.

We compared the spectra of the calibration source IRAM 04191, observed with APEX, Mopra, and with the IRAM 30-m telescope, to pinpoint the source of the systemic velocity inconsistency. In addition, because we have Mopra observations of the central position of Cha-MMS1 from both 2010 and 2012 (as part of a survey targeting starless cores in Cha I and III, Tsitali et al. in prep.), we compared them to the 2011 data that we present in this Chapter. The N_2H^+ 1–0 IRAM 04191 spectra are consistent with each other, and consequently, we cannot draw any conclusions about the velocity shift. However, the N_2H^+ 1–0 central spectrum of Cha-MMS1 observed with Mopra in 2010 and 2012 gives a velocity estimate consistent with the APEX data, i.e. 4.4 kms^{-1}, but inconsistent with the 2011 Mopra data, i.e. 4.3 kms^{-1}. We therefore assume that the Mopra 2010, 2012, and APEX 2011 datasets are correct and apply a correction of 0.1 kms^{-1} to the systemic velocity derived from the 2011 Mopra N_2H^+ 1–0 transition whenever we use it along with the 2011 APEX spectra. We explicitly mention it in the text whenever this correction is applied.

4.3.3 Rotation

We constructed position-velocity (P-V) diagrams for the Mopra $C^{34}S$ 2–1, HC_3N 10–9, N_2H^+ 1–0, CH_3OH–*A* $2_{0,2}$–$1_{0,1}$, and CH_3OH–*E* $2_{1,2}$–$1_{1,1}$ transitions and the APEX CS 5–4, $H^{13}CO^+$ 3–2, $H^{13}CO^+$ 4–3, $C^{17}O$ 2–1, and $C^{18}O$ 2–1 transitions (Figs. 4.4 and 4.5) based on the centroid velocities measured in Sect. 4.3.2. We performed linear fits to these P-V diagrams to search for velocity gradients. The results are listed in Table 4.10 and shown in Figs. 4.4 and 4.5. After combining all tracers, there is no clear velocity gradient parallel to the filament ($\leq$ 2 km s^{-1} pc^{-1}, see Figs. 4.4b and 4.5d).

The P-V diagrams for the direction perpendicular to the filament are given in Figs. 4.4a and 4.5a–c. There is a clear velocity gradient along this direction with an amplitude of $\sim$ 2 km s^{-1} – 4.5 km s^{-1} pc^{-1} up to $\sim$ 8000 AU. The average velocity gradient is $\sim$ 3.1 $\pm$ 0.1 km s^{-1} pc^{-1}. However, the $C^{17}O$ 2–1 and $C^{18}O$ 2–1 curves are significantly flatter at the inner, $r \leq 4000$ AU radii, compared to the range 4000 AU – 8000 AU (Fig. 4.5c), with velocity gradients $\leq$ 2 km s^{-1} pc^{-1}. The $H^{13}CO^+$ 4–3 and $H^{13}CO^+$ 3–2 P-V curves are also consistent with no gradient for the inner $\sim$ 4000 AU.

The P-V curves of $C^{17}O$ 2–1 and $C^{18}O$ 2–1 depart from a straight line for radii larger than $\sim$ 8000 AU. The weighted average velocity gradient for the two transitions between the two outermost positions (at $\pm$ 12500 AU) is $\sim$ 1.5 $\pm$ 0.2 km s^{-1} pc^{-1}, i.e. smaller by a factor of $\sim$ 2 than within 8000 AU. Such an "S" shape was reported by Belloche et al. (2002) for the Class 0 protostar IRAM 04191 and was interpreted as an indication of differential rotation in the envelope beyond a certain radius. If the velocity gradient of Cha-MMS1 perpendicular to the filament is due to rotation, then the bulk of the envelope is roughly in solid-body rotation

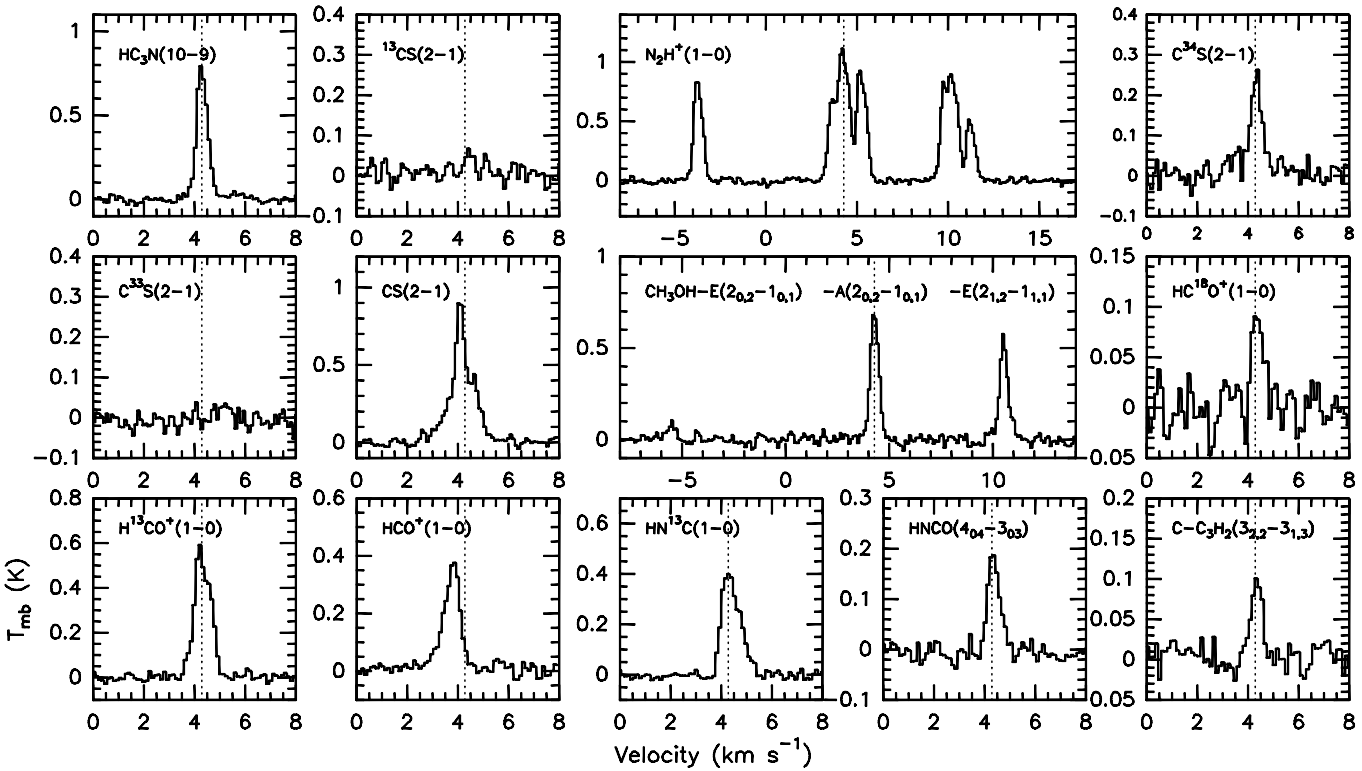

Figure 4.2: Transitions observed with Mopra towards the central position of Cha-MMS1, in main-beam brightness temperature scale. The dotted line shows the systemic velocity of Cha-MMS1, derived from a seven component hyperfine fit to the N_2H^+ 1–0 multiplet.

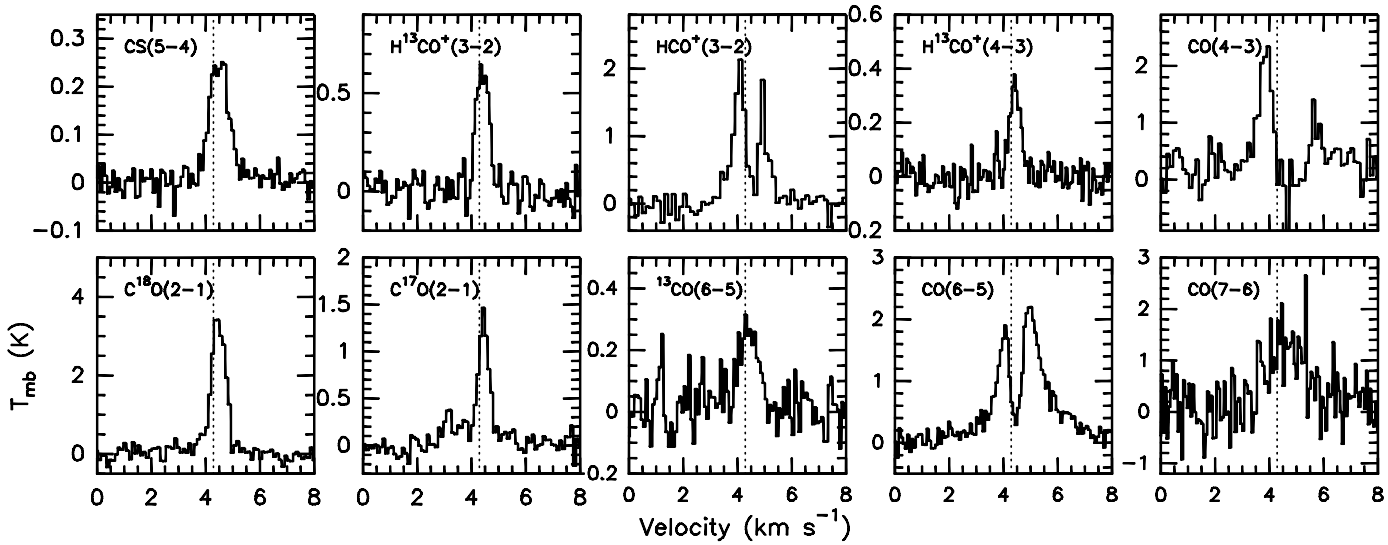

Figure 4.3: Transitions observed with APEX towards the central position of Cha-MMS1, in main-beam brightness temperature scale. The dotted line shows the systemic velocity of Cha-MMS1, derived from a seven component hyperfine fit to the N_2H^+ 1–0 multiplet observed with Mopra *without* correcting for the +0.1 km s^{-1} velocity shift (see Sect. 4.3.2.1).

Table 4.5: Mopra centroid velocities at positions perpendicular and parallel to the filament.

Position[a]	$\Delta\alpha$[b]	$\Delta\delta$[b]	Spacing[c]	V_{LSR}[d] (km s^{-1})				
	(″)	(″)	(″)	$C^{34}S$ 2–1	HC_3N 10–9[e]	N_2H^+ 1–0[e]	CH_3OH–*A* $2_{0,2}$–$1_{0,1}$	CH_3OH–*E* $2_{1,2}$–$1_{1,1}$
P1	0	0	0	4.33±0.02	4.27±0.004	4.299±0.002	4.29±0.01	4.29± 0.01
P_d2	-10.0	14.3	17.5	4.30±0.02	4.29±0.004	4.279±0.002	4.29±0.01	4.28± 0.01
P_d3	-20.1	28.7	35.0	4.26±0.02	4.23±0.004	4.339±0.002	4.25±0.01	4.25± 0.01
P_d4	-30.1	43.0	52.5	4.21±0.02	4.12±0.004	4.168±0.002	4.21±0.01	4.21± 0.01
P_d5	10.0	-14.3	17.5	4.35±0.02	4.34±0.004	4.346±0.003	4.33±0.01	4.34± 0.01
P_d6	20.1	-28.7	35.0	4.39±0.02	4.41±0.004	4.403±0.004	4.37±0.01	4.36± 0.01
P_d7	30.1	-43.0	52.5	4.42±0.02	4.47±0.006	4.435±0.005	4.41±0.01	4.38± 0.01
P_d8	20.1	28.7	35.0	4.39±0.02	4.33±0.006	4.294±0.004	4.29±0.02	4.35± 0.02
P_d9	-20.1	-28.7	35.0	4.35±0.02	4.36±0.001	4.286±0.004	4.36±0.01	4.35± 0.01

Notes. [a] These positions are shown in Fig. 4.1f. [b] J2000 equatorial offset relative to the central position P1. [c] Angular distance to P1. [d] The correction of 0.1 km s^{-1} discussed in Sect. 4.3.2.1 has not been applied. [e] HC_3N 10–9 and N_2H^+ 1–0 both have a hyperfine structure and were therefore fitted using the method “HFS” with CLASS.

Table 4.6: Mopra centroid velocities toward the central position, P1.

Transition[a]	$V_{\rm LSR}$[b] (km s^{-1})
$HN^{13}C$ 1–0	4.37±0.01
HNCO $4_{0,4}$–$3_{0,3}$	4.36±0.02
c-C_3H_2 $3_{2,2}$-$3_{1,3}$	4.35±0.03
$HC^{18}O^+$ 1–0	4.39±0.03
$H^{13}CO^+$ 1–0	4.32±0.01

Notes. [(a)] Only the central position was observed for each of these transitions. [(b)] The correction of 0.1 km s^{-1} discussed in Sect. 4.3.2.1 has not been applied.

Table 4.7: CS 5–4 and $H^{13}CO^+$ 4–3 centroid velocities (APEX) at positions perpendicular to the filament.

Position[a]	$\Delta\alpha$[b]	$\Delta\delta$[b]	Spacing[c]	$V_{\rm LSR}$ (km s^{-1})	
	($''$)	($''$)	($''$)	CS 5–4	$H^{13}CO^+$ 4–3
P1	0	0	0	4.50±0.02	4.43±0.02
P_b2	-6.5	9.3	11.4	4.42±0.02	4.41±0.02
P_b3	-13.1	18.7	22.8	4.40±0.01	4.44±0.06
P_b4	6.5	-9.3	11.4	4.43±0.02	4.42±0.04
P_b5	13.1	-18.7	22.8	4.37±0.02	4.65±0.31

Notes. [(a)] These positions are shown in Fig. 4.1d. [(b)] J2000 equatorial offset relative to the central position. [(c)] Angular distance to the central position.

between ∼ 4000 AU and 8000 AU, and the outermost parts of the filament are rotating more slowly. After correcting for an inclination of 60° – 30° (Sect. 4.3.1), the average angular velocity for radii between 4000 AU and 8000 AU is $\Omega \sim 3.6$ km s^{-1} pc^{-1} – 6.2 km s^{-1} pc^{-1}. At 12500 AU, and for the same inclinations, we obtain $\Omega \sim 1.8$ km s^{-1} pc^{-1} – 3.0 km s^{-1} pc^{-1}.

The P-V diagram of CS 5–4 (Fig. 4.5a) shows a centrally peaked shape. The profile is not well resolved, but the centroid velocity at the central position is significantly higher than at one beam spacing on each side. This velocity shift is because there is an excess of redshifted emission toward the central position that is not reproduced by our radiative transfer modelling (see Sect. 4.4 and Fig. 4.10). This issue is discussed in Sect. 4.5.2.

4.3.4 Turbulence

The spatial variation of the non-thermal velocity dispersion is shown in Fig. 4.6 for several transitions. The ($FWHM$) linewidths were estimated using the "GAUSS" and "HFS" fitting methods in CLASS (see Table 4.11), as mentioned in Sect. 4.3.2. We computed the thermal

Table 4.8: $H^{13}CO^+$ 3–2 centroid velocities (APEX) at positions parallel and perpendicular to the filament.

Position[a]	$\Delta\alpha$[b] (″)	$\Delta\delta$[b] (″)	Spacing[c] (″)	V_{LSR} (km s^{-1}) $H^{13}CO^+$ 3–2
P1	0	0	0	4.41±0.02
perpendicular to the filament				
P_a2	-6.5	9.3	11.4	4.40±0.01
P_a3	-13.1	18.7	22.8	4.41±0.02
P_a4	-19.6	28.0	34.2	4.38±0.02
P_a5	6.5	-9.3	11.4	4.36±0.04
P_a6	13.1	-18.7	22.8	4.44±0.03
parallel to the filament				
P_a8	9.3	6.5	11.4	4.35±0.02
P_a9	18.7	13.1	22.8	4.32±0.04
P_a10	28.0	19.6	34.2	4.41±0.03
P_a11	-9.3	-6.5	11.4	4.41±0.02
P_a12	-18.7	-13.1	22.8	4.44±0.02
P_a13	-28.0	-19.6	34.2	4.43±0.02

Notes. [(a)] These positions are shown in Fig. 4.1c. [(b,c)] Same as Table 4.7.

Table 4.9: $C^{17}O$ 2–1 and $C^{18}O$ 2–1 centroid velocities (APEX) at positions perpendicular to the filament.

Position[a]	$\Delta\alpha$[b] (″)	$\Delta\delta$[b] (″)	Spacing[c] (″)	V_{LSR} (km s^{-1}) $C^{17}O$ 2–1	$C^{18}O$ 2–1
P1	0	0	0	4.45±0.01	4.47±0.01
P_c2	-8	11.5	14.0	4.42±0.02	4.45±0.01
P_c3	-16	23	28.0	4.37±0.02	4.40±0.01
P_c4	-24	34.5	42.0	4.30±0.03	4.32±0.01
P_c5	-32	46	56.0	4.23±0.02	4.28±0.01
P_c6	-40	57.5	70.0	4.22±0.02	4.27±0.01
P_c7	-48	69	84.1	4.38±0.03	4.33±0.02
P_c8	8	-11.5	14.0	4.44±0.02	4.48±0.01
P_c9	16	-23	28.0	4.47±0.03	4.51±0.01
P_c10	24	-34.5	42.0	4.53±0.03	4.52±0.01
P_c11	32	-46	56.0	4.56±0.03	4.55±0.01
P_c12	40	-57.5	70.0	4.55±0.03	4.51±0.01
P_c13	48	-69	84.1	4.50±0.04	4.52±0.02

Notes. [(a)] These positions are shown in Fig. 4.1e. [(b,c)] Same as Table 4.7.

Table 4.10: Velocity gradients perpendicular and parallel to the filament.

	Perpendicular to filament		Parallel to filament	
Transition	∇v^a (km s^{-1} pc^{-1})	Extent^b (AU)	∇v^a (km s^{-1} pc^{-1})	Extent^b (AU)
$C^{34}S$ 2–1	2.6±0.1	15750	0.6±1.0	5250
HC_3N 10–9	4.0±0.5	15750	-1.6±1.5	5250
N_2H^+ 1–0	3.4±0.2	15750	0.1±0.1	5250
CH_3OH–*A* $2_{0,2}$–$1_{0,1}$	2.4±0.2	15750	-2.0±0.7	5250
CH_3OH–*E* $2_{1,2}$–$1_{1,1}$	2.2±0.2	15750	-1.5±1.4	5250
$H^{13}CO^+$ 3–2	0.6±0.6	8550	-1.9±0.8	10260
$H^{13}CO^+$ 4–3	0.6±1.1	5130	-	-
$C^{17}O$ 2–1	3.6±0.5	16800	-	-
$C^{17}O$ 2–1^c	1.3±0.7	6300	-	-
$C^{18}O$ 2–1	3.2±0.5	16800	-	-
$C^{18}O$ 2–1^c	1.7±0.2	6300	-	-

Notes. [(a)] The velocity gradients were estimated from linear fits to the position-velocity curves in Figs. 4.4 and 4.5. [(b)] Total extent over which a linear fit to the data was performed. [(c)] Gradients corresponding to the fits limited to the inner parts in Fig. 4.5c.

velocity dispersion of each molecule as

$$\sigma_{\rm th} = \sqrt{\frac{k_B T}{\mu_M m_H}}, \tag{4.2}$$

where $\mu_{\rm M}$ is the molecular weight of the molecule, $k_{\rm B}$ the Boltzmann's constant, $m_{\rm H}$ the hydrogen mass, and T the kinetic temperature that we assume to be 9 K (see Sect. 4.4). The non-thermal linewidths are computed as

$$\sigma_{\rm nth} = \sqrt{{\sigma_{\rm obs}}^2 - {\sigma_{\rm th}}^2}, \tag{4.3}$$

while their respective uncertainties, denoted as $\delta\sigma$, are calculated using

$$\delta\sigma_{\rm nth} = \sqrt{\left(\frac{\partial\sigma_{\rm nth}}{\partial\sigma_{\rm observed}}\right)^2 {\delta\sigma_{\rm obs}}^2 + \left(\frac{\partial\sigma_{\rm nth}}{\partial\sigma_{\rm th}}\right)^2 {\delta\sigma_{\rm th}}^2}. \tag{4.4}$$

If we assume that $\delta\sigma_{th} = 0$, the above relation gives

$$\delta\sigma_{\rm nth} = \frac{\sigma_{\rm obs} \times \delta\sigma_{\rm obs}}{\sigma_{\rm nth}}. \tag{4.5}$$

We compare the non-thermal velocity dispersion to the thermal dispersion of the mean particle, with $\mu = 2.37$:

$$\sigma_{\rm th,mean} = \sqrt{\frac{k_B T}{\mu m_H}}. \tag{4.6}$$

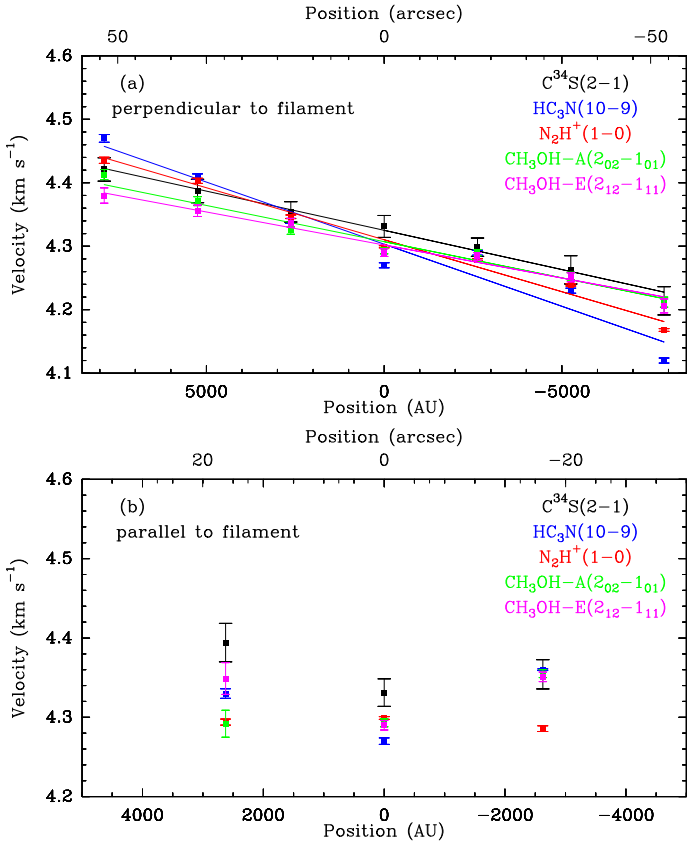

Figure 4.4: Position-velocity diagrams of the Mopra $C^{34}S$ 2–1 (black), HC_3N 10–9 (blue), N_2H^+ 1–0 (red), CH_3OH–*A* $2_{0,2}$–$1_{0,1}$ (green), and CH_3OH–*E* $2_{1,2}$–$1_{1,1}$ (pink) transitions, (a) perpendicular and (b) parallel to the filament. The error bars represent standard deviations (1σ). Linear fits to the velocities for each transition are shown with the same colour as in panel (a).

For $T = 9$ K, $\sigma_{\rm th,mean} \sim 0.18$ km s^{-1}, or $FWHM_{\rm th,mean} \sim 0.42$ km s^{-1}. Table 4.11 lists the observed linewidths and the derived thermal and non-thermal velocity dispersions for all transitions that have a low optical depth.

From Table 4.11 we infer that the non-thermal velocity dispersion is comparable to the mean thermal velocity dispersion. Therefore, there is almost an equipartition between thermal and non-thermal motions, provided that our asumption of $T = 9$ K is valid.

The non-thermal dispersion does not vary significantly along or across the filament (Figs. 4.6 and 4.7). One exception is, however, CS 5–4. Its non-thermal linewidth peaks at the centre and decreases at the outer parts. This is due to the excess redshifted emission observed at the central position (see Sect. 4.3.3, and Sects. 4.4 and 4.5.2 for further discussion).

Average values for the linewidths and non-thermal velocity dispersions over all positions are given in Table 4.12. The non-thermal dispersions, $\sigma_{\rm nth}$, have typical values of 0.2 km s^{-1}, comparable to the mean thermal dispersion. Uniform non-thermal dispersions on scales ~ 0.1 pc of the same order as the thermal dispersions have also been previously observed in other dense cores (e.g., Tafalla et al., 2004; Barranco & Goodman, 1998).

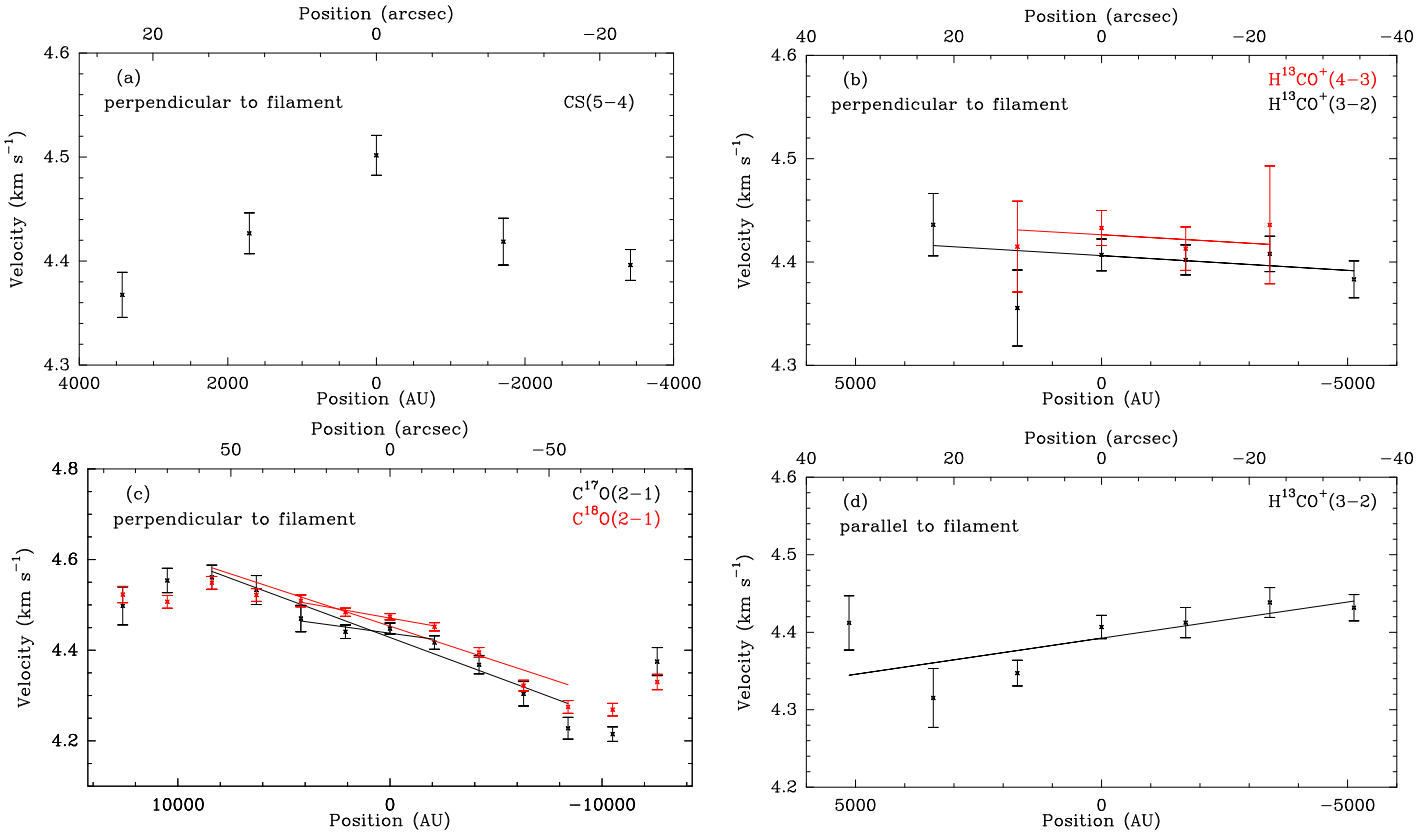

Figure 4.5: Position-velocity diagrams of the APEX CS 5–4, $H^{13}CO^+$ 3–2, $H^{13}CO^+$ 4–3, $C^{17}O$ 2–1, and $C^{18}O$ 2–1 transitions perpendicular (a, b, c) and parallel (d) to the filament. Linear fits are shown as straight lines. For $C^{17}O$ 2–1 and $C^{18}O$ 2–1 in (c) the two outer points from either side of the curve were excluded from the fits. Fits to the innermost positions of $C^{17}O$ 2–1 and $C^{18}O$ 2–1 are also displayed.

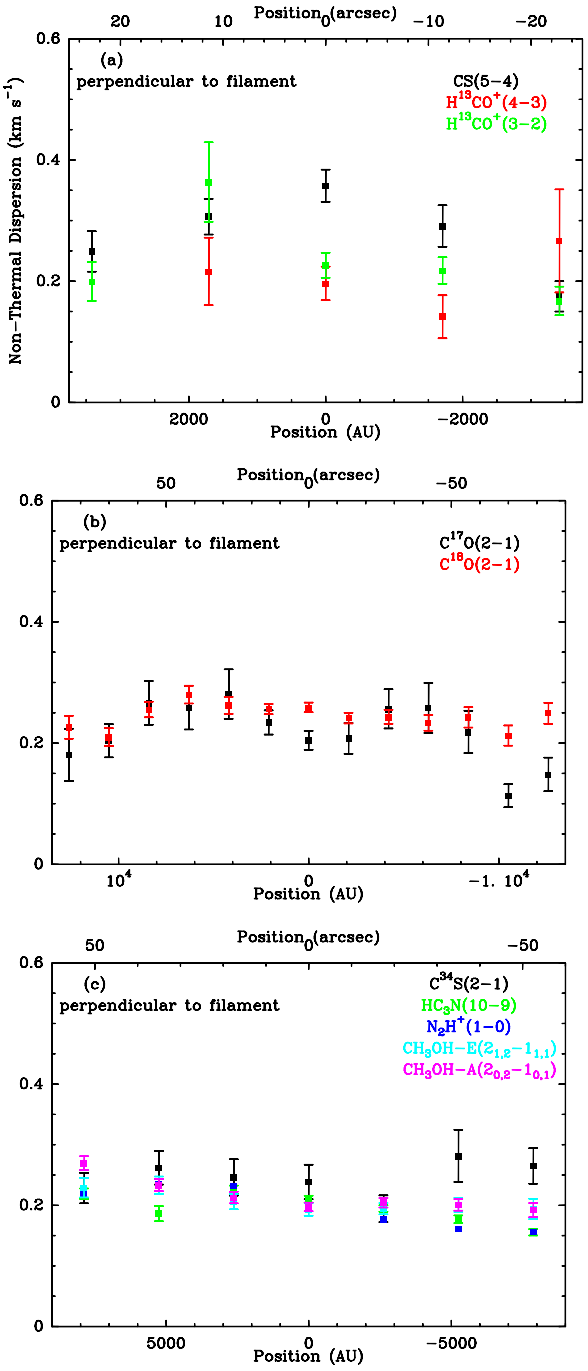

Figure 4.6: Non-thermal velocity dispersion, $\sigma_{\rm nth}$, versus position perpendicular to the filament for (a) CS 5–4 (black), $H^{13}CO$ 4–3 (red), and $H^{13}CO^+$ 3–2 (green), (b) $C^{17}O$ 2–1 and $C^{18}O$ 2–1, all observed with the APEX telescope, and (c) $C^{34}S$ 2–1 (black), HC_3N 10–9 (green), N_2H^+ 1–0 (dark blue), CH_3OH–*E* $2_{1,2}$-$1_{1,1}$ (light blue), and CH_3OH–*A* $2_{0,2}$-$1_{0,1}$ (pink) observed with Mopra. The errorbars are standard deviations. The thermal dispersion was calculated assuming a temperature of T = 9 K.

Table 4.11: Observed linewidth, thermal, and non-thermal velocity dispersions toward the central position.

Line	$FWHM$[a] (km s^{-1})	$\sigma_{\rm th}$[b] (km s^{-1})	$\sigma_{\rm nth}$[c] (km s^{-1})	$\frac{\sigma_{\rm nth}}{\sigma_{\rm th,mean}}$[d]
$C^{34}S$ 2–1	0.57±0.05	0.04	0.24±0.02	1.33±0.11
HC_3N 10–9[e]	0.50±0.009	0.04	0.21±0.006	1.17±0.03
N_2H^+ 1–0[e]	0.48±0.002	0.05	0.20±0.001	1.11±0.006
CH_3OH–*A* $2_{0,2}$–$1_{0,1}$	0.48±0.01	0.05	0.20±0.007	1.11±0.04
CH_3OH–*E* $2_{1,2}$–$1_{1,1}$	0.47±0.02	0.05	0.19±0.01	1.06±0.06
$H^{13}CO^+$ 3–2	0.55±0.03	0.05	0.23±0.02	1.28±0.11
$H^{13}CO^+$ 4–3	0.48±0.04	0.05	0.20±0.03	1.11±0.17
$C^{17}O$ 2–1	0.50±0.04	0.05	0.20±0.02	1.11±0.11
$C^{18}O$ 2–1	0.62±0.02	0.05	0.26±0.008	1.44±0.04
CS 5–4	0.85±0.04	0.04	0.36±0.03	2.00±0.17
$HN^{13}C$ 1–0	0.42±0.03	0.05	0.17±0.01	0.94±0.06
HNCO $4_{0,4}$–$3_{0,3}$	0.54±0.03	0.04	0.22±0.01	1.22±0.06
$HC^{18}O^+$ 1–0	0.50±0.06	0.05	0.21±0.03	1.17±0.17
c-C_3H_2 $3_{2,2}$-$3_{1,3}$	0.52±0.08	0.04	0.22±0.03	1.22±0.17

Notes. [(a)] Observed linewidth deduced from Gaussian or hyperfine fits to the spectra. [(b)] Thermal dispersion computed with Equation 4.2. [(c)] Non-thermal dispersion computed using Equation 4.3. [(d)] Ratio of non-thermal to *mean* thermal dispersion, with μ=2.37. [(e)] These transitions have a hyperfine structure and were fitted with the "HFS" fitting method in CLASS. The other transitions were fitted using the "GAUSS" method.

4.3.5 Infall signature

Cha-MMS1 exhibits the classical signature of infall in various transitions (Fig. 4.8). The infall signature manifests itself as a self-absorbed asymmetric, optically thick line with the blue peak stronger than the red one, and an optically thin line peaking in between these two peaks. This profile is indicative of inward motions as long as the excitation temperature increases towards the centre (e.g., Walker et al., 1986; Zhou, 1992).

Figure 4.8 shows that the absorption dips of CS 2–1 and HCO^+ 3–2 are redshifted with respect to the systemic velocity. The systemic velocity was estimated by a seven-component hyperfine-structure fit to the N_2H^+ 1–0 multiplet, using the HFS method in CLASS, giving a value of 4.299 ± 0.002 km s^{-1}. As discussed in Sect. 4.3.2.1, we apply a correction of 0.1 km s^{-1} to this systemic velocity to compare it to the APEX spectra. The self-absorption dip of the optically thick CS 2–1 transition has a velocity of 4.50 ± 0.05 km s^{-1}, which gives a velocity shift of 0.20 ± 0.05 km s^{-1}. Using the corrected value of the systemic velocity we derive a velocity shift of 0.18 ± 0.05 km s^{-1} for the optically thick HCO^+ 3–2 line, whose absorption dip has a velocity of 4.58 ± 0.06 km s^{-1}. Since the self-absorption dips are produced by the outer parts of the envelope where the opacity of the CS and HCO^+ lines becomes unity, this observed redshift points to the fact that the outer layers of Cha-MMS1 undergo inward

Table 4.12: Linewidths and non-thermal velocity dispersions averaged over all positions.

Line	$FWHM$ (km s^{-1})	$\sigma_{\rm nth}$ (km s^{-1})	$\frac{\sigma_{\rm nth}}{\sigma_{\rm th,mean}}$
$C^{34}S$ 2–1	0.57±0.009	0.24±0.002	1.33±0.17
HC_3N 10–9	0.47±0.003	0.20±0.001	1.09±0.05
N_2H^+ 1–0	0.47±0.005	0.19±0.003	1.08±0.02
CH_3OH–A $2_{0,2}$–$1_{0,1}$	0.51±0.003	0.21±0.001	1.18±0.06
CH_3OH–E $2_{1,2}$–$1_{1,1}$	0.49±0.004	0.20±0.001	1.13±0.08
$H^{13}CO^+$ 3–2	0.51±0.01	0.21±0.004	1.18±0.27
$H^{13}CO^+$ 4–3	0.50±0.02	0.20±0.005	1.14±0.28
$C^{17}O$ 2–1	0.53±0.01	0.22±0.002	1.21±0.17
$C^{18}O$ 2–1	0.59±0.005	0.24±0.001	1.35±0.08
CS 5–4[a]	0.61±0.02	0.26±0.004	1.42±0.17

Notes. [(a)] The linewidth and non-thermal velocity dispersion of the *central* CS 5–4 position was not taken into account for computing the average value, owing to the spectrum's broadened shape. See Sect. 4.5.2 for further discussion.

motions with velocities of the order of 0.2 km s^{-1}.

4.3.6 Overview of CHAMP$^+$ data

We probed Cha-MMS1 in the CO 6–5, CO 7–6, and ^{13}CO 6–5 molecular transitions with the APEX CHAMP$^+$ 2×7-pixel heterodyne receiver array in order to search for emission indicative of outflowing material. Figure 4.9 shows position maps of all spectra obtained for each transition. The CO 6–5 and 7–6 spectra along the filament have slightly higher intensities toward the north-east as opposed to the south-west. This could be due to contamination from the outflow of the Class I object IRAS 11051-7706 lying close to Cha-MMS1 at the north-east direction (Belloche et al., 2006), and it is further discussed in Sect. 4.5.2.

4.4 Radiative transfer modelling

We used the Monte Carlo radiative transfer code MAPYSO (Blinder, 1997; Belloche et al., 2002), which assumes spherical symmetry, to derive kinematic constraints on the dense core Cha-MMS1 by modelling the observed spectra. We modelled the emission of three sets of molecules, namely CS, HCO^+, and CO with their respective isotopologues.

We model all molecular transitions with the *same* density, temperature, and turbulence distributions, as described below. These distributions are shown in Figs. 4.11a, c, and e, respectively. Given the shape of the continuum emission, we assume that Cha-MMS1 is embedded in a filament and that the physical structure perpendicular to the filament in the plane of the sky is similar to the structure along the line-of-sight. We thus model the spectra taken along the direction perpendicular to the filament in addition to the central spectra. We perform the fit

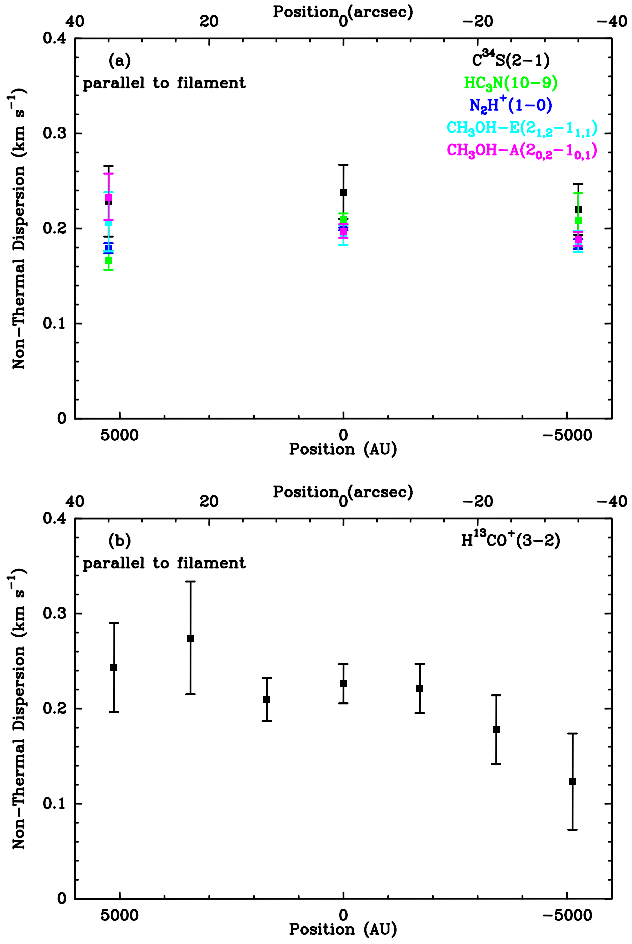

Figure 4.7: Non-thermal velocity dispersion, $\sigma_{\rm nth}$, versus position parallel to the filament for (a) $C^{34}S$ 2–1 (black), HC_3N 10–9 (green), N_2H^+ 1–0 (dark blue), CH_3OH–*E* $2_{1,2}$-$1_{1,1}$ (light blue), and CH_3OH–*A* $2_{0,2}$-$1_{0,1}$ (pink) observed with Mopra, and (b) $H^{13}CO^+$ 3–2 observed with the APEX telescope. The errorbars are standard deviations. The thermal dispersion was calculated assuming a temperature of T = 9 K.

optimisation by eye, by focussing on three main features of the spectra: the peak temperature, the position of the self-absorption dip (when there is one), and the linewidth of each spectrum.

4.4.1 Input parameters

4.4.1.1 Temperature profile

Using the internal luminosity derived in Sect. 4.3.1 we can constrain the inner dust temperature profile of the source, which we assume is dominated by the central heating. Following Terebey et al. (1993) and Motte & André (2001), we assume that in the inner part the dust temperature

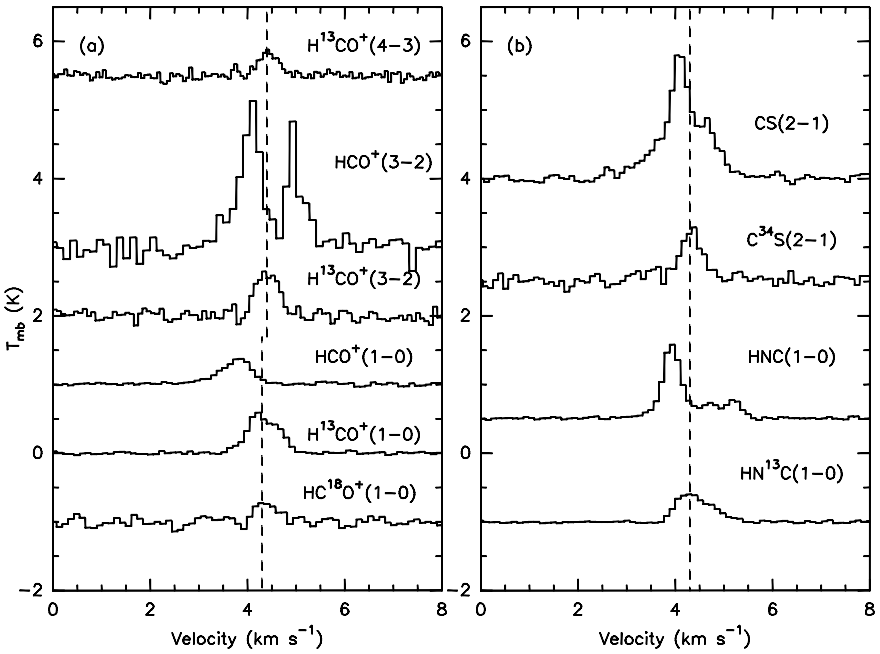

Figure 4.8: Spectra obtained toward the central position of Cha-MMS1 in the optically thick CS 2–1, HCO^+ 3–2, HCO^+ 1–0, and HNC 1–0 transitions and the low optical depth $C^{34}S$ 2–1, $H^{13}CO^+$ 1–0, $H^{13}CO^+$ 3–2, $H^{13}CO^+$ 4–3, $HC^{18}O^+$ 1–0, and $HN^{13}C$ 1–0 transitions. The dashed line corresponds to the systemic velocity derived from a seven-component hyperfine fit to the N_2H^+ 1–0 multiplet (4.3 km s^{-1}). It is corrected to 4.4 km s^{-1} for the APEX transitions HCO^+ 3–2, $H^{13}CO^+$ 3–2, and $H^{13}CO^+$ 4–3 (see Sect. 4.3.2.1).

behaves as

$$T_{\rm dust}(r) = 38\ {\rm K} \times \left(\frac{r}{100\ {\rm AU}}\right)^{-q} \times \left(\frac{L_{\rm int}}{1\ L_\odot}\right)^{q/2}, \tag{4.7}$$

with

$$q = \frac{2}{4+\beta}. \tag{4.8}$$

The constant β depends on the dust properties and the values 2, 1.5, and 1 are often used for molecular clouds, protostellar envelopes, and protostellar disks, respectively. Because this source is possibly at a very early evolutionary stage, perhaps before the protostellar phase, we adopt an intermediate value between the first two, 1.85, which gives $q \sim 0.34$.

We assume that the gas and dust are coupled well for densities above $\sim 10^5$ cm^{-3} (Lesaffre et al., 2005), and we use Equation 4.7 to define the kinetic temperature in the inner part. We assume a uniform temperature in the outer parts. We find from the modelling that a uniform kinetic temperature of 9 K produces spectra in agreement with the observations. More specifically, the optically thick CS 2–1 line sets the major constraints on the outer kinetic temperature, since this transition shows a strong asymmetry in the blue-red peak strengths (infall signature) with the blue peak stronger by about a factor of ~ 2. Its absorption dip and asymmetry require uniform outer temperatures to be well fitted. The radius at which the temperature drops to 9 K is fixed by the central heating (Equation 4.7).

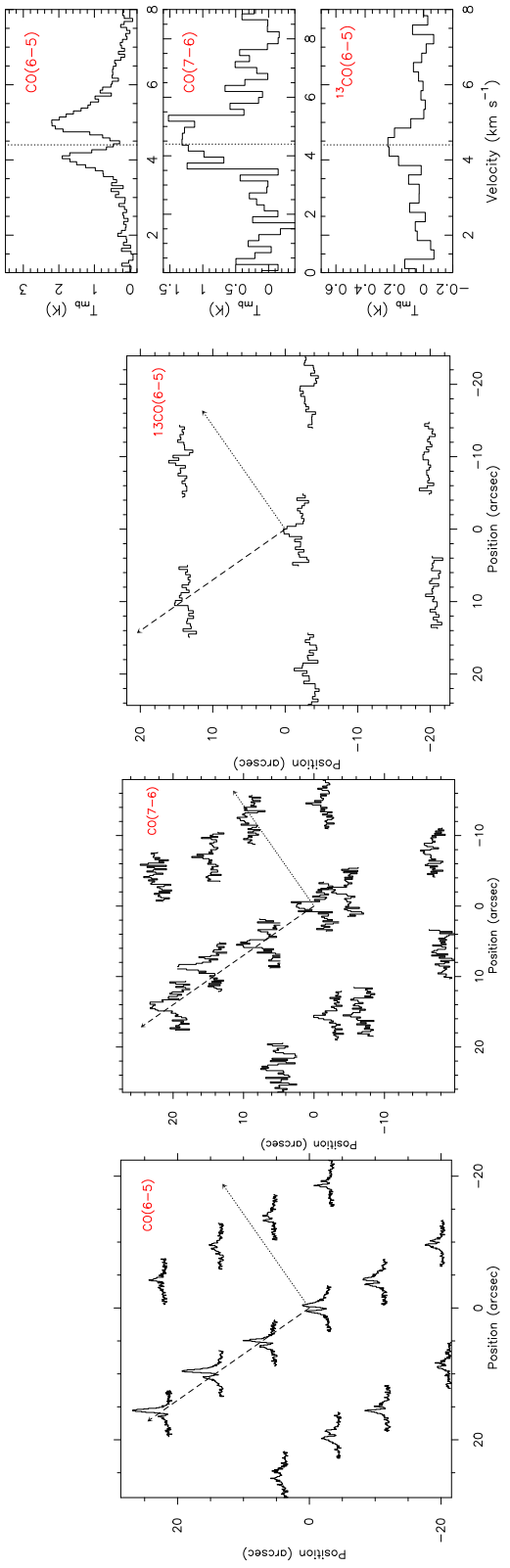

Figure 4.9: CO 6–5, CO 7–6, and ^{13}CO 6–5 spectra observed with the APEX telescope. The central position of Cha-MMS1 is at (0,0). The directions parallel and perpendicular to the filament are shown as dashed and dotted arrows, respectively. The central spectra of the three transitions are plotted in the rightmost panel on the scale of the main-beam brightness temperature. The dotted line shows the systemic velocity of Cha-MMS1 derived from a seven-component hyperfine fit to the N_2H^+ 1–0 multiplet and corrected for the 0.1 km s^{-1} velocity shift (see Sect. 4.3.2.1).

4.4.1.2 Density profile

We use a power-law density profile with an external radius of 60000 AU. We adopt a spherically symmetric r^{-2} density profile for the envelope, as is expected from models of spherical gravitational collapse of non-singular isothermal spheres during the core formation either without the effect of magnetic fields (e.g., Masunaga et al., 1998; Foster & Chevalier, 1993; Bodenheimer & Sweigart, 1968; Larson, 1969; Penston, 1969) or from models of axisymmetric, isothermal cloud contraction with magnetic fields (e.g., Tassis & Mouschovias, 2007; Fiedler & Mouschovias, 1993). Very recently, a 3D radiation hydrodynamic simulation of the collapse of an axisymmetric cloud core towards the formation of a first core led to a r^{-2} density distribution for the first core for $r > 100$ AU (Furuya et al., 2012). Since we do not resolve the inner $r < 700$ AU of Cha-MMS1, a simple, r^{-2} density profile is probably adequate for describing the envelope of Cha-MMS1.

Such density profiles have also been observed in dense cores. Density distributions close to a r^{-2} profile were derived for the starless cores L1498 and L1517B in Taurus (Tafalla et al., 2004). Bacmann et al. (2000) and Alves et al. (2001) also concluded that low-mass prestellar cores are described well by a density profile following an r^{-2} dependence, but excluding the sharp edges and flattened centre. Sharp density edges have been observed at the edges of starless cores, with exponents as steep as $r^{-3.5}$ (Nielbock et al., 2012). For simplicity, we do not account for steep outer density slopes.

The mass of Cha-MMS1 was derived from the LABOCA 870 μm continuum map of the Chamaeleon I cloud. The flux density measured within a radius of 3750 AU gives a mass of $\sim$1.44 $M_{\odot}$ for the Cha-MMS1 core (Belloche et al., 2011a). We use this value to scale our input density profile.

4.4.1.3 Inner turbulent broadening and isotopic ratios

In Sect. 5.3.2, we found that the non-thermal dispersion for all the observed transitions shows no significant spatial variations for radii up to $\sim$ 12500 AU ($\sim$ 0.06 pc). We adopt a *uniform* turbulent broadening up to this radius and keep the shape of the outer profile for 12500 AU $< r <$ 60000 AU ($\sim$ 0.3 pc) as a free parameter. The non-thermal dispersion appears to be uniform on scales $\sim$ 0.1 pc within the interiors of dense cores (e.g., Barranco & Goodman, 1998; Goodman et al., 1998) with increasing dispersion on larger scales (e.g., Goodman et al., 1998) that follows the Larson scaling law (Larson, 1981).

We assume the local ISM abundance isotopic ratios: ^{12}C/^{13}C $\sim$ 77 (Wilson & Rood, 1994), ^{32}S/^{34}S $\sim$ 22 (Frerking et al., 1980), ^{16}O/^{18}O $\sim$ 560 (Wilson & Rood, 1994), and ^{18}O/^{17}O $\sim$ 4.11 (Wouterloot et al., 2005).

4.4.2 CS Modelling

The following transitions of CS and its isotopologues were modelled: CS 2–1 (Mopra), C^{34}S 2–1 (Mopra), and CS 5–4 (APEX). ^{13}CS 2–1 and C^{33}S 2–1 were only used as upper limits due to their non-detections and are not presented here. We perform the modelling of the spectra for the direction perpendicular to the filament, along which five positions were observed for CS 5–4 and seven for the other transitions. Figure 4.10 shows one of the "best fit"

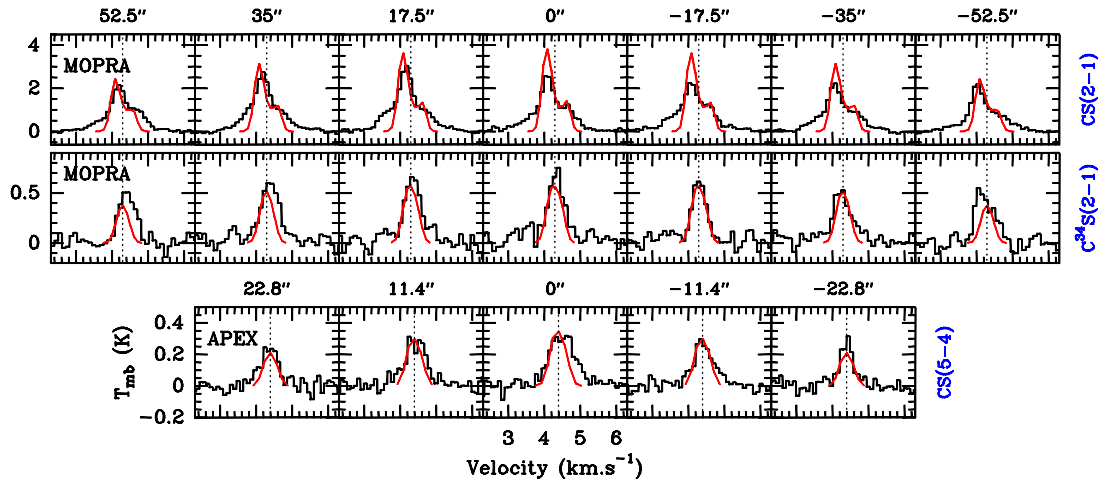

Figure 4.10: Best fit model 'MCS' for the CS and $C^{34}S$ molecular transitions. The black lines represent the observed spectra, while the red spectra are generated by the MAPYSO radiative transfer code. The dotted line shows the systemic velocity of Cha-MMS1 derived from a seven-component hyperfine fit to the N_2H^+ 1–0 multiplet. For the APEX spectra, a correction of 0.1 km s^{-1} was added (see Sect. 4.3.2.1). The angular separation of the different positions with respect to the central spectrum is shown on top of the respective spectra. The model assumes spherical symmetry, so the model spectra at symmetric positions are identical. The telescope used for conducting the obervations is shown at the leftmost box of each row. The spectra from left to right correspond to the south-east to north-west direction perpendicular to the filament.

models (hereafter 'MCS' model) for the CS molecular transitions. The distributions of density, abundance, kinetic temperature, radial velocity, and turbulent broadening characterising 'MCS' can be seen in Fig. 4.11.

4.4.2.1 Abundance

The outer and inner abundances are constrained by the CS 2–1 absorption dip and the CS 5–4 intensity, respectively. In between, the abundance distribution is constrained by the $C^{34}S$ 2–1 spectra, which require a CS abundance of 2.5×10^{-9} at a radius of 8000 AU. The depth of the CS 2–1 self-absorption is mostly determined by the outer abundance distribution of the low-excitation material at radii $\sim$ 10000 AU $< r <$ 30000 AU. We do not constrain the CS abundance at radii larger than 30000 AU. CS 5–4 probes the innermost parts of the core and sets constraints on the abundance at radii $r <$ 2000 AU. As a result, the CS abundance increases up to 8000 AU and drops by a factor of 4 in the outer parts. As long as the temperature is low enough, CS and other sulphur-bearing molecules are expected to be strongly depleted towards the centre of dense cores where the density is high (e.g., Tafalla et al., 2004; Bergin et al., 2001). Depletion occurs due to the freezing-out process onto the dust grains (e.g., Tafalla et al., 2002; Stahler & Yen, 2010) and observations of starless cores, such as L1544, or Class 0 protostars, such as IRAM 04191, also showed CS depletion towards the centre by a factor of $\sim$ 20 (Tafalla et al., 2002; Belloche et al., 2002).

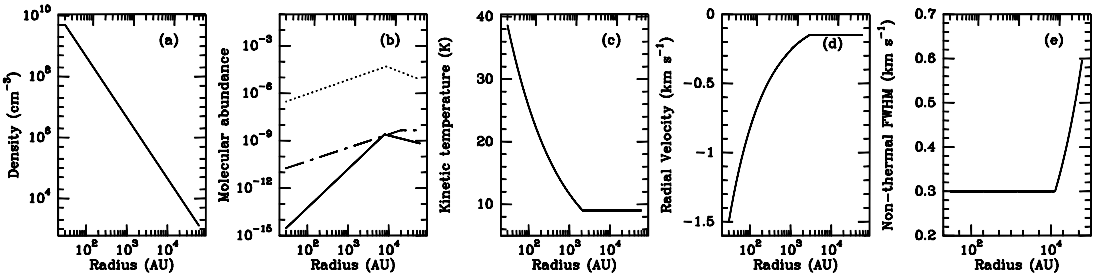

Figure 4.11: Input profiles for the best-fit models 'MCS', 'MHCOP', and 'MCO': (a) density, (b) CS (solid), HCO^+ (dash-dot), and CO (dot) abundance, (c) kinetic temperature, (d) radial velocity, and (e) turbulent linewidth.

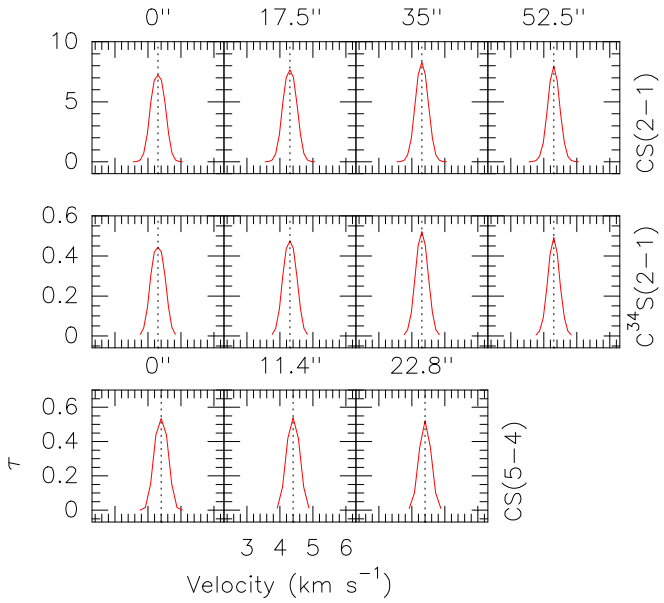

Figure 4.12: Transition opacities for the best fit model 'MCS'. The dotted line shows the systemic velocity of Cha-MMS1. For the APEX spectra, a correction of 0.1 km s^{-1} was added (see Sect. 4.3.2.1).

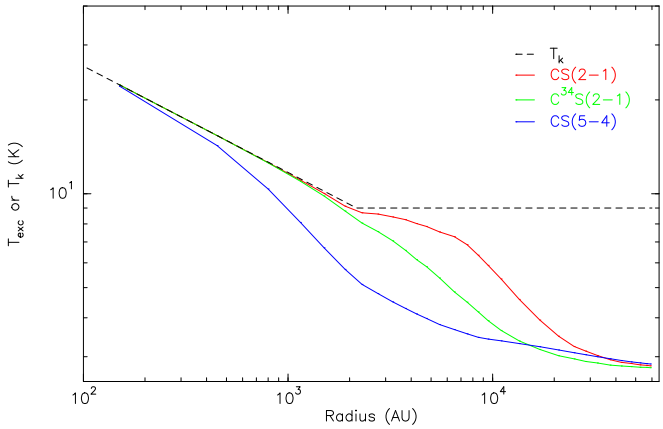

Figure 4.13: Kinetic (black) and excitation temperature (colour) for all the transitions of the best fit model 'MCS'.

4.4.2.2 Turbulence

We keep the turbulent broadening uniform at 0.3 km s^{-1} ($FWHM$) up to ~ 12600 AU as we see no clear variations in our diagrams of turbulent linewidth versus position up to this radius (see Fig. 4.6). We then let the turbulent linewidth double its value from 12600 AU to the outermost envelope radius at 60000 AU. This is a constraint we derive from both the width of the CS 2–1 absorption dip and the CO 3–2 modelling (see Sect. 4.4.4).

4.4.2.3 Opacities and excitation temperatures

All transitions of CS and its isotopologue are optically thin on all positions apart from CS 2–1 (see Fig. 4.12). The model excitation temperatures are shown in Fig. 4.13. CS 2–1, C^{34}S 2–1, and CS 5–4 are thermalised up to ~ 2500 AU, ~ 1500 AU, and ~ 400 AU, respectively.

4.4.2.4 Discrepancies between model and observations

The model reproduces the absorption dip of CS 2–1 well for all positions, however, the intensity of the blue peak at the central position, and at −17.5″ is higher compared to the observations. The discrepancy is not that strong at +17.5″, and the model fits the peak temperature well at the outer positions, i.e., ±35″ and ±52.5″. A peculiarity of the observed CS 2–1 spectra is the existence of velocity wings at all positions. The velocity wings are not reproduced by the model and may partly arise from extended emission stemming from the outflow of the nearby Class I object (see Fig. 4.1). It is, however, unclear whether this can explain *both* the redshifted and blueshifted wing emissions. The C^{34}S 2–1 model is weaker at the outermost ±52.5″ positions while matching the intensity of the spectra at the other positions well. CS 5–4, on the other hand, shows one more peculiar feature: the model does not account for the excess of redshifted emission that is prominent toward the central position.

4.4.2.5 Testing the infall velocity field

Despite the discrepancies, the 'MCS' model provides a consistent overall fit to the data. As we are interested in the infall velocity structure of the core we input different infall velocity profiles to 'MCS' in order to test and constrain its value. The linewidths of the low optical depth lines and the position of the absorption dip of the optically thick lines can be used to place relatively tight constraints on the velocity structure of the source. We first test different *uniform* infall velocity profiles and then velocity profiles with a free-fall, power-law ($v \propto r^{-0.5}$) dependence in the inner parts.

In the case of uniform velocities, the best agreement is found for velocities in the range 0.1 km s^{-1} – 0.2 km s^{-1}. For velocities less than 0.1 km s^{-1} the peak asymmetry of the CS 2–1 spectra reduces considerably with the red peak becoming too strong in comparison to the observations. In addition, the linewidths of both the CS 2–1 and C^{34}S 2–1 lines become narrower than the observed linewidths. In contrast, when the infall velocities exceed 0.2 km s^{-1}, the blue peak of CS 2–1 becomes much broader and the central C^{34}S 2–1 spectrum starts showing a double-peaked structure (also seen in the opacity profile), which is inconsistent with the observations.

We then apply a power law with an exponent of -0.5 for the inner parts at gradually increasing radii while keeping the velocity constant at the outer parts in order to test whether higher inner velocities are consistent with the observations. From now on, we refer to the radius at which the velocity profile changes from a power-law to a uniform r dependence as the 'breakpoint'. Our tests suggest that such a power law velocity distribution matches the observations for radii up to 9000 AU for velocities in the range of $v_{\rm break}$ = 0.1 km s^{-1} – 0.2 km s^{-1}, after which we let the velocity remain uniform. For breakpoint radii exceeding 9000 AU, the wide spatial range of high infall velocities produces broader CS 2–1 linewidths and stronger red peak intensities than the observed spectra. The CS 5–4 and C^{34}S 2–1 models also start showing a double-peaked structure, which disagrees with the observations.

Therefore, the CS modelling suggests that the core's envelope is infalling with subsonic to transonic *outer* velocities of 0.1 km s^{-1} – 0.2 km s^{-1}. Inner free-fall power-law velocity distributions are possible with breakpoints at $r \leq$ 9000 AU, with infall velocities reaching supersonic values at $r \leq$ 3500 AU in this case. We do not constrain the infall velocity structure of the envelope for radii greater than 30000 AU. The infalling motions at the outer parts of the envelope (< 30000 AU) contradict the Shu (1977) assumption of a static envelope in the inside-out collapse model.

The radial velocity structure of the 'MCS' model shown in Fig. 4.11 corresponds to an $r^{-0.5}$ dependence for radii < 3000 AU, and a uniform infall velocity of 0.15 km s^{-1} for 3000 AU $\leq r \leq$ 60000 AU (see Fig. 4.11d).

4.4.3 HCO$^+$ Modelling

The following molecular transitions of HCO$^+$ and its isotopologues were modelled: HCO$^+$ 1–0, HCO$^+$ 3–2, H^{13}CO$^+$ 1–0, H^{13}CO$^+$ 3–2, H^{13}CO$^+$ 4–3, and HC^{18}O$^+$ 1–0. The 1–0 transitions were observed with Mopra, the other ones with APEX. We have central position spectra for HCO$^+$, H^{13}CO$^+$, and HC^{18}O$^+$ 1–0, while HCO$^+$ and H^{13}CO$^+$ 3–2 were also observed at seven and H^{13}CO$^+$ 4–3 at five positions along the direction perpendicular to the filament (see Fig. 4.1). One of the models that provides a good fit to the data is shown in Fig. 4.14, and hereafter we refer to it as 'MHCOP'. The distributions of density, abundance, kinetic temperature, radial velocity, and turbulent broadening characterising 'MHCOP' can be seen in Fig. 4.11.

4.4.3.1 Abundance

We take the following observational constraints into account to define the input abundance profile (Fig. 4.11b). The inner profile is constrained by the intensities of the optically thin H^{13}CO$^+$ 3–2, H^{13}CO$^+$ 4–3, and HC^{18}O$^+$ 1–0 spectra.

A decrease in the HCO$^+$ abundance by a factor of $\sim$ 20 from a radius of 20000 AU down to the centre fits the intensities of the optically thin lines well. As a test, we extended the plateau of uniform outer abundance towards the centre to radii $r <$ 20000 AU, and found that this produced model intensities that were too high for the optically thin spectra. By varying the abundance profile between 20000 AU and 60000 AU, we conclude that we do not constrain the outer, $r \geq$ 20000 AU, abundance profile with our current HCO$^+$ transitions. We therefore use a uniform outer abundance for $r \geq$ 20000 AU as an approximation.

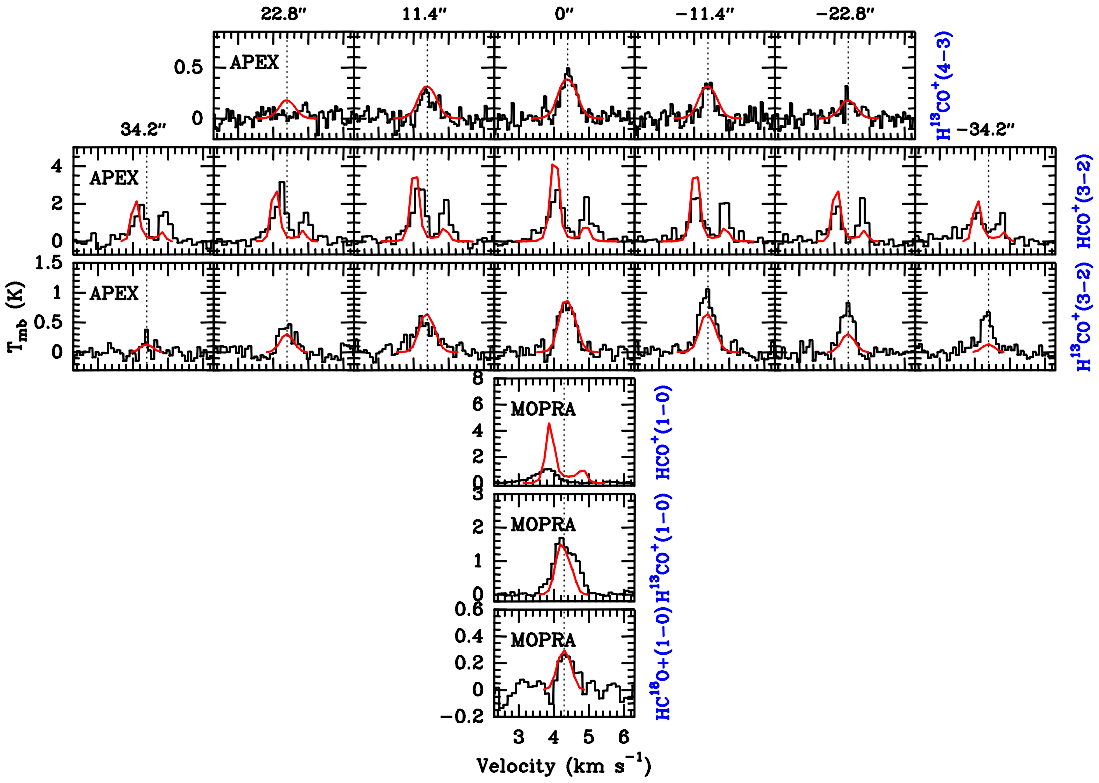

Figure 4.14: Same as Fig. 4.10 but for the best fit model MHCOP.

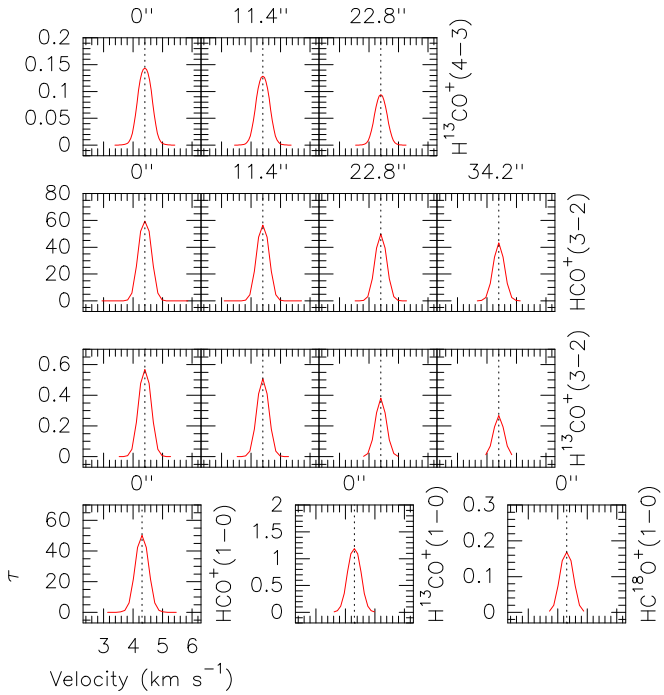

Figure 4.15: Transition opacities for the best fit model 'MHCOP'. The dotted line shows the systemic velocity of Cha-MMS1. For the APEX spectra, a correction of 0.1 km s^{-1} was added (see Sect. 4.3.2.1).

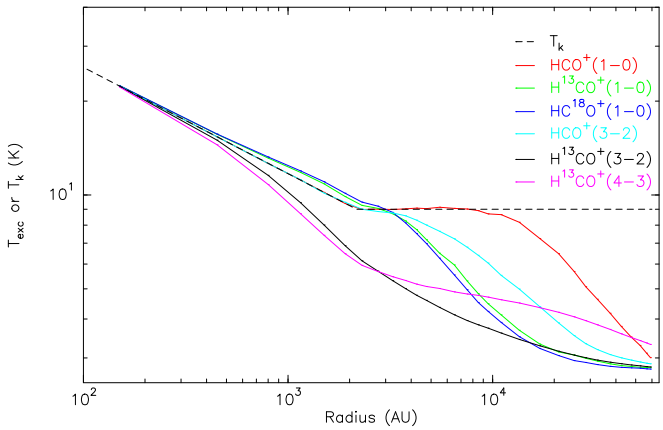

Figure 4.16: Same as Fig. 4.13 for the best fit model 'MHCOP'.

4.4.3.2 Opacities and excitation temperatures

Figures 4.15 and 4.16 show the resulting opacity and excitation temperature profiles of the model for each transition. HCO^+ 3–2, HCO^+ 1–0, and $H^{13}CO^+$ 1–0 are optically thick, while $H^{13}CO^+$ 4–3, $H^{13}CO^+$ 3–2, and $HC^{18}O^+$ 1–0 are in the optically thin range. HCO^+ 1–0 is thermalised up to ~ 10000 AU and HCO^+ 3–2, $H^{13}CO^+$ 1–0, and $HC^{18}O^+$ 1–0 are thermalised up to ~ 3000 AU. $H^{13}CO^+$ 4–3 and $H^{13}CO^+$ 3–2 cease to be thermalised for radii larger than ~ 500 AU. HCO^+ 1–0 is thermalised up to a much larger radius than $H^{13}CO^+$ and $HC^{18}O^+$ 1–0 because of its much higher optical depth.

4.4.3.3 Discrepancies between model and observations

One of the major discrepancies between model and observations is the failure of the model to reproduce the emission of the red peak of the HCO^+ 3–2 transition. Raising the outer temperature of the core does not have a significant effect on the red peak of the model spectrum since this transition is not thermally excited at radii larger than 3000 AU. This disagreement might then be a density effect instead, if the true density profile deviates from the spherically symmetric, r^{-2} dependence. The observed $H^{13}CO^+$ 3–2 spectra show higher intensities in the north-west (−11.4″, −22.8″, −34.2″) direction than in the south-east direction. $H^{13}CO^+$ 3–2 is not the only transition that does not peak at the central position. Higher intensities toward the north-west are also seen in our N_2H^+ 1–0 spectra. The N_2H^+ 1–0 emission in the maps presented by Ladd et al. (2011) is similarly not peaked at Cha-MMS1. 'MHCOP' fits the spectra on the north-west side well, but it does not fit the excess emission on the south-east side. We cannot yet pinpoint the reason for this intensity difference on each side of the central spectrum. $H^{13}CO^+$ 4–3 and the central spectrum of $HC^{18}O^+$ 1–0 are reproduced rather well, as is $H^{13}CO^+$ 1–0, even though the exact lineshape of the observed spectrum is not reproduced. The observed $H^{13}CO^+$ 1–0 is broader than the model at the redshifted part of the spectrum, like CS 5–4 (see Sect. 4.4.2).

The model strongly overestimates the peak temperature of the observed HCO^+ 1–0 transition which is even weaker than $H^{13}CO^+$ 1–0. HCO^+ 1–0 is very optically thick and thermalised

up to large radii. It is certainly affected by significant absorption from the low-density material in the ambient cloud at $r \geq 60000$ AU, which is not included in the modelling.

4.4.3.4 Testing the infall velocity field

There is a range of infall velocity profiles that give consistent fits to the data. In the case of uniform, constant velocities up to 60000 AU the range 0.1 km s^{-1} – 0.2 km s^{-1} agrees well with the observations. For values higher than 0.2 km s^{-1} the HCO^+ 3–2, $H^{13}CO^+$ 3–2, $H^{13}CO^+$ 4–3, and $HC^{18}O^+$ 1–0 spectra become too broad while for velocities lower than 0.1 km s^{-1} the absorption dip is not redshifted enough. We then tested a velocity profile described by a power law following an $r^{-0.5}$ dependence in the inner part of the core up to a certain radius, after which the infall velocity remains uniform, as we did for CS. For a breakpoint at 3000 AU infall velocities of $v_{\rm break}$ = 0.1 km s^{-1} – 0.2 km s^{-1} give consistent fits. When we increase the breakpoint radius, the range of consistent infall velocities decreases. At 6000 AU the breakpoint velocities still consistent with the data are 0.1 km s^{-1} – 0.15 km s^{-1} and at 9000 AU, 0.1 km s^{-1}. Overall, inner power-law profiles at radii larger than 9000 AU produce spectra with too broad linewidths for all transitions, apart from $H^{13}CO^+$ 1–0, and inconsistent double-peaked spectra for $H^{13}CO^+$ 3–2, $H^{13}CO^+$ 4–3, and $HC^{18}O^+$ 1–0. We also varied the outer infall velocity profile to check whether it is constrained by our data. To accomplish this we let the infall velocity drop sharply to zero at gradually increasing radii and found that the model does not constrain the velocities for radii greater than 35000 AU. Even though the dip in the HCO^+3–2 model spectrum in Fig. 4.14 is not as redshifted as in the observed spectrum, a velocity drop to zero at radii smaller than 35000 AU makes this discrepancy even stronger by producing model spectra with almost no apparent redshift of the HCO^+3–2 absorption dip. We therefore cannot accurately constrain the infall velocity structure of the core for $r \geq 35000$ AU from the HCO^+ modelling.

The velocity distribution corresponding to model 'MHCOP' is the same as the one of 'MCS' (see Fig. 4.11d).

4.4.4 CO Modelling

We modelled the following molecular transitions of CO and isotopologues: CO 3–2, CO 4–3, CO 6–5, CO 7–6, ^{13}CO 6–5, and $C^{18}O$ 2–1. Figure 4.17 shows one of the models that fits the data relatively well, hereafter 'MCO'. The distributions of density, abundance, kinetic temperature, radial velocity, and turbulent broadening characterising 'MCO' can be seen in Fig. 4.11.

4.4.4.1 Abundance

The abundance profile of CO down to a radius of $\sim$ 1000 AU is mainly constrained by the intensity variations of the $C^{18}O$ and $C^{17}O$ 2–1 transitions. The ratio of the $C^{17}O$ and $C^{18}O$ 2–1 integrated intensities yields $C^{18}O$ 2–1 opacities ranging from $\sim$ 1.6 toward the centre to less than $\sim$ 0.5 toward the outer parts (see Appendix E.1). We take these opacity values into account to further constrain our model. Finally, the optically thin ^{13}CO 6–5 transition, which traces higher densities and is spatially better resolved, sets strong constraints on the

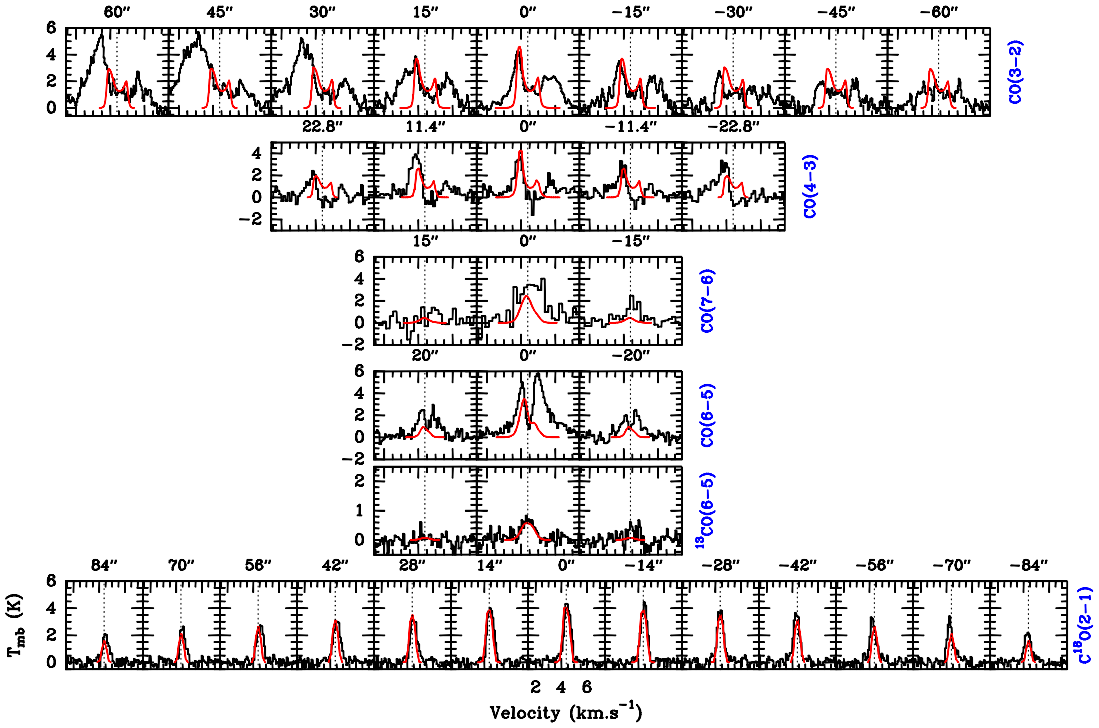

Figure 4.17: Same as Fig. 4.10 but for the best fit model 'MCO' of the CO transitions.

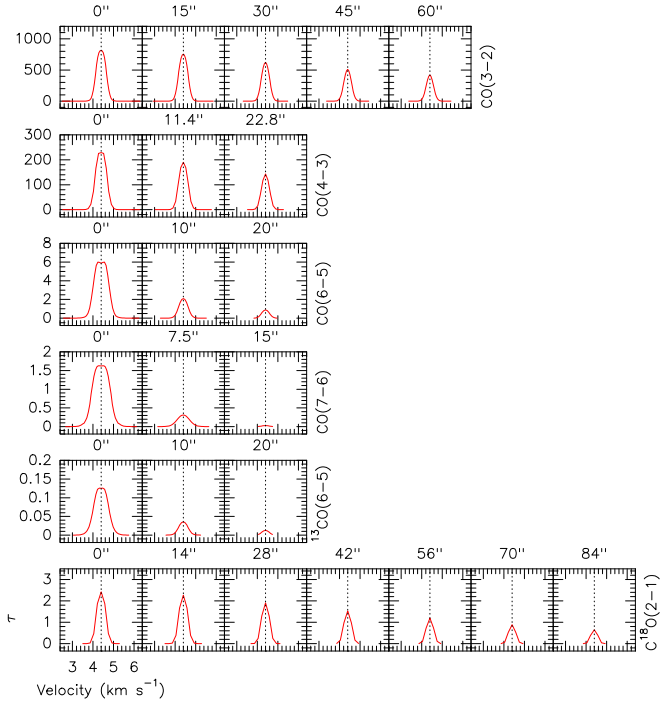

Figure 4.18: Transition opacities for the best fit model 'MCO'. The dotted line shows the systemic velocity of Cha-MMS1. For the APEX spectra, a correction of 0.1 km s^{-1} was added (see Sect. 4.3.2.1).

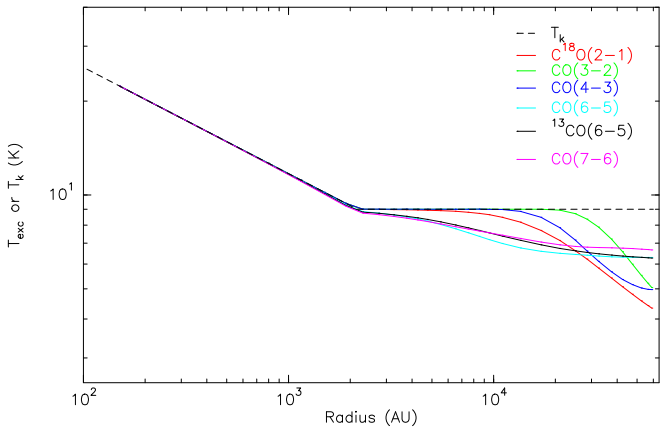

Figure 4.19: Same as Fig. 4.13 for the best-fit model 'MCO'.

abundance in the inner parts of the envelope ($r < 1500$ AU). Overall, we obtain the abundance profile shown in Fig. 4.11b, with a maximum of 5×10^{-5} at 9000 AU, depletion by a factor of ~ 10 from ~ 9000 AU to ~ 700 AU, and also a decrease in the abundance by a factor ~ 7 from ~ 9000 AU to ~ 20000 AU, in order to match the lower outer $C^{18}O$ opacity. We constrain the CO abundance up to 20000 AU. CO depletion has previously been observed towards the inner parts of various prestellar cores (e.g., Bacmann et al., 2002; Christie et al., 2012).

Furuya et al. (2012) coupled a gas-grain chemical network to 3D radiation hydrodynamic simulations to derive molecular abundances at the first core stage. In their model, CO desorbs to the gas phase at a temperature of 25 K, somewhat higher than the commonly used 20 K value, due to the high density of the first-core envelope. The density at which their simulation reaches 25 K is $\sim 10^9$ cm^{-3}, which is similar in our model. We tested the effect of an inner CO desorption region at $r \leq 54$ AU (from Equation 4.7), at which radius the temperature reaches 25 K in our model. We used an inner CO abundance of 1×10^{-4} for the desorption region, which is consistent with the predicted abundance for the first core stage (Furuya et al., 2012). At radii larger than 54 AU, and therefore at temperatures T < 25 K, CO depletion takes place. We found that the model is not sensitive to the abundance within the inner 54 AU and the presence or the absence of a desorption region on these smaller scales has no apparent effect on the spectra. Therefore, we do not account for inner desorption.

4.4.4.2 Turbulence

The self-absorption of the CO 3–2 spectra is very broad, suggesting a large turbulent broadening in the outer parts (radii $r \geq 12500$ AU). We therefore raise it by a factor of ~ 2 from 12500 AU to 60000 AU. In this way, the blueshifted side of the self-absorption is reproduced well, but the redshifted side of the model is still too narrow. The turbulent broadening is kept uniform for radii $r \leq 12500$ AU (see Fig. 4.11), as derived in Sect. 5.3.2.

4.4.4.3 Model opacities and excitation temperatures

Figures 4.18 and 4.19 show the model opacities and excitation temperatures for all the transitions. CO 3–2, CO 4–3, and $C^{18}O$ 2–1 remain thermalised out to ~ 20000 AU, ~ 13000 AU, and ~ 9000 AU, respectively, while CO 6–5 and CO 7–6 cease to be thermalised at ~ 2000 AU. Moreover, all the transitions are optically thick with the exception of ^{13}CO 6–5 at all positions, CO 7–6 at offset positions, and $C^{18}O$ 2–1 at the outermost position (see Fig. 4.18).

4.4.4.4 Discrepancies between model and observations

The spectra of CO 3–2 at 15″, 30″, 45″, and 60″ show strong emission in the blueshifted part of the spectrum, while the spectra at -15″, -30″, -45″, and -60″ show much weaker blueshifted emission. Excess emission in the redshifted part of the spectra is also seen at all positions. We expect the outflow of the neighbouring Class I protostar (see Fig. 4.1) to contaminate the low-density tracers such as CO 3–2, especially at the offset positions, thereby broadening the observed emission. Belloche et al. (2006) presented a CO 3–2 intensity map of the region toward Cha-MMS1 (see Fig. 1 of their paper). The blueshifted emission they show reaches our offset positions, and especially affects the spectra towards the south-east of Cha-MMS1. They also discuss the possible presence of two separate outflows in this region. The highly broadened blue and red peaks of CO 3–2 might *partly* result due to these outflows if they have a wide opening angle and lie close to the plane of the sky (see Cabrit & Bertout, 1990).

The model reproduces the $C^{18}O$ 2–1 emission and its opacity well, as well as the ^{13}CO 6–5 emission. However, the model fails to reproduce the strong redshifted emission of the CO 6–5 and 7–6 transitions, similar to the CS 5–4 emission. Because these transitions probe regions of high densities, this extra emission may be an indication of additional warmer, high-velocity material in the inner core (see Fig. 4.10). This emission may stem from a very compact outflow. To address this question, however, we would need to resolve the very inner part of the core on small scales of a few hundred AU (see Sect. 4.1.1).

4.4.4.5 Testing the infall velocity field

From the CO modelling we draw the following conclusions on the infall velocity structure across the envelope. We find that uniform infall velocities of up to 0.2 km s^{-1} give fits relatively consistent with the data. Velocities above 0.2 km s^{-1} produce $C^{18}O$ 2–1 linewidths that are too broad compared to observed values. We test an inner power-law velocity dependence ($v \propto r^{-0.5}$), with uniform outer velocities. We find that the power-law profile is consistent with the observations up to ~ 6000 AU if the infall velocity is in the range of $v_{\rm break}$ = 0.1 km s^{-1} – 0.15 km s^{-1} at this radius, after which it remains constant. A radius of 9000 AU is also consistent when $v_{\rm break}$ = 0.1 km s^{-1} at this breakpoint and onwards. For larger radii the model spectra are much broader than the observed spectra due to the extended spatial range of high inner infall velocities. However, the opacity of the optically thick transition CO 3–2 does not allow us to set constraints on the lower limit of the infall velocity.

The velocity profile that coresponds to the 'MCO' model is shown in Fig. 4.11, and it is identical to the ones used for 'MHCOP' and 'MCS'.

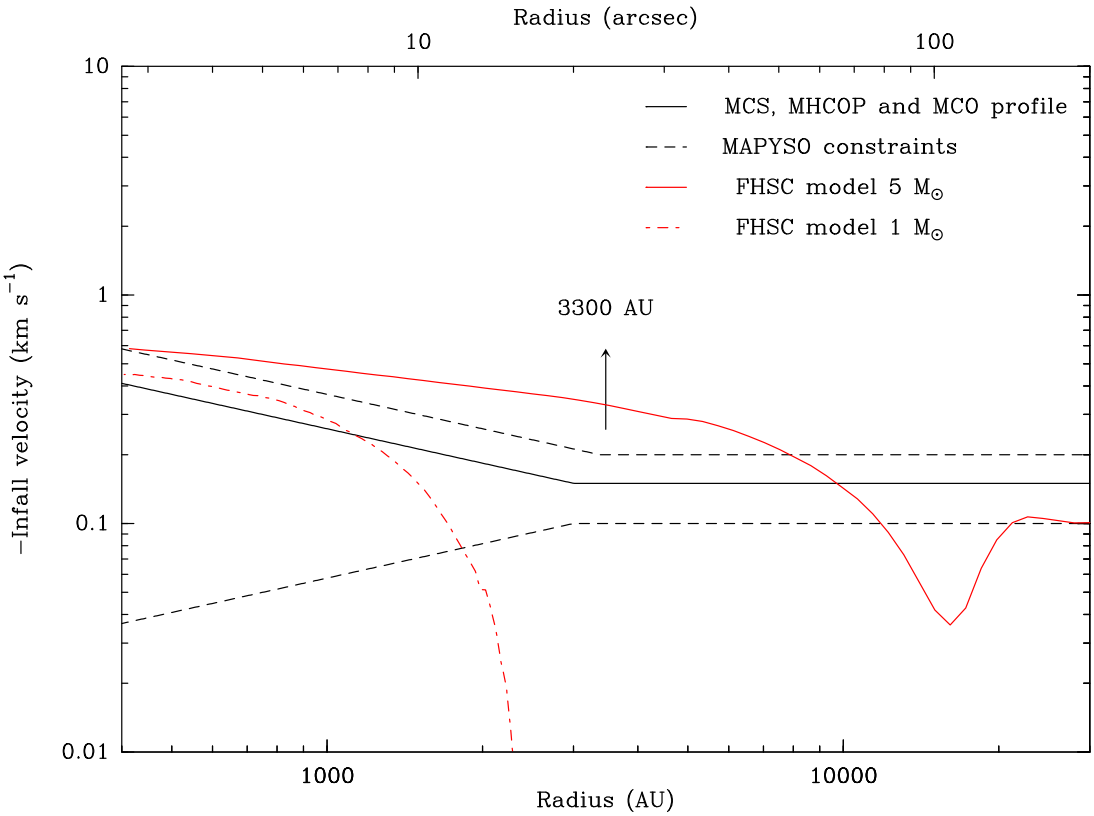

Figure 4.20: Infall velocity field of the envelope of Cha-MMS1 based on the radiative transfer modelling with MAPYSO. The solid black line corresponds to the velocity profile of the 'MCS', 'MHCOP', and 'MCO' models. The dashed lines show the range of velocity fields that are still consistent with the observations. The red solid and dashed curves correspond to the average radial velocity at the equatorial plane of a magnetised FHSC with core masses of 1 $M_\odot$ and 5 $M_\odot$, and ages of 850 yr and 2684 yr, respectively. (Commerçon et al., 2012, , see details in Sect. 4.5.4.2).

4.4.5 Infall velocity distribution of Cha-MMS1: combining modelling results

We obtain slightly different constraints on the infall velocity structure of Cha-MMS1 from the radiative transfer modelling of the CS, HCO^+, and CO molecular transitions. We take the *envelope* of the infall velocity profiles that are consistent with all three datasets as the overall range of possible infall velocities for Cha-MMS1. The consistent velocities are shown as the area enclosed in Fig. 4.20.

The infall velocity is relatively well constrained over the range of radii 3300 AU to 30000 AU, with subsonic/transonic velocities in the range 0.1 km s^{-1} to 0.2 km s^{-1}. Our data do not constrain the velocity field beyond ~ 30000 AU. Below 3300 AU, there are more degeneracies, and the spectra are consistent with an increase in the infall velocity as $r^{-0.5}$, but also with a flat velocity profile, or even a decrease below a radius of ~ 3000 AU.

4.5 Discussion

4.5.1 Far-infrared emission and luminosity

Recent radiation-MHD simulations predict that strongly or weakly magnetised FHSCs are expected not only to emit at 70 μm but also to produce detectable emission at wavelengths down to 20 μm, especially during the latest phase of their evolution (Commerçon et al., 2012). Previous simulations that found no significant first-core emission below 30 μm – 50 μm were either spherical (e.g., Masunaga et al., 1998; Omukai, 2007) or did not take the magnetic field into account and used a barotropic equation of state (Saigo & Tomisaka, 2011). A first core can therefore also be identified by a Spitzer 24 μm (and 70 μm) detection at late phases if its inclination is less than 60° and there is no detection at wavelengths smaller than 20 μm (Commerçon et al., 2012). As seen in Sect. 4.3.1, the 24 μm and 70 μm *Spitzer* fluxes of Cha-MMS1 are consistent with the predictions of the RMHD simulation of Commerçon et al. (2012) for a magnetised FHSC with a normalised mass-to-magnetic-flux ratio of 2 seen at an inclination lower than 60°. The SED of Cha-MMS1 is therefore consistent with Cha-MMS1 being at the FHSC stage. However, if its actual inclination is higher than 60° then Cha-MMS1 would have to be in a more advanced stage (Class 0).

4.5.2 Outflows

Class 0 protostars usually drive fast, extended, and easily detectable outflows, whereas FHSCs are predicted to drive very compact, slow outflows (see Sect. 4.1.1). This is a major observational signature that can be used to distinguish between the two and break the degeneracies that remain in their SEDs when their inclination is not known.

A search for a fast, large-scale outflow driven by Cha-MMS1 in CO 3–2 with APEX was negative (Belloche et al., 2006). We observed the CO 6–5, CO 7–6, and ^{13}CO 6–5 transitions in order to search for signs of a compact, unresolved outflow. The modelling of these transitions gave ambiguous, but maybe promising results (see Sect. 4.4.4). Our model does not reproduce the redshifted part of the CO 6–5 and 7–6 emission, while it fits the C^{18}O 2–1 transition well. This excess emission might point to the presence of unresolved, higher-velocity material at the inner core (see Shinnaga et al., 2009, for a similar case of excess emission in CO 6–5 and 7–6 toward the more evolved protostar L1521F). In addition to this, the CS 5–4 model in Sect. 4.4.2 shows a similar discrepancy. Its observed spectrum has an excess of redshifted emission that the model fails to reproduce, while it fits the lower-J CS and C^{34}S transitions well. CS 5–4 probes material at higher densities, so that its broad spectrum indicates higher velocity, dense material close to the centre of the core, which cannot be seen with the other, lower density transitions.

Despite hints of the presence of dense, higher velocity material confined to the centre of the core, there is also an alternative explanation. Figure 4.21 compares the CO 6–5 spectra at the centre and in the north-east direction of the filament (hence toward the nearby Class I outflow) to the central spectrum of CS 5–4. The CO 6–5 red peak emission becomes stronger as we move up along the filament. It peaks at a velocity where CS 5–4 has some wing emission. This suggests that at least part of the excess emission in the CS 5–4 spectrum is not confined to the inner parts of Cha-MMS1 but instead extends towards the nearby Class I outflow lobe.

The bulk of the CS 5–4 excess emission, however, peaks at a lower velocity, and it is unclear whether it represents a similar extended component. Higher-angular resolution observations are certainly needed to make any reliable conclusions about the presence of a compact, slow outflow driven by Cha-MMS1.

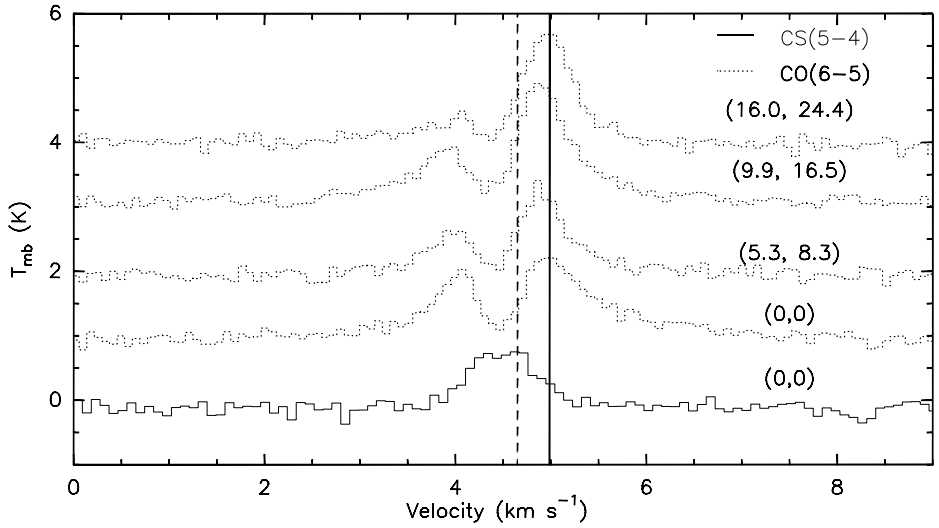

Figure 4.21: Comparison of the CS 5–4 spectrum (solid) toward the central position of Cha-MMS1 and CO 6–5 spectra (dotted) taken at the central position and in the north-east direction toward the nearby Class I protostar. The offset position of each spectrum is given in arcseconds relative to the central position. The CO 6–5 spectra are shifted vertically by a step of 1 K for clarity. The solid vertical line roughly corresponds to the velocity of the CO 6–5 red peak, while the dashed line marks the velocity of the peak of the CS 5–4 excess emission.

As mentioned in Sect. 4.4.2.4, all CS 2–1 spectra in Fig. 4.10 show blueshifted and redshifted wing emissions that are not accounted for by our model. Such wing emissions are even more pronounced in CO 3–2 (Fig. 4.17), the blueshifted one being clearly associated with emission from the outflow driven by the nearby Class I protostar (Belloche et al., 2006). Hiramatsu et al. (2007) and Ladd et al. (2011) propose that the curved shape of the blue lobe of this outflow is due to its partial interaction with the Cha-MMS1 dense core. This would explain the presence of the extended blueshifted CS 2–1 emission around Cha-MMS1. As recalled by Ladd et al. (2011), the HH objects 49 and 50, which are thought to be associated with this outflow, are *redshifted*. This suggests that the outflow axis lies close to the plane of the sky and, provided its opening angle is large enough, it could also explain the presence of extended, redshifted, wing emission in CS 2–1 in the vicinity of Cha-MMS1. This emission is, however, difficult to disentangle from the ambient cloud emission in CO 3–2, and it was excluded from the range of velocities used by Belloche et al. (2006) to produce their map of the redshifted outflow lobe.

4.5.3 Interpretation of the P-V diagrams

Determining the nature of the velocity gradients in position-velocity diagrams is not straightforward because many processes such as rotation, infall, outflow, and turbulence can influence their shape (e.g., Tobin et al., 2012; Burkert & Bodenheimer, 2000). Tobin et al. (2012) suggest that projected infall in filamentary protostellar envelopes can dominate the velocity gradients for scales larger than 1000 AU. Burkert & Bodenheimer (2000) show that turbulence can produce velocity gradients that can be mistaken for rotation. In Sect. 4.3.3 we found no significant velocity gradient in the direction parallel to the filament in which Cha-MMS1 is embedded, but a significant one in the perpendicular direction. If we can approximate the filamentary geometry of the continuum emission as axisymmetric, and if infall plays a significant role in producing these velocity shifts, we would expect to see its contribution in the P-V diagrams in the filament direction. That this is not the case enhances the probability that the velocity gradients we observe perpendicular to the filament are due to rotation.

The P-V diagrams of $C^{18}O$ 2–1 and $C^{17}O$ 2–1 cover almost the same extent as the width of the filament ($\sim$ 0.1 pc). As the outermost positions of $C^{18}O$ 2–1 and $C^{17}O$ 2–1 reach the edges of the filament (see Fig. 4.1d), we cannot exclude the possibility that turbulent motions influence the shape of the velocity gradients on these scales. However, the "S" shape of the $C^{18}O$ 2–1 and $C^{17}O$ 2–1 P-V curve at the outermost positions on either side of the central position is relatively symmetric (see Fig. 4.5c) and therefore, probably indicative of rotation rather than random turbulent motions. If the interpretation in terms of rotation is valid, then the "S" shape of the P-V curve indicates that the filament is rotating in a differential manner, the outer parts ($r > 8000$ AU) rotating more slowly than the inner parts. The turn-over of the $C^{18}O$ and $C^{17}O$ P-V curves occurs very close to the edge of the filament as traced with LABOCA. We speculate that this behaviour is related to the formation process of the filament, but the physics of this process would have to be investigated.

We obtained a velocity gradient of 3.1 ± 0.1 km s^{-1} pc^{-1} over $r < 8000$ AU for Cha-MMS1. This is similar to the velocity gradients often found in dense cores and attributed to rotation, with magnitude typically ranging from ~ 0.3 km s^{-1} pc^{-1} to ~ 6 km s^{-1} pc^{-1} on typical scales of $\sim$ 0.1 pc (e.g., Goodman et al., 1993; Caselli et al., 2002a; Belloche et al., 2002; Tafalla et al., 2004). The "S" shape of the $C^{17}O$ 2–1 and $C^{18}O$ 2–1 P-V diagrams of Cha-MMS1 is very reminiscent of the P-V diagrams of the young Class 0 protostar IRAM 04191 located in Taurus. Belloche et al. (2002) derive a rotational angular velocity of 9 ± 3 km s^{-1} pc^{-1} at a radius of 2800 AU and 1.9 ± 0.2 km s^{-1} pc^{-1} at 7000 AU. They conclude that IRAM 04191 shows clear signs of differential rotation in the envelope. On scales of $\sim$ 1000 AU, the envelope rotates even faster (Belloche & André, 2004). As mentioned in the previous paragraph, the P-V diagram of Cha-MMS1 is also consistent with differential rotation, but a major difference compared to IRAM 04191 is that this concerns only the outer parts of the envelope ($r > 8000$ AU). At smaller radii down to $\sim$ 4000 AU, the velocity profile is consistent with solid-body rotation. However, a puzzling feature of the P-V diagrams of Cha-MMS1 is the even flatter velocity gradient in the inner parts of the envelope below 4000 AU, with an amplitude lower than 2 km s^{-1} pc^{-1}.

If the velocity gradients really trace rotation, then the envelope of Cha-MMS1 has a very peculiar rotational structure: the inner parts rotate more slowly than the bulk of the envelope,

and the outer parts also rotate more slowly. A collapsing, magnetised core is expected to have an angular velocity increasing toward the centre (Basu & Mouschovias, 1995), the exact shape of the profile depending on the initial angular momentum distribution. Since we see evidence of infall motions in the envelope of Cha-MMS1, its peculiar rotational structure suggests that an efficient mechanism removing angular momentum during the collapse is at work over the range of radii 2000 AU to 8000 AU. It would be interesting to investigate whether magnetic braking is efficient enough to account for this angular momentum removal in Cha-MMS1. Measuring the magnetic field structures and ionisation levels of the Cha-MMS1 and IRAM 04191 envelopes would then be necessary to compare the two sources and understand why they behave so differently in terms of rotation.

4.5.3.1 Centrifugal acceleration and rotational energy

If we interpret the velocity gradients in the P-V diagrams as rotation, then we can estimate the dynamical importance of rotation for Cha-MMS1. We assume solid-body rotation for the inner envelope at $r < 8000$ AU and an inclination of the rotation axis in the range 45° – 60°, as derived in Sect. 4.3.1. The angular velocity then ranges from 4.4 km s^{-1} pc^{-1} to 3.6 ± 0.1 km s^{-1} pc^{-1}. We compute the centrifugal acceleration and the local gravitational field as

$$a_{\rm cen} = \frac{v_{\rm rot}^2}{r} = \Omega^2 r, \tag{4.9}$$

$$g = G \times \frac{M_{\rm env} + M_{\rm obj}}{r^2}, \tag{4.10}$$

where $a_{\rm cen}$, $v_{\rm rot}$, Ω, g, G, $M_{\rm env}$, $M_{\rm obj}$, and r are the centrifugal acceleration, the rotational velocity, the angular velocity, the gravitational acceleration, the gravitational constant, the envelope mass, the mass of the central object, and the radius, respectively. We assume that the envelope mass is proportional to the radius (density proportional to r^{-2}) and that a mass of 1.44 $M_\odot$ is enclosed within a radius of 3750 AU, as derived from the LABOCA 870 μm dust continuum map (Belloche et al., 2011a).

Figure 4.22 shows the variation of $a_{\rm cen}/g$ as a function of radius. Within the framework of our assumptions, the centrifugal acceleration represents at most 20% of the gravitational acceleration. Thus rotation does not provide significant support to the envelope on scales of a few thousand AU. A similar conclusion was drawn by, say, Caselli et al. (2002b) for their sample of dense cores, while Belloche et al. (2002) found that the centrifugal acceleration was a sizeable fraction of the gravitational acceleration on such scales in IRAM 04191 (up to ∼ 40%).

The ratio of rotational kinetic energy to the core's gravitational energy for a centrally peaked r^{-2} density profile, $\beta_{\rm rot}$, is given by (Goodman et al., 1993):

$$\beta_{\rm rot} = \frac{\Omega^2 R^3}{9GM}. \tag{4.11}$$

We obtain values of $\beta_{\rm rot} \sim 0.02$ and ~ 0.006 at 8000 AU for inclinations of 30° and 60° degrees, respectively.

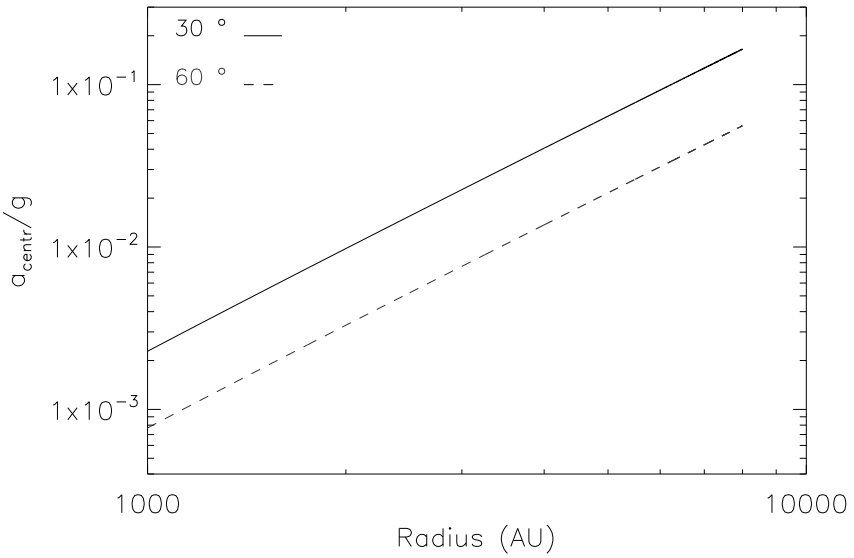

Figure 4.22: Ratio of centrifugal to gravitational accelerations for the inner part of Cha-MMS1 that may be undergoing solid-body rotation. The upper and lower curves are for an inclination of 30° and 60°, respectively.

4.5.4 Implications of the infall velocity structure of Cha-MMS1

In this section we compare the infall velocity distribution of Cha-MMS1 with predictions from theory and observations of other collapsing cores. The number of uncertainties involved is large, both in constraining the velocity profile of Cha-MMS1 from the radiative transfer modelling, as well as in the various existent theoretical collapse models in terms of initial and boundary conditions, and the inclusion or omission of either magnetic fields or rotation. Therefore, a comparison of our source with theoretical models is not straightforward and we only aim to qualitatively discuss which collapse models provide better agreement with the infall profile we derived for Cha-MMS1.

4.5.4.1 Infall in Cha-MMS1 and in other observed cores

Figure 4.20 shows the infall velocities consistent with the envelope of Cha-MMS1 as derived from the radiative transfer modelling in Sect. 4.4. We can discern two distinct regimes in terms of the envelope motions of Cha-MMS1, one below 3300 AU and one within 3300 AU $\leq r \leq$ 30000 AU. At radii larger than 3300 AU we constrain the velocity profile of Cha-MMS1 better (more tightly). The velocities are sub- to transonic within the range of 0.1 km s^{-1} – 0.2 km s^{-1}. At radii below 3300 AU, where the model degeneracies are greater, Cha-MMS1 is consistent both with increasing *and* decreasing central velocities, ranging from 0.04 km s^{-1} to 0.6 km s^{-1}. Therefore, the inner ($r <$ 3300 AU) envelope is characterised by velocities that can reach supersonic values compared to the outer ($r >$ 3300 AU), more quiescent regions.

We also found that an inner, free-fall velocity distribution proportional to $r^{-0.5}$ is consistent

with the envelope of Cha-MMS1 with an upper limit of $r \sim 9000$ AU. If we assume that the latter radius signifies the distance that the reflected expansion wave has so far covered while travelling outwards at the speed of sound, as described in the inside-out collapse scenario (Shu, 1977), then we can estimate an upper limit to the age of Cha-MMS1 as $t \sim \frac{r_s}{a_s} = 2{\times}10^5$ years or 0.2 Myr. The sound speed, $a_s \sim 0.2$ km s^{-1}, is computed for a temperature of 9 K and assumes isothermality. In our models we have an isothermal temperature of 9 K only for $r > 2000$ AU, so this condition does not hold for the very inner radii. However, we only use the derived value as a crude estimate. Since this lifetime is an upper limit, it is consistent with both a first core (see Sect. 4.1.1 for FHSC lifetimes) or a Class 0 protostar. The prestellar phase lifetime is estimated to be ~ 0.5 Myr (Evans et al., 2009), and Class 0 objects have estimated lifetimes ranging from $\sim 4 - 9{\times}10^4$ yr (Maury et al., 2011) to $\sim 1.6{\times}10^5$ yr (Evans et al., 2009).

Belloche et al. (2002) similarly performed radiative transfer modelling of their molecular transitions towards the young Class 0 IRAM 04191 protostar using the MAPYSO code. They obtained an infall velocity of 0.15 km s^{-1} at a radius of 1500 AU and 0.1 km s^{-1} up to $\sim$ 11000 AU for their "best" fit. Their range of consistent infall velocities is similar to ours, albeit better constrained at small radii. For $r \geq 2000$ AU they find infall velocities in the range of $\sim$ 0.07 and $\sim$ 0.15 km s^{-1}, similar to the range 0.1 km s^{-1} – 0.2 km s^{-1} that we obtain for Cha-MMS1 at $r \geq 3300$ AU. Nevertheless, they constrain the inner $r \leq 3000$ AU velocity profile to that of a power law, whereas in the case of Cha-MMS1 power law, uniform *and* decreasing velocity distributions are consistent with our data below 3300 AU. Therefore, the infall velocity structures of both Cha-MMS1 and IRAM 04191 cover a similar range of velocities for $r > 3000$ AU, with Cha-MMS1 being additionally consistent with a wider range of velocity profiles at small radii. The flat, or decreasing velocity distributions at the inner core of Cha-MMS1 could represent a younger evolutionary phase than that of a protostar, if central free-fall has not yet taken place on these scales. The age of IRAM 04191 was estimated to be $\leq 3{\times}10^4$ yr, assuming 2000 AU is the radius below which there is a free-fall velocity field structure, while we previously estimated an age of $\leq 2{\times}10^5$ yr for Cha-MMS1.

The infall velocities we derive are mostly within the sub- to transonic range for $r \geq 3300$ AU (≥ 0.02 pc). Lee et al. (1999) found subsonic inward velocities of 0.04 km s^{-1} – 0.1 km s^{-1} for a sample of 17 starless cores showing evidence of infall motions. L1544 is one of the starless cores that has been extensively studied (e.g., Tafalla et al., 1998; Williams et al., 1999). These studies have shown that L1544 is undergoing inward motions with velocities up to $\sim$ 0.1 km s^{-1} over $\sim$ 0.1 pc. Such extended inward velocities imply that the velocity fields of Cha-MMS1, like that of L1544, are consistent with each other but inconsistent with the static SIS Shu (1977) model.

4.5.4.2 Comparison to theoretical models

In this section, we compare the infall velocity field derived for Cha-MMS1 with the velocities predicted by theoretical models. We resolve radii $r \geq 700$ AU from our observations and find an infall velocity range of $\sim$ 0.05 km s^{-1} – 0.5 km s^{-1} for this radius ($r \sim 700$ AU). We used 3D radiation-magneto-hydrodynamic models to extract the radial velocity structure for a 1 $M_\odot$ (MU2 model; Commerçon et al., 2012) and 5 $M_\odot$ dense core (Fig. 4.20). The mass estimate of Cha-MMS1 from continuum observations yields 1.44 $M_\odot$ within a radius of

3750 AU (Belloche et al., 2011a).

Both models have a normalised mass-to-magnetic-flux ratio of 2. They employ an azimuthal density perpurbation to assist fragmentation. The ratio of thermal to gravitational energy is 0.37 for the 1 $M_\odot$ model and 0.35 for the 5 $M_\odot$ model, the ratio of rotational to gravitational energies 0.045 and 0.03 ($\sim$ 2 and $\sim$ 1.5 times greater than the upper limit of Cha-MMS1's $\beta_{\rm rot}$, respectively), and the initial temperatures are 11 K and 10 K, respectively. Their corresponding initial radii are 3300 AU and 20000 AU. The density profile of the 1 $M_\odot$ case is initially uniform, whereas it scales as r^{-2} at the outer radii in the 5 $M_\odot$ case. The 1 $M_\odot$ and 5 $M_\odot$ models are denser at the equatorial plane of the cores by a factor of $\sim$ 3 and $\sim$ 4, respectively, compared to the density profile we used for Cha-MMS1 in Sect. 4.4.

The models predict the evolution of the 24 μm and 70 μm flux densities during the first core phase. The 3D radiative transfer code RADMC-3D by Dullemond[8] is used for the post-processing of the RMHD calculations (see Commerçon et al., 2012, for more details). The flux densities of Cha-MMS1 are, within a factor of $\sim$ 2, consistent with a first core age of $\sim$850 yr based on the 1 $M_\odot$ model, and 2680 yr based on the 5 $M_\odot$ model (see Sect. 4.3.1.2). The average radial velocity distribution of both first core models close to the equatorial plane (to avoid outflow contamination) are shown in Fig. 4.20. We can only explore the velocity profile of the 1 $M_\odot$ model for $r < 2500$ AU due to its smaller initial radius (3300 AU). The radial velocities it predicts up to $\sim$ 2000 AU are within the range of velocities we constrain for Cha-MMS1. For $r > 2000$ AU the velocities decrease to zero as we approach the boundary of the core. The average velocity extracted from the 5 $M_\odot$ model exhibits a velocity profile that follows the *upper limit* of Cha-MMS1's velocity range up to $\sim$ 8000 AU, and is *within* this range for 8000 AU $< r <$ 12000 AU. The slightly higher velocities predicted by the model compared to our upper limit for Cha-MMS1 may be due to the higher densities of the model.The velocity dip that peaks at $\sim$ 18000 AU in Fig. 4.20 is a remnant of a small initial expansion at the initial core radius of $\sim$ 20000 AU that preceded the first core collapse, and therefore is of no physical importance for interpretating of the collapse process in the model compared to the observational constraints.

We now compare our results with other first core models that show reasonable agreement with the properties of Cha-MMS1. Masunaga et al. (1998) explored the protostellar collapse of a cloud core via radiation hydrodynamic simulations assuming spherical symmetry, and specifically focussed on the formation of the first hydrostatic core. For the typical case of 1 $M_\odot$ and 10 K they find a homogeneous density structure inside the first core and an outer density distribution proportional to r^{-2}. The velocity field structure after the first core formation ($\rho \sim 10^{-13}$ g cm^{-3}) does not change for scales larger than $\sim$ 1000 AU for the different evolutionary times they present. They find supersonic velocities out to radii of $\sim$ 3000 AU, in very good agreement with the radius of $\sim$3300 AU below which supersonic motions are compatible with the envelope of Cha-MMS1. The infall velocities at 1000 AU, 3000 AU, and 9000 AU they predict are $\sim$ 0.25 km s^{-1}, $\sim$ 0.2 km s^{-1}, and $\sim$ 0.1 km s^{-1}. At the same radii we obtain velocity ranges of 0.06 – 0.5 km s^{-1}, 0.1 – 0.25 km s^{-1}, and 0.1 – 0.2 km s^{-1}. The velocity structure of Cha-MMS1 is therefore also consistent with the predictions of Masunaga et al. (1998) for a first core resulting from the collapse of a 1 $M_\odot$ non-rotating, non-magnetised

[8] http://www.ita.uni-heidelberg.de/ dullemond/software/radmc-3d/

cloud.

Saigo et al. (2008) investigated the effect of different initial rotation speeds during protostellar collapse and the formation of the first and second hydrostatic cores by performing 3D hydrodynamical simulations of cores with slow, moderate, and fast initial rotation. For a slowly rotating cloud ($\beta_{\rm rot} \sim 0.015 - 0.09$, i.e., consistent with the respective ratio of Cha-MMS1), the infall velocity structure during the first core phase is described by supersonic motions below a radius of $\sim$ 3000 AU, and infall velocities of ~ 0.4 km s^{-1}, ~ 0.3 km s^{-1}, and ~ 0.15 km s^{-1} at radii of 1000 AU, 3000 AU, and 9000 AU. The infall velocity predictions of Saigo et al. (2008) for the model with slow initial rotation is therefore consistent with the velocity ranges of 0.06 – 0.5 km s^{-1}, 0.1 – 0.25 km s^{-1}, and 0.1 – 0.2 km s^{-1} that we obtain for Cha-MMS1 at the same radial distances.

Finally, Ciolek & Basu (2000) presented an ambipolar diffusion model incorporating the observational constraints and physical parameters previously derived for the protostellar core L1544. They presented a non-rotating, ambipolar diffusion model with a lower background magnetic field strength (initial mass-to-flux ratio 0.8 in units of the critical value), which could reproduce the extended observed infall velocities of L1544, and concluded that L1544 might be a supercritical core undergoing magnetically diluted collapse. Their model predicts infall velocities of ~ 0.2 km s^{-1} and ~ 0.15 km s^{-1} at late times (approaching the first core densities), at 3000 AU and 9000 AU from the supercritical core, respectively, which are consistent with the infall velocity field structure we derive for Cha-MMS1 (Fig. 4.20). The spatial scale for supersonic infall velocities they predict at late times is $\sim$ 2000 AU. The agreement between the velocities of the two cores, especially for the late-time evolution models (approaching first core densities), might be indicating that the initial conditions of the model for L1544 adequately describes the initial conditions of Cha-MMS1. Cha-MMS1 might therefore be undergoing collapse that is physically similar to that of the prestellar dense core L1544.

In general, the velocities of the RMHD model agree with the inner envelope ($r < 2000$ AU) of Cha-MMS1 for a 1 $M_\odot$ collapsing dense core and for $r < 12000$ AU for a 5 $M_\odot$ dense core at the FHSC stage. In the innermost 2000 AU, the velocity predictions of both models "bracket" the upper limit of the observationally constrained velocities for Cha-MMS1, and for larger radii the 5 $M_\odot$ predictions closely follow this upper limit. Non-magnetised, rotating, as well as non-rotating models for the first core phase (Saigo et al., 2008; Masunaga et al., 1998) also produce infall velocity structures that are consistent with the infall motions of Cha-MMS1 on scales of $\sim$ 10000 AU (~ 0.05 pc). Consequently, the collapse motions in the envelope of Cha-MMS1 are consistent with first core predictions.

Since our observations are not sensitive to the very inner part of Cha-MMS1, where rapid infall velocity changes are expected, we cannot distinguish between an evolved prestellar core, a first core, and a young Class 0 object based on the kinematics alone. The 24 μm and 70 μm detections of Cha-MMS1 rule out its prestellar nature, and thus shifts the dilemma between a first core and a young Class 0 protostar. This dilemma can be solved by detecting a slow, compact outflow stemming from Cha-MMS1 via interferometric studies, which would differentiate between the two evolutionary phases. In any case, our kinematic and dynamical study has so far shown that its properties do *not* contradict the first core predictions, and it is an interesting target for exploring the early protostellar stages of star-formation.

4.6 Summary and conclusions

We performed observations of the dense core Cha-MMS1 in various molecular transitions and conducted an analysis of the kinematics within the core in order to investigate its physical properties and dynamical state. We utilised a 1D radiative transfer code to constrain the infall velocity structure of the core. Our conclusions can be summarised as follows.

1. The internal luminosity of Cha-MMS1 is estimated from the predicted inclination-dependent time evolution of SEDs for the first core phase for a 1 $M_\odot$ (Commerçon et al., 2012) and a 5 $M_\odot$ model. The 24 μm and 70 μm flux densities imply inclinations within the range of $30^\circ \leq i < 60^\circ$ and an internal luminosity range of 0.08 $L_\odot$ – 0.18 $L_\odot$.

2. The classical infall signature is detected in optically thick transitions, suggesting that the envelope of Cha-MMS1 is undergoing inward motions.

3. The position-velocity diagrams of optically thin transitions show velocity gradients perpendicular to the filament in which Cha-MMS1 is embedded. The average gradient over an extent of $\sim$ 16000 AU in diameter is 3.1 ± 0.1 km s^{-1} pc^{-1}, while we found no significant gradient along the filament. Interpreted in terms of rotation, these velocity variations imply solid-body rotation in the envelope up to a radius of $\sim$ 8000 AU, and slower, differential rotation from $\sim$ 8000 AU to $\sim$ 12500 AU. The average velocity gradient in the range 2000 AU – 4000 AU is surprisingly flatter, which is difficult to understand in terms of rotation.

4. The turbulent velocity dispersion in the core is uniform within a radius of $r \sim 5000$ AU parallel to the filament and $\sim$ 12500 AU perpendicular to the filament. The non-thermal dispersion is of the same order as the mean thermal dispersion at a temperature of 9 K, therefore implying an equipartition between thermal and non-thermal motions.

5. Our radiative transfer modelling yields subsonic to transonic infall velocities in the range 0.1 km s^{-1} – 0.2 km s^{-1} for 3300 AU $< r <$ 30000 AU. The velocity field is less well constrained in the inner parts for $r <$ 3300 AU. A velocity increasing as $r^{-0.5}$ toward the centre is consistent with the data, but we cannot exclude a decrease either. We find subsonic to supersonic velocities in the range 0.04 km s^{-1} – 0.6 km s^{-1} for $r \leq$ 3300 AU.

6. Part of the redshifted emission of the high-density tracers CS 5–4, CO 7–6, and CO 6–5 is not reproduced by the radiative transfer model. This excess emission may indicate the presence of unresolved, higher velocity material at the inner core originating from a compact outflow driven by Cha-MMS1, or alternatively, it could arise due to contamination from the outflow of the nearby Class I protostar.

7. We find relatively good agreement between the infall velocity profile derived for Cha-MMS1 and predictions of 3D RMHD simulations for the first hydrostatic core phase.

Both the kinematic agreement with the predictions of RMHD simulations and the possible presence of a compact outflow suggested above are consistent with Cha-MMS1 being at the

stage of the first hydrostatic core. However, we cannot affirm the object's nature without high-resolution interferometric observations to search for and image a compact, slow outflow. With the early prestellar core phase ruled out due to the object's 24 μm and 70 μm detection, Cha-MMS1 is either a first core or a young Class 0 protostar, and our kinematical study cannot exclude either possibility.

CHAPTER 5

Star formation in Chamaeleon I and III: a molecular line study of the starless core population

There is a theory which states that if ever anyone discovers exactly what the Universe is for and why it is here, it will instantly disappear and be replaced by something even more bizarre and inexplicable. There is another theory which states that this has already happened.

Douglas Adams

Contents

Abstract

Context: The Chamaeleon I and III molecular clouds are excellent nearby targets for low-mass star formation studies. Even though they belong to the same cloud complex (Cha I, II, and III), Cha I and II are actively forming stars while Cha III shows no sign of ongoing star formation.

Aims: We aim to determine the driving factors that have led to the very different levels of star formation activity in Cha I and III and examine the dynamical state and possible evolution of the starless cores within them.

Methods: Observations were performed in various molecular transitions with the APEX and Mopra telescopes. We examine the kinematics of the starless cores in the clouds through a virial analysis, a search for infall motions, and velocity gradients. The chemical differences in the two clouds are explored through their fractional molecular abundances and comparison to predictions of chemical models.

Results: Five cores are gravitationally bound in Cha I and one in Cha III. The infall signature is seen toward between 9 and 18 cores in Cha I and between 2 and 5 cores in Cha III, which leads to a range of 15–30 % cores in Cha I and 10–25 % cores in Cha III that are contracting and may become prestellar. There is no significant difference in the turbulence level in the two clouds. Future dynamical interactions between the cores will not be dynamically significant in either Cha I or III. Turbulence dissipation in the cores of both clouds is seen in the high-density tracers N_2H^+ 1–0 and HC_3N 10–9 which have lower non-thermal velocity dispersions compared to $C^{17}O$ 2–1, $C^{18}O$ 2–1, and $C^{34}S$ 2–1. Evidence for depletion in the Cha I core interiors is seen in the abundance distributions of the latter three molecules. The average fractional abundances of $C^{18}O$ and CH_3OH are lower in Cha III than Cha I by a factor of $\sim$ 2.4 and 1.8, respectively, indicating a difference in chemistry. Chemical models suitable for the Cha I and III cores are used to constrain the effectiveness of the HC_3N to N_2H^+ abundance ratio as an evolutionary indicator. Both collapse and static chemical models indicate that this ratio is a good evolutionary indicator in the prestellar phase. In the framework of these models, we find that the cores in Cha III and the southern part of Cha I are in a similar evolutionary stage, and might follow the path of the more evolved cores in the central region of Cha I.

Conclusions: The measured HC_3N/N_2H^+ abundance ratio and the infall signatures detected toward the Cha I and III starless cores suggest that Cha III is younger than Cha I, and therefore on the verge of forming stars.

The content of this Chapter has been submitted for publication at the journal Astronomy & Astrophysics.

5.1 Introduction

The Chamaeleon cloud complex is a prime target for studying the earliest phases of low-mass star formation. The molecular clouds Chamaeleon I and III contain a relatively large population of starless condensations at nearby distances. Only few of these starless cores show signs of being gravitationally bound (Belloche et al., 2011a,b). One of our aims is to explore the dynamics and kinematics of these cores in more detail, and determine whether there is a

larger core fraction that will in the future become prestellar, or whether the majority are merely transient structures that will disperse as a result of turbulence. Throughout this Chapter, we use the definition that a starless core is a core without an embedded protostellar object. Prestellar cores are defined as the subset of starless cores that are gravitationally bound and will therefore likely form stars (André et al., 2000; di Francesco et al., 2007). The evolutionary path the condensations will undertake is important in order to assess the dynamical state and the likely future evolution of the clouds themselves.

Studying the initial phase of star formation can help establish the link between the stellar initial mass function (IMF) and the core mass function (CMF) (e.g., André et al., 2007, 2009; Motte et al., 1998; Johnstone et al., 2000). Large and clustered core populations can also be used to shed light into the dominant dynamical processes taking place at the prestellar phase. On the one hand, in the competitive accretion scenario the dynamical interactions between the condensations play an important role in the subsequent core evolution and emergent IMF (e.g., Bate et al., 2003; Bonnell et al., 2004, 1998). On the other hand, the process of gravoturbulent cloud fragmentation suggests that stellar masses are determined at the prestellar phase and dynamical interactions with other cores and the surroundings are not significant (e.g., Padoan & Nordlund, 2002; Myers & Lazarian, 1998; Nakano, 1998).

Chamaeleon I (Cha I) is a nearby, low-mass star forming cloud located at a distance of ∼150 pc (Whittet et al., 1997; Knude & Høg, 1998). The Chamaeleon cloud complex consists of Cha I, II, and III, that despite their close proximity differ greatly in their level of star formation activity. Cha I has the highest level of star formation activity with more than 200 young stellar objects (YSOs) produced so far (Luhman, 2008). It also has the highest dense gas fraction in the Chamaelon cloud complex (Belloche et al., 2011a,b; Mizuno et al., 2001, 1999; Boulanger et al., 1998). Belloche et al. (2011a) performed a deep, unbiased dust continuum survey of Cha I at 870 μm with the APEX telescope. They identified 59 starless cores, 21 YSOs, 1 first hydrostatic core (FHSC) candidate, and a network of five filaments where the majority of the cores are located. They found that at most ∼ 17 % of the starless cores are prestellar based on a simple thermal analysis and concluded that the rate of star formation in Cha I is decreasing. Luhman (2007) had similarly proposed that the star formation activity in Cha I is continuing but gradually declining based on the YSO population. On the other hand, Palla & Stahler (2000) had reached the opposite conclusion that star formation in Cha I is proceeding in an accelerating fashion. The CMF of the starless cores in Cha I seems to be in a good agreement with the shape of the IMF at the high-mass end (Belloche et al., 2011a), as was found for various other molecular clouds (Aquila, Taurus, Pipe nebula, Serpens & Perseus, Ophiuchus; André et al., 2010; Sadavoy et al., 2010; Alves et al., 2007; Enoch et al., 2008; Motte et al., 1998, , respectively), but it ceases to be consistent at the low-mass end of the spectrum.

Chamaeleon III (Cha III) is also located at a distance of ∼ 150 pc (Whittet et al., 1997; Knude & Høg, 1998). Although it belongs to the same cloud complex as Cha I, it contains a lower fraction of dense gas (e.g., Mizuno et al., 1999, 2001) and no YSO (e.g., Luhman, 2008). Belloche et al. (2011b) identified 29 starless condensations in Cha III through an unbiased 870 μm dust continuum survey with LABOCA at APEX, performed with the same sensitivity as for Cha I. They found that only two sources out of the 29 starless cores are prestellar based on the Bonnor-Ebert critical mass criterion. A number of 38 clumps were previously detected

in $C^{18}O$ 1–0 with the Swedish-ESO Submillimeter Telescope (SEST) (Gahm et al., 2002). Only 20 of them correspond to detected 870 μm sources but as the $C^{18}O$ 1 – 0 survey is affected by depletion and is biased toward low-density gas, one-to-one correspondence is not seen. Unlike Cha I, no prominent filamentary structure is seen in the 870 μm dust continuum (Belloche et al., 2011b) but the core distribution within Cha III seems to be tracing out an underlying filamentary structure. The level of turbulence is of the same order in both Cha I and III based on $C^{18}O$ 1–0 (Mizuno et al., 1999) and CO 1–0 (Mizuno et al., 2001; Boulanger et al., 1998) data.

The striking difference in the number of YSOs in Cha I and III is bewildering given their proximity and the similar densities of their starless core population. A scenario that could explain why Cha III contains no YSO, is the cloud being at a younger evolutionary stage than Cha I and not having had enough time to produce protostars. Alternatively, the difference in star formation activity could be the result of environmental effects, such as turbulence, hindering star formation. We have undertaken a spectral survey of the starless core population in Cha I and III, which aims to complement the results obtained from the dust continuum surveys of Belloche et al. (2011a,b). We start by presenting the observational details of our data in Sect. 5.2. We then proceed to the analysis of the kinematics (velocity distribution, infall, turbulence) of the cores in Sect. 5.3 and their molecular abundances which we compare to predictions of chemical models, in Sect. 5.4. Finally, we discuss the implications of our results in Sect. 5.5 and give a summary of the conclusions in Sect. 5.6.

5.2 Observations

The observations were performed toward the starless condensations identified in the continuum surveys of Belloche et al. (2011a,b). The data were reduced with the CLASS software[1].

5.2.1 Chamaeleon I data

The 60 cores detected in continuum emission were observed with the APEX[2] telescope in May and July 2010 in the following molecular lines: $C^{18}O$ 2–1, ^{13}CO 2–1, $C^{17}O$ 2–1, H_2CO $3_{1,2}$–$2_{1,1}$, HCN 3–2, HCO^+ 3–2, and N_2H^+ 3–2. Table 5.1 outlines the transitions observed for each core in our sample. The cores are numbered by decreasing 870 μm peak flux density (see Belloche et al., 2011a). All 60 cores were observed in $C^{18}O$ 2–1. ^{13}CO 2–1 was observed in parallel to $C^{18}O$ 2–1. $C^{17}O$ 2–1 was observed toward the 32 cores with the strongest $C^{18}O$ 2–1 emission so that the transition pair can be used to determine line opacities. H_2CO $3_{1,2}$–$2_{1,1}$ was observed in parallel to $C^{17}O$ 2–1. Due to observing time constraints only the brightest 30 cores were targeted in HCO^+ 3–2 and HCN 3–2, which were observed in parallel. N_2H^+ 3–2 was observed only toward the cores Cha1-C1 – C34 which had N_2H^+ 1–0 Mopra detections (see below), excluding the core Cha1-C29 (very weak emission).

Table 5.2 gives information about the frequencies, resolution, telescope receivers, forward/main beam, efficiencies, system temperatures, and rms for all observed transitions. The

[1] see http://www.iram.fr/IRAMFR/GILDAS.

[2] The Atacama Pathfinder Experiment telescope (APEX) is a collaboration between the Max-Planck Institut für Radioastronomie, the European Southern Observatory, and the Onsala Space Observatory.

coordinates of the cores can be found in Table 2 of Belloche et al. (2011a). The observations were conducted in position-switching mode with a reference position for the CO isotopologues at α_{J2000}=$11^h24^m33^s.5$, δ_{J2000}=-77°01′56.8″, which was free of emission in ^{13}CO 2–1 with an rms of ∼ 60 mK for the spectral resolution given in Table 5.2. A second reference position at α_{J2000}=$11^h05^m23^s.7$, δ_{J2000}=-77°11′02.2″ was used for all other transitions and was also free of emission at all frequencies with an rms of ∼ 50 mK in N_2H^+ 3–2 (spectral resolution listed in Table 5.2).

A subset of 57 cores from the continuum sample was observed with the Mopra telescope in June 2010. The zoom mode of the high resolution spectrometer MOPS was used, with the receiver tuned at 94554 MHz with 12 zoom windows of 138 MHz selected within the 8 GHz bandwidth. The subset consists of cores Cha1-C1 to Cha1-C56 and core Cha1-C60. All cores were observed in the various molecular transitions from which the following were detected: HNC 1–0, HC_3N 10–9, N_2H^+ 1–0, C_4H $10_{10,10}$–$9_{9,9}$, $C^{34}S$ 2–1, CH_3OH 2_1–1_1 E, CH_3OH 2_0–1_0 A^+, and CS 2–1. Information about the parameters of the Mopra observations for each transition (frequency, angular resolution, main beam efficiencies, channel spacings, system temperatures, rms) are given in Table 5.3. Position-switching observations were performed with a reference position at α_{J2000}=$11^h05^m23^s.7$, δ_{J2000}=-77°11′02.2″ (free of emission with an rms of 40 – 53 mK for the transitions and spectral resolutions given in Table 5.3). IRAM 04191+1522 and Oph A SM1N were used as calibration sources. The pointing was checked every ∼ 1 hour . Tsitali et al. (2013) calculated a value of 0.34 for the main beam efficiency of the telescope through a detailed calibration analysis.

The northern part of Cha I was mapped in CO 3–2 with APEX in June 2006 with the on-the-fly mode. The mapped region has a size of $6.9' \times 5.4'$, centered on the offset position ($60''$, $60''$) with respect to Cha-MMS2 at α_{J2000}=$11^h09^m57^s.9$, δ_{J2000}=-76°35′00.1″. The rms of the cube at a region that is free of emission is ∼ 0.6 K at a spectral resolution of 122 kHz. The reference position (α_{J2000}=$11^h23^m01^s.39$, δ_{J2000}=-76°08′53.4″) was also checked to be free of CO 3–2 emission with an rms of ∼ 0.14 K at a spectral resolution of 122 kHz. The pointing was checked every ∼ 1 h on 07454-7112 and the focus was optimised on Saturn. Table 5.2 gives more information about the CO 3–2 observational setup.

5.2.2 Chamaeleon III data

Twenty starless cores in Cha III were observed with the Mopra telescope in May 2012. The sample was chosen by selecting the cores with the highest peak flux density in 870 μm continuum emission (Belloche et al., 2011b). The receiver was tuned at two different frequencies, 94554 MHz and 87190 MHz. Single position observations were performed in various molecular transitions from which we got detections in the following: $H^{13}CO^+$ 1–0, $HN^{13}C$ 1–0, HNCO $4_{0,4}$–$3_{0,3}$, HCN 1–0, HCO^+ 1–0, HNC 1–0, HC_3N 10–9, CH_3OH 2_1–1_1 E, CH_3OH 2_0–1_0 A^+, N_2H^+ 1–0, CS 2–1. We list the observation parameters for all the detected transitions and some of the non-detected transitions in Table 5.4. The coordinates of the observed cores are given in Table 2 of Belloche et al. (2011b). The observations were performed in position-switching mode with the reference position at α_{J2000}=$13^h00^m00^s$, δ_{J2000}=-79°40′00″. The reference position was free of emission at all frequencies with a maximum rms of 56 mK for the spectral resolution given in Table 5.4. IRAM 04191+1522 and Cha1-C1 were used as

Table 5.1: Molecular transitions observed with APEX for the cores in Cha I.

Core	Molecular Transition			
	$C^{18}O$ 2–1[a]	$C^{17}O$ 2–1[b]	HCO^+ 3–2[c]	N_2H^+ 3–2
Cha1-C1	y[d]	y	y	y
Cha1-C2	y	y	y	y
Cha1-C3	y	y	y	y
Cha1-C4	y	y	y	y
Cha1-C5	y	y	y	–
Cha1-C6	y	–	y	–
Cha1-C7	y	y	y	–
Cha1-C8	y	–	y	y
Cha1-C9	y	y	y	–
Cha1-C10	y	y	y	y
Cha1-C11	y	y	y	y
Cha1-C12	y	y	y	–
Cha1-C13	y	–	y	–
Cha1-C14	y	–	y	y
Cha1-C15	y	y	y	–
Cha1-C16	y	–	y	–
Cha1-C17	y	y	y	–
Cha1-C18	y	y	y	–
Cha1-C19	y	y	y	y
Cha1-C20	y	–	y	–
Cha1-C21	y	y	y	y
Cha1-C22	y	–	y	–
Cha1-C23	y	–	y	–
Cha1-C24	y	–	y	–
Cha1-C25	y	–	y	–
Cha1-C26	y	y	y	–
Cha1-C27	y	y	y	–
Cha1-C28	y	–	y	–
Cha1-C29	y	y	y	y
Cha1-C30	y	y	y	y
Cha1-C31	y	–	–	y
Cha1-C32	y	–	–	–
Cha1-C33	y	–	–	y
Cha1-C34	y	y	–	y
Cha1-C35	y	y	–	–
Cha1-C36	y	y	–	–
Cha1-C37	y	–	–	–
Cha1-C38	y	y	–	–
Cha1-C39	y	y	–	–
Cha1-C40	y	–	–	–
Cha1-C41	y	y	–	–
Cha1-C42	y	–	–	–
Cha1-C43	y	y	–	–
Cha1-C44	y	–	–	–
Cha1-C45	y	–	–	–

Table 5.1: continued.

Core	Molecular Transition			
	$C^{18}O$ 2–1[a]	$C^{17}O$ 2–1[b]	HCO^+ 3–2[c]	N_2H^+ 3–2
Cha1-C46	y	–	–	–
Cha1-C47	y	–	–	–
Cha1-C48	y	–	–	–
Cha1-C49	y	y	–	–
Cha1-C50	y	–	–	–
Cha1-C51	y	–	–	–
Cha1-C52	y	–	–	–
Cha1-C53	y	y	–	–
Cha1-C54	y	y	–	–
Cha1-C55	y	–	–	–
Cha1-C56	y	–	–	–
Cha1-C57	y	y	–	–
Cha1-C58	y	y	–	–
Cha1-C59	y	y	–	–
Cha1-C60	y	y	–	–
Total[e]	60	33	30	15

Notes. All cores but Cha1-C1 are starless. Cha1-C1 corresponds to Cha-MMS1, which is a candidate first hydrostatic core (see Tsitali et al., 2013). [(a)] ^{13}CO 2–1 was observed in parallel to $C^{18}O$ 2–1. [(b)] H_2CO $3_{1,2}$–$2_{2,1}$ was observed in parallel to $C^{17}O$ 2–1. [(c)] HCN 3–2 was observed in parallel to HCO^+ 3–2. [(d)] Core was (y) or was not (–) observed in the respective transition. [(e)] Total number of cores observed.

calibration sources.

We observed all 29 continuum sources in $C^{18}O$ 2–1 (and ^{13}CO 2–1 in parallel) and two sources (Cha3-C1 and Cha3-C4) in $C^{17}O$ 2–1 with the APEX telescope in June 2013. Table 5.5 gives the respective observational parameters of the two transitions. The observations were done in position-switching mode with the same reference position at α_{J2000}=$13^h00^m00^s$, δ_{J2000}=-79°40′00″ (free of emission in $C^{18}O$ 2–1 and ^{13}CO 2–1 with an rms of ∼ 100 mK). The pointing was checked every 1 – 1.5 h on 07454-7112.

5.2.3 Complementary $C^{18}O$ 1–0 data

We used the $C^{18}O$ 1–0 emission map of Cha I observed with SEST from Haikala et al. (2005). Details about the observational setup can be found in their paper.

Table 5.2: Parameters of Cha I observations with APEX.

Transition	f[a] (MHz)	σ_ν[b] (kHz)	$HPBW$[c] ($''$)	Receiver	Mixing	Backend	δf[d] (kHz)	δV[e] (km s^{-1})	$N_{\rm cores}$[f]	$F_{\rm eff}$[g] (%)	$B_{\rm eff}$[g] (%)	$T_{\rm sys}$[h] (K)	rms[i] (mK)
$C^{18}O$ 2–1	219560.3541	1.5	27.7	APEX-1	SSB	FFTS1	122	0.17	60	95	75	187–208	62–192
^{13}CO 2–1[j]	220398.6842	0.1	27.6	APEX-1	SSB	FFTS1	122	0.17	60	95	75	174–198	52–160
$C^{17}O$ 2–1[j]	224714.1870	80	27.1	APEX-1	SSB	FFTS1	122	0.16	33	95	75	216–359	65–122
H_2CO $3_{1,2}$–$2_{1,1}$	225697.7750	10	27.0	APEX-1	SSB	FFTS1	122	0.16	33	95	75	198–334	52–95
HCN 3–2	265886.4339	0.4	22.9	APEX-2	SSB	FFTS1	122	0.14	30	95	74	141–269	28–81
HCO^+ 3–2	267557.6259	1.1	22.8	APEX-2	SSB	FFTS1	122	0.14	30	95	74	176–344	35–94
N_2H^+ 3–2[j]	279511.7843	6.3	21.8	APEX-2	SSB	FFTS1	122	0.13	10	95	60	160–290	38–55
N_2H^+ 3–2[j]	279511.7843	6.3	21.8	FLASH345	2SB	XFFTS	76	0.08	5	95	60	172–192	33–63
CO 3–2	345795.9899	0.5	17.6	APEX-2A	DSB	FFTS1	122	0.11	–[k]	95	73	160–235	600

Notes. [(a)] Rest frequency taken from the Cologne Database for Molecular Spectroscopy (CDMS; Müller et al., 2005). [(b)] Frequency uncertainty taken from the CDMS catalog. [(c)] Angular resolution. [(d)] Channel spacing in frequency. [(e)] Channel spacing in velocity. [(f)] Number of observed cores. [(g)] Forward and main-beam efficiencies. [(h)] System temperature. [(i)] rms sensitivity in $T_a^\star$ scale. [(j)] Transition with hyperfine structure. [(k)] Map of part of Cha I North.

Table 5.3: Parameters of Cha I observations with Mopra.

Transition	f[a]	σ_ν[b]	$HPBW$[c]	δf[d]	δV[e]	$N_{\rm cores}$[f]	$B_{\rm eff}$[g]	$T_{\rm sys}$[h]	rms[i]
	(MHz)	(kHz)	($''$)	(kHz)	(km s^{-1})		(%)	(K)	(mK)
HNC 1–0	90663.5680	40.0	38.0	33.7	0.11	57	34	155–218	15–40
HC_3N 10_{11}–9_{10}[j]	90979.0024	1.0	37.9	33.7	0.11	57	34	155–218	15–39
CH_3CN 5–4[k]	91987.0876	0.1	37.4	33.7	0.11	57	34	155–218	15–39
^{13}CS 2–1	92494.3080	50.0	37.2	33.7	0.11	57	34	155–218	16–41
N_2H^+ $1_{2,3}$–$0_{1,2}$[j]	93173.7642	2.4	37.0	33.7	0.11	57	34	160–228	27–50
C_4H $10_{11,11}$–$9_{10,10}$	95150.3971	31.0	36.2	33.7	0.11	57	34	162–232	13–46
CH_3OH 8_0–7_1 A^+[k]	95169.4630	10.0	36.2	33.7	0.11	57	34	162–232	15–43
C_4H $10_{10,10}$–$9_{9,9}$	95188.9481	30.0	36.2	33.7	0.11	57	34	162–232	14–46
$C^{34}S$ 2–1	96412.9495	2.2	35.7	33.7	0.11	57	34	162–232	17–45
CH_3OH 2_1–1_1 E	96739.3620	5.0	35.6	33.7	0.10	57	34	172–248	29–43
CH_3OH 2_0–1_0 A^+	96741.3750	5.0	35.6	33.7	0.10	57	34	172–248	29–47
$C^{33}S$ 2–1[k]	97172.0639	0.2	35.4	33.7	0.10	57	34	172–248	16–47
OCS 8–7[k]	97301.2085	0.1	35.4	33.7	0.10	57	34	172–248	17–49
CS 2–1	97980.9533	2.3	35.2	33.7	0.10	57	34	172–248	15–45

Notes. [a] Rest frequency taken from the CDMS catalog. [b] Frequency uncertainty taken from the CDMS catalog. [c] Angular resolution. [d] Channel spacing in frequency. [e] Channel spacing in velocity. [f] Number of observed cores. [g] Main-beam efficiency derived by Tsitali et al. (2013). [h] System temperature. [i] rms sensitivity in $T_a^\star$ scale. [j] Transition with hyperfine structure. [k] There were no detections in these transitions.

5.3 Results: kinematics

5.3.1 Definitions

We use a detection threshold of 3σ in peak temperature for all spectra used in the analysis. The core systemic velocities and the linewidths of the detected transitions were extracted from Gaussian or hyperfine-structure fits to the spectra. The fitting was performed in CLASS using the methods "GAUSS" or "HFS", respectively. The transitions to which we applied Gaussian or hyperfine structure fits are listed in Table 5.6. For the transitions that do not have a hyperfine structure we apply Gaussian fits as long as their shape is symmetric and not self-absorbed ($N_{\rm fit}$). The number of cores with two velocity components in their spectra is listed as $N_{\rm 2vel}$. We define a core with two velocity components as a core with spectra having two emission peaks in both optically thick *and* optically thin transitions in order to exclude spectra that might be self-absorbed. The results of the "GAUSS" and "HFS" fits in CLASS are given in Tables C.1 and C.2 for Cha I and III, respectively. Transitions that are thought to be optically thick and in particular those that are self-absorbed toward most cores (HNC 1–0, ^{13}CO 2–1, and CS 2–1) are not shown in Tables C.1 and C.2 and are not used to derive kinematical properties or column densities (Sect. 5.4).

In the following sections we also use a 'composite' $C^{18}O$ and $C^{17}O$ sample when discussing average velocities and non-thermal velocity dispersions in the clouds. The $C^{18}O$ 2–1

Table 5.4: Parameters of Cha III observations with Mopra.

Transition	f[a]	σ_ν[b]	$HPBW$[c]	δf[d]	δV[e]	$N_{\rm cores}$[f]	$B_{\rm eff}$[g]	$T_{\rm sys}$[h]	rms[i]
	(MHz)	(kHz)	($''$)	(kHz)	(km s^{-1})		(%)	(K)	(mK)
$H^{13}CO^+$ $1_{2,2}$–$0_{1,1}$[j]	86754.3004	3.9	39.7	33.7	0.12	20	34	177–200	35–55
$HN^{13}C$ $1_{2,3,3}$–$0_{1,2,2}$[j]	87090.8298	3.8	39.5	33.7	0.12	20	34	177–200	35–56
HNCO $4_{0,4,5}$–$3_{0,3,4}$[j]	87925.2178	0.3	39.2	33.7	0.12	20	34	175–198	36–71
HCN 1–0	88631.6022	0.1	38.9	33.7	0.11	20	34	175–264	30–58
HCO^+ 1–0	89188.5247	4.1	38.6	33.7	0.11	20	34	167–189	40–63
HNC 1–0	90663.5680	40.0	38.0	33.7	0.11	20	34	167–264	29–59
HC_3N 10_{11}–9_{10}[j]	90979.0024	1.0	37.9	33.7	0.11	20	34	167–264	28–53
^{13}CS 2–1[k]	92494.3080	50.0	37.2	33.7	0.11	20	34	200–264	28–42
N_2H^+ $1_{2,3}$–$0_{1,2}$[j]	93173.7642	2.4	37.0	33.7	0.11	20	34	208–274	32–45
C_4H $10_{11,11}$–$9_{10,10}$[k]	95150.3971	31.0	36.2	33.7	0.11	20	34	210–279	30–47
C_4H $10_{10,10}$–$9_{9,9}$[k]	95188.9481	30.0	36.2	33.7	0.11	20	34	210–279	30–47
$C^{34}S$ 2–1[k]	96412.9495	2.2	35.7	33.7	0.11	20	34	209–280	33–47
CH_3OH 2_1–1_1 E	96739.3620	5.0	35.6	33.7	0.10	20	34	227–300	35–49
CH_3OH 2_0–1_0 A^+	96741.3750	5.0	35.6	33.7	0.10	20	34	227–300	36–50
$C^{33}S$ 2–1[k]	97172.0639	0.2	35.4	33.7	0.10	20	34	225–300	32–47
CS 2–1	97980.9533	2.3	35.2	33.7	0.10	20	34	227–300	38–47

Notes. [a] Rest frequency taken from the CDMS catalog. [b] Frequency uncertainty taken from the CDMS catalog. [c] Angular resolution. [d] Channel spacing in frequency. [e] Channel spacing in velocity. [f] Number of observed cores. [g] Main-beam efficiency. [h] System temperature. [i] rms sensitivity in $T_a^\star$ scale. [j] Transition with hyperfine structure. [k] There were no detections in these transitions.

transition was observed and detected toward all sixty cores in Cha I so it is a very convenient starting point for a kinematic analysis. However, we calculated the opacity of the $C^{18}O$ 2–1 line for the sample of 32 cores that also have $C^{17}O$ 2–1 detections and found that only 50 % of the cores are optically thin with an opacity $\tau \leq 1$ (see Sect E.1). There is therefore a large fraction of cores that are somewhat optically thick in $C^{18}O$ 2–1. The 32 cores observed in $C^{17}O$ 2–1 were those with the strongest $C^{18}O$ 2–1 emission. Since $C^{17}O$ 2–1 is optically thin toward these cores, the $C^{17}O$ spectra are more reliable in deriving velocities and linewidths toward these 32 cores. For this reason, we create a composite sample of the 32 cores observed in $C^{17}O$ and the remaining 28 cores observed only in $C^{18}O$. Using this composite sample, we gain the advantage of having the *full* set of cores, while reducing the biases introduced by the higher optical depth of $C^{18}O$.

Table 5.5: Parameters of Cha III observations with APEX.

Transition	f[a] (MHz)	σ_ν[b] (kHz)	$HPBW$[c] ($''$)	Receiver	Backend	δf[d] (kHz)	δV[e] (km s^{-1})	$N_{\rm cores}$[f]	$F_{\rm eff}$[g] (%)	$B_{\rm eff}$[g] (%)	$T_{\rm sys}$[h] (K)	rms[i] (mK)
$C^{18}O$ 2–1	219560.3541	1.5	27.7	APEX-1 SSB	XFFTS2	76	0.10	29	95	75	205–261	98–144
$C^{17}O$ 2–1	224714.1870	80	27.1	APEX-1 SSB	XFFTS2	76	0.10	2	95	75	218–220	69–72

Notes. [a] Rest frequency taken from the CDMS catalog. [b] Frequency uncertainty taken from the CDMS catalog. [c] Angular resolution. [d] Channel spacing in frequency. [e] Channel spacing in velocity. [f] Number of observed cores. [g] Forward and main-beam efficiencies. [h] System temperature. [i] rms sensitivity in $T_a^\star$ scale. [j] Transition with hyperfine structure.

Table 5.6: List of transitions to which Gaussian or hyperfine-structure fits were applied.

Transition	N_{obs}[a]	N_{det}[b]	N_{2vel}[c]	N_{gb}[d]	N_{vir}[e]
Chamaeleon I					
HNC 1–0[f]	57	46	–	–	–
HC_3N 10–9[g]	57	18	0	4[h]	1
N_2H^+ 1–0[g]	57	19	0	4[h]	1
C_4H 10_{11}–9_{10}	57	10	0	3[i]	1
C_4H $10_{10,10}$–$9_{9,9}$	57	8	0	3[j]	1
$C^{34}S$ 2–1	57	23	1	1	1
CH_3OH 2_1–1_1 E	57	31	0	3[k]	1
CH_3OH 2_0–1_0 A^+	57	41	0	2[l]	1
CS 2–1[f]	57	56	–	–	–
$C^{18}O$ 2–1	60	60	4	1	1
$C^{17}O$ 2–1[g]	33	32	1	3[j]	1
H_2CO $3_{1,2}$–$2_{1,1}$	33	8	0	2[l]	0
N_2H^+ 3–2	15	5	0	4[h]	1
Chamaeleon III					
$H^{13}CO^+$ 1–0	20	5	0	0	0
HNC 1–0[f]	20	17	–	–	–
HC_3N 10–9[g]	20	3	0	1	0
N_2H^+ 1–0[g]	20	2	0	1	0
$C^{34}S$ 2–1	20	2	0	0	0
CH_3OH 2_1–1_1 E	20	10	0	1	0
CH_3OH 2_0–1_0 A^+	20	15	0	1	0
CS 2–1[f]	20	20	–	–	–
$C^{18}O$ 2–1	29	29	0	1	0
$C^{17}O$ 2–1[g]	2	2	0	1	0

Notes. [a] Number of observed cores. [b] Number of cores with 3σ detections in terms of the peak temperature that were used for the fitting (hyperfine structure fitting or symmetric, Gaussian lines). [c] Number of cores showing (and fitted by) two velocity components in their spectra. [d] Number of gravitationally bound cores assuming a temperature of 10 K to derive the non-thermal velocity dispersion. [e] Number of virialized cores. [f] CS 2–1 is optically thick in both Cha I and III toward all the cores detected in $C^{34}S$ 2–1 (see Sect. E.2). The majority of cores detected in HNC 1–0 have asymmetric, non-Gaussian like spectra which might be a sign of optical thickness. We therefore do not fit these two transitions. [g] Hyperfine-structure fit. [h] Bound cores: Cha1-C1, C2, C3, C4. [i] Bound cores: Cha1-C1, C3, C4. [j] Bound cores: Cha1-C1, C2, C3. [k] Bound cores: Cha1-C1, C2, C5 [l] Bound cores: Cha1-C1, C2.

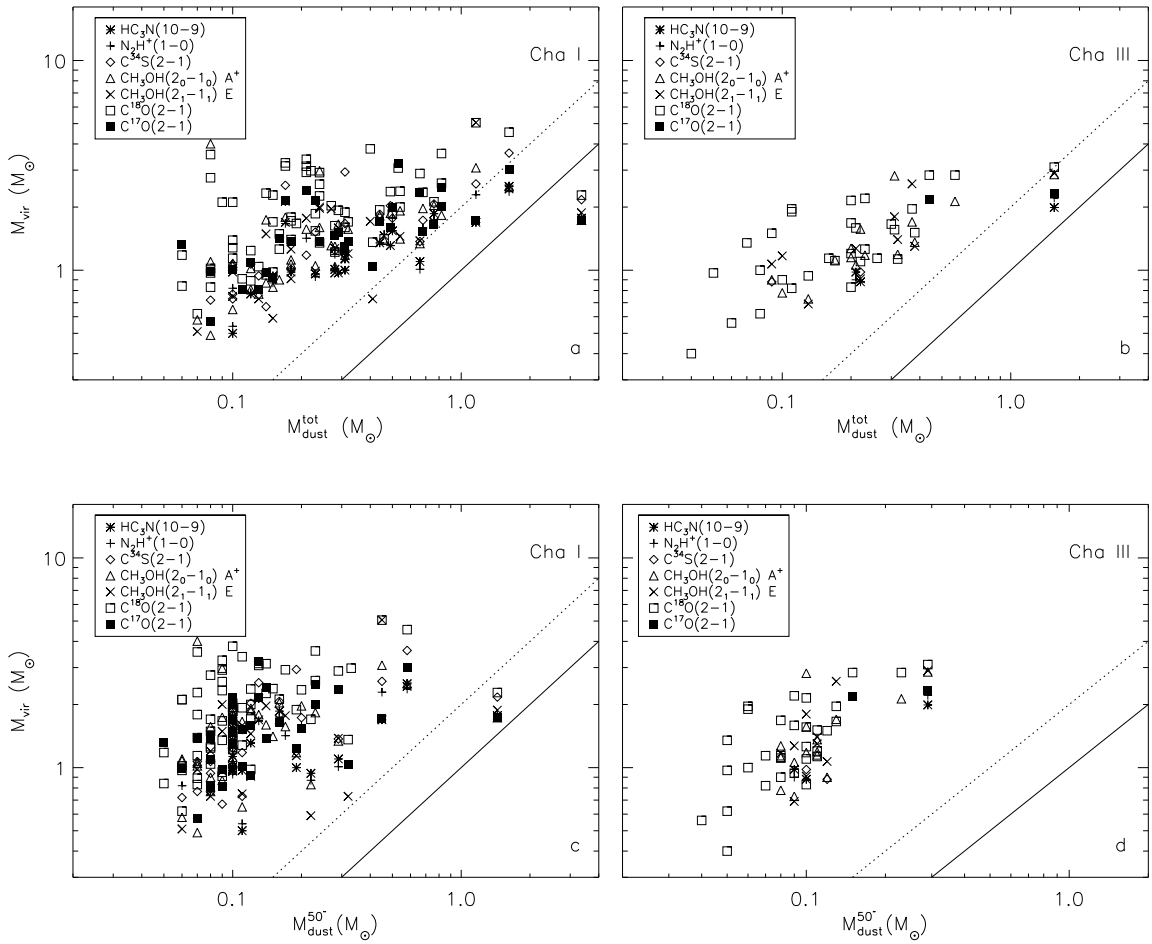

Figure 5.1: Mass derived from dust emission versus virial mass of the Cha I (a, c) and Cha III (b, d) cores computed for the transitions HC_3N 10–9, N_2H^+ 1–0, $C^{34}S$ 2–1, CH_3OH 2_0–1_0 A^+, CS 2–1 (only in Cha III), $C^{18}O$ 2–1, and $C^{17}O$ 2–1. Panels a and b show the total mass of the cores while panels c and d display the mass obtained for an aperture of diameter 50″. The solid line defines the region in which the cores are virialised ($\frac{M_{\rm vir}}{M_{\rm dust}} \leq 1$), while the dotted line marks the border on the right of which cores are considered to be gravitationally bound ($\frac{M_{\rm vir}}{M_{\rm dust}} \leq 2$).

5.3.2 Turbulence

5.3.2.1 Virial analysis

The virial mass of a spherically symmetric core with a density distribution proportional to r^{-2} can be estimated through the following expression if the external pressure is negligible:

$$M_{\rm vir} = 3 \times \frac{R{\sigma_{\rm tot}}^2}{G}, \tag{5.1}$$

where the radius R is given by the square root of the product of the major and minor $FWHM$ axes as measured in the dust maps (Belloche et al., 2011a,b), $\sqrt{FWHM_{\rm maj} \times FWHM_{\rm min}}$, and

$$\sigma_{\rm tot} = \sqrt{({\sigma_{\rm obs}}^2 - {\sigma_{\rm th,mol}}^2 + {\sigma_{\rm th,mean}}^2)}, \tag{5.2}$$

with $\sigma_{\rm obs}$ the measured velocity dispersion computed as

$$\sigma_{\rm obs} = \frac{FWHM_{\rm obs}}{\sqrt{8\ \ln 2}}, \tag{5.3}$$

where $FWHM_{\rm obs}$ is the observed spectral linewidth. The outer gas kinetic temperature of the densest core in Cha I, Cha1-C1 (Cha1-MMS1) was constrained to 9 K through radiative transfer modelling (Tsitali et al., 2013). Less dense cores may have a slightly higher kinetic temperature, and we assume $T = 10$ K as an approximation. The mean thermal velocity dispersions are computed as

$$\sigma_{\rm th,mean} = \sqrt{\frac{k_{\rm B}T}{\mu m_{\rm H}}}, \tag{5.4}$$

$$\sigma_{\rm th,mol} = \sqrt{\frac{k_{\rm B}T}{m_{\rm mol}}}, \tag{5.5}$$

where $k_{\rm B}$ is the Boltzmann's constant and T the kinetic temperature in K. The molecular weight of the mean particle is $\mu m_{\rm H}$ ($\mu = 2.37$), $m_{\rm mol} = \mu_{\rm mol} m_H$ is the molecular mass of the tracer, and $m_{\rm H}$ the proton mass. Equation 5.1 therefore becomes

$$M_{\rm vir} = 3 \times \frac{R}{G}\left({\sigma_{\rm obs}}^2 - \frac{k_{\rm B}T}{m_{\rm mol}} + \frac{k_{\rm B}T}{\mu m_{\rm H}}\right). \tag{5.6}$$

A core is considered to be gravitationally bound if its mass corresponds to at least half its virial mass and it is said to be virialised if its mass is higher than the virial mass. To calculate the respective mass to virial mass ratios, we use the masses derived by Belloche et al. (2011a,b) through dust continuum observations at 870 μm. We calculate the mass ratios both for the total dust mass derived from a Gaussian fit (Figs. 5.1a and 5.1b) and the dust mass derived for an aperture of 50″ (Figs. 5.1c and 5.1d), which corresponds to typical mean densities of $\sim 0.5 - 1 \times 10^5$ cm^{-3} (Belloche et al., 2011a,b). It is not straightforward to decide which dust mass is the most appropriate to compare to the virial masses because the lines trace material along the line of sight the extent of which is not known without a detailed radiative transfer modelling.

Table 5.6 and Fig 5.1a show that at most five cores are gravitationally bound (Cha1-C1, C2, C3, C4, C5) and one is virialised in Cha I when taking the *total* dust mass into account. The virialised core is Cha1-C1 or else known as Cha-MMS1, which is a first hydrostatic core candidate (Belloche et al., 2006, 2011a; Tsitali et al., 2013). On the other hand, we find that no core is virialised in Cha III in any transition and only Cha3-C1 is gravitationally bound (see Tables 5.6 and C.2, and Fig. 5.1b). Repeating the calculations for the dust mass derived from a 50″ aperture we find that only Cha1-C1 is gravitationally bound in Cha I and no core is gravitationally bound in Cha III (Figs. 5.1c and d). From now on, we will only use the *total* dust mass of the cores and consider the numbers of gravitationally bound and virialised cores as upper limits.

5.3.2.2 Comparison between tracers

Table 5.7: Comparison of systemic velocities, linewidths, and non-thermal velocity dispersions for selected pairs of transitions for Cha I and III.

Transitions	$N_{\rm cores}$ [a]	$v_{\rm LSR,mean}$ [b] (km s^{-1})	$FWHM_{\rm mean}$ [c] (km s^{-1})	$\sigma_{\rm nth,mean}$ [d] (km s^{-1})	$[\frac{\sigma_{\rm nth1}}{\sigma_{\rm nth2}}]_{\rm mean}$ [e]	$[\frac{\sigma_{\rm nth}}{\sigma_{\rm th,mean}}]_{\rm mean}$ [f]
			Chamaeleon I			
N_2H^+ 1–0	14	4.72±0.36	0.36±0.11	0.14±0.05	$0.75^{+0.18}_{-0.19}$	0.75±0.28
$C^{34}S$ 2–1	14	4.74±0.33	0.47±0.16	0.19±0.07	–	1.04±0.38
N_2H^+ 1–0	12	4.68±0.35	0.38±0.11	0.15±0.05	$0.85^{+0.22}_{-0.17}$	0.80±0.26
$C^{17}O$ 2–1	12	4.63±0.30	0.46±0.12	0.19±0.05	–	0.99±0.29
N_2H^+ 1–0	19	4.65±0.34	0.37±0.13	0.14±0.06	$0.77^{+0.30}_{-0.30}$	0.77±0.31
$C^{18}O/C^{17}O$[g]	19	4.67±0.29	0.50±0.20	0.20±0.09	–	1.09±0.47
N_2H^+ 1–0	19	4.65±0.34	0.37±0.13	0.14±0.06	$0.87^{+0.17}_{-0.11}$	0.77±0.31
CH_3OH 2_0–1_0 A^+	19	4.66±0.32	0.41±0.13	0.16±0.06	–	0.88±0.31
HC_3N 10–9	17	4.89±0.40	0.30±0.14	0.12±0.06	$0.63^{+0.20}_{-0.22}$	0.64±0.32
$C^{34}S$ 2–1	17	4.83±0.35	0.46±0.15	0.19±0.07	–	1.01±0.35
HC_3N 10–9	15	4.87±0.40	0.31±0.14	0.12±0.06	$0.71^{+0.28}_{-0.20}$	0.66±0.33
$C^{17}O$ 2–1	15	4.73±0.33	0.43±0.12	0.17±0.05	–	0.93±0.29
HC_3N 10–9	18	4.87±0.39	0.31±0.15	0.13±0.07	$0.68^{+0.31}_{-0.17}$	0.68±0.35
$C^{18}O/C^{17}O$[g]	18	4.75±0.33	0.46±0.16	0.19±0.07	–	1.00±0.37
HC_3N 10–9	18	4.87±0.39	0.32±0.15	0.13±0.07	$0.75^{+0.25}_{-0.19}$	0.68±0.35
CH_3OH 2_0–1_0 A^+	18	4.78±0.36	0.41±0.11	0.16±0.05	–	0.88±0.26
HC_3N 10–9	14	4.75±0.36	0.35±0.15	0.14±0.07	$0.96^{+0.17}_{-0.22}$	0.76±0.36
N_2H^+ 1–0	14	4.69±0.36	0.38±0.13	0.15±0.06	–	0.80±0.31
$C^{17}O$ 2–1	24	4.68±0.37	0.41±0.11	0.17±0.05	$1.09^{+0.31}_{-0.30}$	0.89±0.27
CH_3OH 2_0–1_0 A^+	24	4.76±0.34	0.39±0.11	0.16±0.05	–	0.84±0.26
$C^{34}S$ 2–1	18	4.86±0.35	0.45±0.15	0.19±0.06	$1.14^{+0.31}_{-0.35}$	1.00±0.34
$C^{17}O$ 2–1	18	4.78±0.32	0.42±0.12	0.17±0.05	–	0.91±0.28
CH_3OH 2_0–1_0 A^+	28	4.72±0.31	0.41±0.13	0.17±0.06	$1.11^{+0.28}_{-0.24}$	0.88±0.32
CH_3OH 2_1–1_1 E	28	4.72±0.32	0.40±0.16	0.16±0.07	–	0.86±0.39
$C^{18}O/C^{17}O$[g]	41	4.67±0.33	0.45±0.17	0.18±0.07	$1.18^{+0.45}_{-0.30}$	0.98±0.40
CH_3OH 2_0–1_0 A^+	41	4.70±0.32	0.41±0.18	0.17±0.08	–	0.89±0.42
$C^{18}O/C^{17}O$[g]	22	4.77±0.35	0.45±0.13	0.18±0.06	$1.18^{+0.35}_{-0.48}$	0.97±0.32
$C^{34}S$ 2–1	22	4.84±0.36	0.43±0.15	0.18±0.06	–	0.94±0.34

We compare the non-thermal velocity dispersions derived for a pair of transitions by using only the cores for which they are both detected in. Table 5.7 lists the average systemic velocities, linewidths, non-thermal velocity dispersions, the ratio of the non-thermal velocity dispersions, and the mean ratio of the non-thermal to the mean thermal velocity dispersion for selected pairs of transitions in Cha I and III.

N_2H^+ 1–0 has systematically lower (by $\sim$ 20–30 %) non-thermal velocity dispersions when compared to either $C^{17}O$ 2–1, $C^{34}S$ 2–1, and the composite $C^{18}O/C^{17}O$ sample in Cha

Table 5.7: continued.

Transitions	$N_{\rm cores}$ [a]	$v_{\rm LSR,mean}$ [b] (km s^{-1})	$FWHM_{\rm mean}$ [c] (km s^{-1})	$\sigma_{\rm nth,mean}$ [d] (km s^{-1})	$[\frac{\sigma_{\rm nth1}}{\sigma_{\rm nth2}}]_{\rm mean}$ [e]	$[\frac{\sigma_{\rm nth}}{\sigma_{\rm th,mean}}]_{\rm mean}$ [f]
			Chamaeleon III			
HC_3N 10–9	3	1.51±0.04	0.23±0.04	0.09±0.02	0.54±0.04	0.48±0.10
$C^{18}O$ 2–1	3	1.40±0.13	0.42±0.08	0.17±0.04	–	0.91±0.19
HC_3N 10–9	3	1.51±0.04	0.23±0.04	0.09±0.02	0.60±0.19	0.48±0.10
CH_3OH 2_0–1_0 A^+	3	1.43±0.13	0.40±0.08	0.16±0.04	–	0.86±0.19
$C^{18}O$ 2–1	15	1.41±0.16	0.43±0.10	0.18±0.05	$1.15^{+0.21}_{-0.27}$	0.94±0.25
CH_3OH 2_0–1_0 A^+	15	1.41±0.18	0.39±0.09	0.16±0.04	–	0.85±0.22
CH_3OH 2_0–1_0 A^+	10	1.38±0.15	0.38±0.11	0.15±0.05	$1.09^{+0.40}_{-0.34}$	0.83±0.26
CH_3OH 2_1–1_1 E	10	1.37±0.15	0.39±0.12	0.16±0.06	–	0.85±0.30
$C^{18}O$ 2–1	5	1.30±0.07	0.46±0.07	0.19±0.03	1.04±0.16	1.00±0.17
$H^{13}CO^+$ 1–0	5	1.33±0.07	0.46±0.10	0.19±0.05	–	0.99±0.25
$H^{13}CO^+$ 1–0	5	1.33±0.07	0.46±0.10	0.19±0.05	1.35±0.36	0.99±0.25
CH_3OH 2_0–1_0 A^+	5	1.29±0.09	0.36±0.08	0.14±0.04	–	0.76±0.20

Notes. All uncertainties are dispersions around the mean of each distribution apart from the uncertainty of the ratio of the non-thermal velocity dispersions. The latter is the dispersion above or below the mean computed by taking the difference between the largest value within 68 % of the population (above or below the mean) and the mean value itself. [(a)] Number of cores with detections in both tracers. [(b)] Average systemic velocities. [(c)] Average $FWHM$ linewidths. [(d)] Average non-thermal velocity dispersion, calculated for $T = 10$ K. [(e)] Mean ratio of the non-thermal dispersions of each pair of tracers. The transition listed first is denoted with the subscript 1 and the second one with the subscript 2. [(f)] Average ratio of the non-thermal to the mean thermal velocity dispersions. [(g)] Composite $C^{18}O$ and $C^{17}O$ sample (see Sect. 5.3.1).

I. HC_3N 10–9 has a similar behaviour to N_2H^+ 1–0, with non-thermal dispersions lower than $C^{17}O$ 2–1, $C^{34}S$ 2–1, and the composite $C^{18}O$/$C^{17}O$ by ∼ 30–40 %. The non-thermal dispersion ratio of the two latter transitions is around unity. HC_3N 10–9 similarly has a lower non-thermal dispersion in Cha III compared to $C^{18}O$ 2–1 by ∼ 50 % and CH_3OH 2_0–1_0 A^+ by ∼ 40 %. The methanol CH_3OH 2_0–1_0 A^+ and CH_3OH 2_1–1_1 E transitions have consistent non-thermal dispersions in both Cha I and III.

5.3.3 Infall signature

The infall signature is an optical depth effect and is produced when the line excitation temperature increases toward the centre of a collapsing core (Evans et al., 2003). Assuming spherical symmetry, the infall signature of a core consists of two elements. The first one is an asymmetric profile of an optically thick line that is skewed to the blue and sometimes features a self-absorption dip (due to absorption from the outer low-excitation material). In order to exclude the possibility that the observed spectral profile is due to two separate, overlapping velocity components, an optically thin, symmetric (and single-peaked) line is required to peak at a velocity in between the red and blue portions of the optically thick line (Leung & Brown,

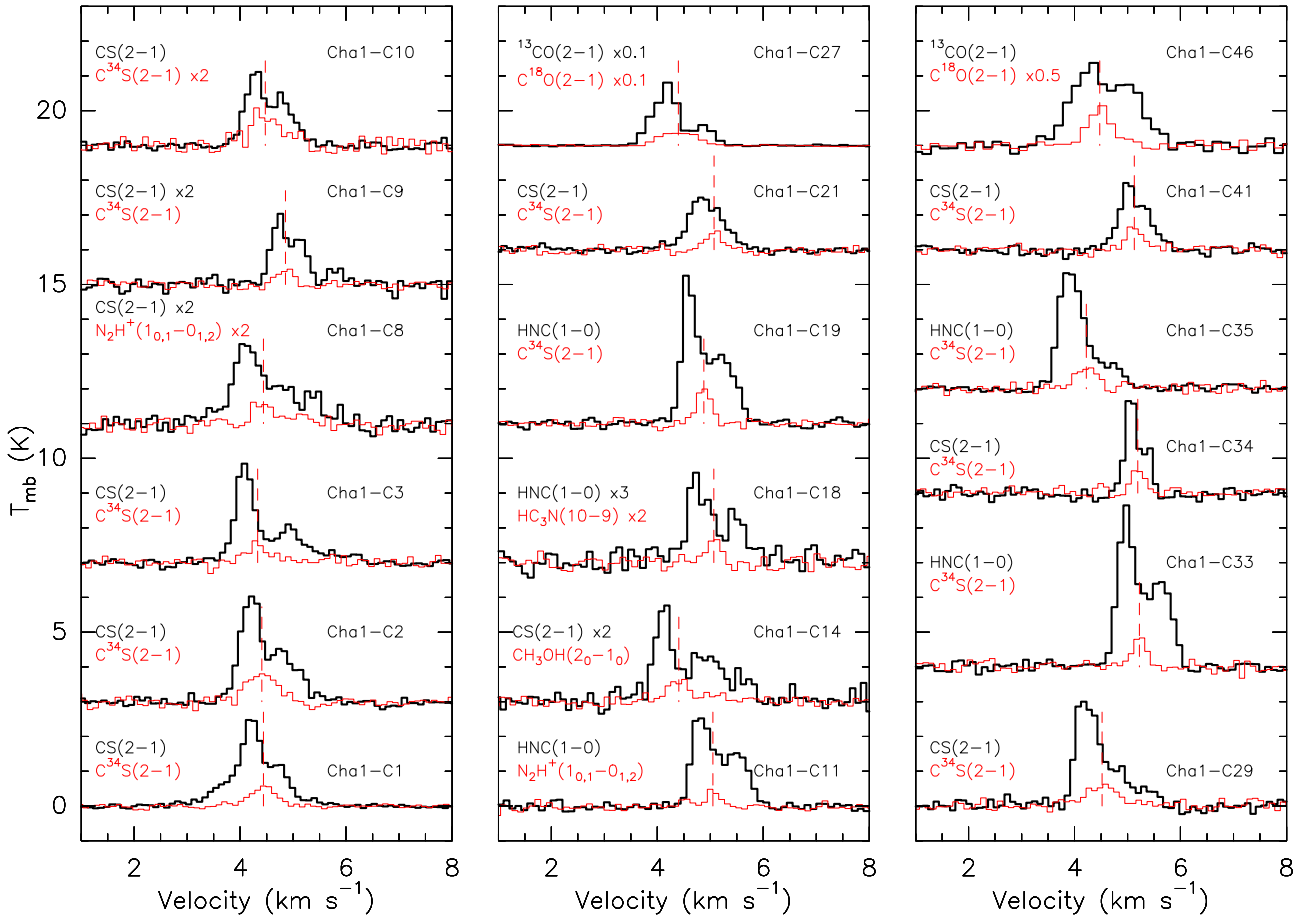

Figure 5.2: Infall signature toward cores in Cha I. The optically thick, self-absorbed transitions are shown in black thick lines and the optically thin transitions in red thin lines. The dashed red line shows the systemic velocity of each core derived from a gaussian or hyperfine-structure fit to the optically thin line shown in red. The name of the cores is given on the right-hand side of each transition depicted. The factor by which each spectrum was multiplied is given next to the name of the transitions and it corresponds to 1 if not specified.

Table 5.8: Infall and opposite signatures.

Source	$Line_{thick}$[a]	$Line_{thin}$[a]	T_{blue}/T_{red}[b]	δV[c]
		Infall Signature - Chamaeleon I		
Cha1-C1	CS 2–1	$C^{34}S$ 2–1	2.09±0.09	-0.41±0.10
Cha1-C2	CS 2–1	$C^{34}S$ 2–1	1.99±0.13	-0.29±0.12
Cha1-C3	CS 2–1	$C^{34}S$ 2–1	2.59±0.23	-0.41±0.28
Cha1-C8	CS 2–1	N_2H^+ 1–0	2.10±0.35	-0.63±0.53
Cha1-C9	CS 2–1	$C^{34}S$ 2–1	1.58±0.26	-0.28±0.26
Cha1-C10	CS 2–1	$C^{34}S$ 2–1	1.39±0.10	-0.25±0.17
Cha1-C11	HNC 1–0	N_2H^+ 1–0	1.65±0.11	-0.80±0.58
Cha1-C14	CS 2–1	CH_3OH[d]	1.97±0.28	-0.50±0.39
Cha1-C18	HNC 1–0	HC_3N 10–9	1.67±0.28	-0.91±0.60
Cha1-C19	HNC 1–0	$C^{34}S$ 2–1	2.15±0.10	-0.79±0.19
Cha1-C21	CS 2–1	$C^{34}S$ 2–1	1.25±0.09	-0.64±0.35
Cha1-C27	^{13}CO 2–1	$C^{18}O$ 2–1	3.05±0.08	-0.27±0.05
Cha1-C29	CS 2–1	$C^{34}S$ 2–1	2.61±0.29	-0.36±0.19
Cha1-C33	HNC 1–0	$C^{34}S$ 2–1	1.90±0.08	-0.78±0.31
Cha1-C34	CS 2–1	$C^{34}S$ 2–1	2.05±0.18	-0.42±0.22
Cha1-C35	HNC 1–0	$C^{34}S$ 2–1	4.47±0.44	-0.62±0.27
Cha1-C41	CS 2–1	$C^{34}S$ 2–1	1.52±0.13	-0.30±0.21
Cha1-C46	^{13}CO 2–1	$C^{18}O$ 2–1	1.36±0.13	-0.36±0.19
		Opposite Signature - Chamaeleon I		
Cha1-C6	^{13}CO 2–1	$C^{18}O$ 2–1	0.85±0.04	0.73±0.12
Cha1-C12	^{13}CO 2–1	$C^{18}O$ 2–1	0.72±0.05	0.43±0.06
Cha1-C17	CS 2–1	$C^{34}S$ 2–1	0.84±0.07	0.29±0.16
Cha1-C22	^{13}CO 2–1	CH_3OH[d]	0.76±0.06	0.82±0.39
Cha1-C24	^{13}CO 2–1	$C^{18}O$ 2–1	0.78±0.06	1.46±0.27
Cha1-C30	CS 2–1	CH_3OH[d]	0.33±0.10	0.93±0.43
Cha1-C31	CS 2–1	CH_3OH[d]	0.58±0.17	0.69±0.40
		Infall Signature - Chamaeleon III		
Cha3-C1	HNC 1–0	CH_3OH[d]	2.00±0.25	-0.40±0.16
Cha3-C9	^{13}CO 2–1	$C^{18}O$ 2–1	1.38±0.09	-0.31±0.12
Cha3-C10	^{13}CO 2–1	$C^{18}O$ 2–1	1.33±0.09	-0.34±0.08
Cha3-C13	HNC 1–0	$C^{18}O$ 2–1	2.21±0.75	-0.55±0.28
Cha3-C20	^{13}CO 2–1	$C^{18}O$ 2–1	1.22±0.06	-0.34±0.10

Notes. [(a)] Optically thick and thin transitions shown in Figs. 5.2, 5.3, and 5.4. [(b)] Ratio of the blue and red peak temperatures of the optically thick spectra and 1σ uncertainty. [(c)] Dimensionless parameter described in equation 5.7. The uncertainty corresponds to the 3σ error. [(d)] CH_3OH 2_0–1_0 A^+.

1977; Walker et al., 1986; Zhou, 1992; Myers et al., 1995, 1996).

The opposite signature, i.e., with the red peak emission of the self-absorbed transition being stronger than the blue peak, has also been seen in other surveys in the past (e.g., Gregersen

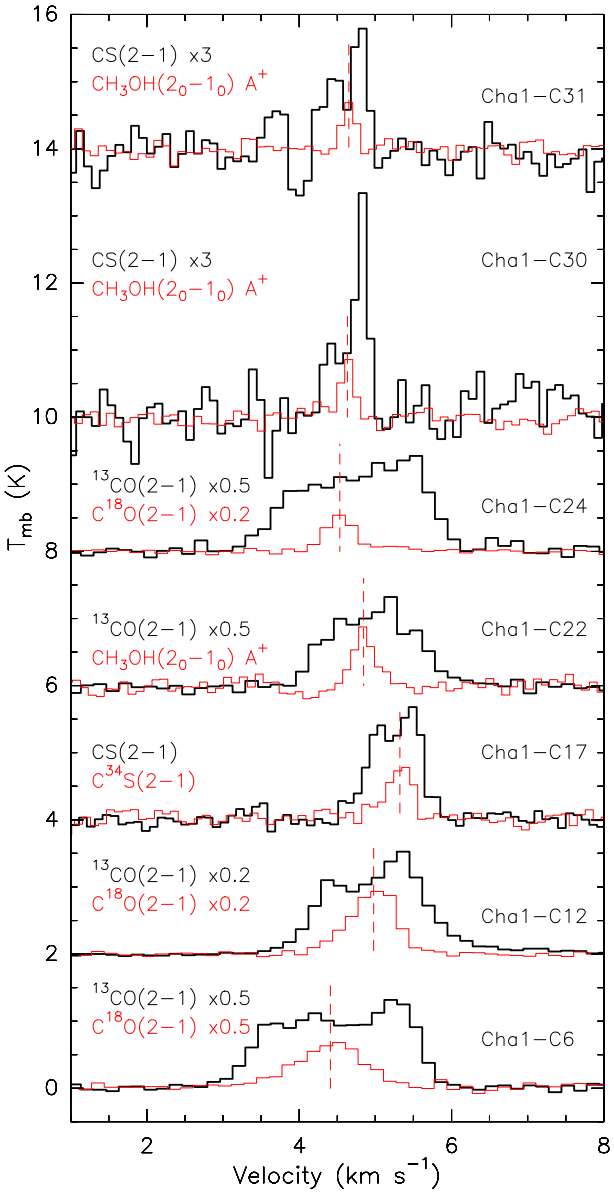

Figure 5.3: Same as Fig. 5.2, for the cores in Cha I showing the opposite signature.

et al., 1997; Mardones et al., 1997; Gregersen & Evans, 2000, 2001). The red-skewed profiles are generally not very well understood. They may arise as a result of outflowing or expanding material (Evans et al., 2003). In most of the aforementioned surveys, the "blue profiles" outnumbered the "red profiles" which was taken as an indication for infall motions.

The infall signature and the opposite one could also equally be produced by oscillations. Such interpretation was proposed for the starless core B68 where both blue-skewed and red-skewed spectra were seen in CS 2–1 (Lada & Lada, 2003) and HCO^+ 3–2 accross the core (Redman et al., 2006). This pattern was interpreted as an oscillation, or pulsation of the outer

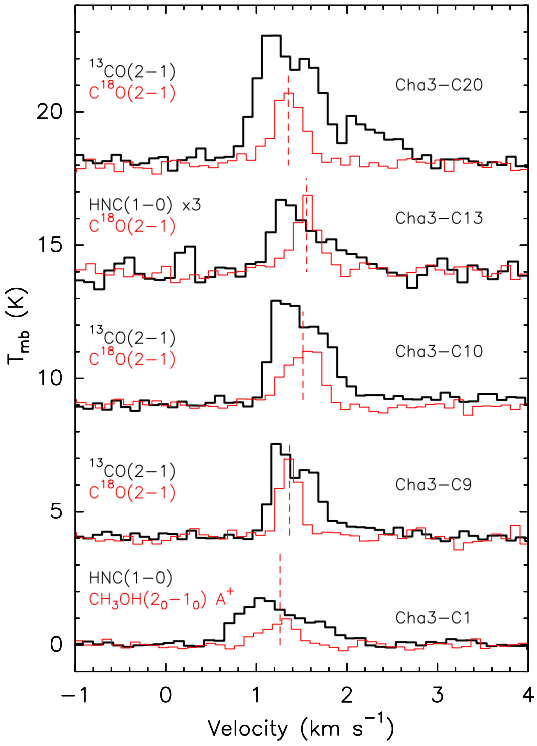

Figure 5.4: Same as Fig. 5.2 but for the cores in Cha III.

core layers about an equilibrium state due to external pressure perturbations (Lada & Lada, 2003; Redman et al., 2006; Keto & Field, 2005).

Mardones et al. (1997) proposed a nondimentional parameter, δV, to quantify the observed asymmetry both for blueskewed and redskewed profiles. This parameter is

$$\delta V = \frac{V_{\rm thick} - V_{\rm thin}}{\Delta V_{\rm thin}}, \tag{5.7}$$

where $V_{\rm thick}$ and $V_{\rm thin}$ are the peak velocities of the brightest optically thick peak and the optically thin peak, respectively, and $\Delta V_{\rm thin}$ is the linewidth ($FWHM$) of the optically thin transition. This parameter is given in Table 5.8 along with the peak temperature ratio of the blueshifted and redshifted peaks of the optically thick line. This way we quantify both the peak asymmetry in the optically thick spectrum and the amount by which the brightest peak of the optically thick line is blueshifted or redshifted with respect to the peak of the optically thin line. The peak velocities, linewidths, and respective uncertainties of the optically thin transitions were derived by performing Gaussian fits in CLASS. The velocity of the strongest optically thick peak ($V_{\rm thick}$) was determined by applying Gaussian fits to the spectrum after masking the channels of the weaker peak. We used the rms of the spectrum as the uncertainty of $V_{\rm thick}$, $T_{\rm blue}$ and $T_{\rm red}$. Negative values of δV correspond to blueskewed profiles (infall signature) and positive values to redskewed profiles (opposite signature).

For Cha I, we look for the infall signature in pairs of optically thick/thin isotopologues, as CS 2–1 and C^{34}S 2–1. In the case of a non-detection in C^{34}S 2–1 we use other detected

optically thin transitions. If CS 2–1 is not self-absorbed, we search for the infall signature in other optically thick tracers, as HNC 1–0 and ^{13}CO 2–1. CS 2–1 was detected toward all 20 cores in Cha III, but no spectrum shows a significant self-absorption in this transition. Only 2 cores have detections in C^{34}S 2–1. We therefore use the HNC 1–0 and ^{13}CO 2–1 as optically thick tracers for the infall signature.

A total of 18 cores have a δV parameter greater than the 3σ uncertainty and thus appear to be infalling based on their spectral profiles (Fig. 5.2). All of them have a peak temperature asymmetry deviating from unity within 1σ and 16 of them have an asymmetry $T_{\rm blue}/T_{\rm red} > 1$ within 3σ, excluding Cha1-C9 (Table 5.8). The total number of cores showing the infall signature is therefore 18, or 30 % of the Cha I cores. Their location within the cloud is shown in Fig. 5.5. The optically thick, self-absorbed transitions CS 2–1, HNC 1–0, and ^{13}CO 2–1, and the optically thin transitions, C^{34}S 2–1, HC$_3$N 10–9, C^{18}O 2–1, N$_2$H$^+$ $1_{0,1}$–$0_{1,2}$ (isolated component), and CH$_3$OH 2_0–1_0 A$^+$ form this typical signature for the 18 cores in Cha I (Fig. 5.2). The core Cha1-C27 is optically thin in C^{18}O 2–1. We do not have an estimate of the C^{18}O 2–1 opacity for Cha1-C46 (see Sect. E.1) but the line looks symmetric and peaks in between the blue and red peaks of the ^{13}CO 2–1 spectrum. 83 % of the cores showing the infall signature (15 out of 18; excluding Cha1-C1, C2, and C3) do not appear to be gravitationally bound based on the virial analysis (Sect. 5.3.2.1).

The opposite signature is seen in 7 cores in Cha I (Fig. 5.3). Four of the cores showing the opposite signature have an asymmetric profile in ^{13}CO 2–1. It is likely that this transition is sensitive to the ambient, low-density gas and might not be appropriate to trace motions within the dense core themselves. In this case, the actual number of inverse signature spectra could be reduced to 3 and the number of infall signature spectra to 16.

If the infall and opposite signatures do also trace oscillating motions, then given that we see the opposite signature in $\sim$ 7 cores we would expect the sample of "infalling" cores to be contaminated by $\sim$ 7 oscillating cores, which would reduce the number of infalling cores to $\sim$ 11 in Cha I. It is not straightforward to conclude if pulsations are truly taking place as no source shows both signatures simultaneously in different tracers and we do not have spatial information.

Five cores in Cha III show the classical infall signature (Fig. 5.4). The spectrum of Cha3-C1 in HNC 1–0 is not self-absorbed, but it is clearly skewed to the blue. CH$_3$OH 2_0–1_0 A$^+$ is redshifted with respect to the blue peak of HNC 1–0, thus making Cha3-C1 a probable collapsing core. The asymmetry is more pronounced for the cores Cha3-C9, Cha3-C10, Cha3-C13, and Cha3-C20 with optically thin lines peaking in between the blue and red peaks of the optically thick spectrum. Cha3-C1 is the only core that also appears to be gravitationally bound from our virial analysis (see Sect 5.3.2.1). All cores in Cha III have a significant δV parameter at the 3σ level. The $T_{\rm blue}/T_{\rm red}$ asymmetry is larger than $\sim$ 1.2 in all cases. Three of the contracting cores, however, show the infall signature in ^{13}CO 2–1. If this transition is not a good tracer of core motions, then only two cores are valid infall candidates.

Therefore, taking into account the observed line profiles, the parameter δV, and the ambiguity of the ^{13}CO 2–1 profiles, the number of the infall candidates is: 9 – 18 (with/without oscillations and without/with ^{13}CO 2–1) cores in Cha I and $\sim$ 2 – 5 (without/with ^{13}CO 2–1) in Cha III. The inverse signature is seen toward 3–7 (without/with ^{13}CO 2–1) cores in Cha I. Using these ranges, 15–30 % of the core population in Cha I and 10–25 % of the observed Cha

III sample (or ~ 7–17 % of the overall Cha III starless core population) are infall candidates.

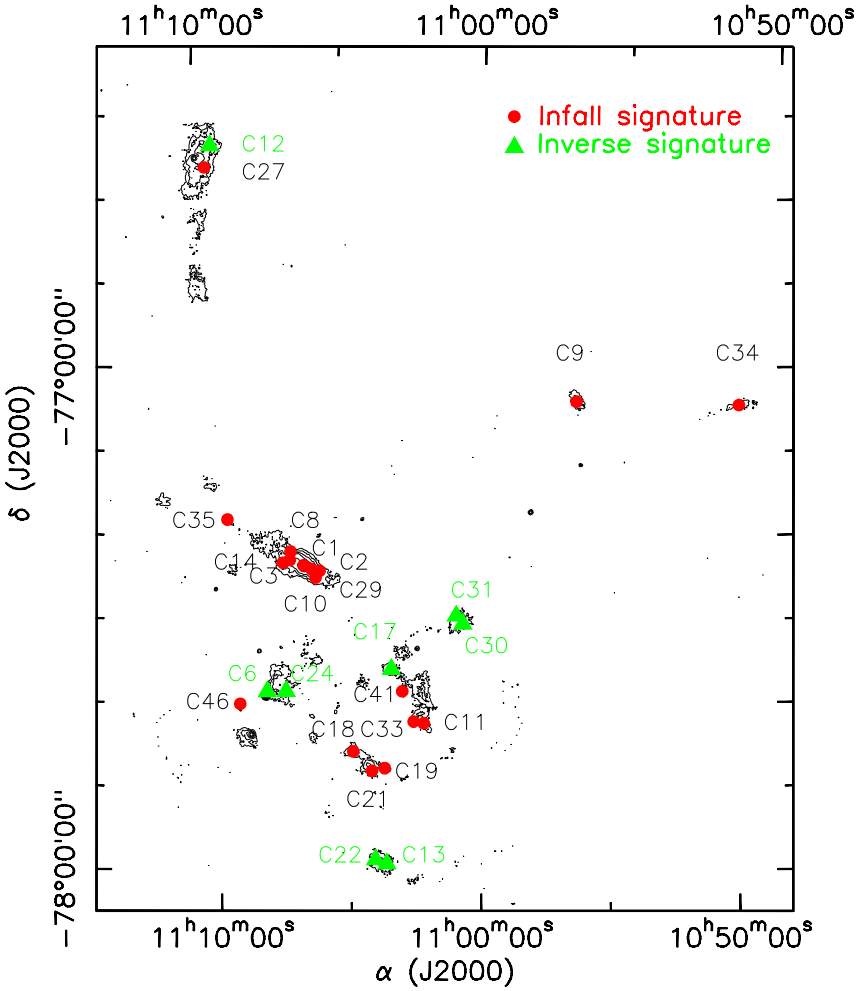

Figure 5.5: The cores showing the infall signature in Cha I (corresponding to Fig. 5.2) are plotted as red filled circles and the cores showing the inverse signature as green triangles. The contours correspond to the 870 μm dust continuum emission obtained with LABOCA (Belloche et al., 2011a) with contour levels of a, 2a, 4a, 8a, 16a, 32a, and a = 48 mJy/21″ beam (4σ).

5.3.4 Centroid velocities

5.3.4.1 Multiple velocity components

Spectra with two emission peaks at different velocities are seen in the transitions $C^{18}O$ 2–1, $C^{17}O$ 2–1, and $C^{34}S$ 2–1 toward some dense structures in the northern and central parts of Cha I (Fig. 5.7). Spectra with two velocity components that are not produced from self-absorption (see Sect. 5.3.1) might arise as projection effects if two physically unconnected regions coincide along the line-of-sight. Alternatively it could be an indication that different

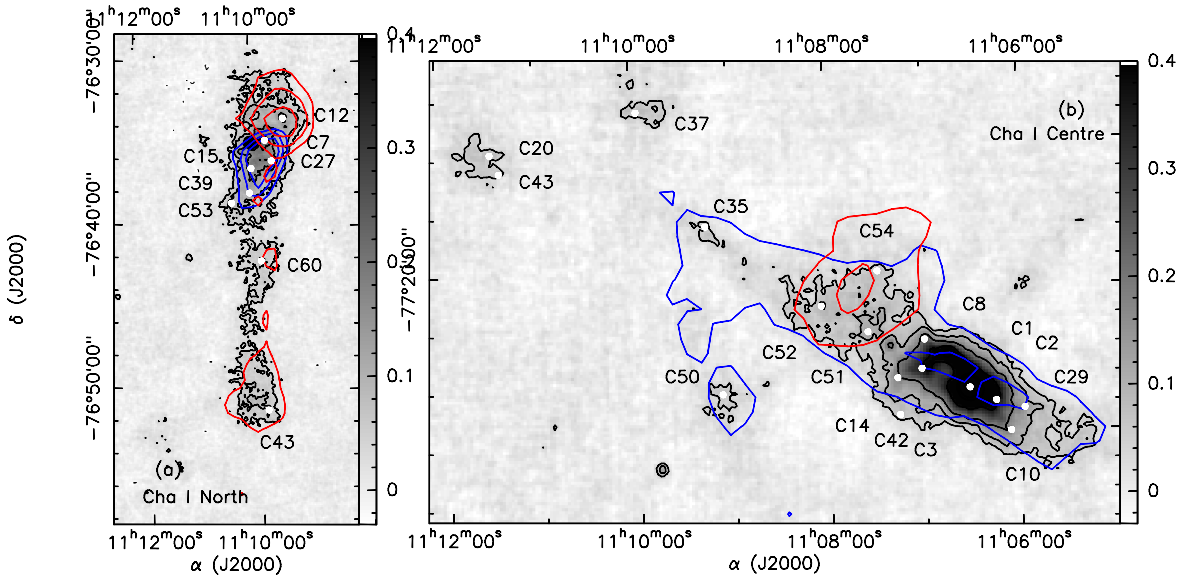

Figure 5.6: $C^{18}O$ 1–0 (Haikala et al., 2005) blueshifted and redshifted emissions in (a) Cha I North, (b) Cha I Centre, and (c) Cha I South overlaid on the 870 μm dust continuum map (Belloche et al., 2011a). The continuum contour levels (black) correspond to a, $2a$, $4a$, $8a$, $16a$, $32a$, with a = 48 mJy/21″-beam (4σ). The blueshifted (subscript b) and redshifted (subscript r) $C^{18}O$ 1–0 contours correspond to the levels (a) $3\sigma_b$ ($3\sigma_r$), $4\sigma_b$ ($4\sigma_r$), $5\sigma_b$ ($5\sigma_r$) with σ_b = 0.17 K km s^{-1} and σ_r = 0.3 K km s^{-1} and (b) $3\sigma_b$ ($3\sigma_r$), $4.5\sigma_b$ ($5\sigma_r$) with σ_b = 0.33 K km s^{-1} and σ_r = 0.22 K km s^{-1}. The velocity ranges for the blueshifted and redshifted integrated intensity emissions are v_b = 3.5 – 4.3 km s^{-1} and v_r = 4.3 – 5.5 km s^{-1} for (a) and v_b = 3.8 – 4.8 km s^{-1} and v_r = 4.8 – 6.0 km s^{-1} for (b). The white dots show the location the cores in each region.

structures in the same region are interacting with one another. We used the $C^{18}O$ 1–0 map of Haikala et al. (2005) alongside our data to better understand the physical origin of these features.

The spectrum of Cha1-C7, located in Cha I North, peaks at the velocities ∼ 4.0 and ∼ 4.8 km s^{-1} in $C^{18}O$ 2–1, $C^{17}O$ 2–1, and CS 2–1 (see Fig. 5.7). The fact that we see the second velocity peak in the optically thin transition $C^{17}O$ 2–1 excludes that it is due to self-absorption. It is located at the northern elongated structure as seen in the 870 μm dust continuum (Fig. 5.6a). Cores Cha1-C12 and Cha1-C15 lie on either side of Cha1-C7 but only have one component each, the former roughly corresponding to the redshifted component of C7 and the latter to the blueshifted one (Fig. 5.7). We produced integrated intensity maps for the velocity ranges corresponding to each $C^{18}O$ 2–1 emission peak using the 1–0 map of Haikala et al. (2005). The intensity contours of both blueshifted and redshifted emissions are overlaid on the 870 μm continuum in Fig. 5.6a. The blueshifted and redshifted integrated intensity emissions peak at different locations on the continuum map. The blueshifted emission seems to follow the peak of the dust continuum emission. The redshifted emission, however, peaks close to the position of Cha1-C12. Both velocity components overlap along the line-of-sight and Cha1-C7 lies in the overlap region which is the reason why its spectra show two velocity components.

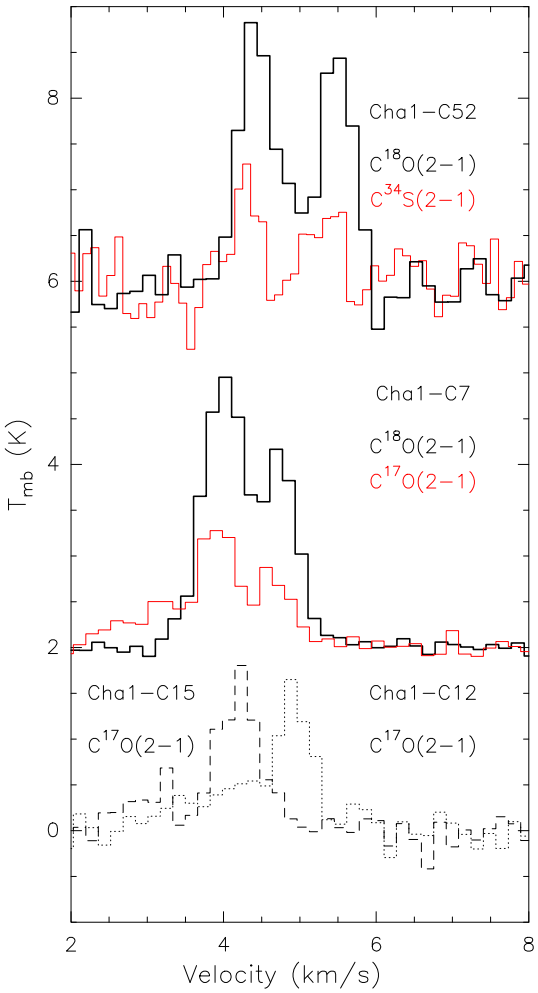

Figure 5.7: Examples of spectra showing two emission peaks at different velocities that are not due to self-absorption. Cha1-C7 and Cha1-C52 have two velocity components in both $C^{18}O$ 2–1 (black thick lines), and in the optically thin $C^{17}O$ 2–1 and $C^{34}S$ 2–1 (red thin lines), respectively. Cha1-C15 (dashed line) and Cha1-C12 (dotted line) are located on either side of Cha1-C7 (see Fig 5.6a). They both have only one emission peak that roughly coincides with *either* the blueshifted or the redshifted peak of Cha1-C7.

A YSO, Cha-MMS2, is located very close to Cha1-C7 and drives a bipolar outflow (see e.g., Bally et al., 2006; Reipurth et al., 1996; Mattila et al., 1989). We examined the possibility that the second, redshifted velocity component that we see in our spectra coincides with the redshifted outflow component. We use our CO 3–2 map of the Cha-MMS2 region (see Sect. 5.2.1) and find that the outflow does not contribute to the redshifted emission in the velocity range $4.5 < v < 5.5$ km s^{-1}.

Two velocity components are seen toward three cores located in (or close to) the central elongated structrure of Cha I Centre: Cha1-C50, C52, and C54. Cha1-C52 and C54 are located at the northern edge of the filament as seen in the dust continuum (Fig. 5.6b) and C50 lies close

to that part of the structure but is not embedded in it. The blueshifted velocity component peaks close to ∼ 4.5 km s^{-1} for all three cores and the redshifted component peaks at ∼ 5.2–5.5 km s^{-1}. The integrated intensity contours of the blueshifted and redshifted C^{18}O 1–0 emissions are shown in Fig. 5.6b overlaid on the dust continuum emission. The blueshifted emission closely follows the dust continuum emission, while the redshifted component is less related to the continuum structure. Its emission seems to trace a direction perpendicular to the filamentary structure traced by the dust continuum and the C^{18}O 1–0 blueshifted emission (see Sect. 5.5.5 for further discussion).

Two sources in Cha III have C^{18}O 2–1 spectra with two emission peaks at different velocities, Cha3-C11 and Cha3-C21, which are located adjacent to each other (see Fig. 3b of Belloche et al., 2011b). The brightest peak of Cha3-C11 is at $v \sim 2$ km s^{-1} and the weakest peak is at $v \sim 1.2$ km s^{-1}. The two emission peaks are also seen at the same velocities in the spectra of ^{13}CO 2–1 and CS 2–1. The C^{18}O 2–1 and ^{13}CO 2–1 spectra of Cha3-C21 peak at ∼ 2 km s^{-1} and ∼ 0.9 km s^{-1}, with the former being the strongest in emission in C^{18}O 2–1 (the opposite is true for ^{13}CO 2–1).

In the spectra that have two emission peaks in either Cha I or Cha III, we select the strongest emission peak as the main velocity component, and the weakest peak as the *second* velocity component. For the cores Cha1-C52 and Cha1-C54 we select the redshifted peak as the second velocity component since we have indication that it is not related to emission arising from the central elongated structure seen in the dust continuum.

5.3.4.2 Core velocity distribution

We follow the analysis in André et al. (2007) to estimate if interactions between cores are likely to be dynamically important for the evolution of Cha I and III. This analysis assumes spherical symmetry, which may not hold very well for the filamentary structure of Cha I and III. We perform the analysis for the whole sample of cores in Cha I and Cha III, and also for the sub-samples of cores in Cha I North, Centre, South, and Cha III North, Centre, and South, separately. We use the average velocity of all cores in each transition for our calculations (Table 5.9).

The global velocity dispersion of the cores in each tracer is given by

$$\sigma_{1D} = \sqrt{\Sigma_{i=1}^{n} \frac{(v_{\mathrm{core},i} - v_{\mathrm{mean}})^2}{N}}, \tag{5.8}$$

where v_{mean} is the average systemic velocity of all cores in one tracer, and v_{core} the systemic velocity of each individual core in the specific tracer. The three-dimensional velocity dispersion is

$$\sigma_{3D} = \sqrt{3} \times \sigma_{1D}. \tag{5.9}$$

We obtain the mean velocity relative to the centre of mass of the system, $v_{\mathrm{rel,COM}}$ using the following relation,

$$v_{\mathrm{rel,COM}} = \sqrt{\frac{8}{\pi}} \times \sigma_{1D}. \tag{5.10}$$

Table 5.9: Average velocity dispersions, crossing time, and collisional time for the Cha I and III cores detected in different tracers.

Transition	D_{cl}[a] (pc)	N$_{fit}$[b]	R_{mean}[c] (AU)	M_{mean}[d] ($M_\odot$)	v_{mean}[e] (km s^{-1})	σ_{1D}[f] (km s^{-1})	σ_{3D}[g] (km s^{-1})	$v_{rel,COM}$[h] (km s^{-1})	$v_{rel,cores}$[i] (km s^{-1})	t_{cross}[j] (Myr)	t_{coll}[k] (Myr)	$\frac{t_{coll}}{t_{cross}}$[l]
					Cha I[m]							
$C^{18}O/C^{17}O$[n]	4.3	60	6462	0.35	4.62	0.34	0.58	0.54	0.77	7.1	203	28.4
CH_3OH 2_0–1_0 A^+	4.3	41	6783	0.42	4.70	0.32	0.56	0.51	0.73	7.5	264	35.0
					Cha I North[p]							
$C^{18}O/C^{17}O$	1.0	7	7761	0.36	4.30	0.28	0.49	0.45	0.63	2.0	17	8.5
CH_3OH 2_0–1_0 A^+	1.0	4	7755	0.39	4.61	0.16	0.27	0.25	0.36	3.6	29	8.2
					Cha I Centre[p]							
$C^{18}O/C^{17}O$	1.0	16	5640	0.52	4.43	0.24	0.42	0.39	0.55	2.3	10	4.5
CH_3OH 2_0–1_0 A^+	1.0	15	5616	0.54	4.50	0.29	0.50	0.46	0.65	2.0	11	5.7
					Cha I South[p]							
$C^{18}O/C^{17}O$	1.4	29	6331	0.26	4.72	0.32	0.55	0.50	0.71	2.5	17	6.7
CH_3OH 2_0–1_0 A^+	1.4	18	6806	0.29	4.85	0.30	0.51	0.47	0.67	2.7	24	8.9
					Cha III[m]							
$C^{18}O$ 2–1	4.9	29	5969	0.25	1.49	0.23	0.39	0.36	0.51	12.2	898	73.8
CH_3OH 2_0–1_0 A^+	4.9	15	6845	0.34	1.41	0.18	0.32	0.29	0.42	15.0	1224	81.6
					Cha III North[p]							
$C^{18}O$ 2–1	0.8	8	6317	0.38	1.36	0.09	0.15	0.14	0.19	5.3	7	1.3
CH_3OH 2_0–1_0 A^+	0.8	6	7276	0.48	1.32	0.09	0.15	0.14	0.20	5.2	7	1.3
					Cha III Centre[p]							
$C^{18}O$ 2–1	1.0	9	5406	0.17	1.53	0.30	0.52	0.48	0.68	1.9	30	15.7
CH_3OH 2_0–1_0 A^+	1.0	4	6911	0.26	1.37	0.18	0.31	0.28	0.40	3.2	44	13.7
					Cha III South[p]							
$C^{18}O$ 2–1	1.5	11	6429	0.23	1.59	0.17	0.29	0.27	0.38	5.0	64	12.7
CH_3OH 2_0–1_0 A^+	1.5	5	6277	0.23	1.56	0.19	0.32	0.30	0.42	4.5	146	32.2

Notes. [a] Approximate diameter of the corresponding region. [b] Number of spectra that were fitted, excluding second velocity components. [c] Mean radius of the cores. [d] Mean total dust mass of the cores. [e] Mean V_{LSR}. [f] 1D velocity dispersion. [g] 3D velocity dispersion. [h] Mean velocity relative to the centre of mass of the system. [i] Mean relative speed between cores. [j] Time needed for a core to cross the region. [k] Ratio of collisional-to-crossing times. [l] Time needed for cores to collide with one another. [m] Results for the whole cloud. [n] Composite $C^{18}O$ and $C^{17}O$ sample. The cores with $C^{17}O$ detections are used instead of their $C^{18}O$ counterparts to minimize optical depth effects. [p] The cores located in Cha I North, Centre, and South are shown in Figs. 5.8 and 5.6, and the cores in Cha III North, Centre, and South are shown in Fig. 5.9.

Finally, the relative speed between cores is computed as

$$v_{\rm rel,cores} = \sqrt{2} \times v_{\rm rel,COM} = \frac{4}{\sqrt{\pi}} \sigma_{\rm 1D}. \tag{5.11}$$

The velocity dispersions are given in Table 5.9 for both Cha I and III as a whole, as well as the sub-regions of Cha I and III.

Figure 5.8 shows the colour-coded (in terms of magnitude) systemic velocities of the cores in Cha I for the molecular tracers $C^{18}O$ 2–1, $C^{17}O$ 2–1, CH_3OH 2_0–1_0 A^+, and N_2H^+ 1–0 overlaid on the 870 μm continuum LABOCA map. The majority of the cores are located in structures that appear to be filamentary in the dust continuum. We define four regions, Cha I North, Centre, South, and West, with the three former containing each at least one of the three distinct elongated structures in Cha I. The sub-region Cha I West does not contain an elongated structure, but rather two small clumps with three cores altogether. Figure 5.9 overlays the systemic velocities that were derived for the Cha III cores in $C^{18}O$ 2–1 and CH_3OH 2_0–1_0 A^+ on the 870 μm map of the cloud. We also define the sub-regions Cha III North, Centre, and South, in which the cores appear more clustered.

We find a mean systemic velocity ($v_{\rm mean}$) of 4.62 ± 0.34 km s^{-1} for the composite $C^{18}O$ and $C^{17}O$ sample in Cha I. The uncertainty is the 1D velocity dispersion. Second velocity components are excluded in this calculation. We believe that the redshifted peak, or second velocity component, is likely not associated with the material in the region we are studying and arises either due to projection effects or due to material interacting with those regions (see Sect. 5.3.4.1). The mean velocities for Cha I North, Centre, and South yield 4.30±0.28 km s^{-1}, 4.43 ± 0.24 km s^{-1}, and 4.72 ± 0.32 km s^{-1} for the composite sample and for the number of cores given by $N_{\rm fit}$ in Table 5.9.

All 29 cores in Cha III were detected ($> 3\sigma$) in $C^{18}O$ 2–1. We only observed $C^{17}O$ 2–1 toward the two cores showing the strongest $C^{18}O$ emission in Cha III, Cha3-C1 and Cha3-C4. Since we estimated opacities of ≤ 1 in these two cores (Sect E.1), we expect lower opacities for cores with weaker $C^{18}O$ emission. We derive a mean velocity of 1.49±0.23 km s^{-1} in $C^{18}O$ 2–1, with the uncertainty being the 1D velocity dispersion. The mean systemic velocities in $C^{18}O$ 2–1 for the sub-regions of Cha III are 1.36 ± 0.09 km s^{-1} (Cha III North), 1.53 ± 0.30 km s^{-1} (Cha III Centre), and 1.59 ± 0.17 km s^{-1} (Cha III South) for the number of cores given by $N_{\rm fit}$ in Table 5.9.

5.3.4.3 Crossing and collisional times

Given the diameter, $D_{\rm cl}$, and radius, $R_{\rm cl}$ of the region over which the cores are distributed, we can estimate the crossing time, $t_{\rm cross}$ of the cores, as well as the ratio of the collisional to crossing times, $\frac{t_{\rm coll}}{t_{\rm cross}}$ (see André et al., 2007):

$$t_{\rm cross} = \frac{D_{\rm cl}}{\sigma_{\rm 3D}}, \tag{5.12}$$

$$\frac{t_{\rm coll}}{t_{\rm cross}} = \frac{1}{2}\sqrt{\frac{\pi}{3}} \times \frac{R_{\rm cl}}{N R_{\rm mean}} \times \frac{1}{1+\Theta}, \tag{5.13}$$

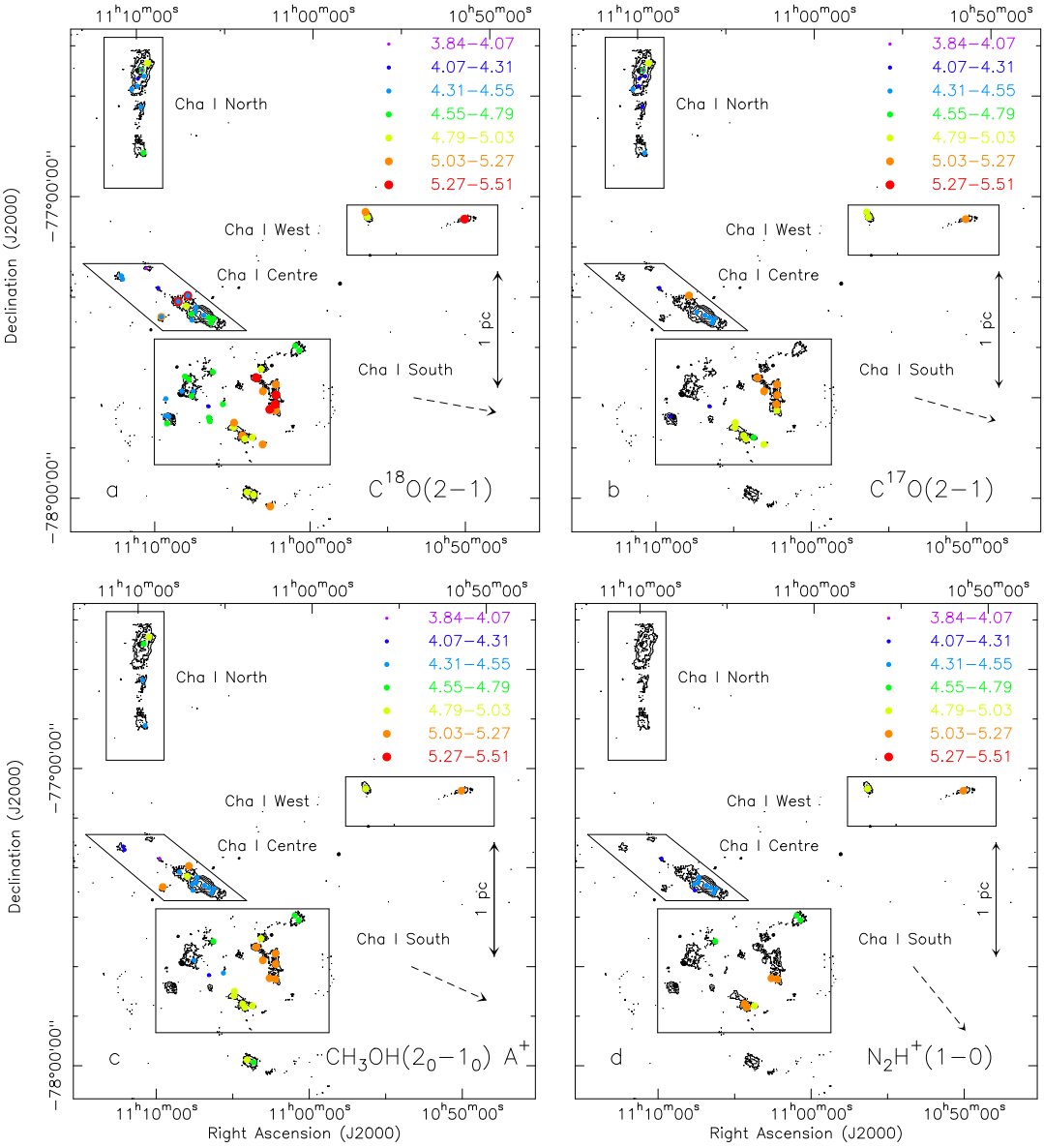

Figure 5.8: Systemic velocities of the cores in Cha I overplotted on the 870 μm map obtained with LABOCA (Belloche et al., 2011a) for the transitions: (a) $C^{18}O$ 2–1, (b) $C^{17}O$ 2–1, (c) CH_3OH 2_0–1_0 A^+, and (d) N_2H^+ 1–0. The contour levels correspond to a, 2a, 4a, 8a, 16a, 32a, with a = 48 mJy/21″ beam (4σ). The core velocities were derived from Gaussian or hyperfine-structure fits to the observed spectra. The filled circles are colour-coded and increase in size to emphasize increasing velocities. Cores with two velocity components are shown with the lower velocity overplotted onto the higher velocity component. The dashed arrow indicates the position angle of the velocity gradient fit.

where

$$1 + \Theta = 1 + \frac{GM_{\rm mean}}{\sigma_{\rm 3D}^2 R_{\rm mean}}. \qquad (5.14)$$

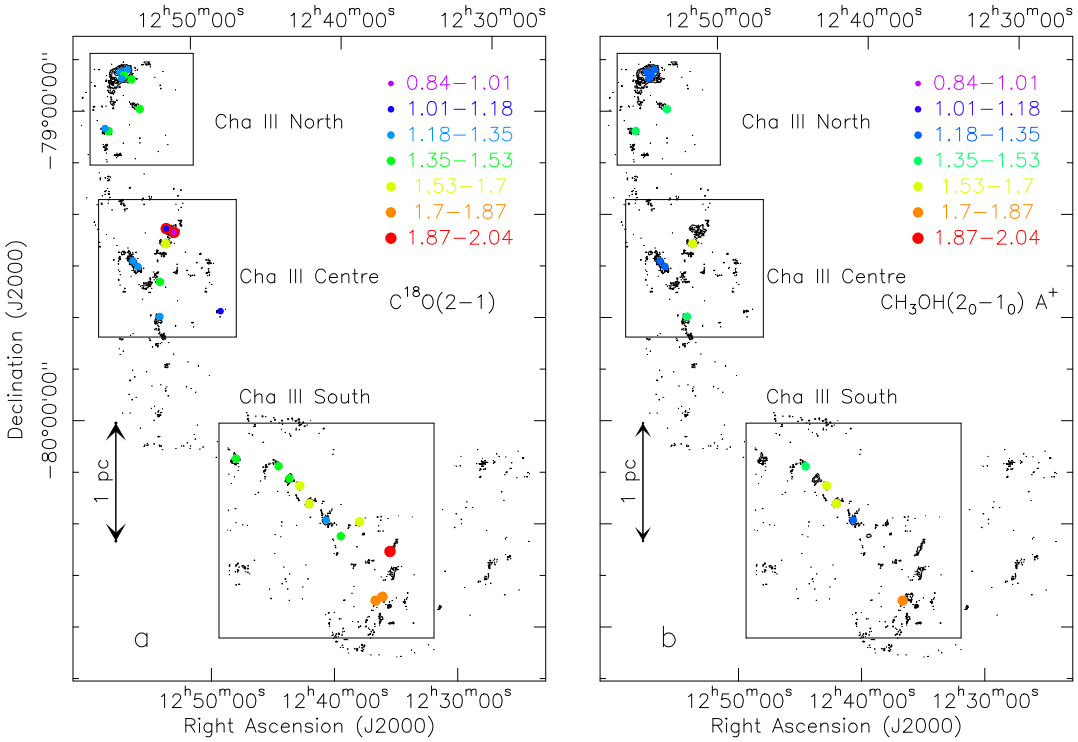

Figure 5.9: Same as Fig 5.8 but for Cha III and the transitions (a) $C^{18}O$ 2–1 and (b) CH_3OH 2_0–1_0 A^+. The contour levels correspond to the 870 μm emission obtained with LABOCA (Belloche et al., 2011b) at a, 2a, 4a, 6a, with a = 34.5 mJy/21″ beam (3σ).

We take as the diameter of each sample the largest projected distance between two sources. The mean mass ($M_{\rm mean}$), mean radius ($R_{\rm mean}$), number of cores (N) used in each tracer and the resulting velocity dispersions and times are given in Table 5.9. We select the $C^{18}O/C^{17}O$ 2–1 composite sample and CH_3OH $2_0 - 1_0$ A^+ for Cha I as they are observed toward many cores, and $C^{18}O$ 2–1 and CH_3OH $2_0 - 1_0$ A^+ for Cha III.

We compute a cloud crossing time $t_{\rm cross}$ ~ 7–7.5 Myr for Cha I as a whole, ~ 2–4 Myr for Cha I North, ~ 2 Myr for Cha I Centre, and ~ 3 Myr for Cha I South. The resulting times for core collisions are ~ 203–264 Myr for the whole Cha I cloud, but they are much lower in its sub-regions. We find collision times of ~ 17–29 Myr for Cha I North, ~ 10–11 Myr for Cha I Centre, and ~ 17–24 for Cha I South. Interactions between cores in Cha I Centre could therefore occur at a higher rate compared to the other regions.

We repeat the same calculations for the cores in Cha III and its sub-regions. The velocity dispersions and timescales for every transition are listed in Table 5.9. We find cloud crossing times of ~ 12 – 15 Myr for the cloud as a whole, and ~ 5 Myr, ~ 2–3 Myr, and ~ 5 Myr for Cha III North, Centre, and South, respectively. The collisional times are of the order ~ 1000 Myr for the whole cloud, and therefore significantly larger than in Cha I. They decrease, however, by a large amount when focussing on the Cha III sub-regions, for which we find ~ 7 Myr (Cha III North), ~ 30–44 Myr (Cha III Centre), and ~ 64–146 Myr (Cha III South). The collisional times therefore become gradually larger as we move from the north to the south.

5.3.4.4 Velocity gradients

Table 5.10: Velocity gradients in Cha I and III.

Transition	D[a] (pc)	N_{fit}[b]	Gradient (km s^{-1} pc^{-1})	$\theta_{\rm Grad}$ (°)
	Chamaeleon I			
$C^{18}O$ 2–1	4.3	65	0.36±0.06	-100
$C^{17}O$ 2–1	4.3	33	0.34±0.08	-106
CH_3OH 2_0–1_0 A^+	4.3	42	0.34±0.07	-114
N_2H^+ 1–0	4.3	19	0.63±0.06	-141
	Chamaeleon III			
$C^{18}O$ 2–1	4.9	29	< 0.24[c]	–
CH_3OH 2_0–1_0 A^+	4.9	15	< 0.28[c]	–

Notes. [a] Projected distance between most distant cores. [b] Number of Gaussian and hyperfine-structure fits used to compute the velocity gradients. [c] Upper limit as three times the uncertainty obtained from Equation 5.16.

To search for velocity gradients in Cha I, we performed a 2D least-square fit on the systemic velocities of the cores detected in each tracer. We perform the fitting with the following 3-parameter function (Goodman et al., 1993):

$$v_{LSR} = v_0 + a\Delta\alpha + b\Delta\beta, \tag{5.15}$$

where v_{LSR}, $\Delta\alpha$, and $\Delta\beta$ are the systemic velocity of the cores, the offset of the cores in right ascension, and the offset in declination (radians). The magnitude of the linear velocity gradient (which assumes solid-body rotation) and its direction (east of north) are given by (Goodman et al., 1993)

$$Grad = \frac{\sqrt{(a^2 + b^2)}}{D}, \tag{5.16}$$

$$\theta_{\rm Grad} = \tan^{-1}\frac{a}{b}, \tag{5.17}$$

where D is the distance of the cloud. The derived velocity gradients and their position angles are given in Table 5.10. The higher velocities of the cores in the south-western part of Cha I (Fig. 5.8) are mostly responsible for the velocity gradient in Cha I. All tracers give consistent results, the significantly higher value derived for N_2H^+ 1–0 being due to its non-detection in Cha I North. We find no significant velocity gradient in Cha III but we list the CH_3OH 2_0–1_0 A^+ and $C^{18}O$ 2–1 upper limits in the same table.

5.4 Results: Molecular abundances

5.4.1 Observed molecular abundances

To calculate the column densities of HC_3N, $C^{34}S$, CH_3OH, $C^{18}O$, and $C^{17}O$ we use the Einstein A-emission coefficients and lower state energies from the LAMDA database[3]. We assume that LTE holds and that the kinetic temperature is $T_k = 10$ K. Integrated intensities from second velocity components are not used to calculate column densities. We have no sign that HC_3N 10–9, $C^{34}S$ 2–1, CH_3OH 2_0–1_0 A^+, CH_3OH 2_1–1_1 E, and $C^{17}O$ 2–1 might be optically thick judging from the symmetric, Gaussian-like spectra (see Sects. E.1 and E.2 for estimates of $C^{17}O$ and $C^{34}S$ opacities). $C^{18}O$ 2–1 is slightly optically thick for some cores in Cha I (Sect. E.1). We do not expect the cores in Cha III to be optically thick in $C^{18}O$ 2–1 as the brightest core, Cha3-C1, is only at the limit of being optically thick. Cha3-C4 is indeed optically thin in $C^{18}O$ 2–1 (see Sect. E.1).

For the cores that have a measured opacity we apply a correction factor to the observed integrated intensity for any opacity greater than 0.2. We apply the correction to the cores for which we derive opacities in $C^{18}O$ 2–1, $C^{17}O$ 2–1, and $C^{34}S$ 2–1 in Sects. E.1 and E.2. The correction factor for the opacity reads

$$c_\tau = \frac{\tau}{1 - \exp(-\tau)} \tag{5.18}$$

where τ is the line's opacity.

We also apply an opacity correction for N_2H^+ 1–0 for the cores that have a *full* line opacity greater than 4. The N_2H^+ 1–0 opacity is derived from the hyperfine-structure fits. The N_2H^+ 1–0 cores that we apply the opacity correction factor c_τ to, are: Cha1-C1 ($\tau = 13.0 \pm 0.1$, with τ the total opacity of the multiplet), Cha1-C2 ($\tau = 4.6 \pm 0.3$), Cha1-C3 ($\tau = 4.7 \pm 0.4$), and Cha1-C4 ($\tau = 4.9 \pm 0.4$). To calculate the opacity correction factor for the isolated N_2H^+ $1_{0,1}$–$0_{1,2}$ component we use the opacity of the full line divided by 9 in Eq. 5.18. For those cores, instead of the total saturated integrated intensity we use the integrated intensity of the N_2H^+ $1_{0,1}$–$0_{1,2}$ isolated component to compute column densities.

The column density of a molecule is computed as

$$N = \frac{8\pi\nu^3}{c^3 g_u A_{ul}} Z(T_k) e^{\frac{E_l}{kT_k}} \frac{1}{1 - e^{\frac{-h\nu}{kT_k}}} \frac{1}{J_\nu(T_k) - J_\nu(T_{bg})} \int J_\nu(T_b)\, dv \tag{5.19}$$

with u and l denoting the upper and lower levels of the transition, ν the transition's frequency and A_{ul} the spontaneous emission coefficient. The values for the partition function for $T_k = 10$ K, $Z(10)$, were interpolated based on the values given in the CDMS catalog. The upper level degeneracies and the ground state energies E_l were also taken from the CDMS catalog. The partition function for CH_3OH was obtained from the JPL database (Pickett et al., 1998). The effective brightness temperature $J_\nu(T_b)$ is defined as

$$J_\nu(T) = \frac{c^2}{2k\nu^2} B_\nu(T), \tag{5.20}$$

[3] http://home.strw.leidenuniv.nl/ moldata/

where $B_\nu(T)$ is the Planck function:

$$B_\nu(T) = \frac{2h\nu^3}{c^2}\frac{1}{exp(\frac{h\nu}{kT}) - 1}. \quad (5.21)$$

We compute the abundances relative to H_2 averaged along the line-of-sight using the dust column densities of the cores from Belloche et al. (2011a,b). We interpolate between the peak dust column density and the column density computed from the flux contained in a $50''$ aperture to derive the dust column density of the cores in each transition within their individual *HPBW* (listed in Tables 5.2, 5.3, and 5.4). We refer to the interpolated dust column density as $N_{\rm inter}$. The average and median abundances relative to H_2, and the abundance dispersion derived from $C^{34}S$ 2–1, CH_3OH 2_0–1_0 A^+, CH_3OH 2_1–1_1 E, N_2H^+ 1–0, HC_3N 10–9, $C^{18}O$ 2–1, and $C^{17}O$ 2–1 are listed in Table 5.11 for both Cha I and III. Figure 5.10 plots the individual core abundances derived for each tracer against their interpolated dust column densities.

$C^{18}O$ and CH_3OH are on average more abundant in Cha I than in Cha III by a factor of $\sim$ 2.4 and 1.8, respectively. This difference in molecular abundances can also be seen in Fig. 5.10. The majority of the aforementioned Cha III molecular abundances lie at the *lower end* of the range of abundances in Cha I.

Benedettini et al. (2012) found that the ratio of HC_3N/N_2H^+ varies between the (prestellar and protostellar) cores in the Lupus 1, 3, and 4 molecular clouds. They conclude that this ratio decreases as a dense core or a protostar evolves, both observationally in their core sample and in their chemical model predictions. The HC_3N/N_2H^+ ratio for the cores in Cha I and III is shown in Fig. 5.11a. Fig. 5.11b overplots the observed HC_3N/N_2H^+ ratio in Cha I on the 870 μm continuum map. Two cores in Cha III have detections in both molecules and fourteen in Cha I. We calculate *lower limits* for one additional core in Cha III (Cha3-C13) and four cores in Cha I (Cha1-C17, C18, C26, C38) that have a HC_3N detection and a N_2H^+ upper limit. The cores located in Cha I South and West have on average a higher HC_3N/N_2H^+ ratio than the ones in Cha I Centre, while the cores in Cha III have values similar to Cha I South (Figs. 5.11a,b).

5.4.2 Depletion

The distributions of the $C^{18}O$, $C^{17}O$, CH_3OH, and $C^{34}S$ abundances suggest that these molecules are affected by depletion in the core interiors in Cha I (Fig. 5.10). The abundances of the aforementioned molecules appear to systematically decrease for cores of higher column density. $C^{17}O$ and $C^{34}S$ in particular show this abundance decrease with a narrower dispersion at each column density compared to $C^{18}O$ and CH_3OH that have a larger spread of abundances. For instance, the abundances of $C^{17}O$ are of the order $\sim$ 5–20$\times10^{-8}$ at a column density of $\sim 5 \times 10^{21}$ cm^{-2} and $\sim$ 2–5$\times10^{-8}$ at a column density of $\sim 15 \times 10^{21}$ cm^{-2}. There is also a hint of HC_3N depletion at higher densities (Fig. 5.10f), but the trend of HC_3N abundance decrease as a function of increasing density is more uncertain in this molecule than in $C^{18}O$, $C^{17}O$, CH_3OH, and $C^{34}S$. The sample of cores in Cha III is not large enough to conclude about depletion within the cores, but the detections and upper limits in HC_3N seem to follow the same behaviour as in Cha I.

Table 5.11: Average and median molecular abundances in Cha I and III.

Line		Cha I			Cha III		
		Abundance[a]	Dispersion[b]	N_{cores}[c]	Abundance[a]	Dispersion[b]	N_{cores}[c]
$C^{18}O$ 2–1[e]	Average[d]	2.6×10^{-7}	1.6×10^{-7}	60	1.1×10^{-7}	3.0×10^{-8}	29
	Median	2.1×10^{-7}			1.1×10^{-7}		
$C^{17}O$ 2–1	Average	6.4×10^{-8}	3.1×10^{-8}	32	2.1×10^{-8}	3.1×10^{-9}	2
	Median	6.4×10^{-8}			2.1×10^{-8}		
CH_3OH 2_0–1_0 A^+	Average	3.6×10^{-9}	2.0×10^{-9}	41	2.0×10^{-9}	7.8×10^{-10}	15
	Median	3.3×10^{-9}			2.2×10^{-9}		
CH_3OH 2_1–1_1 E	Average	2.0×10^{-9}	1.1×10^{-9}	32	2.3×10^{-9}	6.8×10^{-10}	10
	Median	1.8×10^{-9}			2.1×10^{-9}		
N_2H^+ 1–0	Average	2.6×10^{-10}	1.1×10^{-10}	19	6.9×10^{-11}	1.3×10^{-11}	2
	Median	2.2×10^{-10}			6.9×10^{-11}		
$C^{34}S$ 2–1	Average	2.1×10^{-10}	1.2×10^{-10}	23	9.5×10^{-11}	1.00×10^{-11}	2
	Median	2.0×10^{-10}			9.5×10^{-11}		
HC_3N 10–9[f]	Average	5.2×10^{-10}	5.6×10^{-10}	18	3.0×10^{-10}	2.8×10^{-10}	3
	Median	2.7×10^{-10}			1.2×10^{-10}		

Notes. [a] Abundance relative to H_2. [b] Standard deviation of abundance values shown in Fig. 5.10. [c] Number of cores used when calculating the mean and median abundances. [d] Average abundance. [e] $C^{18}O$ 2–1 is slightly optically thick for some cores in Cha I and its abundance should therefore be considered with caution. [f] We have no sign that HC_3N 10–9 might be optically thick judging from the symmetric, Gaussian-like spectra.

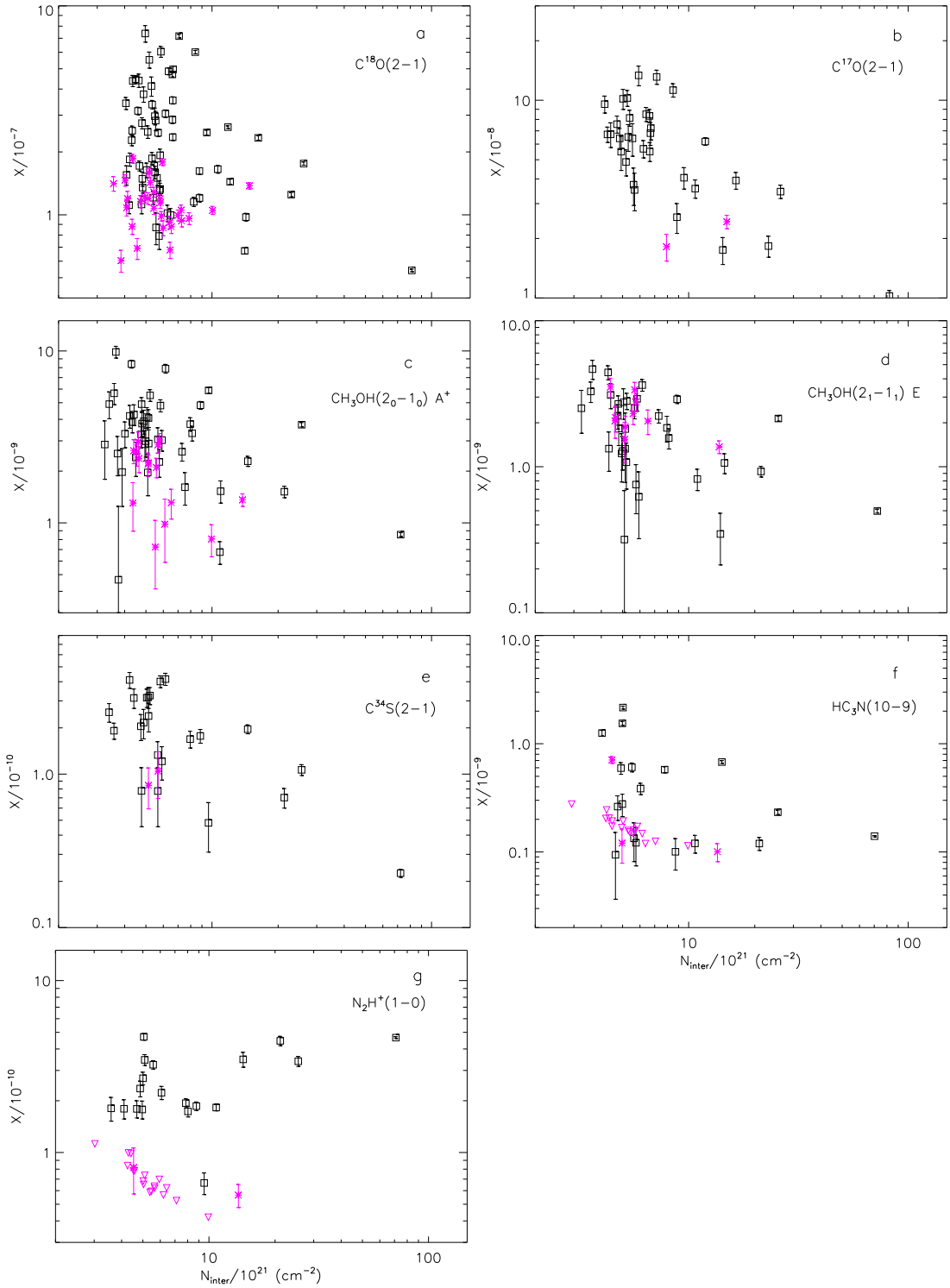

Figure 5.10: Molecular abundances relative to H_2 against dust column densities interpolated within an aperture of diameter equal to the *HPBW* of each transition. The abundances of the Cha I and III cores are shown in black squares and pink asterisks, respectively. Upper limits (3σ uncertainties) are shown as downward triangles for Cha III. The N_2H^+ abundance of the four densest cores in panel (g) was derived from the observed integrated intensity of the isolated component ($1_{0,1}$-$0_{1,2}$) only (see Sect. 5.4.1).

5.4.3 Comparison to predictions of chemical models

New, physically-static models have been run for a selection of gas densities. The models adopt total hydrogen number densities of $n_{\rm H} = 8.5 \times 10^4$, 8.5×10^5, and 8.5×10^6 cm^{-3} corresponding to free-particle densities of 5×10^4, 5×10^5, and 5×10^6 cm^{-3}, assuming a mean molecular weight of 2.37. These densities are comparable to the peak densities of the Cha I and III cores (Cha I; $n_{\rm peak} \sim 3 \times 10^5$– 5×10^6 cm^{-3}, Cha III; $n_{\rm peak} \sim 3 \times 10^5$–$9 \times 10^5$ cm^{-3}). Visual extinctions are sufficient to render unimportant those processes that depend on the external UV radiation field. The chemical model (MAGICKAL) and reaction network are those presented by Garrod (2013), which employ a fully-coupled gas-phase and dust grain-surface chemistry. Due to the low dust temperatures assumed here (8 K), only surface chemistry is considered; chemistry within the bulk ices is switched off. All material except hydrogen begins in atomic/ionic form in the gas phase, as shown in Table 1 of Garrod (2013). A gas temperature of 9 K is assumed. We expect lower-density cores to have slightly higher temperatures (e.g., $\sim$ 10–12 K). Somewhat higher temperatures do not significantly affect the model predictions ($T = 12$ K has been tested). Vasyunina et al. (2012) also present abundance predictions from a static, gas-grain model of constant density and temperature. We use their HC_3N and N_2H^+ abundance predictions from the model with gas temperature of 10 K and free-particle densities of 8.4×10^4 cm^{-3} and 8.4×10^5 cm^{-3} (total H_2 densities of 10^5 and 10^6 cm^{-3}) in order to complement our static model results.

The evolution of the N_2H^+ and HC_3N fractional abundances, and the HC_3N/N_2H^+ abundance ratio for the static models are shown in Fig. 5.12. The two static models show a similar evolution of the HC_3N/N_2H^+ abundance ratio. After an initial peak, the abundance ratio decreases from values of $\sim 10^3$–10^4 down to $\sim 10^{-3}$ (Fig. 5.12i), or from values of $\sim 5 \times 10^2$–5×10^3 to 10^{-4}–10^{-3} (Fig. 5.12j). After it reaches a minimum value it increases once more by a factor of $\sim$ 10 toward the end of the core evolution. The range of observed values of the HC_3N/N_2H^+ abundance ratio ($\sim$ 0.2 – 10) is shown in Fig. 5.12. For model free-particle densities of $\sim 5 \times 10^5$ cm^{-3} and 5×10^6 cm^{-3} in Fig. 5.12i, and 8.4×10^4 cm^{-3} and 8.4×10^5 cm^{-3} in Fig. 5.12j the observed values match the model predictions in a phase during which the HC_3N/N_2H^+ abundance ratio decreases with increasing time. At the lower density of 5×10^4 cm^{-3} the predicted abundance ratio is consistent with the measured values at early times, $< 2 \times 10^3$ yr and at $\sim 10^5$ yr, but the former is excluded based on the predicted abundances of N_2H^+ and HC_3N that are too low (Figs. 5.12a, e).

The static models therefore appear to support the hypothesis that a greater HC_3N/N_2H^+ abundance ratio is associated with early-time chemistry. However, these models include no treatment of the time-dependent condensation of a core, nor account for the chemistry in regions outside of the central density peak. Furthermore, the initial chemical abundances correspond to diffuse, atomic conditions that are not appropriate to the higher densities observed in the cores. Since the early formation of HC_3N appears to be dependent on the availability of atomic carbon, which is not fully locked up in CO at early times, the consideration of static models alone is not sufficient to support the interpretation of the observed trend.

To remedy these shortcomings, comparison is made with chemical models of cloud cores investigated by Garrod et al. (2005) and later publications. These models trace the chemical evolution at 12 depth points arranged along a radius through a cloud core, as it condenses from

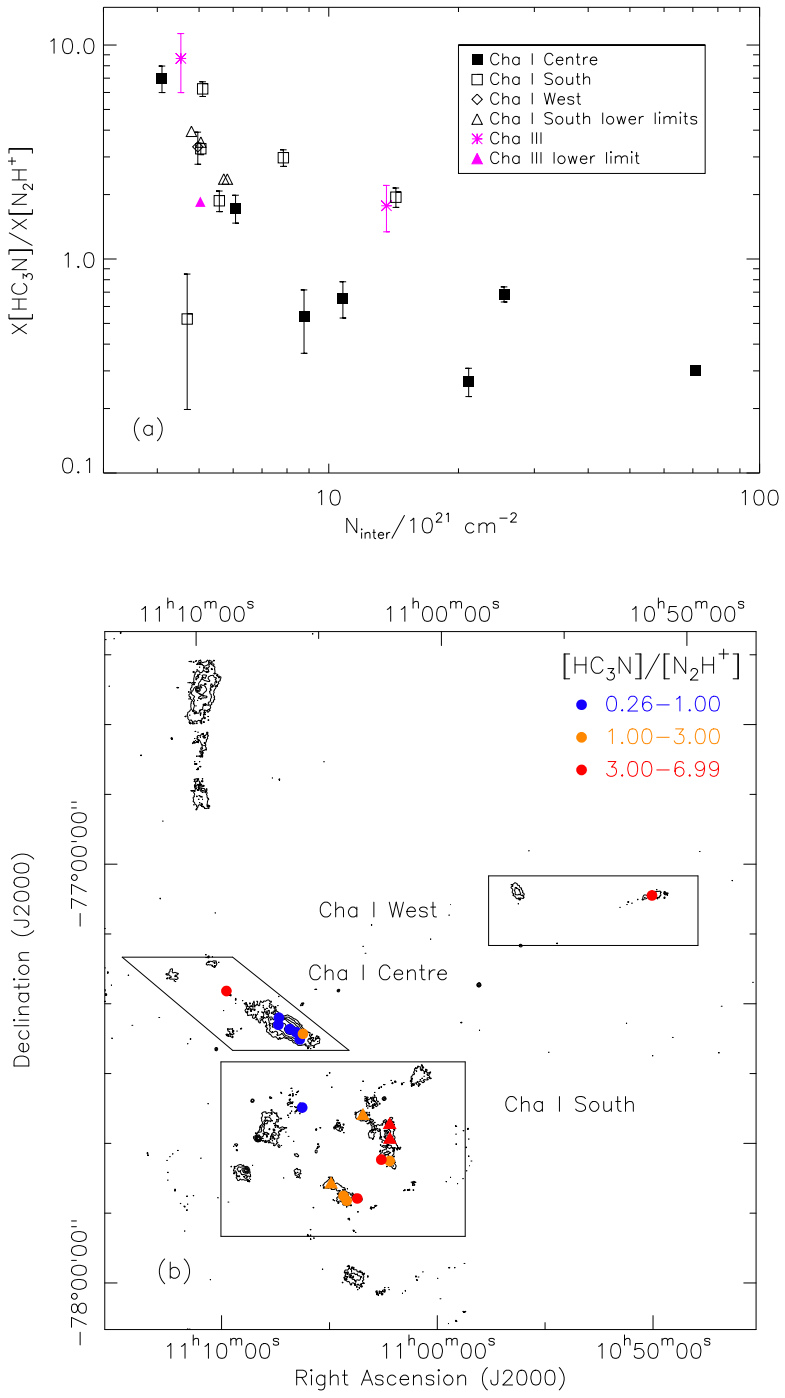

Figure 5.11: (a) Observed HC_3N/N_2H^+ abundance ratio as a function of H_2 column density for the cores in Cha I Centre (filled squares), Cha I South (empty squares), Cha I West (diamond), Cha I South lower limits (empty triangles), Cha III (asterisks), and Cha III lower limits (filled triangle). (b) Observed HC_3N/N_2H^+ abundance ratios for Cha I (circles) and lower limits (triangles) overplotted on the 870 μm dust continuum emission obtained with LABOCA (Belloche et al., 2011a). The contour levels correspond to a, 2a, 4a, 8a, 16a, 32a, with a = 48 mJy/21″ beam (4σ).

diffuse to dense conditions over a period of 1 Myr. The core then disperses back to the initial physical profile over the same time period. Initial total hydrogen densities follow a Gaussian profile; values range from 300 to 1000 cm^{-3} between the outermost point and the central core position, with visual extinctions ranging from 0.65 to 1.7 mag. This profile is held steady for an arbitrary period of time until a chemical steady-state is achieved (no freeze-out onto dust grains is active during this time). This produces an initial chemical composition that is appropriate to the physical conditions.

During the main period of physical evolution of the core, the initial density profile follows a Gaussian time-dependence. This process is described in detail by Garrod et al. (2005). A total hydrogen peak central density of 5×10^4 cm^{-3} and visual extinction of 5 mag are achieved after 1 Myr. The densities and visual extinctions at each modeled depth point vary with time. As points achieve visual extinctions greater than 2.5 mag, the freeze-out of gas-phase material begins. No surface chemistry is explicitly modeled in this treatment; accreted atoms are assumed to be fully hydrogenated, and remain on the grain surfaces (until the visual extinction again falls below the threshold value of 2.5 mag). The central visual extinction achieved in this model of 5 mag corresponds to an edge-to-edge value of 10 mag (for comparison with observations).

These models allow column densities to be calculated along lines of sight passing through each depth point. Values calculated in this way take account of both the chemical abundances and gas densities specific to each point. Figures in Garrod et al. (2006a,b) show column densities calculated in this way, as a function of time during the physical evolution of the core. Species that are strongly dependent on carbon for their formation are found to peak prior to the attainment of maximum core density, while other species, such as N_2H^+, are found to trace the density more closely. Figures 5.12c, g show values for HC_3N and N_2H^+, normalized to the total H_2 column density, to provide a comparison with the single-point fractional-abundance results. The ratio of these values shown in the bottom panel (Fig. 5.12k) confirms the single-point, static-model trend.

A similar model is also presented (previously unpublished) that adopts the same density profile and peak central density, except that a greater radial extent is assumed for the core, so that the peak, central visual extinction achieved in the model is 10 mag, corresponding to an edge-to-edge value of 20 mag. The initial central value is $\sim$ 3.1 mag.

This model also shows the same trend in the HC_3N/N_2H^+ abundance ratio, although extended to a somewhat later time. The growth in each abundance appears at the same point in this model, but the values are higher over a broader period of time. The plots shown here extend beyond the peak density and into the regime where the core has begun to disperse, although the fall in density and visual extinction is slow to begin with.

The maximum H_2 column densities for the collapse models with final edge-to-edge visual extinctions A_V 10 and 20 mag are achieved at 1 Myr and they are 6.2×10^{21} cm^{-2} and 1.3×10^{22} cm^{-2}, respectively. The observed H_2 column densities for the Mopra beam of $37''$ (for N_2H^+ 1–0) are found after interpolating between the peak H_2 column density (for *HPBW* $21.2''$, $\sim$ 3200 AU) and the column density within an aperture of $50''$. They are 3.3×10^{21}–1.4×10^{22} cm^{-2} for the cores in Cha III and 3.6×10^{21}–7.1×10^{22} cm^{-2} in Cha I (or 3.6×10^{21}–1.4×10^{22} cm^{-2} excluding the 3 densest cores) (Belloche et al., 2011a,b). The *HPBW* of HC_3N 10–9 is similar to N_2H^+ 1–0 ($37.9''$). The observed H_2 column densities averaged

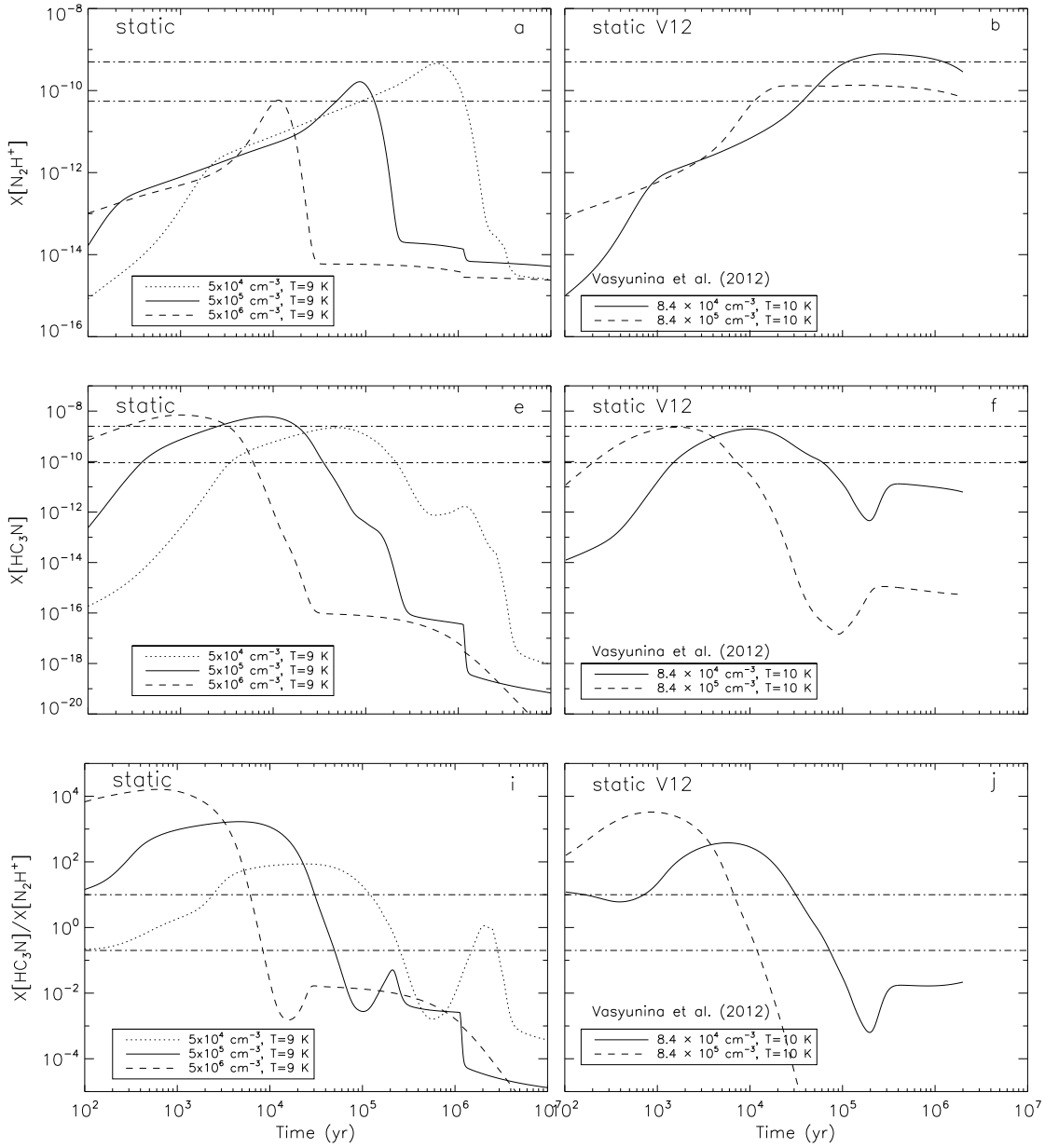

Figure 5.12: Continued.

over the Mopra beam are therefore comparable to the model values. The visual extinctions derived from 2MASS range from 5.1–19 mag for the Cha I cores with an average extinction of $\sim$ 10 mag, and $\sim$ 2–9 mag for the Cha III cores, with an average of $\sim$ 5 mag (Belloche et al., 2011a,b). The cores in Cha III and the low A_V cores in Cha I are therefore expected to be better described by the collapse model with a final edge-to-edge extinction of 10 mag, while the model with the final A_V of 20 mag is better suited for the Cha I cores with visual extinctions higher than 10 mag. Both collapse models reach total hydrogen ($n_{\rm H}$ + 2$n_{\rm H2}$) peak

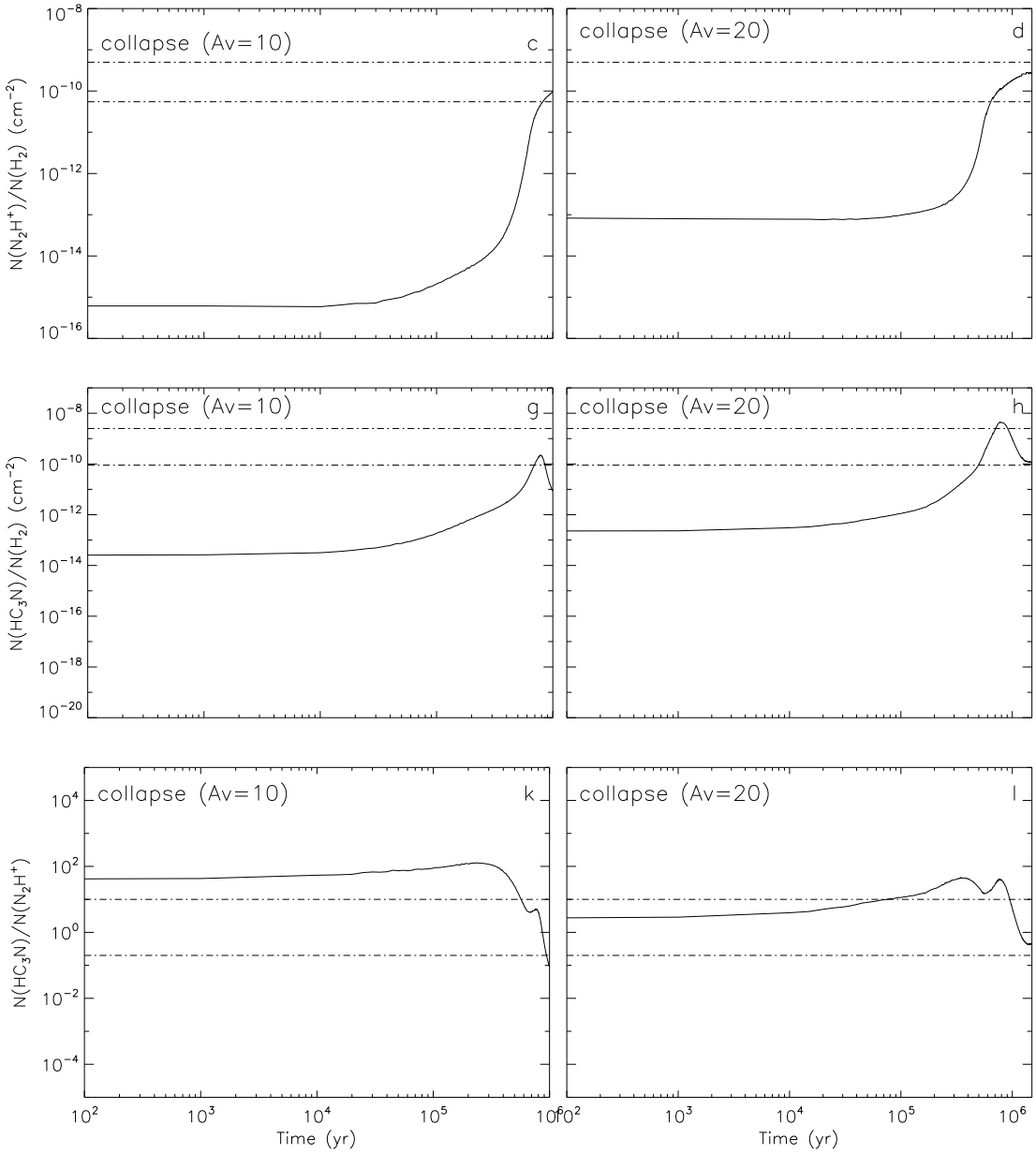

Figure 5.12: Evolution of the N_2H^+ (a, b, c, d) and HC_3N (e, f, g, h) abundances, and the HC_3N to N_2H^+ abundance ratio (i, j, k, and l) as a function of time for free-particle densities of 5×10^4 cm^{-3} (dotted), 5×10^5 cm^{-3} (solid), and 5×10^6 cm^{-3} (dashed line) and a kinetic temperature of 9 K. The model predictions from Vasyunina et al. (2012) (V12, panels b, f, j) are shown for free-particle densities of 8.4×10^4 cm^{-3} (solid) and 8.4×10^5 cm^{-3} 10^5 cm^{-3} (dashed line) and $T = 10$ K. Each column shows predictions from one specific model ('static', 'static V12', 'collapse (Av=10)', 'collapse (Av=20)'). Panels (a), (b), (e), (f), (i), and (j) correspond to predictions of *static* models, while panels (c), (d), (g), (h), (k), and (l) show predictions from *collapse* models. The horizontal dotted-dashed lines indicate the *range* of observed values for the N_2H^+ (top row), HC_3N abundances (middle row), and the HC_3N to N_2H^+ ratio (bottom row). The maximum H_2 column densities for the collapse models with final visual extinctions Av 10 and 20 mag are achieved at 1 Myr and they are 6.2×10^{21} cm^{-2} and 1.3×10^{22} cm^{-2}, respectively.

central densities of 5×10^4 cm^{-3}, with equivalent free-particle densities of $\sim 3 \times 10^4$ cm^{-3}. The observed free-particle densities (for an $HPBW = 37''$) are $\sim 5 \times 10^4$–2.2×10^5 cm^{-3} for the cores in Cha I (excluding the 3 densest cores) and $\sim 3.8 \times 10^4$–2.0×10^5 cm^{-3} for the Cha III cores. This difference in density is small enough that it is unlikely to affect the quantitative results.

While the hypothesized cause of the trend in the downward HC_3N/N_2H^+ abundance ratio appears to agree with the models, i.e. that a lower ratio is indicative of a greater degree of physical evolution, it is unlikely that a more specific determination of core age may be made without a more specific model for individual cores in the cloud.

By interpreting the HC_3N/N_2H^+ abundance ratio as an evolutionary indicator we deduce from Fig. 5.11 that the cores in Cha I Centre are more evolved than the cores in Cha I South and West. The densest and most evolved core in Cha I, Cha1-C1 (Cha-MMS1; first hydrostatic core candidate) is also located in Cha I centre and has an HC_3N/N_2H^+ ratio of ~ 0.3. The cores in Cha I South and West may therefore follow the same evolutionary path as the ones in Cha I Centre given that they belong to the same cloud. Likewise, the cores in Cha III might evolve in a similar manner owing to the similar abundance ratios and densities with the cores in Cha I South and West. It is interesting to note that all the cores in Cha I Centre show infall motions with cores showing the inverse signature mainly being distributed in Cha I South (Fig. 5.5).

5.4.4 Comparison to other clouds

Starting with the low-density tracers (in terms of critical density), the mean abundances of $C^{18}O$ and $C^{17}O$ 2–1 in Cha I relative to H_2 are $\sim 2.6 \times 10^{-7}$ and $\sim 6.4 \times 10^{-8}$, respectively. We derive lower abundances in Cha III by a factor of ~ 2.4 and ~ 3, respectively. Frerking et al. (1982) estimated a $C^{18}O$ abundance of 1.7×10^{-7} within cloud interiors in ρ Ophiuchus and Taurus. Miettinen et al. (2011) derived $C^{17}O$ abundances ranging from 4×10^{-8} to 1.6×10^{-7} toward seven clumps in massive infrared dark clouds (IRCDs). Friberg et al. (1988) observed methanol toward three dark clouds. They found CH_3OH abundances of $\sim 2 \times 10^{-9}$ for TMC1 and L134N, and $\sim 0.5 - 1 \times 10^{-9}$ for the Class 0 object B335 and for a kinetic temperature of 10 K. The observed $C^{18}O$, $C^{17}O$, and CH_3OH abundances toward the aforementioned clouds are all very similar to the mean abundances we derive for both Cha I and Cha III (see Table 5.11).

We now discuss the abundances of the high-density tracers. Vasyunina et al. (2011) report an average N_2H^+ abundance of 7.7×10^{-10} for a sample of low-mass IRDCs. The average N_2H^+ abundances we derive are *lower* by a factor of ~ 3 in Cha I and ~ 11 in Cha III. The low-mass IRDC abundance average for HC_3N is $\sim 1.5 \times 10^{-9}$ (Vasyunina et al., 2011), which is higher than the mean abundance we find in Cha I and III by a factor of ~ 3 and ~ 5, respectively. Molecular abundances of $\sim 5.8 - 17 \times 10^{-11}$ were found for $C^{34}S$ in the IC5146 dark cloud (Bergin et al., 2001). Our reported $C^{34}S$ abundances in Cha I and III are similar to the high-end value. We therefore see a significant abundance difference between Cha I, III and other low-mass dark clouds only in N_2H^+ and HC_3N. These molecules are both *less* abundant in Cha I and III than in other low-mass clouds.

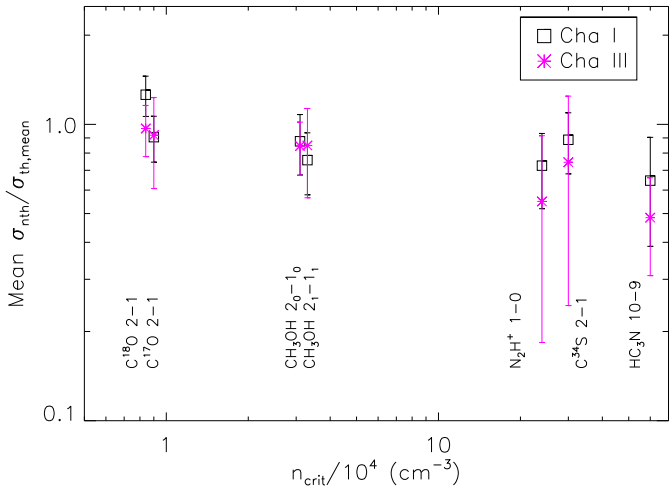

Figure 5.13: Mean ratio of non-thermal to thermal (of the mean particle) velocity dispersions against the critical density for the transitions listed in Table 5.12 for the Cha I (black squares) and III (pink asterisks) clouds. The errorbars show the dispersions from the mean.

5.5 Discussion

5.5.1 Turbulence in Cha I and III

In order to directly compare the linewidths and non-thermal velocity dispersions of the transitions detected in both clouds, we choose to only compare core samples of similar peak column densities. This way we compare cores of similar physical properties. For this reason we exclude the cores Cha1-C1, Cha1-C2, and Cha1-C3, whose observed peak column densities are higher by a factor of 1.5–6 than the maximum peak column densities in Cha III. We also *omit* the second velocity components (see definition in Sect. 5.3.1) for this calculation. We assume the *same kinetic temperature* of 10 K for both clouds, which is plausible since both clouds have similar dust temperatures (see Tóth et al., 2000) and mean densities (Belloche et al., 2011a,b).

A direct comparison of the non-thermal to thermal velocity dispersion ratios of the transitions $C^{34}S$ 2–1, CH_3OH 2_0–1_0 A^+, CH_3OH 2_1–1_1 E, N_2H^+ 1–0, $C^{18}O$ 2–1, $C^{17}O$ 2–1, and HC_3N 10–9 shows that they are similar in both clouds (see Table 5.12 and Fig. 5.13). This ratio is larger in $C^{18}O$ 2–1 in Cha I, but as the line is affected by optical depth effects (see Sect. E.1) the difference between the two clouds is most likely not significant. Hence, there is no significant difference in the turbulence level within Cha I and III that could account for the difference in their star formation activities.

5.5.1.1 Turbulence dissipation

N_2H^+ 1–0 and HC_3N 10–9 are both high-density tracers with critical densities of $\sim 2.4 \times 10^5$ cm^{-3} and $\sim 6.0 \times 10^5$ cm^{-3}, respectively (Table D.1). Both transitions have non-thermal

Table 5.12: Linewidths and non-thermal velocity dispersions in Cha I and III.

Line	Cha I[a]					Cha III				
	$FWHM$[b] average (km s^{-1})	$FWHM$[c] median (km s^{-1})	$[\frac{\sigma_{\rm nth}}{\sigma_{\rm th,mean}}]$[d] average	$[\frac{\sigma_{\rm nth}}{\sigma_{\rm th,mean}}]$[e] median	N[f]	$FWHM$ average (km s^{-1})	$FWHM$ median (km s^{-1})	$[\frac{\sigma_{\rm nth}}{\sigma_{\rm th,mean}}]$ average	$[\frac{\sigma_{\rm nth}}{\sigma_{\rm th,mean}}]$ median	N
$C^{18}O$ 2–1[g]	0.57±0.07	0.52	1.26±0.07	1.15	57	0.45±0.03	0.44	0.97±0.06	0.96	29
$C^{17}O$ 2–1[h]	0.42±0.06	0.40	0.91±0.05	0.86	29	0.42±0.04	0.42	0.92±0.10	0.92	2
CH_3OH 2_1–1_1 E	0.36±0.06	0.36	0.76±0.06	0.74	28	0.39±0.04	0.40	0.85±0.09	0.86	10
CH_3OH 2_0–1_0 A^+	0.41±0.06	0.36	0.88±0.07	0.77	38	0.39±0.02	0.40	0.85±0.06	0.87	15
N_2H^+ 1–0[h]	0.35±0.07	0.32	0.73±0.07	0.64	16	0.27±0.05	0.27	0.55±0.12	0.55	2
$C^{34}S$ 2–1	0.40±0.07	0.37	0.89±0.07	0.81	20	0.34±0.07	0.34	0.74±0.17	0.74	2
HC_3N 10–9[h]	0.30±0.06	0.27	0.65±0.09	0.55	15	0.23±0.02	0.23	0.48±0.06	0.48	3

Notes. [(a)] Average values exclude cores Cha1-C1, C2, and C3 as we only compare cores with the same range of peak column densities in both clouds. The errors are dispersions from the mean value. [(b)] Average $FWHM$ linewidths over all cores in each transition. [(c)] Median $FWHM$ linewidth in each transition. [(d)] Average ratio of the non-thermal-to-mean-thermal velocity dispersions for the core sample in each transition. [(e)] Median non-thermal-to-mean-thermal velocity dispersion ratio. [(f)] Number of cores used for the calculation. [(g)] A fraction of the $C^{18}O$ 2–1 spectra in Cha I are marginally optically thick and may therefore be slightly broadened (see Sect. E.1). [(h)] Intrinsic linewidths ($FWHM$) derived from a seven-component hyperfine-structure fit.

velocity dispersions comparable to each other in both Cha I and III (Sect. 5.3.2.2). This is expected if they both trace regions of similar density. The non-thermal velocity dispersions of these transitions are also found to be systematically smaller than the non-thermal dispersions of $C^{17}O$ 2–1 and $C^{18}O$ 2–1 in both Cha I and III.

$C^{17}O$ 2–1 and $C^{18}O$ 2–1 are excited at densities above $\sim 9 \times 10^3$ cm^{-3}, assuming they have a high enough abundance in these regions. They are therefore low-density tracers and in addition, they are usually depleted in the cold starless core interiors. High-density transitions, as N_2H^+ 1–0 and HC_3N 10–9, are expected to trace core interiors. The dense, inner parts of the cores are expected to be regions of minimum turbulence in contrast to the less dense, outer parts of the cores, which are less shielded from the ambient turbulent motions (Goodman et al., 1998; Larson, 1981). The low-density transitions likely trace these outer, and more turbulent core regions. The larger non-thermal dispersions that we find in $C^{17}O$ 2–1 and $C^{18}O$ 2–1 compared to HC_3N and N_2H^+ in both clouds are consistent with the picture of turbulence dissipation in the core interiors in Cha I and III. CH_3OH 2_0–1_0 A^+ has a similar critical density to $C^{17}O$, $C^{18}O$, within a factor of ~ 3, as well as a similar abundance distribution (see Fig. 5.10). Indeed, we also find that CH_3OH 2_0–1_0 A^+, $C^{17}O$ and $C^{18}O$ have similar non-thermal velocity dispersions in both Cha I and III, therefore indicating that these transitions likely trace similar regions.

We obtain a N_2H^+ 1–0 to $C^{34}S$ 2–1 mean non-thermal velocity dispersion ratio of $0.75^{+0.18}_{-0.19}$ in Cha I. $C^{34}S$ 2–1 is excited at densities similar to N_2H^+ 1–0 and those two transitions would therefore be expected to have similar non-thermal velocity dispersions if they both have similar abundance profiles. The higher $C^{34}S$ 2–1 non-thermal dispersions is a sign of $C^{34}S$ depletion in the core interiors, making this molecule sensitive to the outer, more turbulent core regions. Indeed, we also find evidence of $C^{34}S$ depletion in the distribution of core abundances in Cha I as a function of their column density (Fig. 5.10e). The fact that $C^{34}S$ 2–1 and $C^{17}O$ 2–1 have a mean non-thermal dispersion ratio close to unity, is an additional hint that $C^{34}S$ 2–1 traces similar lower-density regions as $C^{17}O$ 2–1 and that N_2H^+ 1–0 and HC_3N 10–9 trace the quiescent inner core regions.

5.5.2 Core interactions in Cha I and III

The free-fall time for spherically symmetric gravitational collapse is given by,

$$t_{\rm ff} = \sqrt{\frac{3\pi}{32 G \rho_{\rm mean}}}, \tag{5.22}$$

where $\rho_{\rm mean}$ is the mean mass density of the cores. We estimate the core densities as $\rho = n_{\rm mean} \times \mu m_{\rm H}$, with $n_{\rm mean}$ taken from Belloche et al. (2011b) for Cha III, and computed using the total mass and a radius of $\sqrt{FWHM_{\rm maj} \times FWHM_{\rm min}}$ for the cores in Cha I (total mass and radius from Belloche et al., 2011a). We use a mean molecular weight of $\mu \sim 2.37$. We find *average* free-fall times of 0.18 Myr for both Cha I and III.

The expected lifetimes and evolution of dense cores largely depend on the theoretical model used to describe the gravitational collapse of the cloud (see Ward-Thompson et al., 2007, for a review on core lifetimes). Collapse models governed by ambipolar diffusion tend to predict core lifetimes longer than the free-fall time, which increases the more the initial core

conditions depart from the magnetically supercritical state (Shu et al., 1987; Mouschovias, 1991; Myers & Khersonsky, 1995). The collapse proceeds faster when the core is initially nearly supercritical (e.g., Nakano, 1998) and if turbulence is dynamically important (Ciolek & Basu, 2001; Fatuzzo & Adams, 2002; Vázquez-Semadeni et al., 2005). In models of initially magnetically subcritical, turbulent clouds the dense cores produced have lifetimes that range from $\sim$ 1.5 to $\sim$ 10 times the free-fall time (e.g., Nakamura & Li, 2005). Models of magnetically supercritical, turbulent cloud collapse also predict core lifetimes of the order of a few times the free-fall time (Galván-Madrid et al., 2007; Vázquez-Semadeni et al., 2005) compared to the turbulence dominated star formation scenario that supports faster evolution timescales of the order of one free-fall time (Elmegreen, 2000; Ward-Thompson et al., 2007; Kirk et al., 2005; Ballesteros-Paredes et al., 1999; Vazquez-Semadeni et al., 2000; Mac Low & Klessen, 2004b; Ballesteros-Paredes & Hartmann, 2007). Galván-Madrid et al. (2007) find mean core lifetimes of the order of $\sim 6t_{\rm ff}$ in their numerical simulations of magnetically supercritical, turbulent, and isothermal clouds.

Observationally, there are various estimates of the core lifetimes, some of which are: $\sim$0.5 Myr (Evans et al., 2009), $\sim$0.3–1.6 Myr (Lee & Myers, 1999), $\sim$0.4 Myr (Onishi et al., 1998, 2002), $\sim$0.3 Myr (Kirk et al., 2005). Ward-Thompson et al. (2007) conclude that most observational estimates yield core lifetimes of $\sim$2–5 free-fall times for densities of $\sim 10^4$–10^5 cm^{-3}.

If we assume core lifetimes of the order of 3–6 times the free-fall time as suggested by both the observational evidence (e.g., Ward-Thompson et al., 2007) and collapse models (e.g., Galván-Madrid et al., 2007), we obtain a dynamical lifetime of $\sim$ 0.5–1 Myr for Cha I and III. A direct comparison of these lifetime estimates to the collisional times we obtained in Table 5.9 for both Cha I and III as a whole and their sub-regions shows that the collisional times we obtain are much larger than the dynamical lifetimes. Cha I Centre has the lowest collisional time in Cha I Centre ($\sim$ 10 Myr) and in Cha III we obtain the lowest collisional time in Cha III North, with $t_{\rm coll} \sim 7$ Myr. These values are still higher by a factor of $\sim$ 10–20 and $\sim$ 7–14, respectively, than the average core lifetimes of $\sim$ 0.5–1 Myr in Cha I and III. As Cha I and III as a whole are quite filamentary these estimates are likely to deviate from the true values. Nevertheless, the collision time estimate within each substructure of Cha I and III offers us a better insight into the dynamical interactions between the neighbouring cores rather than taking the whole clouds into account.

André et al. (2007) estimated a collision time of $\sim 1-10$ Myr between the 57 starless cores in Ophiuchus and a dynamical core lifetime of $\sim 0.02-0.5$ Myr (assuming $3\times t_{\rm ff}$ and using the mean core density). André et al. (2007) concluded that interactions between the condensations in Ophiuchus cannot happen within their lifetimes. Sadavoy et al. (2012) studied nine dense cores in Perseus B1-E and found that the cores have near-neighbour separations less than one Jeans length and interactions might occur on a timescale of $\sim$ 1 Myr, which makes competitive accretion plausible for that region.

We conclude that, as is the case for Ophiuchus, dynamical interactions between cores are unlikely to be dynamically significant in either Cha I, Cha III, or their sub-regions, and competitive accretion will therefore probably not affect the future dynamical state of the Cha I and Cha III cores.

5.5.3 Dynamical state of starless cores

Our virial equilibrium analysis suggests that up to five cores are gravitationally bound in Cha I (Cha1-C1, Cha1-C2, Cha1-C3, Cha1-C4, Cha1-C5) and only one is virialized (Cha1-C1 or 'Cha-MMS1'). Cha1-C1 is virialized in most detected transitions (see Table 5.6). Therefore, a total of five cores, or ∼ 8 % of the whole sample, show evidence of *already* being gravitationally bound in Cha I.

Nevertheless, we found that 15 % – 30 % of the total core population are either already prestellar or likely to become gravitationally bound and therefore prestellar in the future based on the infall signature (see Sect. 5.3.3). The upper limit corresponds to the full sample of cores showing the infall signature, while the lower limit reflects a more conservative number after considering the number of infall signatures that might not be indicating pure infall motions within the core. Anathpindika & Francesco (2013) also stress that inward motions are not a sufficient criterion for gravitational boundedness. Belloche et al. (2011a) found that ∼ 17 % of the starless cores are *currently* prestellar based on their Bonnor-Ebert analysis and Belloche et al. (2011b) estimated that up to ∼ 50 % might become unstable in the future based on theoretical predictions. We therefore find that the fraction of the cores that might become prestellar based on *observational evidence* and the infall signature (∼ 15–30 %) is in agreement with the ∼ 50 % upper limit of Belloche et al. (2011b).

The estimated fraction of prestellar cores in Aquila amounts to ∼ 60 % (André et al., 2010), while it is as high as ∼ 70 % in Ophiuchus (Motte et al., 1998). Curtis & Richer (2011) found that the majority of the dense cores in Perseus seem to be close to the critical virial ratio, thus implying that they are gravitationally bound, thus prestellar (also, Enoch et al., 2008). Belloche et al. (2011a) suggested that Cha I is experiencing the end of its star formation activity. Overall, the data show that Cha I is experiencing significantly lower star formation activity compared to other nearby clouds and our kinematical analysis so far suggests that only up to ∼ 30 % of the Cha I starless cores might become prestellar in the future. Morales Ortiz et al. (2012) also found that almost all the starless cores in the Vela-D molecular cloud are not virialized or gravitationally bound. Overall, they estimated that approximately 30 % of the whole core population in Vela-D is gravitationally bound, which is comparable to the number of cores in Cha I that will likely become unstable in the future.

We find that no core is virialized in Cha III and only one, Cha3-C1, is gravitationally bound based on our virial analysis. We also find that 2–5 cores are likely to become prestellar based on the infall signature, which corresponds to 10–25 % of the observed sample (see Sect. 5.3.3). Belloche et al. (2011b) concluded that two cores in Cha III are gravitationally unstable (Cha3-C1 and Cha3-C2) from their Bonnor-Ebert analysis.

The virial analysis of Cha I and Cha III confirms the result previously suggested that Cha I is in general more active than Cha III (Belloche et al., 2011b). When taking the infall signature into account we find that the cores suggested to be gravitationally bound in Cha III from the dust continuum survey are, indeed, infalling and that three additional cores are likely to become prestellar.

Smith et al. (2012) modeled the line emission of irregular cores embedded in filaments via radiative transfer and found that the number of collapsing cores are underestimated when only taking the infall signature into account. The line profiles are extremely variable depending on

the viewing angle and other effects, such as one-sided accretion onto filaments. These may result in a line profile not showing the expected blue asymmetry even if the core is indeed collapsing. The fraction of infalling cores in Cha I and III might therefore be even larger than what observational evidence has shown so far.

5.5.4 Core evolutionary state

Observationally, we find a significant difference in the HC_3N/N_2H^+ abundance ratio between Cha I Centre, and Cha I South and West (see Fig. 5.11b). The highest density cores belonging to Cha I Centre have on average lower HC_3N/N_2H^+ abundance ratios than the lower density cores in Cha I South and West. In the framework of the static and collapse models shown in Figure 5.12, the HC_3N/N_2H^+ abundance ratio appears to be a good evolutionary tracer. Nevertheless, the use of abundance ratios as evolutionary clocks is strongly model dependent and requires knowledge of the initial conditions of the region being studied in order to be used as such.

The observed HC_3N to N_2H^+ abundance ratios in Fig. 5.11 imply that the cores in the central part of Cha I (Cha I Centre) are more evolved than the cores in the southern part of the cloud (Cha I South). The cores in the latter region might therefore evolve in a similar manner as the cores in Cha I Centre, given that they belong to the same cloud. The HC_3N to N_2H^+ abundance ratio for the Cha III cores is found to be similar to Cha I South, although with low statistics for Cha III. Since the cores in Cha I South and Cha III have similar densities, they might undertake the same evolutionary path as the more evolved cores of Cha I Centre.

5.5.5 Overlapping velocity components

The *Herschel* image of Cha I shown in Winston et al. (2012) (PACS 160 μm, SPIRE 250 μm, and SPIRE 500 μm) reveals the dust structure of the cloud in great detail. The elongated filament in Cha I Centre (Fig. 5.6b) corresponds to the "Ced 110" cluster on the *Herschel* image of Winston et al. (2012). It similarly appears very bright and dense, while retaining the same elongated structure as in the Cha I 870 μm LABOCA map (Belloche et al., 2011a). The direction as well as the location of the redshifted emission in our maps seems to correspond to fainter, more dispersed and lower density material seen on the *Herschel* image that is "threading" the dense, elongated filament in the perpendicular direction. Alternatively, the redshifted component could simply be a projection effect.

As the redshifted velocity component that we observe in Cha I North (Fig. 5.6a) is not related to the bipolar outflow of Cha-MMS2 (see Sect. 5.3.4.1) it might also be due to material in the cloud interacting with this elongated structure or a projection effect. The dust continuum *Herschel* map of Cha I North ('Ced 112'; Winston et al., 2012) shows that there is some fainter material close to the very northern part of the filament where the peak of the resdshifted emission is located and it seems to be oriented perpendicular to it. However, the material in Cha I North as seen on the *Herschel* map is not as dense and homogeneous in direction as it appears in Cha I Centre.

5.6 Summary and conclusions

We performed spectral line observations with the APEX and Mopra telescopes toward 60 cores in Cha I and 29 cores in Cha III. The aim of this study is to explore the kinematical state of the cores, their future dynamical evolution, and to determine what the main driver of the different star formation activities in the two clouds is. Our conclusions are the following:

1. We find 5 prestellar cores ($\sim$ 8 %) in Cha I and one in Cha III based on a virial analysis. Between 9 to 18 cores show the infall signature in Cha I, bringing the total percentage of cores that might become, if not already, prestellar to 15–30 %. The infall signature is seen toward between 2 to 5 cores in Cha III, and thus 10–25 % cores of the observed sample might become, if not already, prestellar in the future, which corresponds to 7–17 % of the whole core population.

2. Multiple velocity components are observed in Cha I toward a few cores in the northern and central parts of the cloud. The $C^{18}O$ 1–0 integrated emission of the redshifted velocity component in the central elongated structure in Cha I (Cha I Centre) is oriented *perpendicular* to the dust continuum emission. The redshifted velocity component might be caused by more disperse material "interacting" with the elongated structure along this direction, as suggested by the *Herschel* continuum data.

3. We derive $C^{18}O$ and CH_3OH average abundances relative to H_2 that are lower in Cha III than in Cha I by a factor of $\sim$ 2.4 and 1.8, respectively. The distributions of the individual core abundances in Cha III in these molecules lie at the lower end of the core abundances in Cha I.

4. The abundance distribution of the Cha I cores in $C^{18}O$, $C^{17}O$, CH_3OH, and $C^{34}S$ decreases with increasing density, therefore suggesting that these molecules are affected by depletion in the inner parts of the cores.

5. The turbulence level is similar in both clouds in various transitions. There is therefore no indication of turbulence playing a role in the different star formation activities of Cha I and III.

6. Turbulence dissipation in the core interiors is seen in both clouds with the non-thermal dispersions of the high-density tracers N_2H^+ 1–0 and HC_3N 10–9 being smaller than the non-thermal dispersions of $C^{18}O$ 2–1 and $C^{17}O$ 2–1. $C^{34}S$ 2–1 has a higher non-thermal velocity dispersion compared to N_2H^+ 1–0 in Cha I, which is consistent with $C^{34}S$ being affected by depletion in the inner parts of the cores.

7. The dynamical evolution of the cores in Cha I and III on a cloud scale is not likely to be affected by interactions between the cores and competitive accretion.

8. Both collapse and static chemical abundance models indicate that the HC_3N to N_2H^+ abundance ratio is a good core evolutionary indicator. In the framework of these models, the observed HC_3N/N_2H^+ abundance ratios in Cha I and III suggest that the cores in Cha I Centre are more evolved than in Cha I South, and that the cores in Cha III are in

a similar evolutionary state as the cores in Cha I South. The Cha III and Cha I South cores might therefore evolve in a similar manner as the cores in Cha I Centre.

The measured HC_3N/N_2H^+ abundance ratio and the infall signatures detected toward the Cha I and III starless cores suggest that Cha III is younger than Cha I, and therefore on the verge of forming stars.

CHAPTER 6

Conclusions and Outlook

If I were again beginning my studies, I would follow the advice of Plato and start with mathematics.

Galileo Galilei

Contents

Chapters 4 and 5 present a detailed study of star formation in the Chamaeleon I and III molecular clouds. The dynamical state of the first hydrostatic core candidate Cha-MMS1 is explored in Chapter 4, while Chapter 5 examines the overall "status" of star formation in both clouds.

6.1 Cha-MMS1

Cha-MMS1 presents a great opportunity to study the very early stage of star formation, and especially the link between the prestellar and protostellar stages. It is very faint, with an internal luminsity of just $\sim$ 0.08–0.18 $L_{\odot}$, thus agreeing with luminsity predictions of MHD numerical simulations for the first core phase. The classical signature of infall is observed in various molecular transitions and provides evidence for contracting motions in its envelope. Velocity gradients accross Cha-MMS1's envelope are used to examine its rotational structure. The position-velocity diagrams reveal an interesting image consisting of the envelope undergoing solid-body rotation up to a radius of $\sim$ 8000 AU with a gradient $\sim 3.1 \pm 0.1$ km s^{-1} pc^{-1}, while "switching" to differential rotation for radii between $\sim$ 8000–12000 AU. Even more surprising is the finding of an even "flatter" gradient for the inner $\sim$ 2000–4000 AU, perhaps implying the slowing down of rotation in the inner core. Such a slow-down could perhaps be accounted for if magnetic braking is very efficient for Cha-MMS1 at these scales. Regarding turbulent motions within the core, an equipartition of thermal and non-thermal velocity dispersions is seen at the scales that are probed (up to $\sim$ 0.06 pc) and for a temperature of 9 K.

The infall velocity structure of Cha-MMS1's envelope is constrained through radiative transfer modelling of several CS, HCO^+, and CO isotopologues. The modelling yields subsonic to transonic envelope infall velocities from a radius of $\sim$ 3300 AU to 30000 AU, with values of 0.1 km s^{-1} – 0.2 km s^{-1}. The infall velocities for radii less than 3300 AU are less strongly constrained and they are found to be subsonic to supersonic with a range of

0.04 km s^{-1} – 0.6 km s^{-1}. The velocity field of the envelope up to a radius of $\sim$ 9000 AU is consistent with a velocity increase that follows a power-law of $v \propto r^{-0.5}$. An interesting outcome of the radiative transfer modeling, is that the model cannot reproduce the CS 5–4, CO 7–6, and CO 6–5 emission. These transitions are high-density tracers and likely probe material at the innermost regions of the core. The excess emission in these molecular transitions might therefore be indicative of a compact outflow driven by Cha-MMS1, which we cannot yet resolve. This would be in agreement with the main observational signature of first cores (compact, slow outflow), but excess emission due to contamination from an outflow driven by a neighbouring Class I protostar cannot be ruled out.

3D MHD simulations for the first core phase (Commerçon et al., 2012) are finally used so that infall velocity predictions for this phase can be directly compared with the velocity structure that is constrained from the radiative transfer modelling of the observed data. The 3D MHD models of the first cores are chosen so that they are consistent with the observed mass of Cha-MMS1. The infall velocity structure of Cha-MMS1 is found to be consistent with the first core stage predictions, thus further supporting the idea that it belongs to this evolutionary phase. Nevertheless, it cannot be ruled out that this object might also be a young Class 0 protostar.

ALMA will be the first submillimeter interferometer able to resolve and detect a compact, slow outflow in the first hydrostatic core candidate Cha-MMS1 due to its low declination. The detection of such an outflow would serve as a confirmation that this source is indeed at the phase of the first hydrostatic core.

We used predictions of one MHD simulation (Commerçon et al., 2010) in order to determine the observational characteristics of a first core outflow that one should expect from a source like Cha-MMS1. The model follows the collapse of a magnetised 1 $M_\odot$ dense core up to the formation of the first core and the appearance of the first, slow outflow (Commerçon et al., 2010). The overall extent of the outflow that this model produces is approximately 400 AU at a "snapshot" just before the "second collapse" (i.e., just before the protostar is formed), while the density is about 10^8 cm^{-3}. The typical outflow velocities are $\sim$ 1.5 km s^{-1}. Figure 6.1 shows the temperature and velocity distributions of the simulation at xy and xz-plane cuts through the centre.

We used the 3D radiative transfer code LIME (Lime Modeling Engine; Brinch & Hogerheijde, 2010) to predict the observational characteristics of that first core outflow, with the assumption that its inclination to the line-of-sight is 45 degrees. We modelled the CO 3–2 line assuming no depletion in the outflow, as a result of desorption due to grain sputtering in the outflow shock, and a typical depletion factor of 10 for the envelope. Abundances of 10^{-4} and 10^{-5} were used for the outflowing material and the envelope, respectively. A turbulent broadening of FWHM = 0.35 km s^{-1} was added to account for the non-thermal linewidths measured in our single-dish spectra. Infall and rotation within the core are predicted to have similar velocities on these scales (Fig. 6.1) thus making it a priori difficult to disentangle these different motions. Nevertheless, based on our simulations we expect to be able to distinguish the outflow from these motions as we predict the core to have a flattened structure with the outflow oriented perpendicularly (see Fig. 6.2). As the mass of the Cha-MMS1 dense core is $\sim$ 3 times higher than the one assumed in the MHD simulation, the outflow may well be more massive and thus easier to detect. In addition, higher outflow velocities could be produced de-

pending on the magnetic field configuration (e.g., Ciardi & Hennebelle, 2010), which would also make the outflow more easily detectable.

Our simulations predict very compact, but distinct CO 3–2 outflow wings with the peaks of the outflow lobes at an angular distance of 0.5″ from one anther (Fig. 6.2). The intensity of the outflow wings was integrated over the velocity ranges [-2.3, -1.6] and [1.6, 2.3] km s^{-1}. The CO 3–2 single-dish study by Belloche et al. (2006) shows that contamination by cloud emission in this range would be small, especially because it is optically thin and spatially extended, and hence it will be filtered out by the interferometer. Currently, with the ALMA Cycle 1 extended configurations C32-3,4,5,6 (i.e., ∼ 443–1091 meters), angular resolutions 0.16–0.40″ can be achieved in Band 7 (CO 3–2; 345.8 GHz) and a resolution as high as 0.12″ could be achieved with Cycle 2. These resolutions would be sufficient to resolve such a compact outflow.

To conclude, a future ALMA study that could detect of a slow, compact outflow from Cha-MMS1, would confirm the first core nature of Cha-MMS1. In addition, the dynamical age of the outflow and hence an estimate of the age of the compact, central object could be derived. The detection of a first core outflow would also provide constraints to MHD simulations that predict the formation of a slow outflow before the onset of a jet and fast outflow. Finally, it could also set indirect constraints on the magnetic field configuration from the measurement of the spatial extent and velocities of the outflow.

6.2 Star formation in Cha I and III

The main goal of the spectral line survey conducted towards the starless core population of the Chamaeleon I and III molecular clouds that was revealed by the dust continuum survey with LABOCA at APEX (Belloche et al., 2011a,b), was to determine the source of the significant difference in their star formation activity. Cha I is already known to be actively forming stars from previous studies, whereas no star formation in Cha III has been observed.

As a first step, a search for virialised cores is conducted. The virial analysis shows that 5 out of 60 (∼ 8 %) of the Cha I core population is currently gravitationally bound, hence prestellar, and will therefore form stars, while only one core out of 20 is found to be prestellar in Cha III. The next step is to determine the number of cores that might become prestellar in the future. This is achieved with the aid of the infall signature, which we interpret as evidence for contracting core motions. The infall signature is observed toward between 9 and 18 cores in Cha I and between 2 and 5 cores in Cha III. The percentage of cores that may become prestellar and form stars in the future is therefore 15–30 % in Cha I and 10–25 % in Cha III.

No evidence is found for different levels of turbulence in the starless cores of Cha I and III. It is therefore unlikely that turbulence was the underlying reason for producing the different star formation activities in the two clouds. The likelihood of future dynamical interactions between the cores within Cha I and III is also investigated. Such interactions could possibly alter the future dynamical evolution of the cores. It is found that core interactions are unlikely to occur on cloud scales, thus ruling out competitive accretion as a possible scenario for Cha I and III. The time for collisions is significantly reduced when focussing on separate cloud regions where core “clumping” is observed, but it still greatly exceeds the estimated lifetime

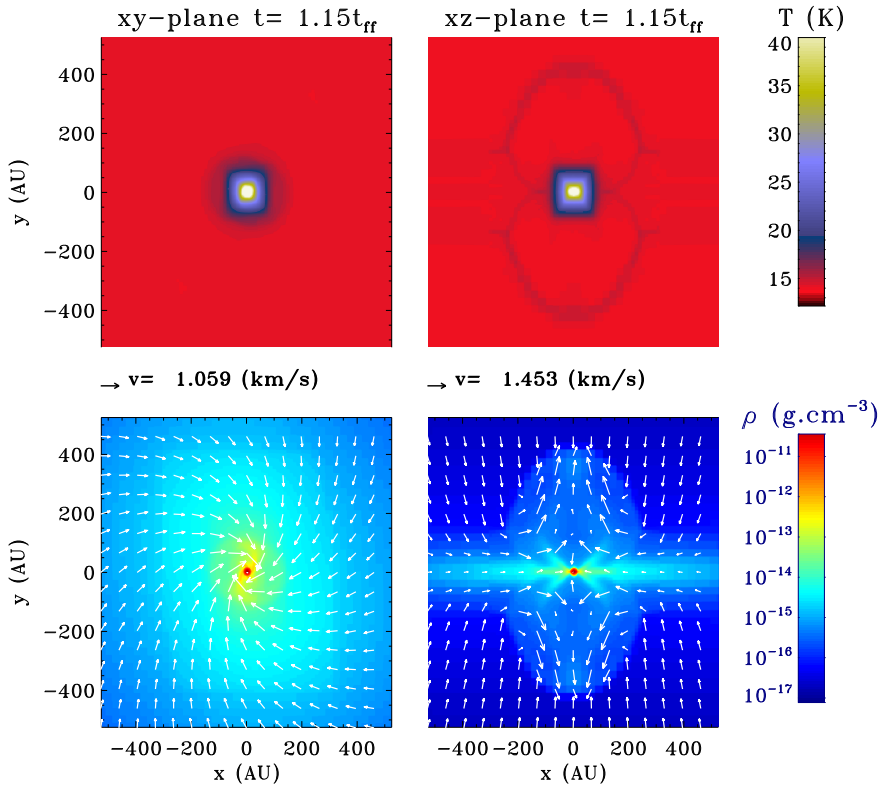

Figure 6.1: XY-plane and XZ-plane cuts of the MHD simulation at a snapshot just before the second collapse (Commerçon et al., 2010). The temperature distribution of the cuts is shown at the two top figures while the velocity and density distributions at the bottom two. The slow outflow can be seen at the bottom right panel with typical velocities of 1.5 km s^{-1}.

of the cores.

Molecular abundances relative to H_2 are derived for the cores in Cha I and III in order to search for differences in chemistry. Abundances are derived for the molecules $C^{18}O$, $C^{17}O$, CH_3OH, $C^{34}S$, N_2H^+, and HC_3N, which show optically thin emission. A difference in chemistry is first indicated by the distribution of core abundances as a function of density in Cha III compared to Cha I in these molecules. The majority of the Cha III core abundances are found to lie at the lower end of the Cha I abundances distribution for the same densities. Comparisons between average values show that $C^{18}O$ and CH_3OH have a lower fractional abundance in Cha III than in Cha I by a factor of $\sim$ 2.4 and $\sim$ 1.8. The origin of this abundance difference remains unclear. The distributions of core fractional abundances as a function of density suggest that the molecules $C^{18}O$, $C^{17}O$, CH_3OH, and $C^{34}S$ are affected by depletion in the interiors of the Cha I cores, as the fractional abundances tend to decrease with increasing core density.

Turbulence dissipation is seen in the high-density tracers N_2H^+ 1–0 and HC_3N 10–9. Their non-thermal velocity dispersions are systematically smaller than the non-thermal dispersions

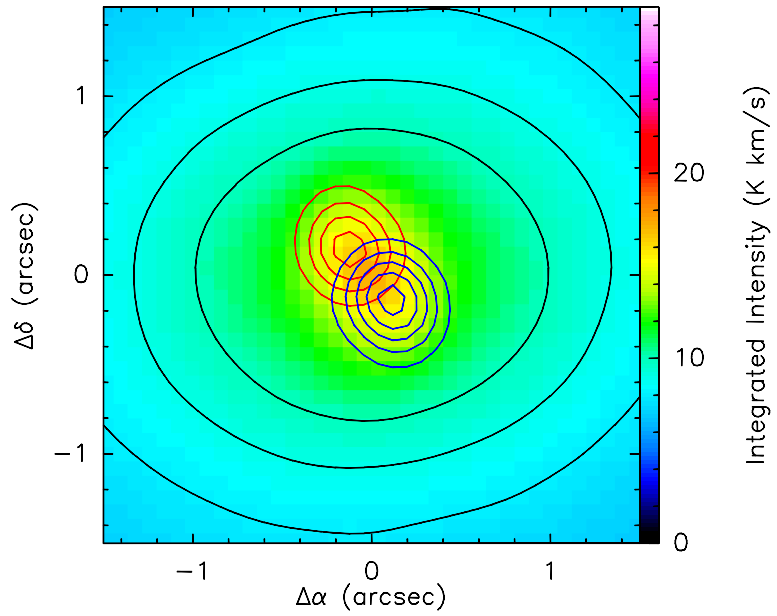

Figure 6.2: LIME CO 3–2 3D radiative transfer simulation of the MHD model shown in Fig. 1, with the z-axis inclined by 45 degrees along the line-of-sight. The full integrated intensity map is shown on the background with the black contours at steps of 1 K km/s from 8 to 10 K km/s, emphasizing the flattened structure of the core due to rotation. The outflow wings are shown by the red (redshifted) and blue (blueshifted) contours. They represent the integrated intensity for the velocity ranges [1.6, 2.3] and [-2.3, -1.6] km/s respectively, overlaid at steps of 2α, 4α, 6α, 8α, 10α, with $\alpha = 0.3$ K km s^{-1}. The outflow wings lie at a direction perpendicular to the flattening of the core. The resolution of this image is 0.35″ with a pixel size of 0.08″ and the results are directly comparable to the ALMA Cycle 1 and 2 achievable resolutions.

of $C^{18}O$ 2–1 and $C^{17}O$ 2–1 in both Cha I and III, which likely trace the less dense, outer core regions. The fact that the high-density transition $C^{34}S$ 2–1 is found to have a higher non-thermal velocity dispersion than N_2H^+ 1–0 in Cha I also points to $C^{34}S$ depletion at the starless core interiors, in agreement with the observed trend in the observed fractional abundances.

Static and collapse chemical models show that the HC_3N to N_2H^+ abundance ratio is a good evolutionary indicator for cores in the prestellar phase (previously seen for starless and protostellar cores in Lupus; Benedettini et al., 2012). The cores in the central region of Cha I have systematically smaller HC_3N/N_2H^+ abundance ratios than the cores in the southern region, thus suggesting that the latter are at a younger physical stage. Abundance ratios similar to the southern Cha I cores are found for the cores in Cha III, but with low statistics. The suggested interpretation of these results is that the southern cores in Cha I will likely undertake the same evolutionary path as the central ones, given that they belong to the same cloud. Additionally, the similar HC_3N to N_2H^+ abundance ratios between the Cha III and the southern Cha I cores, as well as their similar core densities, indicate that the cores in these two regions may evolve in a similar manner. The measured HC_3N to N_2H^+ abundance ratios and the

detected core infall signatures in Cha I and III suggest that Cha III is younger than Cha I and that star formation in Cha III is about to begin.

As a final remark, particularly interesting was the fact that several spectra towards cores in the central and northern elongated structures in Cha I show emission peaks at two different velocities. After self-absorption was ruled out as the source of this feature, $C^{18}O$ 1–0 integrated intensity maps were utilised to further understand the multiple velocity components. The outcome is especially striking for the central part of Cha I. The map shows that the $C^{18}O$ 1–0 integrated intensity of the blueshifted velocity component follows the dust continuum emission of the elongated structure well, whereas the emission of the redshifted component emission traces a region perpendicular to it. One explanation is the interaction of more diffuse material with the central "filamentary" structure along this direction, as is suggested by the morphology of *Herschel* continuum data.

As an outlook, the evolutionary status of the Chamaeleon complex as a whole could be explored. As it was previously suggested, Cha I is the most actively star forming cloud in the complex having produced more than 200 YSOs (Luhman, 2008). $\sim$ 15–30 % of its starless core population is likely to form stars in the future (cf. Chapter 5), but its star formation rate continues at a declining rate (Luhman, 2007; Belloche et al., 2011a,b). Cha III on the other hand, contains n YSO (e.g., Luhman, 2008) and our analysis in Chapter 5 has indicated that it may be younger than Cha I and about to form stars.

Determining the evolutionary state of the cloud Cha II would be worth investigating. The results of our study in Chapter 5, as well those from earlier studies hint a likely evolutionary sequence from the youngest Cha III cloud to the eldest Cha I cloud. Mizuno et al. (1999) derived a star formation efficiency (SFE) of ~7–13 % for Cha I, 1 % for Cha II, and 0 % for Cha III. They observed the three clouds in $C^{18}O$ 1–0 and found that the $C^{18}O$ cores are almost in virial equilibrium in Cha I, having high column densities, and high ratios of core to cloud masses, with the opposite being the case for Cha III. Interestingly, they found that the properties of the $C^{18}O$ cores in Cha II are *in between* those of the two other clouds. Spezzi et al. (2008) and Young et al. (2005) detected about 50 YSOs in Cha II with the *Spitzer* Space Telescope as part of the c2d survey (see Evans et al., 2003) and the former obtained a SFE of 1–4 %. Therefore, Cha II seems to be star forming but at a much slower rate than Cha I and it has so far produced a YSO population in between that of Cha I and Cha III. Finally, Cha II was found to have the largest fraction of Class II to Class III YSOs in all the c2d clouds (Spezzi et al., 2008). There are more Class II objects by approximately a factor of 2 in Cha II (Spezzi et al., 2008), while these numbers are equal in Cha I ($\sim$ 95 Class II and III Luhman, 2008). The higher number of Class II objects in Cha II compared to Cha I likely indicates that the YSOs in Cha II have not yet had time to reach the Class III phase. Therefore, the three Chamaeleon clouds might indeed represent an evolutionary sequence with Cha II being at an intermediate stage of evolution.

Since the goal of such a project would be a direct comparison of the starless core properties and dynamical state between the three clouds, an unbiased census of the starless core population in Cha II conducted in continuum emission with at least the same sensitivity as in Cha I and III, would be necessary. Young et al. (2005) present a millimeter map of Cha II (at 1.2 mm), observed with the bolometer array SIMBA at the Swedish-ESO Submillimeter Telescope (SEST). The map has an angular resolution of $\sim 24''$ ($HPBW$) and the rms noise

level of the map is 32 mJy/beam. Less sensitive dust continuum observations towards Cha II were performed in 2007-2008 at 1.1 mm with the AzTEC camera on the submillimiter ASTE telescope (Momose et al., 2009). A point-source detection limit of $\sim$ 45 mJy with a beam of 28″ was reached for the Chamaeleon clouds. For comparison, the dust continuum surveys conducted towards Cha I and Cha III at 870 μm with LABOCA at APEX achieved an rms noise level of the maps were 12 mJy and 11.5 mJy for Cha I and III, respectively and with an angular resolution (*HPBW*) of 21.2″ (Belloche et al., 2011a,b). Assuming a dust temperature for Cha I and III of 12 K (e.g., Tóth et al., 2000), a dust opacity of $\sim$ 0.01 cm^2 g^{-1} at 870 μm, and a dust opacity index $\beta = 1.85$ (see Belloche et al., 2011a), the equivalent sensitivities in column densities are $\sim 1.1 \times 10^{21}$ cm^{-2} for LABOCA (for an rms of 12 mJy) and $\sim 2.4 \times 10^{21}$ cm^{-2} for the maps with SIMBA at SEST and with AzTEC at ASTE. The Cha I and III LABOCA dust continuum map therefore probes column densities lower by a factor of $\sim$ 2. A deep, unbiased dust continuum survey at 870 μm for Cha II should therefore be conducted with LABOCA at APEX to match the sensitivity achieved with the Cha I and III surveys so that the core population of Cha II can be extracted. The A-MKID camera due to be commissioned at the end of 2013 at APEX could also be used to map Cha II with a high sensitivity and less integration time, with the advantage of operating at 350 μm and 850 μm simultaneously and with a total of 25000 pixels.

After having extracted the starless core population of the cloud from a deep dust continuum survey, a molecular line survey similar to the one of Cha I and III could be performed. The prestellar cores could thus be determined from a virial analysis and a search for the infall signature would indicate the number of cores that might be undergoing contracting motions. Given the analysis conducted in Chapter 5 and the results of the chemical models presented therein, the abundance ratio of the HC_3N to N_2H^+ could be used to provide further insight on the evolutionary state of the cloud's starless core population. Comparisons could then be made with the ratios found for the cores in Cha I and III to obtain direct clues about the cores' evolutionary stage relative to those of the other two clouds. By observing Cha II with the same molecular transitions as Cha I and III, the abundance distributions of the individual cores in each molecule and as a function of density could be derived and directly compared to the equivalent abundance distributions of Cha I and III. The differences in chemistry between the three clouds could thus be probed.

Appendix A

Mopra calibration and efficiency

A.1 Calibration ambiguities

Some of our Mopra data show differences in the peak temperatures of the two polarisations, POL0 and POL1. The differences are not systematic for all the transitions observed. The two polarisations in some cases differ up to ~ 10%. The CS 2–1 POL1 intensity for position P6 is stronger by ~ 5% within the uncertainties, while $C^{34}S$ 2–1 has a stronger POL0 intensity by ~ 9%. POL0 also shows higher intensities for positions P1 and P6 of the N_2H^+ 1–0 transition by ~7% and ~6%, respectively. Most of the other transitions (and positions) do not show any significant differences. As the observed discrepancies are not systematic and are only seen in very few cases, we use the average of both polarisations per transition for the analysis in Chapter 4.

Pronounced differences in intensity are seen when comparing a pair of spectra belonging to the same transition that was observed with different tuning frequencies. HC_3N 10–9 and HNC 1–0 are the two transitions observed in both setups and show intensity differences of ~ 38% and ~ 33%. Unfortunately, we have not yet found a satisfactory explanation for these discrepancies.

A.2 Efficiency

Even though the expected Mopra beam efficiency at the 90 GHz band is ~ 0.5[1], we derive a value that is lower by ~ 30% after performing independent calibration tests. IRAM 04191 in Taurus and OPH A SM1N in Ophiuchus were observed with both the Mopra and the IRAM 30 m telescopes (Belloche et al., 2002; André et al., 2007). IRAM 04191 was observed in the molecular transitions CS 2–1, N_2H^+ 1–0, $C^{34}S$ 2–1, and $H^{13}CO^+$ 1–0, while OPH A SM1N in N_2H^+ 1–0. After smoothing the 30 m data to the Mopra angular resolution we directly compared their integrated intensities with the equivalent Mopra intensities. We derived lower efficiencies for most of the observed transitions (see Table A.1) with the overall weighted average efficiency being ~ 0.34.

Table A.1: Mopra beam efficiencies[a]

Source	Line	Mopra efficiency
IRAM 04191	N_2H^+ 1–0	0.25 ± 0.01
IRAM 04191	CS 2–1	0.35 ± 0.02
IRAM 04191	$C^{34}S$ 2–1	0.52 ± 0.13
IRAM 04191	$H^{13}CO^+$ 1–0	0.36 ± 0.03
OPH A SM1N	N_2H^+ 1–0	0.36 ± 0.003

Notes [a] Mopra efficiencies derived after comparing independent observations from the IRAM 30 m and Mopra telescopes. The IRAM 30 m spectra were smoothed to the Mopra angular resolution.

[1] see http://www.narrabri.atnf.csiro.au/mopra/obsinfo.html.

Appendix B

Cha-MMS1 opacity

B.1 Opacity of the $C^{18}O$ 2–1 line

We observed both $C^{18}O$ 2–1 and $C^{17}O$ 2–1 at 13 positions perpendicular to the filament (Fig. 4.1). An isotopic ratio of $[^{18}O]/[^{17}O] \sim 4.11$ was found for the nearby (140 pc) low-mass cloud ρ Ophiuchus (Wouterloot et al., 2005). We use this value to derive the opacity of $C^{18}O$ 2–1 using the following relation:

$$\frac{I_{C^{18}O}}{I_{C^{17}O}} = \frac{1 - e^{-\tau_{C^{18}O}}}{1 - e^{-\tau_{C^{17}O}}} \tag{B.1}$$

where $I_{C^{18}O}$ and $I_{C^{17}O}$ are the intensities of the two transitions, $\tau_{C^{18}O}$ and $\tau_{C^{17}O}$ their opacities and $\tau_{C^{17}O}=\tau_{C^{18}O}/4.11$. We find opacities that gradually increase from ≤ 0.5 at the outermost position to ~ 1.6 at the centre of the core for the $C^{18}O$ 2–1 transition.

Appendix C

Detailed physical parameters of Cha I and III cores

Tables C.1 and C.2 provide a detailed list of the observationally derived physical parameters of the cores for each transition separately. The method for extracting these values is described in Sect. 5.3. For the spectra that have two velocity components the derived properties based on both components are listed. The integrated intensities are listed only for the transitions that were used to derive column densities.

Table C.1: Line parameters and physical parameters of cores in Cha I.

Core	Transition	$I_{\rm int}$[a] (K km s^{-1})	$V_{\rm LSR}$[b] (km s^{-1})	$FWHM$[c] (km s^{-1})	$M_{\rm vir}$[d] ($M_\odot$)	$\frac{M_{\rm tot}}{M_{\rm vir}}$[e]	$\frac{M_{50}}{M_{\rm vir}}$[f]	$\frac{\sigma_{\rm nth}}{\sigma_{\rm th,mean}}$[g]	Gr.[h]	Vir.[i]
Cha1-C1										
	C_4H $10_{10,10}$–$9_{9,9}$		4.44±0.02	0.41±0.04	1.55	2.17	0.93	0.91± 0.10	yes	yes
	C_4H 11_{11}–9_{10}		4.49±0.02	0.64±0.05	2.61	1.29	0.55	1.44± 0.11	yes	yes
	H_2CO $3_{1,2}$–$2_{1,1}$		4.33±0.03	0.81±0.06	3.65	0.92	0.40	1.82±0.13	yes	no
	$C^{18}O$ 2–1	3.17±0.05	4.55±0.01	0.59±0.01	2.28	1.47	0.63	1.30± 0.02	yes	yes
	$C^{17}O$ 2–1	1.05±0.07	4.40±0.01	0.47±0.03	1.73	1.94	0.83	1.02± 0.07	yes	yes
	CH_3OH 2_0–1_0 A^+	1.01±0.03	4.39±0.01	0.47±0.01	1.73	1.94	0.83	1.02± 0.03	yes	yes
	CH_3OH 2_1–1_1 E	0.80±0.02	4.40±0.01	0.50±0.01	1.88	1.79	0.77	1.10± 0.03	yes	yes
	N_2H^+ 1–0	1.55±0.02	4.40±0.01	0.49±0.01	1.81	1.85	0.79	1.07± 0.01	yes	yes
	$C^{34}S$ 2–1	0.35±0.02	4.44±0.01	0.56±0.04	2.17	1.55	0.66	1.25± 0.08	yes	yes
	HC_3N 10–9	1.26±0.02	4.45±0.01	0.47±0.01	1.77	1.90	0.81	1.04± 0.02	yes	yes
	N_2H^+ 3–2		4.47±0.01	0.53±0.01	1.98	1.70	0.73	1.16± 0.03	yes	yes
Cha1-C2										
	C_4H 11_{11}–9_{10}		4.49±0.04	0.46±0.08	2.28	0.71	0.26	1.02±0.18	yes	no
	H_2CO $3_{1,2}$–$2_{1,1}$		4.27±0.04	0.60±0.10	3.10	0.52	0.19	1.34±0.22	yes	no
	$C^{18}O$ 2–1	3.30±0.06	4.61±0.01	0.78±0.01	4.55	0.36	0.13	1.76± 0.03	no	no
	$C^{17}O$ 2–1	1.13±0.09	4.39±0.02	0.59±0.06	3.01	0.54	0.19	1.31±0.13	yes	no
	CH_3OH 2_0–1_0 A^+	1.56±0.05	4.40±0.01	0.51±0.01	2.52	0.64	0.23	1.13±0.04	yes	no
	CH_3OH 2_1–1_1 E	1.23±0.05	4.39±0.01	0.50±0.02	2.44	0.66	0.24	1.09±0.05	yes	no
	N_2H^+ 1–0	0.60±0.04	4.32±0.01	0.48±0.01	2.37	0.69	0.24	1.06±0.03	yes	no
	$C^{34}S$ 2–1	0.52±0.04	4.41±0.02	0.67±0.05	3.62	0.45	0.16	1.50± 0.11	no	no
	HC_3N 10–9	0.76±0.04	4.42±0.01	0.50±0.07	2.51	0.65	0.23	1.12±0.17	yes	no
	N_2H^+ 3–2		4.32±0.01	0.51±0.04	2.53	0.64	0.23	1.13±0.09	yes	no
Cha1-C3										
	C_4H $10_{10,10}$–$9_{9,9}$		4.40±0.04	0.37±0.09	1.61	0.72	0.28	0.81±0.21	yes	no
	C_4H 11_{11}–9_{10}		4.52±0.05	0.54±0.11	2.37	0.49	0.19	1.20± 0.25	no	no
	$C^{18}O$ 2–1	3.21±0.08	4.54±0.01	0.91±0.03	5.05	0.23	0.09	2.05± 0.06	no	no
	$C^{17}O$ 2–1	0.65±0.08	4.33±0.02	0.41±0.04	1.72	0.68	0.26	0.88±0.11	yes	no
	CH_3OH 2_0–1_0 A^+	0.53±0.04	4.42±0.02	0.66±0.06	3.08	0.38	0.15	1.47± 0.13	no	no
	CH_3OH 2_1–1_1 E	0.44±0.04	4.44±0.04	0.91±0.14	5.06	0.23	0.09	2.05± 0.33	no	no
	N_2H^+ 1–0	0.65±0.04	4.36±0.01	0.53±0.01	2.29	0.51	0.20	1.17±0.04	yes	no
	$C^{34}S$ 2–1	0.32±0.05	4.33±0.04	0.57±0.10	2.58	0.45	0.18	1.29± 0.22	no	no
	HC_3N 10–9	0.32±0.04	4.33±0.03	0.39±0.01	1.69	0.69	0.27	0.86±0.04	yes	no
	N_2H^+ 3–2		4.38±0.03	0.31±0.05	1.36	0.85	0.33	0.64±0.13	yes	no
Cha1-C4										
	C_4H $10_{10,10}$–$9_{9,9}$		5.06±0.02	0.33±0.04	1.27	0.52	0.23	0.72±0.09	yes	no
	C_4H 11_{11}–9_{10}		5.10±0.01	0.24±0.03	1.06	0.62	0.28	0.51±0.08	yes	no
	H_2CO $3_{1,2}$–$2_{1,1}$		4.95±0.06	0.42±0.12	1.53	0.43	0.19	0.90± 0.28	no	no
	$C^{18}O$ 2–1	2.68±0.07	5.06±0.01	0.70±0.02	2.89	0.23	0.10	1.56± 0.04	no	no
	$C^{17}O$ 2–1	0.80±0.08	4.92±0.03	0.60±0.08	2.35	0.28	0.12	1.34± 0.18	no	no
	CH_3OH 2_0–1_0 A^+	0.54±0.04	5.00±0.01	0.36±0.02	1.34	0.49	0.22	0.77± 0.06	no	no
	CH_3OH 2_1–1_1 E	0.35±0.05	5.01±0.01	0.37±0.03	1.38	0.48	0.21	0.80± 0.07	no	no
	N_2H^+ 1–0	0.34±0.03	5.06±0.01	0.23±0.01	1.01	0.66	0.29	0.45±0.02	yes	no
	$C^{34}S$ 2–1	0.49±0.03	5.04±0.01	0.36±0.02	1.37	0.48	0.21	0.79± 0.05	no	no
	HC_3N 10–9	1.23±0.04	5.11±0.01	0.26±0.01	1.10	0.60	0.27	0.55±0.04	yes	no
	N_2H^+ 3–2		5.03±0.02	0.22±0.03	0.98	0.67	0.30	0.41±0.09	yes	no

Table C.1: continued.

Core	Transition	$I_{\rm int}$[a] (K km s^{-1})	$V_{\rm LSR}$[b] (km s^{-1})	$FWHM$[c] (km s^{-1})	$M_{\rm vir}$[d] ($M_\odot$)	$\frac{M_{\rm tot}}{M_{\rm vir}}$[e]	$\frac{M_{50}}{M_{\rm vir}}$[f]	$\frac{\sigma_{\rm nth}}{\sigma_{\rm th,mean}}$[g]	Gr.[h]	Vir.[i]
Cha1-C5										
	$C^{18}O$ 2–1	1.58±0.07	4.33±0.01	0.45±0.02	1.36	0.30	0.23	0.98± 0.04	no	no
	$C^{17}O$ 2–1	0.39±0.06	4.17±0.03	0.34±0.05	1.04	0.39	0.30	0.71± 0.12	no	no
	CH_3OH 2_1–1_1 E	0.11±0.04	4.18±0.01	0.16±0.04	0.73	0.56	0.43	0.23±0.16	yes	no
Cha1-C6										
	$C^{18}O$ 2–1	1.45±0.05	4.41±0.02	1.08±0.04	2.98	0.07	0.11	2.44± 0.10	no	no
Cha1-C7										
	$C^{18}O$ 2–1	4.28±0.06	4.00±0.01	0.66±0.02	3.60	0.23	0.06	1.47± 0.04	no	no
	–[j]	–	4.76±0.01	0.51±0.02	2.60	0.32	0.09	1.13± 0.05	no	no
	$C^{17}O$ 2–1	1.13±0.05	3.85±0.02	0.49±0.06	2.49	0.33	0.09	1.08± 0.14	no	no
	–[j]	–	4.57±0.03	0.40±0.08	2.01	0.41	0.11	0.87± 0.19	no	no
	CH_3OH 2_0–1_0 A^+	0.12±0.02	4.65±0.04	0.36±0.08	1.83	0.45	0.12	0.78± 0.19	no	no
Cha1-C8										
	$C^{18}O$ 2–1	2.66±0.08	4.51±0.01	0.91±0.03	1.70	0.09	0.13	2.04± 0.06	no	no
	CH_3OH 2_0–1_0 A^+	0.27±0.04	4.40±0.04	0.55±0.10	0.83	0.18	0.27	1.23± 0.24	no	no
	CH_3OH 2_1–1_1 E	0.20±0.03	4.37±0.02	0.41±0.06	0.59	0.25	0.38	0.89± 0.14	no	no
	N_2H^+ 1–0	1.57±0.07	4.46±0.02	0.58±0.04	0.87	0.17	0.26	1.28± 0.09	no	no
	HC_3N 10–9	0.16±0.03	4.53±0.05	0.61±0.12	0.94	0.15	0.24	1.36± 0.28	no	no
	N_2H^+ 3–2		4.65±0.02	0.44±0.09	0.63	0.23	0.35	0.96± 0.22	no	no
Cha1-C9										
	H_2CO $3_{1,2}$–$2_{1,1}$		4.86±0.05	0.40±0.11	1.93	0.35	0.10	0.87± 0.26	no	no
	$C^{18}O$ 2–1	1.78±0.08	4.96±0.01	0.49±0.01	2.35	0.29	0.08	1.07± 0.03	no	no
	$C^{17}O$ 2–1	0.53±0.06	4.88±0.01	0.31±0.04	1.53	0.44	0.13	0.64± 0.09	no	no
	CH_3OH 2_0–1_0 A^+	0.93±0.04	4.86±0.01	0.41±0.01	1.97	0.34	0.10	0.89± 0.03	no	no
	N_2H^+ 1–0	0.50±0.07	4.86±0.02	0.32±0.05	1.59	0.42	0.12	0.68± 0.11	no	no
	$C^{34}S$ 2–1	0.10±0.04	4.86±0.02	0.35±0.04	1.73	0.39	0.12	0.76± 0.11	no	no
Cha1-C10										
	$C^{18}O$ 2–1	2.29±0.06	4.60±0.01	0.57±0.01	1.89	0.16	0.10	1.26± 0.03	no	no
	$C^{17}O$ 2–1	0.53±0.07	4.44±0.02	0.39±0.06	1.24	0.25	0.15	0.83± 0.13	no	no
	CH_3OH 2_0–1_0 A^+	0.70±0.04	4.44±0.01	0.36±0.02	1.18	0.26	0.16	0.78± 0.04	no	no
	CH_3OH 2_1–1_1 E	0.57±0.04	4.46±0.01	0.35±0.02	1.14	0.27	0.17	0.74± 0.04	no	no
	N_2H^+ 1–0	1.30±0.07	4.44±0.01	0.39±0.04	1.23	0.25	0.15	0.83± 0.09	no	no
	$C^{34}S$ 2–1	0.34±0.03	4.48±0.04	0.77±0.09	2.94	0.10	0.06	1.74± 0.21	no	no
	HC_3N 10–9	0.11±0.04	4.55±0.04	0.28±0.04	1.00	0.31	0.19	0.61± 0.10	no	no
Cha1-C11										
	C_4H $10_{10,10}$–$9_{9,9}$		5.05±0.02	0.22±0.05	1.52	0.50	0.11	0.45± 0.12	no	no
	C_4H 11_{11}–9_{10}		5.09±0.01	0.16±0.03	1.38	0.55	0.12	0.30±0.09	yes	no
	H_2CO $3_{1,2}$–$2_{1,1}$		4.96±0.04	0.47±0.09	2.65	0.29	0.06	1.04± 0.21	no	no
	$C^{18}O$ 2–1	1.61±0.07	5.15±0.01	0.38±0.01	2.12	0.36	0.08	0.82± 0.03	no	no
	$C^{17}O$ 2–1	0.35±0.06	4.96±0.02	0.27±0.03	1.65	0.46	0.10	0.55± 0.07	no	no
	CH_3OH 2_0–1_0 A^+	0.49±0.04	5.08±0.01	0.36±0.03	2.04	0.37	0.08	0.78± 0.06	no	no
	CH_3OH 2_1–1_1 E	0.33±0.07	5.06±0.01	0.28±0.02	1.70	0.45	0.10	0.58± 0.06	no	no
	N_2H^+ 1–0	1.21±0.07	5.06±0.01	0.29±0.02	1.74	0.44	0.09	0.61± 0.05	no	no
	$C^{34}S$ 2–1	0.29±0.04	5.05±0.01	0.36±0.03	2.07	0.37	0.08	0.79± 0.08	no	no
	HC_3N 10–9	0.58±0.04	5.10±0.01	0.32±0.01	1.86	0.41	0.09	0.68± 0.04	no	no

Table C.1: continued.

Core	Transition	$I_{\rm int}$[a] (K km s^{-1})	$V_{\rm LSR}$[b] (km s^{-1})	$FWHM$[c] (km s^{-1})	$M_{\rm vir}$[d] ($M_\odot$)	$\frac{M_{\rm tot}}{M_{\rm vir}}$[e]	$\frac{M_{50}}{M_{\rm vir}}$[f]	$\frac{\sigma_{\rm nth}}{\sigma_{\rm th,mean}}$[g]	Gr.[h]	Vir.[i]
Cha1-C12										
	$C^{18}O$ 2–1	3.66±0.07	4.98±0.01	0.71±0.01	2.26	0.11	0.06	1.59± 0.03	no	no
	$C^{17}O$ 2–1	1.20±0.09	4.83±0.02	0.49±0.06	1.37	0.18	0.10	1.07± 0.13	no	no
	CH_3OH 2_0–1_0 A^+	0.31±0.04	4.84±0.04	0.55±0.10	1.60	0.15	0.09	1.22± 0.22	no	no
	CH_3OH 2_1–1_1 E	0.36±0.04	4.90±0.03	0.64±0.08	1.97	0.12	0.07	1.44± 0.19	no	no
Cha1-C13										
	$C^{18}O$ 2–1	1.46±0.07	4.85±0.01	0.48±0.03	2.38	0.23	0.07	1.06± 0.06	no	no
	CH_3OH 2_0–1_0 A^+	0.20±0.04	4.73±0.01	0.26±0.03	1.41	0.38	0.11	0.51± 0.06	no	no
Cha1-C14										
	$C^{18}O$ 2–1	2.17±0.08	4.56±0.02	0.87±0.04	2.93	0.07	0.06	1.95± 0.10	no	no
	CH_3OH 2_0–1_0 A^+	0.44±0.04	4.40±0.03	0.57±0.12	1.57	0.14	0.11	1.26± 0.29	no	no
	CH_3OH 2_1–1_1 E	0.29±0.04	4.31±0.04	0.62±0.08	1.77	0.12	0.10	1.38± 0.19	no	no
	N_2H^+ 1–0	1.11±0.08	4.37±0.03	0.52±0.05	1.42	0.15	0.12	1.15± 0.11	no	no
Cha1-C15										
	$C^{18}O$ 2–1	3.83±0.08	4.25±0.01	0.57±0.01	3.07	0.17	0.04	1.27± 0.02	no	no
	$C^{17}O$ 2–1	1.19±0.10	4.12±0.02	0.59±0.05	3.22	0.16	0.04	1.32± 0.11	no	no
Cha1-C16										
	$C^{18}O$ 2–1	2.38±0.09	4.74±0.01	0.87±0.04	3.38	0.06	0.03	1.97± 0.08	no	no
	$C^{34}S$ 2–1	0.09±0.04	4.63±0.04	0.38±0.11	1.18	0.18	0.09	0.83± 0.26	no	no
Cha1-C17										
	$C^{18}O$ 2–1	2.00±0.07	5.29±0.01	0.51±0.01	1.93	0.15	0.06	1.12± 0.04	no	no
	$C^{17}O$ 2–1	0.58±0.07	5.11±0.02	0.41±0.06	1.52	0.19	0.07	0.88± 0.13	no	no
	CH_3OH 2_0–1_0 A^+	0.46±0.04	5.18±0.01	0.44±0.03	1.66	0.18	0.07	0.96± 0.07	no	no
	CH_3OH 2_1–1_1 E	0.38±0.07	5.19±0.02	0.42±0.05	1.59	0.18	0.07	0.92± 0.11	no	no
	$C^{34}S$ 2–1	0.41±0.04	5.32±0.01	0.40±0.04	1.52	0.19	0.07	0.87± 0.09	no	no
	HC_3N 10–9	0.10±0.04	5.45±0.02	0.18±0.07	0.97	0.30	0.12	0.36± 0.20	no	no
Cha1-C18										
	$C^{18}O$ 2–1	2.03±0.08	5.03±0.01	0.47±0.02	2.37	0.21	0.05	1.02± 0.04	no	no
	$C^{17}O$ 2–1	0.60±0.08	4.89±0.02	0.30±0.04	1.59	0.31	0.07	0.61± 0.10	no	no
	CH_3OH 2_0–1_0 A^+	0.29±0.04	4.91±0.02	0.36±0.04	1.87	0.26	0.06	0.78± 0.10	no	no
	$C^{34}S$ 2–1	0.15±0.04	4.95±0.04	0.39±0.15	2.03	0.24	0.06	0.86± 0.35	no	no
	HC_3N 10–9	0.09±0.03	5.05±0.02	0.18±0.02	1.31	0.37	0.09	0.36± 0.06	no	no
Cha1-C19										
	C_4H $10_{10,10}$–$9_{9,9}$		4.93±0.01	0.25±0.03	1.08	0.26	0.09	0.53± 0.07	no	no
	C_4H 11_{11}–9_{10}		4.96±0.01	0.29±0.03	1.18	0.24	0.08	0.62± 0.07	no	no
	H_2CO $3_{1,2}$–$2_{1,1}$		4.82±0.07	0.50±0.12	1.87	0.15	0.05	1.10± 0.28	no	no
	$C^{18}O$ 2–1	1.99±0.08	4.95±0.01	0.44±0.02	1.63	0.17	0.06	0.96± 0.04	no	no
	$C^{17}O$ 2–1	0.54±0.05	4.77±0.02	0.40±0.05	1.47	0.19	0.07	0.86± 0.11	no	no
	CH_3OH 2_0–1_0 A^+	0.47±0.04	4.86±0.01	0.34±0.03	1.30	0.22	0.08	0.73± 0.06	no	no
	CH_3OH 2_1–1_1 E	0.33±0.04	4.88±0.02	0.34±0.04	1.27	0.22	0.08	0.71± 0.10	no	no
	N_2H^+ 1–0	1.40±0.10	4.91±0.01	0.31±0.02	1.19	0.23	0.08	0.64± 0.05	no	no
	$C^{34}S$ 2–1	0.33±0.04	4.88±0.01	0.32±0.03	1.24	0.23	0.08	0.68± 0.06	no	no
	HC_3N 10–9	1.39±0.04	4.98±0.01	0.21±0.01	1.01	0.28	0.10	0.44± 0.03	no	no
Cha1-C20										
	$C^{18}O$ 2–1	1.18±0.08	4.35±0.01	0.52±0.03	2.03	0.13	0.05	1.16± 0.06	no	no
	CH_3OH 2_0–1_0 A^+	0.24±0.05	4.29±0.02	0.34±0.05	1.31	0.20	0.07	0.72± 0.12	no	no
	CH_3OH 2_1–1_1 E	0.14±0.04	4.36±0.04	0.51±0.07	1.96	0.14	0.05	1.12± 0.18	no	no

Table C.1: continued.

Core	Transition	$I_{\rm int}$[a] (K km s^{-1})	$V_{\rm LSR}$[b] (km s^{-1})	$FWHM$[c] (km s^{-1})	$M_{\rm vir}$[d] ($M_\odot$)	$\frac{M_{\rm tot}}{M_{\rm vir}}$[e]	$\frac{M_{50}}{M_{\rm vir}}$[f]	$\frac{\sigma_{\rm nth}}{\sigma_{\rm th,mean}}$[g]	Gr.[h]	Vir.[i]
Cha1-C21										
	H_2CO $3_{1,2}$–$2_{1,1}$		4.90±0.05	0.45±0.13	0.86	0.12	0.13	0.98± 0.32	no	no
	$C^{18}O$ 2–1	1.96±0.08	5.03±0.01	0.62±0.03	1.28	0.08	0.09	1.38± 0.06	no	no
	$C^{17}O$ 2–1	0.66±0.05	4.84±0.04	0.52±0.09	1.01	0.10	0.11	1.14± 0.20	no	no
	CH_3OH 2_0–1_0 A^+	0.28±0.05	5.01±0.02	0.33±0.04	0.65	0.16	0.17	0.69± 0.09	no	no
	CH_3OH 2_1–1_1 E	0.32±0.05	4.96±0.02	0.39±0.05	0.75	0.14	0.15	0.84± 0.11	no	no
	N_2H^+ 1–0	1.43±0.08	5.05±0.01	0.25±0.01	0.54	0.19	0.21	0.48± 0.04	no	no
	$C^{34}S$ 2–1	0.16±0.04	5.07±0.02	0.37±0.06	0.73	0.14	0.16	0.81± 0.13	no	no
	HC_3N 10–9	0.43±0.04	5.08±0.01	0.18±0.01	0.50	0.21	0.23	0.36± 0.00	no	no
Cha1-C22										
	$C^{18}O$ 2–1	0.98±0.09	4.93±0.01	0.35±0.02	2.00	0.27	0.06	0.73± 0.05	no	no
	CH_3OH 2_0–1_0 A^+	0.21±0.04	4.84±0.01	0.33±0.04	1.92	0.28	0.06	0.69± 0.09	no	no
	CH_3OH 2_1–1_1 E	0.10±0.04	4.81±0.01	0.19±0.03	1.45	0.37	0.08	0.34± 0.07	no	no
Cha1-C23										
	$C^{18}O$ 2–1	2.14±0.08	4.97±0.01	0.78±0.03	2.33	0.06	0.04	1.74± 0.07	no	no
	CH_3OH 2_0–1_0 A^+	0.25±0.04	4.80±0.05	0.64±0.09	1.74	0.08	0.05	1.43± 0.20	no	no
	CH_3OH 2_1–1_1 E	0.24±0.05	4.86±0.04	0.57±0.11	1.49	0.09	0.06	1.26± 0.26	no	no
	$C^{34}S$ 2–1	0.19±0.04	5.12±0.02	0.20±0.06	0.67	0.21	0.13	0.41± 0.15	no	no
Cha1-C24										
	$C^{18}O$ 2–1	1.44±0.07	4.53±0.01	0.45±0.03	1.26	0.13	0.06	0.98± 0.06	no	no
	CH_3OH 2_0–1_0 A^+	0.18±0.04	4.39±0.03	0.30±0.06	0.90	0.18	0.09	0.63± 0.16	no	no
Cha1-C25										
	$C^{18}O$ 2–1	0.99±0.07	4.34±0.02	0.56±0.06	1.72	0.11	0.07	1.25± 0.14	no	no
	CH_3OH 2_1–1_1 E	0.08±0.04	4.50±0.03	0.29±0.07	0.91	0.20	0.14	0.59± 0.18	no	no
Cha1-C26										
	C_4H 11_{11}–9_{10}		5.25±0.03	0.26±0.07	1.48	0.30	0.07	0.54± 0.18	no	no
	$C^{18}O$ 2–1	1.60±0.10	5.22±0.01	0.39±0.01	1.94	0.23	0.05	0.83± 0.04	no	no
	$C^{17}O$ 2–1	0.84±0.10	5.06±0.02	0.33±0.05	1.70	0.26	0.06	0.69± 0.12	no	no
	CH_3OH 2_0–1_0 A^+	0.24±0.05	5.14±0.02	0.36±0.06	1.82	0.24	0.06	0.76± 0.14	no	no
	CH_3OH 2_1–1_1 E	0.21±0.06	5.11±0.02	0.34±0.04	1.74	0.25	0.06	0.72± 0.11	no	no
	$C^{34}S$ 2–1	0.23±0.05	5.11±0.03	0.36±0.06	1.85	0.24	0.06	0.78± 0.14	no	no
	HC_3N 10–9	0.18±0.04	5.30±0.02	0.21±0.02	1.35	0.32	0.07	0.42± 0.06	no	no
Cha1-C27										
	$C^{18}O$ 2–1	3.05±0.08	4.40±0.01	0.80±0.02	3.13	0.07	0.04	1.80± 0.05	no	no
	$C^{17}O$ 2–1	0.76±0.06	4.24±0.04	0.67±0.11	2.40	0.09	0.06	1.50± 0.26	no	no
Cha1-C28										
	$C^{18}O$ 2–1	1.34±0.09	4.76±0.03	0.89±0.07	3.25	0.05	0.03	2.00± 0.17	no	no
Cha1-C29										
	H_2CO $3_{1,2}$–$2_{1,1}$		4.43±0.03	0.50±0.07	1.43	0.12	0.09	1.10± 0.16	no	no
	$C^{18}O$ 2–1	2.88±0.12	4.68±0.02	0.88±0.04	3.14	0.05	0.04	1.97± 0.09	no	no
	$C^{17}O$ 2–1	0.56±0.06	4.45±0.04	0.69±0.10	2.16	0.08	0.06	1.54± 0.24	no	no
	CH_3OH 2_0–1_0 A^+	0.79±0.05	4.52±0.01	0.60±0.04	1.79	0.10	0.07	1.33± 0.09	no	no
	CH_3OH 2_1–1_1 E	0.50±0.05	4.54±0.02	0.57±0.04	1.69	0.10	0.08	1.28± 0.10	no	no
	N_2H^+ 1–0	1.08±0.09	4.42±0.01	0.57±0.05	1.67	0.10	0.08	1.26± 0.11	no	no
	$C^{34}S$ 2–1	0.49±0.04	4.52±0.03	0.76±0.09	2.54	0.07	0.05	1.72± 0.21	no	no
	HC_3N 10–9	0.30±0.04	4.46±0.04	0.68±0.13	2.13	0.08	0.06	1.52± 0.30	no	no

Table C.1: continued.

Core	Transition	$I_{\rm int}$[a] (K km s^{-1})	$V_{\rm LSR}$[b] (km s^{-1})	$FWHM$[c] (km s^{-1})	$M_{\rm vir}$[d] ($M_\odot$)	$\frac{M_{\rm tot}}{M_{\rm vir}}$[e]	$\frac{M_{50}}{M_{\rm vir}}$[f]	$\frac{\sigma_{\rm nth}}{\sigma_{\rm th,mean}}$[g]	Gr.[h]	Vir.[i]
Cha1-C30										
	$C^{18}O$ 2–1	0.74±0.13	4.78±0.01	0.21±0.07	1.41	0.32	0.07	0.38± 0.21	no	no
	CH_3OH 2_0–1_0 A^+	0.23±0.05	4.63±0.01	0.20±0.03	1.39	0.33	0.07	0.35± 0.07	no	no
	CH_3OH 2_1–1_1 E	0.14±0.05	4.67±0.01	0.22±0.03	1.46	0.31	0.07	0.43± 0.07	no	no
	N_2H^+ 1–0	0.91±0.10	4.64±0.01	0.23±0.02	1.48	0.31	0.07	0.45± 0.05	no	no
Cha1-C31										
	$C^{18}O$ 2–1	0.69±0.10	4.75±0.01	0.28±0.03	1.22	0.23	0.08	0.57± 0.07	no	no
	CH_3OH 2_0–1_0 A^+	0.16±0.04	4.65±0.01	0.20±0.03	1.04	0.27	0.10	0.36± 0.07	no	no
	CH_3OH 2_1–1_1 E	0.04±0.04	4.62±0.01	0.16±0.05	0.97	0.29	0.10	0.24± 0.16	no	no
	N_2H^+ 1–0	1.08±0.09	4.64±0.01	0.19±0.02	1.02	0.27	0.10	0.33± 0.05	no	no
Cha1-C32										
	$C^{18}O$ 2–1	1.71±0.12	4.56±0.03	0.69±0.08	3.79	0.10	0.03	1.54± 0.19	no	no
	CH_3OH 2_1–1_1 E	0.12±0.04	4.37±0.04	0.34±0.08	1.71	0.23	0.06	0.72± 0.20	no	no
Cha1-C33										
	C_4H $10_{10,10}$–$9_{9,9}$		5.30±0.02	0.30±0.05	0.99	0.18	0.10	0.64± 0.11	no	no
	C_4H 11_{11}–9_{10}		5.38±0.02	0.26±0.04	0.93	0.20	0.11	0.56± 0.10	no	no
	$C^{18}O$ 2–1	1.15±0.13	5.32±0.02	0.45±0.04	1.40	0.13	0.07	0.99± 0.10	no	no
	CH_3OH 2_0–1_0 A^+	0.34±0.04	5.22±0.02	0.36±0.04	1.12	0.16	0.09	0.77± 0.10	no	no
	CH_3OH 2_1–1_1 E	0.15±0.06	5.19±0.03	0.41±0.07	1.26	0.15	0.08	0.88± 0.16	no	no
	N_2H^+ 1–0	1.89±0.08	5.22±0.01	0.31±0.02	1.00	0.18	0.10	0.65± 0.04	no	no
	$C^{34}S$ 2–1	0.31±0.05	5.22±0.01	0.30±0.03	1.01	0.18	0.10	0.65± 0.08	no	no
	HC_3N 10–9	0.99±0.04	5.32±0.01	0.29±0.03	0.98	0.19	0.10	0.62± 0.06	no	no
Cha1-C34										
	C_4H $10_{10,10}$–$9_{9,9}$		5.25±0.02	0.27±0.05	1.68	0.30	0.06	0.57± 0.12	no	no
	C_4H 11_{11}–9_{10}		5.33±0.02	0.27±0.04	1.69	0.30	0.06	0.57± 0.10	no	no
	$C^{18}O$ 2–1	1.29±0.10	5.29±0.01	0.33±0.03	1.86	0.27	0.06	0.68± 0.06	no	no
	$C^{17}O$ 2–1	0.31±0.07	5.09±0.03	0.35±0.07	1.99	0.25	0.05	0.75± 0.18	no	no
	CH_3OH 2_0–1_0 A^+	0.34±0.05	5.18±0.01	0.36±0.03	2.01	0.25	0.05	0.76± 0.07	no	no
	CH_3OH 2_1–1_1 E	0.31±0.07	5.19±0.02	0.35±0.04	1.97	0.26	0.05	0.74± 0.11	no	no
	N_2H^+ 1–0	0.70±0.08	5.18±0.01	0.30±0.03	1.77	0.28	0.06	0.63± 0.07	no	no
	$C^{34}S$ 2–1	0.28±0.04	5.20±0.01	0.29±0.03	1.77	0.28	0.06	0.63± 0.08	no	no
	HC_3N 10–9	0.38±0.05	5.28±0.01	0.23±0.03	1.54	0.33	0.07	0.46± 0.08	no	no
Cha1-C35										
	C_4H $10_{10,10}$–$9_{9,9}$		4.21±0.04	0.49±0.08	1.12	0.11	0.07	1.09± 0.18	no	no
	$C^{18}O$ 2–1	1.94±0.13	4.31±0.01	0.54±0.04	1.24	0.10	0.06	1.19± 0.09	no	no
	$C^{17}O$ 2–1	0.39±0.06	4.13±0.03	0.48±0.07	1.09	0.11	0.07	1.06± 0.17	no	no
	CH_3OH 2_0–1_0 A^+	0.29±0.04	4.01±0.03	0.35±0.10	0.81	0.15	0.10	0.76± 0.25	no	no
	N_2H^+ 1–0	0.59±0.08	4.13±0.02	0.34±0.03	0.78	0.16	0.10	0.72± 0.08	no	no
	$C^{34}S$ 2–1	0.37±0.04	4.22±0.02	0.47±0.05	1.07	0.12	0.07	1.04± 0.12	no	no
	HC_3N 10–9	0.65±0.04	4.23±0.01	0.33±0.03	0.77	0.16	0.10	0.72± 0.07	no	no
Cha1-C36										
	$C^{18}O$ 2–1	1.35±0.14	4.29±0.01	0.35±0.03	0.95	0.15	0.10	0.76± 0.07	no	no
	$C^{17}O$ 2–1	0.28±0.06	4.12±0.03	0.37±0.08	0.98	0.15	0.10	0.78± 0.19	no	no
	CH_3OH 2_0–1_0 A^+	0.30±0.05	4.18±0.01	0.32±0.03	0.87	0.17	0.11	0.66± 0.09	no	no
	CH_3OH 2_1–1_1 E	0.20±0.05	4.14±0.03	0.36±0.07	0.96	0.15	0.10	0.76± 0.16	no	no
Cha1-C37										
	$C^{18}O$ 2–1	1.52±0.10	3.88±0.02	0.53±0.04	1.67	0.12	0.05	1.16± 0.10	no	no

Table C.1: continued.

Core	Transition	$I_{\rm int}$[a] (K km s^{-1})	$V_{\rm LSR}$[b] (km s^{-1})	$FWHM$[c] (km s^{-1})	$M_{\rm vir}$[d] ($M_\odot$)	$\frac{M_{\rm tot}}{M_{\rm vir}}$[e]	$\frac{M_{50}}{M_{\rm vir}}$[f]	$\frac{\sigma_{\rm nth}}{\sigma_{\rm th,mean}}$[g]	Gr.[h]	Vir.[i]
Cha1-C38										
	C_4H 11_{11}–9_{10}		5.32±0.03	0.25±0.05	1.26	0.25	0.08	0.51± 0.12	no	no
	$C^{18}O$ 2–1	1.51±0.14	5.31±0.01	0.36±0.03	1.60	0.19	0.06	0.78± 0.07	no	no
	$C^{17}O$ 2–1	0.48±0.09	5.15±0.02	0.27±0.03	1.30	0.24	0.07	0.55± 0.08	no	no
	CH_3OH 2_0–1_0 A^+	0.31±0.05	5.19±0.01	0.27±0.03	1.30	0.24	0.07	0.55± 0.07	no	no
	$C^{34}S$ 2–1	0.20±0.04	5.21±0.03	0.37±0.07	1.67	0.19	0.06	0.82± 0.17	no	no
	HC_3N 10–9	0.16±0.04	5.32±0.02	0.18±0.08	1.13	0.28	0.09	0.36± 0.22	no	no
Cha1-C39										
	$C^{18}O$ 2–1	2.75±0.13	4.52±0.01	0.49±0.02	1.86	0.13	0.05	1.09± 0.05	no	no
	$C^{17}O$ 2–1	0.68±0.06	4.31±0.02	0.56±0.06	2.16	0.11	0.04	1.24± 0.15	no	no
Cha1-C40										
	$C^{18}O$ 2–1	0.99±0.07	4.75±0.01	0.42±0.03	1.54	0.15	0.06	0.90± 0.07	no	no
	CH_3OH 2_0–1_0 A^+	0.38±0.04	4.62±0.01	0.25±0.02	1.05	0.21	0.09	0.49± 0.06	no	no
	CH_3OH 2_1–1_1 E	0.29±0.04	4.63±0.01	0.22±0.02	0.99	0.23	0.10	0.42± 0.06	no	no
	N_2H^+ 1–0	0.67±0.08	4.61±0.01	0.19±0.02	0.93	0.24	0.10	0.32± 0.05	no	no
	$C^{34}S$ 2–1	0.07±0.03	4.63±0.05	0.41±0.14	1.52	0.15	0.06	0.89± 0.33	no	no
	HC_3N 10–9	0.06±0.03	4.68±0.01	0.18±0.01	0.96	0.23	0.10	0.36± 0.02	no	no
Cha1-C41										
	$C^{18}O$ 2–1	1.83±0.16	5.23±0.01	0.42±0.03	1.04	0.12	0.08	0.90± 0.07	no	no
	$C^{17}O$ 2–1	0.65±0.06	5.11±0.01	0.31±0.04	0.81	0.16	0.10	0.65± 0.10	no	no
	CH_3OH 2_0–1_0 A^+	0.31±0.04	5.14±0.01	0.28±0.03	0.77	0.17	0.11	0.58± 0.08	no	no
	CH_3OH 2_1–1_1 E	0.31±0.06	5.17±0.01	0.26±0.03	0.73	0.17	0.11	0.53± 0.07	no	no
	$C^{34}S$ 2–1	0.27±0.04	5.13±0.02	0.37±0.05	0.94	0.14	0.09	0.80± 0.11	no	no
Cha1-C42										
	$C^{18}O$ 2–1	1.22±0.07	4.52±0.02	0.85±0.06	2.11	0.05	0.03	1.90± 0.13	no	no
	CH_3OH 2_0–1_0 A^+	0.15±0.04	4.42±0.05	0.53±0.09	1.08	0.09	0.06	1.17± 0.22	no	no
	N_2H^+ 1–0	0.51±0.08	4.17±0.03	0.41±0.07	0.82	0.12	0.08	0.89± 0.17	no	no
Cha1-C43										
	$C^{18}O$ 2–1	1.31±0.12	4.70±0.01	0.37±0.02	1.70	0.19	0.05	0.78± 0.05	no	no
	$C^{17}O$ 2–1	0.49±0.06	4.47±0.01	0.27±0.04	1.37	0.23	0.06	0.55± 0.10	no	no
	CH_3OH 2_0–1_0 A^+	0.27±0.04	4.51±0.02	0.33±0.04	1.57	0.20	0.05	0.70± 0.09	no	no
	CH_3OH 2_1–1_1 E	0.13±0.04	4.53±0.02	0.20±0.04	1.20	0.26	0.07	0.37± 0.11	no	no
Cha1-C44										
	$C^{18}O$ 2–1	1.09±0.09	4.59±0.02	0.68±0.04	2.28	0.07	0.03	1.51± 0.10	no	no
Cha1-C45										
	$C^{18}O$ 2–1	0.82±0.08	4.34±0.01	0.36±0.03	0.89	0.14	0.08	0.78± 0.06	no	no
	CH_3OH 2_0–1_0 A^+	0.22±0.04	4.22±0.03	0.42±0.07	1.02	0.12	0.07	0.92± 0.16	no	no
Cha1-C46										
	$C^{18}O$ 2–1	1.19±0.09	4.48±0.02	0.52±0.04	0.84	0.07	0.06	1.15± 0.10	no	no
Cha1-C47										
	$C^{18}O$ 2–1	1.26±0.10	4.61±0.02	0.62±0.05	2.57	0.09	0.04	1.37± 0.12	no	no
Cha1-C48										
	$C^{18}O$ 2–1	1.50±0.09	5.07±0.02	0.85±0.05	2.11	0.04	0.03	1.92± 0.11	no	no
Cha1-C49										
	$C^{18}O$ 2–1	1.70±0.12	5.04±0.01	0.45±0.04	0.83	0.10	0.09	0.98± 0.09	no	no
	$C^{17}O$ 2–1	0.47±0.05	4.83±0.01	0.29±0.04	0.57	0.14	0.12	0.59± 0.10	no	no
	CH_3OH 2_0–1_0 A^+	0.13±0.05	4.80±0.03	0.21±0.07	0.49	0.17	0.15	0.40± 0.19	no	no

Table C.1: continued.

Core	Transition	$I_{\rm int}$[a] (K km s^{-1})	$V_{\rm LSR}$[b] (km s^{-1})	$FWHM$[c] (km s^{-1})	$M_{\rm vir}$[d] ($M_\odot$)	$\frac{M_{\rm tot}}{M_{\rm vir}}$[e]	$\frac{M_{50}}{M_{\rm vir}}$[f]	$\frac{\sigma_{\rm nth}}{\sigma_{\rm th,mean}}$[g]	Gr.[h]	Vir.[i]
Cha1-C50										
	$C^{18}O$ 2–1	1.00±0.06	4.46±0.01	0.31±0.04	1.35	0.18	0.06	0.65± 0.09	no	no
	–[j]	–	5.18±0.02	0.65±0.05	2.92	0.08	0.03	1.44± 0.11	no	no
	CH_3OH 2_0–1_0 A^+	0.59±0.03	5.11±0.03	0.66±0.07	2.98	0.08	0.03	1.46± 0.17	no	no
	CH_3OH 2_1–1_1 E	0.43±0.05	5.17±0.03	0.48±0.06	2.00	0.12	0.04	1.05± 0.14	no	no
Cha1-C51										
	$C^{18}O$ 2–1	3.05±0.12	4.86±0.03	1.15±0.06	3.56	0.02	0.02	2.60± 0.13	no	no
	CH_3OH 2_0–1_0 A^+	0.59±0.05	4.83±0.06	1.23±0.11	4.01	0.02	0.02	2.78± 0.26	no	no
Cha1-C52										
	$C^{18}O$ 2–1	1.67±0.09	4.44±0.02	0.59±0.04	1.39	0.07	0.05	1.31± 0.10	no	no
	–[j]	–	5.48±0.02	0.50±0.04	1.14	0.09	0.06	1.11± 0.09	no	no
	CH_3OH 2_0–1_0 A^+	0.33±0.05	4.52±0.03	0.47±0.06	1.05	0.10	0.06	1.03± 0.15	no	no
	CH_3OH 2_1–1_1 E	0.26±0.04	4.49±0.03	0.44±0.07	0.98	0.10	0.07	0.96± 0.16	no	no
	$C^{34}S$ 2–1	0.15±0.02	4.29±0.03	0.33±0.07	0.77	0.13	0.08	0.71± 0.16	no	no
	–[j]	–	5.33±0.06	0.47±0.10	1.07	0.09	0.06	1.05± 0.24	no	no
Cha1-C53										
	$C^{18}O$ 2–1	2.01±0.12	4.54±0.01	0.47±0.03	1.49	0.10	0.06	1.03± 0.06	no	no
	$C^{17}O$ 2–1	0.48±0.06	4.40±0.03	0.45±0.05	1.42	0.11	0.06	0.98± 0.12	no	no
Cha1-C54										
	$C^{18}O$ 2–1	0.71±0.06	4.51±0.03	0.51±0.09	1.02	0.07	0.06	1.13± 0.21	no	no
	–[j]	–	5.33±0.01	0.49±0.03	0.97	0.08	0.06	1.08± 0.06	no	no
	$C^{17}O$ 2–1	0.44±0.04	5.13±0.03	0.50±0.09	0.99	0.08	0.06	1.11± 0.21	no	no
	CH_3OH 2_0–1_0 A^+	0.27±0.05	5.10±0.05	0.55±0.12	1.10	0.07	0.06	1.21± 0.28	no	no
	$C^{34}S$ 2–1	0.18±0.03	5.22±0.06	0.36±0.14	0.72	0.11	0.08	0.79± 0.33	no	no
Cha1-C55										
	$C^{18}O$ 2–1	2.21±0.09	4.67±0.02	0.99±0.04	2.76	0.03	0.03	2.23± 0.10	no	no
Cha1-C56										
	$C^{18}O$ 2–1	0.97±0.10	4.58±0.01	0.32±0.03	0.62	0.12	0.09	0.67± 0.08	no	no
	CH_3OH 2_0–1_0 A^+	0.15±0.06	4.49±0.02	0.29±0.06	0.58	0.13	0.10	0.59± 0.14	no	no
	CH_3OH 2_1–1_1 E	0.18±0.06	4.44±0.03	0.23±0.06	0.51	0.14	0.11	0.44± 0.16	no	no
Cha1-C57										
	$C^{18}O$ 2–1	1.10±0.12	5.08±0.01	0.30±0.02	0.98	0.15	0.12	0.62± 0.05	no	no
	$C^{17}O$ 2–1	0.38±0.06	4.90±0.02	0.27±0.00	0.92	0.16	0.13	0.55± 0.01	no	no
Cha1-C58										
	$C^{18}O$ 2–1	1.62±0.14	5.31±0.01	0.36±0.02	0.91	0.12	0.10	0.77± 0.06	no	no
	$C^{17}O$ 2–1	0.36±0.07	5.14±0.02	0.31±0.07	0.81	0.14	0.11	0.65± 0.16	no	no
Cha1-C59										
	$C^{18}O$ 2–1	2.12±0.14	5.24±0.02	0.63±0.04	1.18	0.05	0.04	1.41± 0.09	no	no
	$C^{17}O$ 2–1	0.61±0.06	5.02±0.03	0.69±0.07	1.32	0.05	0.04	1.53± 0.16	no	no
Cha1-C60										
	$C^{18}O$ 2–1	2.00±0.12	4.47±0.01	0.48±0.03	1.79	0.10	0.04	1.07± 0.06	no	no
	$C^{17}O$ 2–1	0.46±0.07	4.27±0.02	0.37±0.05	1.37	0.14	0.05	0.80± 0.13	no	no
	CH_3OH 2_0–1_0 A^+	0.03±0.05	4.42±0.03	0.26±0.09	1.07	0.17	0.07	0.53± 0.22	no	no

Notes. [a] Integrated intensities used to calculate the column densities in Sect. 5.4.1. The integrated intensities are computed in $T_{\rm mb}$ scale. [b] Systemic velocities derived from Gaussian and hyperfine-structure fits to the spectra. [c] Linewidths derived from Gaussian and hyperfine-structure fits to the spectra. [d] Virial mass. [e] Ratio of the total dust mass to the virial mass. [f] Ratio of the dust mass within a $50''$ aperture to the virial mass. [g] Non-thermal to the mean thermal velocity dispersion computed for a kinetic temperature of 10 K. [h] Gravitational boundedness of the core as $M_{\rm tot}/M_{\rm vir} > 0.5$. [i] Core is virialised if $M_{\rm tot}/M_{\rm vir} \geq 1$. [j] The dashed lines indicate the kinematic results of the same transition as the previous one listed, but at a different velocity. The integrated intensities are only listed for the velocity components used in the analysis (i.e., the strongest emission peak).

Table C.2: Line parameters and physical parameters of cores in Cha III.

Core	Transition	$I_{\rm int}$[a] (K km s^{-1})	$V_{\rm LSR}$[b] (km s^{-1})	$FWHM$[c] (km s^{-1})	$M_{\rm vir}$[d] ($M_\odot$)	$\frac{M_{\rm tot}}{M_{\rm vir}}$[e]	$\frac{M_{50}}{M_{\rm vir}}$[f]	$\frac{\sigma_{\rm nth}}{\sigma_{\rm th,mean}}$[g]	Gr.[h]	Vir.[i]
Cha3-C1										
	$C^{18}O$ 2–1	1.89±0.07	1.23±0.01	0.49±0.02	3.10	0.50	0.09	1.07± 0.04	no	no
	$C^{17}O$ 2–1	0.49±0.04	1.21±0.01	0.36±0.03	2.32	0.67	0.13	0.77±0.07	yes	no
	CH_3OH 2_0–1_0 A^+	0.42±0.04	1.26±0.01	0.45±0.03	2.86	0.54	0.10	0.99±0.08	yes	no
	CH_3OH 2_1–1_1 E	0.31±0.03	1.29±0.02	0.46±0.04	2.90	0.54	0.10	1.00±0.10	yes	no
	$H^{13}CO^+$ 1–0		1.24±0.03	0.57±0.07	3.75	0.41	0.08	1.26±0.16	no	no
	N_2H^+ 1–0	0.61±0.09	1.24±0.03	0.34±0.07	2.21	0.70	0.13	0.72±0.17	yes	no
	HC_3N 10–9	0.17±0.03	1.46±0.04	0.28±0.04	1.99	0.78	0.15	0.61±0.10	yes	no
Cha3-C2										
	$C^{18}O$ 2–1	1.61±0.07	1.24±0.01	0.57±0.03	2.84	0.20	0.08	1.28± 0.06	no	no
	CH_3OH 2_0–1_0 A^+	0.18±0.04	1.19±0.05	0.45±0.11	2.13	0.27	0.11	0.99± 0.25	no	no
	$H^{13}CO^+$ 1–0		1.30±0.05	0.52±0.10	2.50	0.23	0.09	1.15±0.22	no	no
Cha3-C3										
	$C^{18}O$ 2–1	1.04±0.07	1.45±0.01	0.46±0.03	1.20	0.17	0.09	1.00± 0.08	no	no
	CH_3OH 2_0–1_0 A^+	0.13±0.05	1.45±0.06	0.44±0.09	1.15	0.17	0.10	0.96± 0.22	no	no
Cha3-C4										
	$C^{18}O$ 2–1	1.15±0.08	1.42±0.02	0.60±0.05	2.84	0.15	0.05	1.34± 0.11	no	no
	$C^{17}O$ 2–1	0.22±0.03	1.40±0.04	0.49±0.08	2.18	0.20	0.07	1.07± 0.19	no	no
Cha3-C5										
	$C^{18}O$ 2–1	1.17±0.07	1.69±0.01	0.47±0.03	1.96	0.19	0.07	1.02± 0.07	no	no
	CH_3OH 2_0–1_0 A^+	0.19±0.04	1.69±0.03	0.40±0.09	1.70	0.22	0.08	0.87± 0.21	no	no
	CH_3OH 2_1–1_1 E	0.22±0.04	1.73±0.06	0.58±0.13	2.58	0.14	0.05	1.30± 0.31	no	no
Cha3-C6										
	$C^{18}O$ 2–1	1.06±0.06	1.49±0.01	0.44±0.03	1.66	0.18	0.08	0.96± 0.07	no	no
Cha3-C7										
	$C^{18}O$ 2–1	0.67±0.06	1.62±0.01	0.39±0.04	1.26	0.18	0.08	0.84± 0.09	no	no
	CH_3OH 2_0–1_0 A^+	0.09±0.04	1.64±0.05	0.36±0.10	1.18	0.20	0.09	0.77± 0.23	no	no
Cha3-C8										
	$C^{18}O$ 2–1	0.87±0.06	1.23±0.01	0.34±0.02	1.51	0.25	0.07	0.72± 0.05	no	no
	CH_3OH 2_0–1_0 A^+	0.39±0.04	1.19±0.01	0.29±0.02	1.36	0.28	0.08	0.61± 0.05	no	no
	CH_3OH 2_1–1_1 E	0.26±0.04	1.17±0.01	0.27±0.03	1.30	0.29	0.09	0.55± 0.07	no	no
Cha3-C9										
	$C^{18}O$ 2–1	0.90±0.06	1.37±0.01	0.25±0.01	1.13	0.28	0.10	0.50± 0.04	no	no
	CH_3OH 2_0–1_0 A^+	0.26±0.03	1.36±0.02	0.28±0.05	1.19	0.27	0.09	0.57± 0.12	no	no
	CH_3OH 2_1–1_1 E	0.21±0.03	1.38±0.02	0.35±0.05	1.40	0.23	0.08	0.74± 0.13	no	no
Cha3-C10										
	$C^{18}O$ 2–1	1.06±0.05	1.51±0.01	0.47±0.03	1.14	0.14	0.07	1.03± 0.06	no	no
Cha3-C11										
	$C^{18}O$ 2–1	–	1.16±0.06	0.63±0.12	2.15	0.09	0.05	1.41± 0.28	no	no
	–	0.79±0.07	2.05±0.01	0.21±0.01	0.83	0.24	0.12	0.40± 0.04	no	no
Cha3-C12										
	$C^{18}O$ 2–1	1.01±0.06	1.32±0.01	0.37±0.02	1.56	0.20	0.06	0.79± 0.05	no	no
	CH_3OH 2_0–1_0 A^+	0.25±0.04	1.42±0.05	0.62±0.15	2.82	0.11	0.04	1.39± 0.35	no	no
	CH_3OH 2_1–1_1 E	0.13±0.04	1.31±0.05	0.43±0.11	1.80	0.17	0.06	0.94± 0.26	no	no
Cha3-C13										
	$C^{18}O$ 2–1	0.88±0.05	1.55±0.01	0.31±0.02	1.10	0.20	0.09	0.65± 0.05	no	no
	CH_3OH 2_0–1_0 A^+	0.26±0.03	1.57±0.03	0.46±0.08	1.57	0.14	0.06	1.01± 0.19	no	no
	CH_3OH 2_1–1_1 E	0.16±0.03	1.50±0.02	0.22±0.06	0.91	0.25	0.11	0.41± 0.17	no	no
	$C^{34}S$ 2–1	0.09±0.03	1.57±0.03	0.24±0.05	0.98	0.23	0.10	0.51± 0.12	no	no
	HC_3N 10–9	0.08±0.03	1.55±0.03	0.18±0.34	0.88	0.25	0.11	0.36± 0.90	no	no

Table C.2: continued.

Core	Transition	$I_{\rm int}$[a] (K km s^{-1})	$V_{\rm LSR}$[b] (km s^{-1})	$FWHM$[c] (km s^{-1})	$M_{\rm vir}$[d] ($M_\odot$)	$\frac{M_{\rm tot}}{M_{\rm vir}}$[e]	$\frac{M_{50}}{M_{\rm vir}}$[f]	$\frac{\sigma_{\rm nth}}{\sigma_{\rm th,mean}}$[g]	Gr.[h]	Vir.[i]
Cha3-C14										
	$C^{18}O$ 2–1	1.07±0.06	1.75±0.01	0.43±0.02	1.11	0.15	0.07	0.93± 0.06	no	no
	CH_3OH 2_0–1_0 A^+	0.26±0.05	1.81±0.03	0.43±0.07	1.12	0.15	0.07	0.93± 0.17	no	no
Cha3-C15										
	$C^{18}O$ 2–1	0.89±0.06	1.42±0.01	0.46±0.03	1.59	0.14	0.06	1.01± 0.07	no	no
	CH_3OH 2_0–1_0 A^+	0.25±0.04	1.47±0.02	0.28±0.05	1.06	0.20	0.08	0.58± 0.11	no	no
	CH_3OH 2_1–1_1 E	0.17±0.03	1.42±0.03	0.36±0.07	1.27	0.17	0.07	0.78± 0.18	no	no
	$H^{13}CO^+$ 1–0		1.44±0.04	0.54±0.08	1.90	0.11	0.05	1.18±0.18	no	no
	N_2H^+ 1–0	0.30±0.09	1.45±0.01	0.21±0.04	0.90	0.24	0.10	0.38± 0.11	no	no
	HC_3N 10–9	0.41±0.03	1.51±0.01	0.23±0.01	0.98	0.22	0.09	0.48± 0.04	no	no
Cha3-C16										
	$C^{18}O$ 2–1	0.93±0.06	1.29±0.01	0.49±0.04	1.68	0.12	0.05	1.07± 0.09	no	no
	CH_3OH 2_0–1_0 A^+	0.13±0.04	1.27±0.05	0.36±0.12	1.27	0.16	0.07	0.79± 0.29	no	no
Cha3-C17										
	$C^{18}O$ 2–1	1.24±0.06	1.52±0.02	0.65±0.04	0.97	0.06	0.05	1.46± 0.10	no	no
Cha3-C18										
	$C^{18}O$ 2–1	1.63±0.06	1.39±0.01	0.69±0.03	1.50	0.06	0.08	1.54± 0.07	no	no
	CH_3OH 2_0–1_0 A^+	0.36±0.04	1.34±0.02	0.46±0.05	0.90	0.10	0.14	1.00± 0.11	no	no
	CH_3OH 2_1–1_1 E	0.31±0.04	1.37±0.03	0.53±0.08	1.07	0.09	0.12	1.19± 0.19	no	no
	$C^{34}S$ 2–1	0.13±0.04	1.48±0.05	0.44±0.09	0.88	0.10	0.14	0.98± 0.21	no	no
Cha3-C19										
	$C^{18}O$ 2–1	1.14±0.06	1.29±0.01	0.36±0.02	0.94	0.14	0.10	0.78± 0.05	no	no
	CH_3OH 2_0–1_0 A^+	0.31±0.04	1.24±0.01	0.26±0.04	0.73	0.17	0.12	0.51± 0.11	no	no
	CH_3OH 2_1–1_1 E	0.16±0.04	1.24±0.01	0.23±0.02	0.69	0.18	0.13	0.44± 0.06	no	no
	$H^{13}CO^+$ 1–0		1.28±0.04	0.32±0.09	0.84	0.15	0.11	0.68±0.23	no	no
Cha3-C20										
	$C^{18}O$ 2–1	1.26±0.06	1.35±0.01	0.41±0.02	0.90	0.12	0.09	0.88± 0.05	no	no
	CH_3OH 2_0–1_0 A^+	0.26±0.04	1.29±0.02	0.34±0.05	0.78	0.14	0.11	0.73± 0.12	no	no
	CH_3OH 2_1–1_1 E	0.25±0.04	1.30±0.04	0.52±0.08	1.17	0.09	0.07	1.14± 0.20	no	no
	$H^{13}CO^+$ 1–0		1.38±0.05	0.34±0.12	0.76	0.14	0.11	0.71±0.31	no	no
Cha3-C21										
	$C^{18}O$ 2–1	–	0.86±0.08	0.73±0.27	1.96	0.06	0.03	1.65± 0.62	no	no
	–	0.58±0.05	2.04±0.04	0.72±0.09	1.90	0.06	0.03	1.61± 0.21	no	no
Cha3-C22										
	$C^{18}O$ 2–1	0.84±0.06	1.53±0.01	0.32±0.02	0.82	0.14	0.09	0.68± 0.06	no	no
Cha3-C23										
	$C^{18}O$ 2–1	0.48±0.06	1.89±0.01	0.27±0.03	1.14	0.23	0.06	0.55± 0.07	no	no
Cha3-C24										
	$C^{18}O$ 2–1	0.92±0.06	1.76±0.02	0.54±0.03	2.20	0.10	0.04	1.20± 0.08	no	no
Cha3-C25										
	$C^{18}O$ 2–1	0.67±0.06	1.18±0.01	0.29±0.02	0.62	0.13	0.08	0.59± 0.05	no	no
Cha3-C26										
	$C^{18}O$ 2–1	0.90±0.06	1.35±0.01	0.34±0.02	0.40	0.10	0.14	0.72± 0.05	no	no
Cha3-C27										
	$C^{18}O$ 2–1	0.36±0.04	1.65±0.05	0.64±0.12	1.35	0.05	0.04	1.43± 0.29	no	no
Cha3-C28										
	$C^{18}O$ 2–1	0.77±0.06	1.25±0.01	0.33±0.03	0.56	0.10	0.07	0.70± 0.06	no	no
Cha3-C29										
	$C^{18}O$ 2–1	0.75±0.06	1.55±0.02	0.48±0.04	1.00	0.08	0.06	1.05± 0.09	no	no

Notes. Same as Table C.1.

Appendix D

Critical densities

For the calculation of critical densities we use the Einstein A-coefficients, the collisional rate coefficients, and energies from the Leiden Atomic and Molecular Database (LAMDA[1]).

The critical density is the density at which the rate of spontaneous emission is equal to the emission arising from collisional excitation,

$$n_{cr} = \frac{A_{ul}}{\gamma_{ul}}, \tag{D.1}$$

where A_{ul} is the Einstein coefficient for spontaneous emmision (s^{-1}), $C_{ul} = n_{H_2}\gamma_{ul}$ the collision coefficient (collision de-excitation rate, s^{-1}), and γ_{ul} the collision rate ($cm^3\ s^{-1}$). The critical densities we derive are listed in Table D.1 for various molecular transitions.

Table D.1: Critical densities.

Transition	A_{ul}[a] (s^{-1})	γ_{ul}[b] ($cm^{-3}\ s^{-1}$)	T[c] (K)	n_{cr}[d] (cm^{-3})
$C^{18}O$ 2–1	6.01×10^{-7}	7.15×10^{-11}	10	8.4×10^{3}
$C^{17}O$ 2–1	6.43×10^{-7}	7.15×10^{-11}	10	9.0×10^{3}
$CH_3OH\ 2_0–1_0\ A^+$	3.41×10^{-6}	1.10×10^{-10}	10	3.1×10^{4}
$CH_3OH\ 2_1–1_1\ E$	2.49×10^{-6}	7.50×10^{-11}	10	3.3×10^{4}
$H^{13}CO^+$ 1–0	3.85×10^{-5}	2.60×10^{-10}	10	1.5×10^{5}
N_2H^+ 1–0	3.90×10^{-5}	1.60×10^{-10}	10	2.4×10^{5}
HNC 1–0	2.69×10^{-5}	9.71×10^{-11}	10	2.8×10^{5}
$C^{34}S$ 2–1	1.60×10^{-5}	5.30×10^{-11}	20	3.0×10^{5}
CS 2–1	1.68×10^{-5}	5.30×10^{-11}	20	3.2×10^{5}
HC_3N 10–9	5.81×10^{-5}	9.70×10^{-11}	10	6.0×10^{5}

Notes. [(a)] Einstein coefficient for the molecular transition with quantum numbers u to l. [(b)] Collision rate. [(c)] Temperature corresponding to the listed collision rate. [(d)] Critical density computed as $n_{cr} = \frac{A_{ul}}{\gamma_{ul}}$.

[1] http://home.strw.leidenuniv.nl/ moldata/

Appendix E

Optical depths of the Cha I and III cores

E.1 $C^{18}O$ 2–1 opacity

$C^{18}O$ 2–1 was observed toward all 60 cores in Cha I and $C^{17}O$ 2–1 toward 32. We estimate the optical depth of the $C^{18}O$ 2–1 transition for this sample of 32 cores. We assume an isotopic ratio of $[^{18}O]/[^{17}O] \sim 4.11$, as was found for the nearby (140 pc) low-mass cloud ρ Ophiuchus (Wouterloot et al., 2005) to derive the opacity of $C^{18}O$ 2–1 with the following relation:

$$\frac{I_{C^{18}O}}{I_{C^{17}O}} = \frac{1 - e^{-\tau_{C^{18}O}}}{1 - e^{-\tau_{C^{17}O}}} \tag{E.1}$$

where $I_{C^{18}O}$ and $I_{C^{17}O}$ are the integrated intensities of the two transitions, $\tau_{C^{18}O}$ and $\tau_{C^{17}O}$ their opacities and $\tau_{C^{17}O}=\tau_{C^{18}O}/4.11$. Table E.1 lists the opacity estimates for the sample of 32 cores in Cha I. Approximately half of them are somewhat optically thick ($4.2 > \tau_{C^{18}O} \geq 1$) in $C^{18}O$ 2–1.

We can only calculate the $C^{18}O$ 2–1 opacities for the two cores in Cha III that were also observed in $C^{17}O$ 2–1, Cha3-C1 and Cha3-C4. Cha3-C1 is borderline optically thick/thin with an opacity of ~ 1, while Cha3-C4 is optically thin (Table E.2). They are both optically thin in $C^{17}O$ 2–1.

E.2 CS 2–1 opacity

We assume an isotopic ratio of $[^{32}S]/[^{34}S] \sim 22$ (Frerking et al., 1980) to calculate the opacity of the CS 2–1 line in Cha I. All 57 CS 2–1 spectra feature detections and 23 out of the 57 are detected in $C^{34}S$ 2–1. We follow the same method as above to estimate the CS 2–1 opacities toward the 23 cores that are detected in both transitions. The results are given in Table E.3.

For the rest 34 spectra we calculate upper limits for the CS 2–1 opacity by using the ratio of the CS 2–1 integrated intensity to the value of $3 \times rms$ of the $C^{34}S$ 2–1 spectra. The opacity upper limits are listed in Table E.4. All 23 cores that have detections in $C^{34}S$ 2–1 are optically thick in CS 2–1, with opacities ranging from $\sim 2 - 10$.

Two cores in Cha III are detected in $C^{34}S$ 2–1 and their CS 2–1 opacity is listed in Table E.5. Both have CS 2–1 opacities greater than one, while they are optically thin in $C^{34}S$ 2–1. CS 2–1 is detected toward all remaining cores, for which we calculate upper limits (Table E.6) in the same way as for the Cha I cores.

Table E.1: $C^{18}O$ 2–1 and $C^{17}O$ 2–1 opacities of the Cha I cores.

Core	$\frac{I_{c18o}}{I_{c17o}}$ [a]	τ_{c18o} [b]	τ_{c17o} [c]
Cha1-C1	2.37±0.12	1.76	0.43
Cha1-C2	2.37±0.18	1.77	0.43
Cha1-C3	3.26±0.27	0.66	0.16
Cha1-C4	2.34±0.20	1.81	0.44
Cha1-C5	3.29±0.48	0.63	0.15
Cha1-C7	3.80±0.17	0.21	0.05
Cha1-C9	3.03±0.47	0.89	0.22
Cha1-C10	2.95±0.33	0.97	0.24
Cha1-C11	3.97±0.91	0.09	0.02
Cha1-C12	2.40±0.17	1.73	0.42
Cha1-C15	2.46±0.21	1.63	0.40
Cha1-C17	2.12±0.24	2.26	0.55
Cha1-C18	2.71±0.38	1.27	0.31
Cha1-C19	3.14±0.40	0.77	0.19
Cha1-C21	2.18±0.21	2.11	0.51
Cha1-C26	1.76±0.25	3.24	0.79
Cha1-C27	2.97±0.24	0.96	0.23
Cha1-C29	4.42±0.55	0.00	0.00
Cha1-C35	4.17±0.78	0.00	0.00
Cha1-C36	2.71±0.47	1.27	0.31
Cha1-C38	2.84±0.66	1.10	0.27
Cha1-C39	4.08±0.64	0.01	0.00
Cha1-C41	2.20±0.29	2.09	0.51
Cha1-C43	1.54±0.25	4.20	1.02
Cha1-C49	2.64±0.40	1.36	0.33
Cha1-C53	4.38±0.66	0.00	0.00
Cha1-C54	4.79±0.93	0.00	0.00
Cha1-C57	1.88±0.31	2.86	0.70
Cha1-C58	2.74±0.51	1.23	0.30
Cha1-C59	5.31±1.36	0.00	0.00
Cha1-C60	3.09±0.41	0.81	0.20

Notes. [a] Integrated intensity ratio of the two isotopologues. [b] $C^{18}O$ 2–1 opacity. [c] $C^{17}O$ 2–1 opacity.

Table E.2: $C^{18}O$ 2–1 and $C^{17}O$ 2–1 opacities of the Cha III cores.

Core	$\frac{I_{c18o}}{I_{c17o}}$ [a]	τ_{c18o} [b]	τ_{c17o} [c]
Cha3-C1	2.83±0.21	1.11	0.27
Cha3-C4	3.85±0.54	0.17	0.04

Notes. [(a)] Integrated intensity ratio of the two isotopologues. [(b)] $C^{18}O$ 2–1 opacity. [(c)] $C^{17}O$ 2–1 opacity.

Table E.3: CS 2–1 and $C^{34}S$ 2–1 opacities of the Cha I cores.

Core	$\frac{I_{cs}}{I_{c34s}}$ [a]	τ_{cs} [b]	τ_{c34s} [c]
Cha1-C1	6.63±0.55	3.49	0.16
Cha1-C2	4.74±0.45	5.17	0.24
Cha1-C3	5.90±0.87	4.00	0.18
Cha1-C4	2.71±0.27	10.11	0.46
Cha1-C9	9.24±5.91	2.23	0.10
Cha1-C10	5.44±0.85	4.40	0.20
Cha1-C11	6.43±1.13	3.60	0.16
Cha1-C16	2.94±0.35	9.17	0.42
Cha1-C17	2.94±0.35	9.17	0.42
Cha1-C18	7.47±3.04	3.00	0.14
Cha1-C19	5.35±0.77	4.49	0.20
Cha1-C21	6.87±1.93	3.31	0.15
Cha1-C23	5.15±1.41	4.71	0.21
Cha1-C26	4.27±1.00	5.86	0.27
Cha1-C29	4.73±0.54	5.20	0.24
Cha1-C33	5.05±0.89	4.80	0.22
Cha1-C34	3.08±0.52	8.66	0.39
Cha1-C35	5.52±0.75	4.34	0.20
Cha1-C38	5.07±1.56	4.80	0.22
Cha1-C40	5.12±3.22	4.74	0.22
Cha1-C41	5.06±1.10	4.80	0.22
Cha1-C52	8.77±2.39	2.40	0.11
Cha1-C54	8.57±3.38	2.49	0.11

Notes. [(a)] Integrated intensity ratio of the two isotopologues. [(b)] CS 2–1 opacity. [(c)] $C^{34}S$ 2–1 opacity.

Table E.4: CS 2–1 upper limit opacities of the Cha I cores.

Core	$\frac{I_{cs}}{3\times\sigma_{I,c34s}}$ [a]	τ_{cs} [b]
Cha1-C5	3.56±0.29	7
Cha1-C6	4.69±0.36	5
Cha1-C7	7.73±0.39	3
Cha1-C8	9.54±0.35	2
Cha1-C12	6.43±0.34	4
Cha1-C13	2.40±0.35	12
Cha1-C14	9.58±0.43	2
Cha1-C15	3.34±0.28	8
Cha1-C16	1.77±0.33	18
Cha1-C20	1.76±0.42	18
Cha1-C22	3.94±0.29	6
Cha1-C24	0.92±0.37	> 1000[c]
Cha1-C25	2.06±0.35	15
Cha1-C27	2.18±0.38	14
Cha1-C28	2.25±0.36	13
Cha1-C30	1.36±0.37	29
Cha1-C31	3.58±0.36	7
Cha1-C32	2.90±0.36	9
Cha1-C36	3.40±0.34	8
Cha1-C37	3.45±0.39	8
Cha1-C39	6.18±0.37	4
Cha1-C42	5.34±0.30	5
Cha1-C43	1.18±0.38	41
Cha1-C44	1.81±0.32	18
Cha1-C45	2.04±0.30	15
Cha1-C46	2.91±0.35	9
Cha1-C47	2.27±0.40	13
Cha1-C48	3.95±0.37	6
Cha1-C49	6.48±0.31	4
Cha1-C50	8.82±0.34	2
Cha1-C51	1.56±0.39	23
Cha1-C53	4.31±0.34	6
Cha1-C55	1.97±0.32	16
Cha1-C56	2.40±0.35	12

Notes. [(a)] Ratio of CS 2–1 integrated intensity to 3σ of the $C^{34}S$ 2–1 non-detections. [(b)] CS 2–1 upper limit opacity. [(c)] For integrated intensity ratios < 1 the estimated upper limit opacity is > 1000.

Table E.5: CS 2–1 and $C^{34}S$ 2–1 opacities of the Cha III cores.

Core	$\frac{I_{cs}}{I_{c34s}}$ [a]	τ_{cs} [b]	τ_{c34s} [c]
Cha3-C13	7.26±2.23	3.11	0.14
Cha3-C18	6.91±1.66	3.31	0.15

Notes. [(a)] Integrated intensity ratio of the two isotopologues. [(b)] CS 2–1 opacity. [(c)] $C^{34}S$ 2–1 opacity.

Table E.6: CS 2–1 upper limit opacities of the Cha III cores.

Core	$\frac{I_{cs}}{3\times\sigma_{I,c34s}}$ [a]	τ_{cs} [b]
Cha3-C1	13.76±0.36	1
Cha3-C2	7.26±0.32	3
Cha3-C3	2.71±0.36	10
Cha3-C4	4.30±0.33	6
Cha3-C5	5.28±0.38	5
Cha3-C6	2.94±0.34	9
Cha3-C7	4.22±0.49	6
Cha3-C8	4.08±0.30	6
Cha3-C9	4.64±0.37	5
Cha3-C10	4.19±0.44	6
Cha3-C11	4.21±0.59	6
Cha3-C12	5.54±0.48	4
Cha3-C14	7.40±0.66	3
Cha3-C15	6.57±0.40	4
Cha3-C16	7.19±0.43	3
Cha3-C17	5.57±0.43	4
Cha3-C19	5.90±0.36	4
Cha3-C20	6.92±0.33	3

Notes. [(a)] Ratio of CS 2–1 integrated intensity to 3σ of the $C^{34}S$ 2–1 non-detections. [(b)] CS 2–1 upper limit opacity.

Bibliography

Adams, W. S. 1941, ApJ, 93, 11 (Not cited.)

Aikawa, Y., Herbst, E., Roberts, H., & Caselli, P. 2005, ApJ, 620, 330 (Not cited.)

Aikawa, Y., Ohashi, N., Inutsuka, S.-i., Herbst, E., & Takakuwa, S. 2001, ApJ, 552, 639 (Not cited.)

Alves, J., Lombardi, M., & Lada, C. J. 2007, A&A, 462, L17 (Not cited.)

Alves, J. F., Lada, C. J., & Lada, E. A. 2001, Nature, 409, 159 (Not cited.)

Anathpindika, S. & Francesco, J. D. 2013, MNRAS, 430, 1854 (Not cited.)

André, P. 2013, ArXiv e-prints (Not cited.)

André, P., Basu, S., & Inutsuka, S. 2009, The formation and evolution of prestellar cores, ed. G. Chabrier (Cambridge University Press), 254 (Not cited.)

André, P., Belloche, A., Motte, F., & Peretto, N. 2007, A&A, 472, 519 (Not cited.)

André, P., Men'shchikov, A., Bontemps, S., et al. 2010, A&A, 518, L102 (Not cited.)

André, P., Ward-Thompson, D., & Barsony, M. 1993, ApJ, 406, 122 (Not cited.)

André, P., Ward-Thompson, D., & Barsony, M. 2000, Protostars and Planets IV, 59 (Not cited.)

Andre, P., Ward-Thompson, D., & Motte, F. 1996, A&A, 314, 625 (Not cited.)

Arons, J. & Max, C. E. 1975, ApJ, 196, L77 (Not cited.)

Arzoumanian, D., André, P., Didelon, P., et al. 2011, A&A, 529, L6 (Not cited.)

Bacmann, A., André, P., Puget, J.-L., et al. 2000, A&A, 361, 555 (Not cited.)

Bacmann, A., Lefloch, B., Ceccarelli, C., et al. 2002, A&A, 389, L6 (Not cited.)

Bacmann, A., Lefloch, B., Ceccarelli, C., et al. 2003, ApJ, 585, L55 (Not cited.)

Bacmann, A., Taquet, V., Faure, A., Kahane, C., & Ceccarelli, C. 2012, A&A, 541, L12 (Not cited.)

Ballesteros-Paredes, J. & Hartmann, L. 2007, Rev. Mexicana Astron. Astrofis., 43, 123 (Not cited.)

Ballesteros-Paredes, J., Klessen, R. S., Mac Low, M.-M., & Vazquez-Semadeni, E. 2007, Protostars and Planets V, 63 (Not cited.)

Ballesteros-Paredes, J., Klessen, R. S., & Vázquez-Semadeni, E. 2003, ApJ, 592, 188 (Not cited.)

Ballesteros-Paredes, J., Vázquez-Semadeni, E., & Scalo, J. 1999, ApJ, 515, 286 (Not cited.)

Bally, J., Walawender, J., Luhman, K. L., & Fazio, G. 2006, AJ, 132, 1923 (Not cited.)

Barranco, J. A. & Goodman, A. A. 1998, ApJ, 504, 207 (Not cited.)

Basu, S. & Mouschovias, T. C. 1995, ApJ, 452, 386 (Not cited.)

Bate, M. R., Bonnell, I. A., & Bromm, V. 2003, MNRAS, 339, 577 (Not cited.)

Bates, D. R. & Spitzer, Jr., L. 1951, ApJ, 113, 441 (Not cited.)

Beichman, C. A., Myers, P. C., Emerson, J. P., et al. 1986, ApJ, 307, 337 (Not cited.)

Belloche, A. 2002, PhD thesis, Service d'Astrophysique, CEA/DSM/DAPNIA, C.E. Saclay, 91191, Gif-sur-Yvette Cedex, France (Not cited.)

Belloche, A. 2013, ArXiv e-prints (Not cited.)

Belloche, A. & André, P. 2004, A&A, 419, L35 (Not cited.)

Belloche, A., André, P., Despois, D., & Blinder, S. 2002, A&A, 393, 927 (Not cited.)

Belloche, A., André, P., & Motte, F. 2001, in Astronomical Society of the Pacific Conference Series, Vol. 243, From Darkness to Light: Origin and Evolution of Young Stellar Clusters, ed. T. Montmerle & P. André, 313 (Not cited.)

Belloche, A., Parise, B., van der Tak, F. F. S., et al. 2006, A&A, 454, L51 (Not cited.)

Belloche, A., Schuller, F., Parise, B., et al. 2011a, A&A, 527, A145 (Not cited.)

Belloche, A., Parise, B., Schuller, F., et al. 2011b, A&A, 535, A2 (Not cited.)

Benedettini, M., Pezzuto, S., Burton, M. G., et al. 2012, MNRAS, 419, 238 (Not cited.)

Benson, P. J., Caselli, P., & Myers, P. C. 1998, ApJ, 506, 743 (Not cited.)

Bergin, E. A., Alves, J., Huard, T., & Lada, C. J. 2002, ApJ, 570, L101 (Not cited.)

Bergin, E. A., Ciardi, D. R., Lada, C. J., Alves, J., & Lada, E. A. 2001, ApJ, 557, 209 (Not cited.)

Bergin, E. A., Hartmann, L. W., Raymond, J. C., & Ballesteros-Paredes, J. 2004, ApJ, 612, 921 (Not cited.)

Bergin, E. A., Langer, W. D., & Goldsmith, P. F. 1995, ApJ, 441, 222 (Not cited.)

Bergin, E. A., Melnick, G. J., Gerakines, P. A., Neufeld, D. A., & Whittet, D. C. B. 2005, ApJ, 627, L33 (Not cited.)

Bernes, C. 1979, A&A, 73, 67 (Not cited.)

Blinder, S. 1997, Thesis, Université de Bordeaux I (Not cited.)

Blitz, L. 1993, in Protostars and Planets III, ed. E. H. Levy & J. I. Lunine, 125–161 (Not cited.)

Bodenheimer, P. 1995, ARA&A, 33, 199 (Not cited.)

Bodenheimer, P. & Sweigart, A. 1968, ApJ, 152, 515 (Not cited.)

Bohlin, R. C., Savage, B. D., & Drake, J. F. 1978, ApJ, 224, 132 (Not cited.)

Bonnell, I. A., Bate, M. R., & Zinnecker, H. 1998, MNRAS, 298, 93 (Not cited.)

Bonnell, I. A., Vine, S. G., & Bate, M. R. 2004, MNRAS, 349, 735 (Not cited.)

Bonnor, W. B. 1956, MNRAS, 116, 351 (Not cited.)

Bontemps, S., André, P., Könyves, V., et al. 2010, A&A, 518, L85 (Not cited.)

Boulanger, F., Bronfman, L., Dame, T. M., & Thaddeus, P. 1998, A&A, 332, 273 (Not cited.)

Bourke, T. L., Myers, P. C., Evans, II, N. J., et al. 2006, ApJ, 649, L37 (Not cited.)

Brinch, C. & Hogerheijde, M. R. 2010, A&A, 523, A25 (Not cited.)

Burkert, A. & Bodenheimer, P. 2000, ApJ, 543, 822 (Not cited.)

Cabrit, S. & Bertout, C. 1990, ApJ, 348, 530 (Not cited.)

Caselli, P., Benson, P. J., Myers, P. C., & Tafalla, M. 2002a, ApJ, 572, 238 (Not cited.)

Caselli, P., Benson, P. J., Myers, P. C., & Tafalla, M. 2002b, ApJ, 572, 238 (Not cited.)

Caselli, P., Walmsley, C. M., Terzieva, R., & Herbst, E. 1998, ApJ, 499, 234 (Not cited.)

Caselli, P., Walmsley, C. M., Zucconi, A., et al. 2002c, ApJ, 565, 331 (Not cited.)

Caselli, P., Walmsley, C. M., Zucconi, A., et al. 2002d, ApJ, 565, 344 (Not cited.)

Chapman, N. L., Davidson, J. A., Goldsmith, P. F., et al. 2013, ApJ, 770, 151 (Not cited.)

Chen, X., Arce, H. G., Dunham, M. M., et al. 2012, ApJ, 751, 89 (Not cited.)

Chen, X., Arce, H. G., Zhang, Q., et al. 2010, ApJ, 715, 1344 (Not cited.)

Cheung, A. C., Rank, D. M., Townes, C. H., Thornton, D. D., & Welch, W. J. 1968, Physical Review Letters, 21, 1701 (Not cited.)

Christie, H., Viti, S., Yates, J., et al. 2012, MNRAS, 422, 968 (Not cited.)

Ciardi, A. & Hennebelle, P. 2010, MNRAS, 409, L39 (Not cited.)

Ciolek, G. E. & Basu, S. 2000, ApJ, 529, 925 (Not cited.)

Ciolek, G. E. & Basu, S. 2001, ApJ, 547, 272 (Not cited.)

Ciolek, G. E. & Mouschovias, T. C. 1994a, ApJ, 425, 142 (Not cited.)

Ciolek, G. E. & Mouschovias, T. C. 1994b, ApJ, 425, 142 (Not cited.)

Ciolek, G. E. & Mouschovias, T. C. 1995, ApJ, 454, 194 (Not cited.)

Commerçon, B., Hennebelle, P., Audit, E., Chabrier, G., & Teyssier, R. 2010, A&A, 510, L3 (Not cited.)

Commerçon, B., Launhardt, R., Dullemond, C., & Henning, T. 2012, A&A, 545, A98 (Not cited.)

Crapsi, A., Caselli, P., Walmsley, C. M., et al. 2004, A&A, 420, 957 (Not cited.)

Crapsi, A., van Dishoeck, E. F., Hogerheijde, M. R., Pontoppidan, K. M., & Dullemond, C. P. 2008, A&A, 486, 245 (Not cited.)

Crutcher, R. M. 1999, ApJ, 520, 706 (Not cited.)

Crutcher, R. M., Nutter, D. J., Ward-Thompson, D., & Kirk, J. M. 2004, ApJ, 600, 279 (Not cited.)

Curtis, E. I. & Richer, J. S. 2011, MNRAS, 410, 75 (Not cited.)

Di Francesco, J., André, P., & Myers, P. C. 2004, ApJ, 617, 425 (Not cited.)

di Francesco, J., Evans, II, N. J., Caselli, P., et al. 2007, Protostars and Planets V, 17 (Not cited.)

Diaz-Miller, R. I., Franco, J., & Shore, S. N. 1998, ApJ, 501, 192 (Not cited.)

Draine, B. T. 2011, Physics of the Interstellar and Intergalactic Medium (Not cited.)

Dunham, M. M., Chen, X., Arce, H. G., et al. 2011, ApJ, 742, 1 (Not cited.)

Dunham, M. M., Crapsi, A., Evans, II, N. J., et al. 2008, ApJS, 179, 249 (Not cited.)

Dunham, M. M., Evans, II, N. J., Bourke, T. L., et al. 2006, ApJ, 651, 945 (Not cited.)

Ebert, R. 1957, ZAp, 42, 263 (Not cited.)

Elmegreen, B. G. 1993, ApJ, 411, 170 (Not cited.)

Elmegreen, B. G. 2000, ApJ, 530, 277 (Not cited.)

Elmegreen, B. G. & Elmegreen, D. M. 1987, ApJ, 320, 182 (Not cited.)

Enoch, M. L., Evans, II, N. J., Sargent, A. I., et al. 2008, ApJ, 684, 1240 (Not cited.)

Enoch, M. L., Lee, J.-E., Harvey, P., Dunham, M. M., & Schnee, S. 2010, ApJ, 722, L33 (Not cited.)

Enoch, M. L., Young, K. E., Glenn, J., et al. 2006, ApJ, 638, 293 (Not cited.)

Evans, II, N. 2003, in SFChem 2002: Chemistry as a Diagnostic of Star Formation, ed. C. L. Curry & M. Fich, 157 (Not cited.)

Evans, II, N. J., Allen, L. E., Blake, G. A., et al. 2003, PASP, 115, 965 (Not cited.)

Evans, II, N. J., Dunham, M. M., Jørgensen, J. K., et al. 2009, ApJS, 181, 321 (Not cited.)

Falgarone, E., Troland, T. H., Crutcher, R. M., & Paubert, G. 2008, A&A, 487, 247 (Not cited.)

Fatuzzo, M. & Adams, F. C. 2002, ApJ, 570, 210 (Not cited.)

Fiedler, R. A. & Mouschovias, T. C. 1993, ApJ, 415, 680 (Not cited.)

Fiege, J. D. & Pudritz, R. E. 2000, MNRAS, 311, 85 (Not cited.)

Foster, P. N. & Chevalier, R. A. 1993, ApJ, 416, 303 (Not cited.)

Frerking, M. A., Langer, W. D., & Wilson, R. W. 1982, ApJ, 262, 590 (Not cited.)

Frerking, M. A., Wilson, R. W., Linke, R. A., & Wannier, P. G. 1980, ApJ, 240, 65 (Not cited.)

Friberg, P., Hjalmarson, A., Madden, S. C., & Irvine, W. M. 1988, A&A, 195, 281 (Not cited.)

Furuya, K., Aikawa, Y., Tomida, K., et al. 2012, ApJ, 758, 86 (Not cited.)

Gahm, G. F., Lehtinen, K., Carlqvist, P., et al. 2002, A&A, 389, 577 (Not cited.)

Galván-Madrid, R., Vázquez-Semadeni, E., Kim, J., & Ballesteros-Paredes, J. 2007, ApJ, 670, 480 (Not cited.)

Gammie, C. F. & Ostriker, E. C. 1996, ApJ, 466, 814 (Not cited.)

Garrod, R. T. 2013, ApJ, 765, 60 (Not cited.)

Garrod, R. T., Weaver, S. L. W., & Herbst, E. 2008, ApJ, 682, 283 (Not cited.)

Garrod, R. T., Williams, D. A., Hartquist, T. W., Rawlings, J. M. C., & Viti, S. 2005, MNRAS, 356, 654 (Not cited.)

Garrod, R. T., Williams, D. A., & Rawlings, J. M. C. 2006a, ApJ, 638, 827 (Not cited.)

Garrod, R. T., Williams, D. A., & Rawlings, J. M. C. 2006b, MNRAS, 373, 577 (Not cited.)

Gerin, M., de Luca, M., Black, J., et al. 2010, A&A, 518, L110 (Not cited.)

Gibb, E. L., Whittet, D. C. B., Boogert, A. C. A., & Tielens, A. G. G. M. 2004, ApJS, 151, 35 (Not cited.)

Gillett, F. C. & Forrest, W. J. 1973, ApJ, 179, 483 (Not cited.)

Girart, J. M., Beltrán, M. T., Zhang, Q., Rao, R., & Estalella, R. 2009, Science, 324, 1408 (Not cited.)

Girart, J. M., Rao, R., & Marrone, D. P. 2006, Science, 313, 812 (Not cited.)

Gómez, M., Persi, P., Marenzi, A. R., Roth, M., & Tapia, M. 2004, A&A, 423, 629 (Not cited.)

Goodman, A. A., Barranco, J. A., Wilner, D. J., & Heyer, M. H. 1998, ApJ, 504, 223 (Not cited.)

Goodman, A. A., Benson, P. J., Fuller, G. A., & Myers, P. C. 1993, ApJ, 406, 528 (Not cited.)

Gould, B. G. 1879, Resultados del Observatorio Nacional Argentino, 1, 0 (Not cited.)

Gould, R. J. & Salpeter, E. E. 1963, ApJ, 138, 393 (Not cited.)

Greene, T. P. & Lada, C. J. 1996, AJ, 112, 2184 (Not cited.)

Greene, T. P., Wilking, B. A., Andre, P., Young, E. T., & Lada, C. J. 1994, ApJ, 434, 614 (Not cited.)

Gregersen, E. M. & Evans, II, N. J. 2000, ApJ, 538, 260 (Not cited.)

Gregersen, E. M. & Evans, II, N. J. 2001, ApJ, 553, 1042 (Not cited.)

Gregersen, E. M., Evans, II, N. J., Zhou, S., & Choi, M. 1997, ApJ, 484, 256 (Not cited.)

Haikala, L. K., Harju, J., Mattila, K., & Toriseva, M. 2005, A&A, 431, 149 (Not cited.)

Hall, J. S. 1949, Science, 109, 166 (Not cited.)

Hartmann, L. 2001, Accretion Processes in Star Formation (Not cited.)

Hartmann, L., Ballesteros-Paredes, J., & Bergin, E. A. 2001, ApJ, 562, 852 (Not cited.)

Hartquist, T. W. & Williams, D. A. 1990, MNRAS, 247, 343 (Not cited.)

Hasegawa, T. I., Herbst, E., & Leung, C. M. 1992, ApJS, 82, 167 (Not cited.)

Hennebelle, P. 2013, in EAS Publications Series, Vol. 62, EAS Publications Series, 67–94 (Not cited.)

Hennebelle, P. & André, P. 2013, ArXiv e-prints (Not cited.)

Hennebelle, P. & Fromang, S. 2008, A&A, 477, 9 (Not cited.)

Herbst, E. & Klemperer, W. 1973, ApJ, 185, 505 (Not cited.)

Herbst, E. & Leung, C. M. 1989, ApJS, 69, 271 (Not cited.)

Herschel, Sir, J. F. W. 1847, Results of astronomical observations made during the years 1834, 5, 6, 7, 8, at the Cape of Good Hope; being the completion of a telescopic survey of the whole surface of the visible heavens, commenced in 1825 (Not cited.)

Heyer, M. H. & Terebey, S. 1998, ApJ, 502, 265 (Not cited.)

Hill, T., André, P., Arzoumanian, D., et al. 2012, A&A, 548, L6 (Not cited.)

Hill, T., Motte, F., Didelon, P., et al. 2011, A&A, 533, A94 (Not cited.)

Hiltner, W. A. 1949, Science, 109, 165 (Not cited.)

Hiramatsu, M., Hayakawa, T., Tatematsu, K., et al. 2007, ApJ, 664, 964 (Not cited.)

Hollenbach, D. J., Werner, M. W., & Salpeter, E. E. 1971, ApJ, 163, 165 (Not cited.)

Inutsuka, S.-I. & Miyama, S. M. 1992, ApJ, 388, 392 (Not cited.)

Inutsuka, S.-I. & Miyama, S. M. 1997, ApJ, 480, 681 (Not cited.)

Jappsen, A.-K. & Klessen, R. S. 2004, A&A, 423, 1 (Not cited.)

Johnstone, D., Di Francesco, J., & Kirk, H. 2004, ApJ, 611, L45 (Not cited.)

Johnstone, D., Wilson, C. D., Moriarty-Schieven, G., et al. 2000, ApJ, 545, 327 (Not cited.)

Keto, E. & Field, G. 2005, ApJ, 635, 1151 (Not cited.)

Kirk, J. M., Ward-Thompson, D., & André, P. 2005, MNRAS, 360, 1506 (Not cited.)

Kirk, J. M., Ward-Thompson, D., & Crutcher, R. M. 2006, MNRAS, 369, 1445 (Not cited.)

Kirk, J. M., Ward-Thompson, D., Palmeirim, P., et al. 2013, MNRAS, 432, 1424 (Not cited.)

Knowles, S. H., Mayer, C. H., Cheung, A. C., Rank, D. M., & Townes, C. H. 1969, Science, 163, 1055 (Not cited.)

Knude, J. & Høg, E. 1998, A&A, 338, 897 (Not cited.)

Könyves, V., André, P., Men'shchikov, A., et al. 2010a, A&A, 518, L106 (Not cited.)

Könyves, V., André, P., Men'shchikov, A., et al. 2010b, A&A, 518, L106 (Not cited.)

Krumholz, M. R. 2012, ApJ, 759, 9 (Not cited.)

Lada, C. J. 1987, in IAU Symposium, Vol. 115, Star Forming Regions, ed. M. Peimbert & J. Jugaku, 1–17 (Not cited.)

Lada, C. J. & Lada, E. A. 2003, ARA&A, 41, 57 (Not cited.)

Ladd, E. F., Wong, T., Bourke, T. L., & Thompson, K. L. 2011, ApJ, 743, 108 (Not cited.)

Lai, S.-P., Crutcher, R. M., Girart, J. M., & Rao, R. 2002, ApJ, 566, 925 (Not cited.)

Larson, R. B. 1969, MNRAS, 145, 271 (Not cited.)

Larson, R. B. 1981, MNRAS, 194, 809 (Not cited.)

Larson, R. B. 1985, MNRAS, 214, 379 (Not cited.)

Lazarian, A. 2007, Journal of Quant. Spectr. & Radiative Transfer, 106, 225 (Not cited.)

Lee, C. W. & Myers, P. C. 1999, ApJS, 123, 233 (Not cited.)

Lee, C. W., Myers, P. C., & Tafalla, M. 1999, ApJ, 526, 788 (Not cited.)

Lehtinen, K., Haikala, L. K., Mattila, K., & Lemke, D. 2001, A&A, 367, 311 (Not cited.)

Lehtinen, K., Harju, J., Kontinen, S., & Higdon, J. L. 2003, A&A, 401, 1017 (Not cited.)

Lesaffre, P., Belloche, A., Chièze, J.-P., & André, P. 2005, A&A, 443, 961 (Not cited.)

Leung, C. M. & Brown, R. L. 1977, ApJ, 214, L73 (Not cited.)

Li, Z.-Y. & Shu, F. H. 1996, ApJ, 472, 211 (Not cited.)

Luhman, K. L. 2007, ApJS, 173, 104 (Not cited.)

Luhman, K. L. 2008, Chamaeleon, ed. B. Reipurth, 169 (Not cited.)

Mac Low, M.-M. 2003, in Lecture Notes in Physics, Berlin Springer Verlag, Vol. 614, Turbulence and Magnetic Fields in Astrophysics, ed. E. Falgarone & T. Passot, 182–212 (Not cited.)

Mac Low, M.-M. & Klessen, R. S. 2004a, Reviews of Modern Physics, 76, 125 (Not cited.)

Mac Low, M.-M. & Klessen, R. S. 2004b, Reviews of Modern Physics, 76, 125 (Not cited.)

Machida, M. N., Inutsuka, S.-i., & Matsumoto, T. 2008, ApJ, 676, 1088 (Not cited.)

Mardones, D., Myers, P. C., Tafalla, M., et al. 1997, ApJ, 489, 719 (Not cited.)

Masunaga, H., Miyama, S. M., & Inutsuka, S.-I. 1998, ApJ, 495, 346 (Not cited.)

Mattila, K., Liljeström, T., & Toriseva, M. 1989, in European Southern Observatory Conference and Workshop Proceedings, Vol. 33, European Southern Observatory Conference and Workshop Proceedings, ed. B. Reipurth, 153–171 (Not cited.)

Maury, A. J., André, P., Men'shchikov, A., Könyves, V., & Bontemps, S. 2011, A&A, 535, A77 (Not cited.)

McCall, B. J., Huneycutt, A. J., Saykally, R. J., et al. 2003, Nature, 422, 500 (Not cited.)

McKee, C. F. 1999, in NATO ASIC Proc. 540: The Origin of Stars and Planetary Systems, ed. C. J. Lada & N. D. Kylafis, 29 (Not cited.)

Men'shchikov, A., André, P., Didelon, P., et al. 2010, A&A, 518, L103 (Not cited.)

Merrill, P. W. 1934, PASP, 46, 206 (Not cited.)

Mestel, L. 1985, in Protostars and Planets II, ed. D. C. Black & M. S. Matthews, 320–339 (Not cited.)

Miettinen, O., Harju, J., Haikala, L. K., & Juvela, M. 2010, A&A, 524, A91 (Not cited.)

Miettinen, O., Hennemann, M., & Linz, H. 2011, A&A, 534, A134 (Not cited.)

Miville-Deschênes, M.-A., Martin, P. G., Abergel, A., et al. 2010, A&A, 518, L104 (Not cited.)

Mizuno, A., Hayakawa, T., Tachihara, K., et al. 1999, PASJ, 51, 859 (Not cited.)

Mizuno, A., Yamaguchi, R., Tachihara, K., et al. 2001, PASJ, 53, 1071 (Not cited.)

Molinari, S., Swinyard, B., Bally, J., et al. 2010, A&A, 518, L100 (Not cited.)

Momose, M., Hiramatsu, M., Tsukagoshi, T., et al. 2009, in American Institute of Physics Conference Series, Vol. 1158, American Institute of Physics Conference Series, ed. T. Usuda, M. Tamura, & M. Ishii, 141–142 (Not cited.)

Morales Ortiz, J. L., Olmi, L., Burton, M., et al. 2012, A&A, 543, A65 (Not cited.)

Motte, F. & André, P. 2001, A&A, 365, 440 (Not cited.)

Motte, F., Andre, P., & Neri, R. 1998, A&A, 336, 150 (Not cited.)

Motte, F., André, P., Ward-Thompson, D., & Bontemps, S. 2001, A&A, 372, L41 (Not cited.)

Mouschovias, T. C. 1976, ApJ, 206, 753 (Not cited.)

Mouschovias, T. C. 1977, ApJ, 211, 147 (Not cited.)

Mouschovias, T. C. 1979, ApJ, 228, 475 (Not cited.)

Mouschovias, T. C. 1987, in NATO ASIC Proc. 210: Physical Processes in Interstellar Clouds, ed. G. E. Morfill & M. Scholer, 453–489 (Not cited.)

Mouschovias, T. C. 1991, ApJ, 373, 169 (Not cited.)

Mouschovias, T. C., Tassis, K., & Kunz, M. W. 2006, ApJ, 646, 1043 (Not cited.)

Müller, H. S. P., Schlöder, F., Stutzki, J., & Winnewisser, G. 2005, Journal of Molecular Structure, 742, 215 (Not cited.)

Myers, P. C. 1983, ApJ, 270, 105 (Not cited.)

Myers, P. C. 2009, ApJ, 700, 1609 (Not cited.)

Myers, P. C., Bachiller, R., Caselli, P., et al. 1995, ApJ, 449, L65 (Not cited.)

Myers, P. C. & Khersonsky, V. K. 1995, ApJ, 442, 186 (Not cited.)

Myers, P. C. & Lazarian, A. 1998, ApJ, 507, L157 (Not cited.)

Myers, P. C., Mardones, D., Tafalla, M., Williams, J. P., & Wilner, D. J. 1996, ApJ, 465, L133 (Not cited.)

Nakamura, F. & Li, Z.-Y. 2005, ApJ, 631, 411 (Not cited.)

Nakano, T. 1998, ApJ, 494, 587 (Not cited.)

Nguyen Luong, Q., Motte, F., Schuller, F., et al. 2011, A&A, 529, A41 (Not cited.)

Nielbock, M., Launhardt, R., Steinacker, J., et al. 2012, A&A, 547, A11 (Not cited.)

Nutter, D. & Ward-Thompson, D. 2007, MNRAS, 374, 1413 (Not cited.)

Öberg, K. I., Boogert, A. C. A., Pontoppidan, K. M., et al. 2011, ApJ, 740, 109 (Not cited.)

Öberg, K. I., van Dishoeck, E. F., & Linnartz, H. 2009, A&A, 496, 281 (Not cited.)

Omukai, K. 2007, PASJ, 59, 589 (Not cited.)

Onishi, T., Mizuno, A., Kawamura, A., Ogawa, H., & Fukui, Y. 1998, ApJ, 502, 296 (Not cited.)

Onishi, T., Mizuno, A., Kawamura, A., Tachihara, K., & Fukui, Y. 2002, ApJ, 575, 950 (Not cited.)

Padoan, P., Juvela, M., Goodman, A. A., & Nordlund, Å. 2001, ApJ, 553, 227 (Not cited.)

Padoan, P. & Nordlund, Å. 2002, ApJ, 576, 870 (Not cited.)

Pagani, L., Pardo, J.-R., Apponi, A. J., Bacmann, A., & Cabrit, S. 2005, A&A, 429, 181 (Not cited.)

Palla, F. & Stahler, S. W. 2000, ApJ, 540, 255 (Not cited.)

Palmeirim, P., André, P., Kirk, J., et al. 2013, A&A, 550, A38 (Not cited.)

Penston, M. V. 1969, MNRAS, 144, 425 (Not cited.)

Pezzuto, S., Elia, D., Schisano, E., et al. 2012, A&A, 547, A54 (Not cited.)

Pickett, H. M., Poynter, R. L., Cohen, E. A., et al. 1998, Journal of Quant. Spectr. & Radiative Transfer, 60, 883 (Not cited.)

Pilbratt, G. L., Riedinger, J. R., Passvogel, T., et al. 2010, A&A, 518, L1 (Not cited.)

Pineda, J. E., Arce, H. G., Schnee, S., et al. 2011, ApJ, 743, 201 (Not cited.)

Pineda, J. E., Goodman, A. A., Arce, H. G., et al. 2010, ApJ, 712, L116 (Not cited.)

Pirogov, L., Zinchenko, I., Caselli, P., Johansson, L. E. B., & Myers, P. C. 2003, A&A, 405, 639 (Not cited.)

Pon, A., Johnstone, D., & Heitsch, F. 2011, ApJ, 740, 88 (Not cited.)

Przybilla, N., Nieva, M.-F., & Butler, K. 2008, ApJ, 688, L103 (Not cited.)

Rao, R., Girart, J. M., Marrone, D. P., Lai, S.-P., & Schnee, S. 2009, ApJ, 707, 921 (Not cited.)

Rathborne, J. M., Lada, C. J., Muench, A. A., et al. 2009, ApJ, 699, 742 (Not cited.)

Redman, M. P., Keto, E., & Rawlings, J. M. C. 2006, MNRAS, 370, L1 (Not cited.)

Reipurth, B., Nyman, L.-A., & Chini, R. 1996, A&A, 314, 258 (Not cited.)

Robitaille, T. P., Whitney, B. A., Indebetouw, R., Wood, K., & Denzmore, P. 2006, ApJS, 167, 256 (Not cited.)

Sadavoy, S. I., di Francesco, J., André, P., et al. 2012, A&A, 540, A10 (Not cited.)

Sadavoy, S. I., Di Francesco, J., Bontemps, S., et al. 2010, ApJ, 710, 1247 (Not cited.)

Saigo, K. & Tomisaka, K. 2011, ApJ, 728, 78 (Not cited.)

Saigo, K., Tomisaka, K., & Matsumoto, T. 2008, ApJ, 674, 997 (Not cited.)

Schwartz, R. D. 1977, ApJS, 35, 161 (Not cited.)

Shinnaga, H., Phillips, T. G., Furuya, R. S., & Kitamura, Y. 2009, ApJ, 706, L226 (Not cited.)

Shu, F. H. 1977, ApJ, 214, 488 (Not cited.)

Shu, F. H., Adams, F. C., & Lizano, S. 1987, ARA&A, 25, 23 (Not cited.)

Sipilä, O., Hugo, E., Harju, J., et al. 2010, A&A, 509, A98 (Not cited.)

Smith, R. J., Shetty, R., Stutz, A. M., & Klessen, R. S. 2012, ApJ, 750, 64 (Not cited.)

Solomon, P. M. & Rivolo, A. R. 1989, ApJ, 339, 919 (Not cited.)

Solomon, P. M., Sanders, D. B., & Rivolo, A. R. 1985, ApJ, 292, L19 (Not cited.)

Solomon, P. M. & Werner, M. W. 1971, ApJ, 165, 41 (Not cited.)

Solomon, P. M. & Wickramasinghe, N. C. 1969, ApJ, 158, 449 (Not cited.)

Spezzi, L., Alcalá, J. M., Covino, E., et al. 2008, ApJ, 680, 1295 (Not cited.)

Spitzer, L. 1968, Diffuse matter in space (Not cited.)

Spitzer, L. 1978, Physical processes in the interstellar medium (Not cited.)

Stahler, S. W. & Palla, F. 2005, The Formation of Stars (Not cited.)

Stahler, S. W. & Yen, J. J. 2010, MNRAS, 407, 2434 (Not cited.)

Sugitani, K., Nakamura, F., Tamura, M., et al. 2010, ApJ, 716, 299 (Not cited.)

Swings, P. 1937, MNRAS, 97, 212 (Not cited.)

Swings, P. & Rosenfeld, L. 1937, ApJ, 86, 483 (Not cited.)

Tafalla, M., Mardones, D., Myers, P. C., et al. 1998, ApJ, 504, 900 (Not cited.)

Tafalla, M., Myers, P. C., Caselli, P., & Walmsley, C. M. 2004, A&A, 416, 191 (Not cited.)

Tafalla, M., Myers, P. C., Caselli, P., Walmsley, C. M., & Comito, C. 2002, ApJ, 569, 815 (Not cited.)

Tassis, K. & Mouschovias, T. C. 2007, ApJ, 660, 388 (Not cited.)

Terebey, S., Chandler, C. J., & André, P. 1993, ApJ, 414, 759 (Not cited.)

Testi, L. & Sargent, A. I. 1998, ApJ, 508, L91 (Not cited.)

Tobin, J. J., Hartmann, L., Bergin, E., et al. 2012, ApJ, 748, 16 (Not cited.)

Tomida, K., Machida, M. N., Saigo, K., Tomisaka, K., & Matsumoto, T. 2010, ApJ, 725, L239 (Not cited.)

Tomisaka, K. 2002, ApJ, 575, 306 (Not cited.)

Tomisaka, K. & Tomida, K. 2011, PASJ, 63, 1151 (Not cited.)

Tóth, L. V., Hotzel, S., Krause, O., et al. 2000, A&A, 364, 769 (Not cited.)

Townes, C. H. & Schawlow, A. L. 1955, Microwave Spectroscopy (Not cited.)

Troland, T. H. & Crutcher, R. M. 2008, ApJ, 680, 457 (Not cited.)

Tsitali, A. E., Belloche, A., Commerçon, B., & Menten, K. M. 2013, A&A, 557, A98 (Not cited.)

Tsitali, A. E., Bourke, T. L., Peterson, D. E., et al. 2010, ApJ, 725, 2461 (Not cited.)

Turner, B. E. & Ziurys, L. M. 1988, Interstellar molecules and astrochemistry, ed. K. I. Kellermann & G. L. Verschuur, 200–254 (Not cited.)

Vasyunina, T., Linz, H., Henning, T., et al. 2011, A&A, 527, A88 (Not cited.)

Vasyunina, T., Vasyunin, A. I., Herbst, E., & Linz, H. 2012, ApJ, 751, 105 (Not cited.)

Vázquez-Semadeni, E., Kim, J., Shadmehri, M., & Ballesteros-Paredes, J. 2005, ApJ, 618, 344 (Not cited.)

Vazquez-Semadeni, E., Ostriker, E. C., Passot, T., Gammie, C. F., & Stone, J. M. 2000, Protostars and Planets IV, 3 (Not cited.)

Walker, C. K., Lada, C. J., Young, E. T., Maloney, P. R., & Wilking, B. A. 1986, ApJ, 309, L47 (Not cited.)

Walmsley, C. M., Flower, D. R., & Pineau des Forêts, G. 2004, A&A, 418, 1035 (Not cited.)

Ward-Thompson, D., Di Francesco, J., Hatchell, J., et al. 2007, PASP, 119, 855 (Not cited.)

Ward-Thompson, D., Kirk, J. M., André, P., et al. 2010, A&A, 518, L92 (Not cited.)

Ward-Thompson, D., Motte, F., & Andre, P. 1999, MNRAS, 305, 143 (Not cited.)

Ward-Thompson, D., Scott, P. F., Hills, R. E., & Andre, P. 1994, MNRAS, 268, 276 (Not cited.)

Ward-Thompson, D. & Whitworth, A. P. 2011, An Introduction to Star Formation (Not cited.)

Watson, W. D. & Salpeter, E. E. 1972, ApJ, 174, 321 (Not cited.)

Weaver, H., Williams, D. R. W., Dieter, N. H., & Lum, W. T. 1965, Nature, 208, 29 (Not cited.)

Weinreb, S., Barrett, A. H., Meeks, M. L., & Henry, J. C. 1963, Nature, 200, 829 (Not cited.)

Whitney, B. A., Wood, K., Bjorkman, J. E., & Cohen, M. 2003, ApJ, 598, 1079 (Not cited.)

Whittet, D. C. B., Cook, A. M., Herbst, E., Chiar, J. E., & Shenoy, S. S. 2011, ApJ, 742, 28 (Not cited.)

Whittet, D. C. B., Prusti, T., Franco, G. A. P., et al. 1997, A&A, 327, 1194 (Not cited.)

Williams, J. P., Bergin, E. A., Caselli, P., Myers, P. C., & Plume, R. 1998, ApJ, 503, 689 (Not cited.)

Williams, J. P., Blitz, L., & McKee, C. F. 2000, Protostars and Planets IV, 97 (Not cited.)

Williams, J. P., Myers, P. C., Wilner, D. J., & di Francesco, J. 1999, ApJ, 513, L61 (Not cited.)

Wilson, T. L., Rohlfs, K., & Hüttemeister, S. 2009, Tools of Radio Astronomy (Springer-Verlag) (Not cited.)

Wilson, T. L. & Rood, R. 1994, ARA&A, 32, 191 (Not cited.)

Winston, E., Cox, N. L. J., Prusti, T., et al. 2012, A&A, 545, A145 (Not cited.)

Wouterloot, J. G. A., Brand, J., & Henkel, C. 2005, A&A, 430, 549 (Not cited.)

Yorke, H. W. & Bodenheimer, P. 1999, ApJ, 525, 330 (Not cited.)

Yorke, H. W., Bodenheimer, P., & Laughlin, G. 1993, ApJ, 411, 274 (Not cited.)

Yorke, H. W., Bodenheimer, P., & Laughlin, G. 1995, ApJ, 443, 199 (Not cited.)

Young, K. E., Harvey, P. M., Brooke, T. Y., et al. 2005, ApJ, 628, 283 (Not cited.)

Zhou, S. 1992, ApJ, 394, 204 (Not cited.)

Zweibel, E. G. 2002, ApJ, 567, 962 (Not cited.)

Zweibel, E. G. & McKee, C. F. 1995, ApJ, 439, 779 (Not cited.)

Acknowledgements

The PhD journey has certainly been a remarkable experience that has now come to an end. I owe my gratitude to several outstanding people who either directly or indirectly contributed toward its completion.

First of all, I would like to thank Prof. Karl Menten for giving me the opportunity to be part of his group consisting of incredible scientists that I have had the pleasure to learn a lot from. His guidance and willingness to always offer insightful suggestions despite his hectic schedule are greatly appreciated.

I am deeply indebted to Dr. Arnaud Belloche who has been a constant source of incredible advice and guidance. This work would certainly not have reached its current state without him. His knowledge, meticulousness, scientific curiosity, and support have not only had a major influence on the scientific content of this work; on a personal level, they also served as motivation and inspiration that helped me overcome hardships along the way. For this I will always be grateful.

I have also been privileged to be a member of the IMPRS School of Astronomy & Astrophysics in Bonn and Cologne, which has offered me not only the financial support necessary to conduct the largest part of this work, but also made me part of a welcoming scientific community that has strived to teach and inspire us as scientists and individuals. The students of the IMPRS school are not only great scientists, but also incredible people, and friends, so I thank them for them being there for me and for giving me lots of joyful memories.

More specifically, I would like to thank Dr. Manolis Angelakis for always providing me with great advice when mostly needed and for dedicating a great part of his time to personally support the students of the IMPRS school though their respective studies. I am also grateful to the IMPRS secretary, Frau Simone Pott, for her behing-the-scenes organisational work that has greatly contributed to the smooth running of our IMPRS events.

I would also like to express my appreciation to Mrs Barbara Menten and Mrs Le Tran for the immense help I received regarding settling in Germany at the beginning of my PhD.

Words are inadequate to express my gratitude to my family for their invaluable support throughout my studies. My mother, Annie Kavaka, has been a consistent source of optimism, unceasing support, and the cornerstone of every success. The same is to be said for my grandparents, Anastasia & Zisis, who never fail to support me. I thank my aunt and uncle, Simela & Sakis, for always succeeding in making my work sound full of mystery and adventure with their entertaining questions about my daily experiences with alien findings and dangerous comets, which I attempt to do justice with great effort.

Last but not least, I thank Brian for all the time he has spent sitting on airplanes, for his support, and for patiently waiting for me to finish my work.

Erklärung

Ich versichere, dass ich die von mir vorgelegte Dissertation selbständig angefertigt, die benutzten Quellen und Hilfsmittel vollständig angegeben und die Stellen der Arbeit – einschliesslich Tabellen, Karten und Abbildungen –, die anderen Werken im Wortlaut oder dem Sinn nach entnommen sind, in jedem Einzelfall als Entlehnung kenntlich gemacht habe; dass diese Dissertation noch keiner anderen Fakultät oder Universität zur Prüfung vorgelegen hat; dass sie noch nicht veröffentlicht worden ist sowie, dass ich eine solche Veröffentlichung vor Abschluss des Promotionsverfahrens nicht vornehmen werde. Die Bestimmungen dieser Promotionsordnung sind mir bekannt. Die von mir vorgelegte Dissertation ist von Prof. Dr. Karl Menten betreut worden.

Unterschift:

_____

Datum:

_____

Curriculum Vitae

Education

2010 – 2013, *PhD in Astronomy*
Max-Planck Institute for Radio Astronomy & University of Bonn, Germany
Supervisors: Prof. Dr. Karl Menten, Dr. Arnaud Belloche
Topic: Submillimiter studies of low-mass star-forming regions

2006 – 2010, *Master of Physics: Mphys Astrophysics with a Year Abroad*
University of Southampton, UK
Tutor: Prof. Dr. Tom Maccarone
Subjects: Physics, astronomy, mathematics
Grade: First Class Honours

2009 – 2010, *Year abroad: research for Master thesis*
Harvard-Smithsonian Center for Astrophysics, Cambridge, USA
Supervisor: Dr. Tyler Bourke
Topic: Low-mass star formation

2003 – 2006, *High School Diploma 'Apolytirio'*
1st Eniaio Lyceum, Edessa, Greece

Refereed publications

1. The Spitzer c2d Survey of Nearby Dense Cores. X. Star Formation in L673 and CB188
   Tsitali, A. E.; Bourke, T. L.; Peterson, D. E.; Myers, P. C.; Dunham, M. M.; Evans, N. J., II; Huard, T. L.
   The Astrophysical Journal, Volume 725, Issue 2, article id. 2461-2479 (2010)
2. The dynamical state of the first hydrostatic core candidate Chamaeleon-MMS1
   Tsitali, A. E.; Belloche, A.; Commerçon, B.; Menten, K. M.
   Astronomy & Astrophysics, Volume 557, id.A98, 25 pp (2013)

Submitted for publication

1. Star formation in Chamaeleon I and III: a molecular line study of the starless core population
   Tsitali, A. E.; Belloche, A.; Garrod, R. T.; Parise, B.; Menten, K. M.
   Submitted for publication to Astronomy & Astrophysics (2013)